An Intense Attosecond Light Source - from Generation to Application

Rading, Linnea

2016

Document Version:
Publisher's PDF, also known as Version of record

An Intense Attosecond Light Source - from Generation to Application

Linnea Rading

Doctoral Thesis
2017

Lund University

An Intense Attosecond Light Source -
from Generation to Application

Printed in Sweden by Media-Tryck, Lund, 2016

Division of Atomic Physics
Department of Physics
Faculty of Engineering, LTH
Lund University
P.O. Box 118
221 00 Lund
Sweden
www.atomic.physics.lu.se

ISSN: 0281-2762
Lund Reports on Atomic Physics, LRAP 532 (2016)
ISBN: 978-91-7753-088-6 (print)
ISBN: 978-91-7753-089-3 (pdf)

Abstract

Short and intense XUV pulses are important tools to study ultrafast dynamics and non-linear processes in matter. These pulses can be generated by free electron lasers (FELs) or by high-order harmonic generation (HHG), which are two complementary techniques. The advantage of HHG is the possibility to generate pulses with durations on the attosecond timescale, but the low conversion efficiency of the process makes it difficult to achieve pulses sufficiently intense for non-linear ionization.

In HHG an infrared (IR) laser pulse is focused into a gas and new, higher frequencies in the extreme ultraviolet (XUV) regime are generated. To achieve intense XUV light, many photons must be generated and subsequently focused tightly in the experiment. This thesis describes the build-up of the Intense XUV Beamline in Lund and development of spectrometers used to study the charged fragments resulting from the non-linear ionization.

An energetic and low repetition rate laser is used, and by focusing the pulse using a long focal length lens, the optimum intensity for HHG can be achieved in a large volume of gas. The XUV beam is tightly focused in the experiment using a short focal length mirror. Due to the low repetition rate in the experiment, a spectrometer that can record many events per shot was designed and constructed. The spectrometer is a double sided velocity map imaging spectrometer (DVMIS) that can record electrons and ions simultaneously. By using covariance techniques, correlations between fragments can be retrieved.

The XUV pulses generated in the beamline are sufficiently intense to induce non-linear effects in matter and have been used to study two-photon double ionization of neon.

Populärvetenskaplig sammanfattning

Människan behöver ljus för att kunna se och på så sätt försöka förstå världen omkring henne. Solens strålar består av olika våglängder och de våglängder som vi kan se är mellan 400 och 700 nanometer. När ljuset träffar ett föremål så absorberas vissa av dessa våglängder medan andra reflekteras så att vi kan se dem med våra ögon och på så sätt bilda oss en uppfattning om vilken färg ett föremål har. Båda ögonen ser samma föremål, men från lite olika vinklar, och det är därför vi kan se ett föremåls 3-dimensionella form. Människan kan se föremål som är ca 0.04 mm vilket är lite mindre än bredden på ett hårstrå, men för att se mindre föremål, som cellerna i hårstrået, behöver vi använda ett mikroskop. Oavsett vilket hjälpmedel vi använder kan man inte se saker som är mindre än våglängden på ljuset som används, och vi behöver använda ljus med en kortare våglängd än vad som är synligt för ögat när vi vill studera naturens små byggstenar, alltså molekyler, atomer och elektroner.

För ca en halv miljon år sedan [1] lärde sig människan att bemästra elden och först då kunde människor se och arbeta efter att solen gått ned på kvällen. Sedan dess har människan blivit bättre och bättre på att kontrollera ljus och 1960 uppfanns lasern av Theodore Maiman, vilket är ett exempel på precis kontroll av ljus. Ljuset från en laser är en välriktad ljusstråle som kan vara mycket intensiv. Med lasrar, som ofta sänder ut synligt ljus eller ljus med våglängder nära det synliga spektrumet, kan man åstadkomma extremt korta pulser. Pulserna från en laser kan vara så korta som några få femtosekunder. En femtosekund är en extremt kort tid och skriver man ut en femtosekund i siffror så är det 0,000000000000001 s eller 10^{-15} s. Ett annat sätt att förstå begreppet femtosekund är att det tar några tiotals femtosekunder för en molekyl som består av två atomer att dela på sig och bilda två joner. Även om extremt korta pulser kan genereras från en laser så vill vi kunna generera *ännu* kortare pulser för att studera än snabbare förlopp än det när en molekyl delar sig, som elektronernas rörelse i en molekyl eller atom. Dessa pulser kan vi generera i en process som kallas övertonsgenerering (high-order harmonic generation på engelska) där vi fokuserar en laserpuls i en gas och genererar pulser som är kortare än en femtosekund och dessutom har en våglängd som är hundra gånger kortare än den hos synligt ljus. Dessa pulser kallas XUV-pulser där XUV står för extreme ultraviolet.

Hur använder vi dessa korta pulser med XUV-ljus för att studera den mikroskopiska världen omkring oss som är osynlig för våra ögon? En XUV-foton har så mycket energi att om en atom eller molekyl absorberar en foton kan en elektron frigöra sig och en

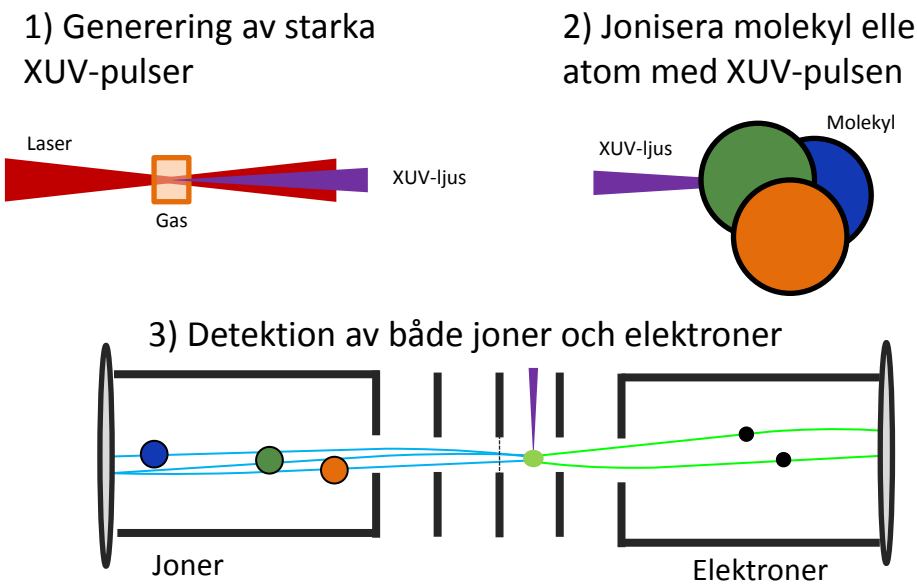

positivt laddad jon blir kvar. För att förstå hur en molekyl, och elektronerna i den, beter sig så skickar vi korta XUV-pulser på ett prov av atomer eller molekyler och mäter energin och riktningen på elektronen och/eller jonen som bildas med ett mätinstrument. Elektronerna och jonerna bär på information om systemet som joniserades. I bilden ovan så beskrivs det hur vi gör detta i tre steg. Först genererar vi korta och starka XUV-pulser, sedan belyser vi atomer eller molekyler med ljuset så att en eller flera elektroner frigör sig. Till sist studerar vi både elektronerna och jonerna för att försöka förstå mer om atomen eller molekylen.

För att förstå hur något ändras över tid i en atom eller molekyl så utför man pump-prob studier. Det betyder att man startar en händelse i ett system med en första puls och att man mäter vad som händer i systemet med en andra puls. Tiden mellan pulserna ändras och en bild tas för varje tidsskillnad och läggs ihop till en film. För att kunna använda XUV-pulser i pump-probstudier så krävs det att det finns tillräckligt många fotoner i pulserna för att det ska vara sannolikt att den atomen eller molekylen som träffades av pump-pulsen även träffas av prob-pulsen. För vanliga laserpulser är detta inget problem men att däremot generera XUV-pulser med många fotoner är en utmaning.

I denna doktorsavhandling beskrivs utvecklingen av ett strålrör där vi genererar starka XUV-pulser och experiment som visar att de innehåller tillräckligt många fotoner för att samma atom ska ha en möjlighet att bli träffad två gånger. De starka XUV-pulserna genereras genom att använda en energirik laserpuls i en stor volym gas. För att mäta både elektroner och joner så har jag utvecklat en spektrometer som använder sig av elektriska fält för att styra de laddade partiklarna mot två detektorer, elektronerna går åt ett håll och de positiva jonerna åt motsatt håll på grund av deras motsatta laddning. Genom att mäta både elektroner och joner så kan vi dra fler slutsatser om systemet som blev joniserat av XUV-pulserna än om vi endast mäter en av dem.

List of Publications

This thesis is based on Papers I-VIII. The papers are referred to by their Roman numerals in the text and appended at the end of the thesis.

I **Efficient high-order harmonic generation boosted by below-threshold harmonics**
F. Brizuela, C. M. Heyl, P. Rudawski, D. Kroon, L. Rading, J. M. Dahlström, J. Mauritsson, P. Johnsson, C. L. Arnold and A. L'Huillier.
Sci. Rep. **3**, 1410 (2013).

II **A high-flux high-order harmonic source**
P. Rudawski, C. M. Heyl, F. Brizuela, J. Schwenke, A. Persson, E. Mansten, R. Rakowski, L. Rading, F. Campi, B. Kim, P. Johnsson, and A. L'Huillier.
Rev. Sci. Inst. **84**, 073103 (2013).

III **Two-photon double ionization of neon using an intense attosecond pulse train**
B. Manschwetus*, L. Rading*, F. Campi, S. Maclot, H. Coudert-Alteirac, J. Lahl, H. Wikmark, P. Rudawski, C. M. Heyl, B. Farkas, T. Mohamed, A. L'Huillier, and P. Johnsson. (*Both authors contributed equally).
Phys. Rev. A **93**, 061402 (2016).

IV **Design and test of a broadband split-and-delay unit for attosecond XUV-XUV pump-probe experiments**
F. Campi, H. Coudert-Alteirac, M. Miranda, L. Rading, B. Manschwetus, P. Rudawski, A. L'Huillier, and P. Johnsson.
Rev. Sci. Inst. **87**, 023106 (2016).

V **Compression of TW class laser pulses in a planar hollow waveguide for applications in strong-field physics**
A. Jarnac, F. Brizuela, C. M. Heyl, P. Rudawski, F. Campi, B. Kim, L. Rading, P. Johnsson, A. Mysyrowicz, A. L'Huillier, A. Houard, and C. L. Arnold.
Optica **93**, 061402 (2015).

VI **Gating attosecond pulses in a noncollinear geometry**
M. Louisy, C. L. Arnold, M. Miranda, E. W. Larsen, S. N. Bengtsson, D. Kroon, M. Kotur, D. Guenot, L. Rading, P. Rudawski, F. Brizuela, F. Campi, B. Kim, A. Jarnac, A. Houard, J. Mauritsson, P. Johnsson, A. L'Huillier, and C. M. Heyl.
Optica **93**, 061402 (2015).

VII **Interference in the angular distribution of photoelectrons in superimposed XUV and optical laser fields**
S. Düsterer, L. Rading, P. Johnsson, A. Rouzée, A. Hundertmark, M. J. J. Vrakking, P. Radcliffe, M. Meyer, A. K. Kazansky, and N. M. Kabachnik.
J. Phys. B: At., Mol. Opt. Phys. **46**, 164026 (2013).

VIII **A versatile velocity map ion-electron covariance imaging spectrometer for high intensity XUV experiments**
L. Rading, S. Maclot, J. Lahl, F. Campi, H. Wikmark, B. Oostenrijk, M. Gisselbrecht, and P. Johnsson.
Manuscript in preparation.

Other related publications by the author:

Towards imaging of ultrafast molecular dynamics using FELs
A. Rouzée, P. Johnsson, L. Rading, A. Hundertmark, W. Siu, Y. Huismans, S. Düsterer, H. Redlin, F. Tavella, N. Stojanovic, A. Al-Shemmary, F. Lépine, D. M. P. Holland, T. Schlatholter, R. Hoekstra, H. Fukuzawa, K. Ueda, and M. J. J. Vrakking.
J. Phys. B: At., Mol. Opt. Phys. **46**, 164029 (2013).

Contents

Papers

Chapter 1

Introduction

When matter is irradiated by light, the energy of the light can be absorbed by an electron, and if this energy is higher than the so-called work function of the material, the electron will be ejected from the atom. This is called the photoelectric effect. If the impinging light has sufficiently high energy, increasing the intensity leads to a proportional increase in the number of electrons emitted. However, if the energy is lower than the work function, no electrons will be emitted, regardless of the intensity. At the beginning of the 20th century, light was regarded as electromagnetic waves, and the observation of the photoelectric effect therefore puzzled the scientists.

In 1905, Einstein explained the photoelectric effect by showing that light could also be regarded as particles, or photons. He showed that it was not the intensity of the light, but the frequency, that determined whether an electron would be ejected or not. He formulated the energy of a photon, E_{ph}, as hf, where f is the frequency and h is Planck's constant [2].

We now know that the observation of the photoelectric effect, which led to the description of light as quantized packets of energy, was not complete. If the intensity is sufficient, it *is* possible to eject an electron, through non-linear effects, even if the energy of the individual photons are less than the work function of the material.

In 1961, shortly after the invention of the laser, Peter Franken and co-workers observed the first non-linear effect in the visible region [3]. They focused a ruby laser with wavelength of 694.3 nm into a crystal and observed the second harmonic at 347.15 nm. By combining two photons of the same wavelength, they had created light with a new, shorter, wavelength. In the same way, it is possible to combine two or more photons to overcome the work function (often referred to as the ionization potential, Ip) of an atom or molecule, and in 1965 Voronov and Delone demonstrated multiphoton ionization of xenon for the first time [4].

In the years that followed, high-intensity laser light led to the discovery of many new phenomena, such as above-threshold ionization (ATI) [5], where the atom absorbs more photons than are required to eject an electron and high-order harmonic generation [6], where the ejected electron recombines with the ion, leading to the emission of light consisting of odd harmonics of the driving field. At such high intensities, the field can no longer be regarded as a perturbation to the atomic or molecular potential, and new theories were required to understand this new strong-field regime. These

discoveries have not only led to the development of new theories, but also to the creation of new fields of science, such as of high-order harmonic generation (HHG) and attosecond physics.

During the past 15 years, the research community has been striving to extend non-linear optics into the XUV and X-ray regimes. This means finding some way of generating XUV light or X-rays with sufficiently high intensity to be able to use at least two photons to ionize an atom. Today, two types of sources are available that can generate intense XUV light: free electron lasers (FELs) and high-order harmonic generation (HHG).

1.1 Motivation behind this work

The understanding of fundamental processes, such a ionization, excitation and dissociation, leads to a better understanding of the world around us. Light pulses can be used to trigger these processes, and by studying the resulting charged fragments, we can obtain insight into the structure and dynamics of the atoms and molecules. The ionization potential (Ip) of an atom or a small molecule is typically between 10 and 25 eV (helium has an Ip of 24.6 eV, while that of ammonia is 10.16 eV) and thus XUV radiation is well suited for studying these systems, since the absorption of one XUV photon leads to ionization. The fundamental processes involve fast dynamics on the attosecond and femtosecond timescales. For example, nuclear dynamics typically take place on the 10-100 fs scale, while charge migration in a molecule might take place during a few fs [7]. A light pulse cannot be shorter than the period of light, and by using XUV light with an energy of 30 eV, a theoretical pulse duration of 140 as can be achieved which can be compared to 2.7 fs for 800 nm infrared (IR) light.

To study dynamics in a system, we want to follow the system evolving in time by performing XUV pump-XUV probe experiments. In an XUV pump-XUV probe experiment, the first XUV pulse (the pump) is used to initiate dynamics, and the second XUV pulse is used to probe the system after a certain delay, which can be varied. These experiments require intense pulses because two photons, one from each pulse, must interact with the same target.

XUV pulses, with time durations on the attosecond time scale, and sufficiently intense to induce non-linear effects, are the perfect tool to study ultrafast dynamics in atoms and molecules.

1.2 Intense and short-pulse XUV sources

The two intense XUV radiation sources mentioned previously, namely HHG and FEL, use techniques that are fundamentally different as is reflected in the properties of the resulting XUV pulses.

In HHG, higher order harmonics of a driving laser are generated through a non-linear process by focusing an energetic laser pulse onto a target, e.g. a gas or a solid. The frequencies generated are odd orders of the driving field, which means that a train of pulses is created in the time domain. The length of the pulse train is typically slightly shorter than the length of the driving pulse, and the individual pulses in the train can have durations of less than 100 attoseconds. It is possible to generate a single attosecond pulse (SAP) by using various techniques which all involve the manipulation

of the driving field, and a SAP with pulse duration of 67 as at a central frequency of 60 eV has been reported [8]. The conversion efficiency of the HHG process is very low, typically 10^{-5} for generation in argon, and the generation of XUV pulses, especially single attosecond pulses (SAPs), using HHG, that are sufficiently intense to enable non-linear processes is very challenging.

Due to the low intensity of the XUV pulses from HHG, the most common way to study dynamics is by combining the XUV pulse with an ultrashort IR pulse in pump-probe experiments. This method has been succesful in studies of, for example, charge migration in molecules [9]. However, the IR pulse risks to distort the molecular potential. An XUV pulse, having the same intensity as an IR pulse, distorts the molecular potential much less due to its shorter wavelength and thus smaller effect on the bound electrons, and the intrinsic behaviour of the system can be studied.

In 2003, sufficiently high intensities were obtained through HHG to observe two-photon ionization with XUV radiation (7th to 13th harmonics of the 800 nm driving field) [10]. Since then, a number of XUV pump - XUV probe experiments have been performed, but the main focus has been to understand the two-photon process and to perform autocorrelations of the XUV pulse [11–13]. A few experiments have been reported where dynamics in atoms or small molecules are studied [14–16].

The XUV pulses from an FEL are generated from a beam of electrons that are accelerated in a linear accelerator to almost the speed of light. The accelerated electrons go into a magnetic structure, an undulator, causing them to follow a sinusoidal path and as they are accelerated, photons are sent out.

At first, the photons are emitted incoherently, and the number of photons generated is proportional to the number of electrons in the electron beam. The photons can, for a sufficiently long undulator, start to interact with the oscillating electrons, which leads to microbunching of the electrons. The microbunches emit light coherently, and the result is an exponential increase in the number of photons emitted. The process that initiates bunching of the light is called self-amplified spontaneous emission (SASE), and this stochastic process leads to a spectrum with a noisy structure that varies from shot to shot. The duration of the XUV pulse is limited by the minimum duration of the electron bunches that can be generated, and pulse lengths of a few tens of femtoseconds have been achieved for XUV wavelengths. An overview of short wavelength FELs is found in Ref. [17]. The XUV pulse energies generated by FELs widely surpass those possible with HHG, and as an example, the FEL in Hamburg (FLASH) generates pulse energies of a few hundred microjoules. The high intensites that can be achieved allows for studies of extreme non-linear processes in the XUV, and for XUV pump-XUV probe experiments [18, 19].

In 2007, two years after FLASH came into operation [20], ion charges up to Xe^{21+} were observed using 93 eV photons [18]. These highly non-linear processes are interesting in themselves, as it is an unexploited field of physics where we lack understanding of even the basic multiphoton ionization mechanisms.

XUV FELs have been extensively used to study fast dynamics, both using the XUV as pump and probe [19, 21], but also by combining the XUV pulse with an IR or VUV pulse [22]. However, the experiments are limited by the time resolution due to the pulse duration and the jitter between the pulses, if an IR or VUV pulse is used, and fast dynamics, such as electron motion, cannot be studied.

HHG cannot compete with the pulse energies generated by FELs, however, an important advantage of HHG is the shorter pulses and that the time resolution in an

IR-XUV experiment is better as the XUV and IR pulse are inherently synchronized since they are derived from the same source.

1.3 Background to this work and introduction to the papers

To study dynamics on the time scale where electron motion takes place, intense and short XUV pulses from HHG must be used. The main goal of this thesis work has been to build up a beamline, where energetic XUV pulses are genereated through HHG, together with an end-station for tight focusing of the XUV pulses, to achieve intensities that allow for non-linear ionization, and an spectrometer that can measure both the resulting positive and negative fragments.

Shortly after I started my PhD studies, the laboratory that hosts the Intense XUV Beamline was re-built and extended to allow for long focusing of the driving IR pulse, and the build-up of an end-station chamber, where the XUV could be focused to a smaller spot size to achieve higher intensities. Much experimental work had until then focused on the generation process and the characterization of the XUV radiation. By complementing the beamline with an end-station, the long-term goal was to study molecules and the fast processes taking place after ionization or excitation using a pulsed molecular source for gas, liquid and solid samples together with a double-sided velocity map imaging spectrometer (DVMIS) to record ions and electrons simultaneously.

My work has mainly been concerned with constructing this beamline, especially the end-station chamber, and the spectrometers. A milestone was reached when it was shown that the XUV intensity was sufficiently high for double ionization of neon with two photons, as presented in Paper III. Since then, I have designed and constructed a double-sided velocity map imaging spectrometer (DVMIS), and the first synchronized ion and electron VMI images were recently obtained.

I have also had the chance to do experiments at FLASH in Hamburg just after starting as a PhD student. The common denominators between the experiments at FLASH and at the Intense XUV Beamline in Lund are the intense XUV pulses and also the VMI spectrometers used. At FLASH we studied molecular dynamics by IR/UV-pump XUV-probe studies [22]. The synchronization of the pump and the probe pulse at FELs limits the time resolution, this is not the case in HHG since the XUV and the IR pulse derive from the same source and this is one of the strong motivations to develop intense XUV table-top sources based on high harmonic generation.

Papers I, II, III and V describe experiments conducted at the Intense XUV Beamline in Lund. Paper II describes experimental studies of the HHG process, including multiparameter scans to optimize the generation conditions and the phase matching for a loose focusing regime. Paper III describes an experiment in which an experimental chamber was added to the beamline. Non-linear ionization was observed, demonstrating that high intensities had been achieved. Paper I describes how HHG can be enhanced using a two-cell set-up, while Paper V describes the testing of a scheme for the compression of energetic ultra-short laser pulses. The experiment presented in Paper VI was performed on an HHG beamline using a kHz driving laser (not described in this thesis), but the idea was initially tested using the Intense XUV Beamline. Paper IV describes a split-and-delay unit for XUV pump-XUV probe experiments and off-line tests using an IR pulse. In Paper VIII, the double-sided velocity

map imaging spectrometer constructed for the Intense XUV Beamline, is described and the first experimental results are presented. Paper VII describes experiments performed at the FEL in Hamburg where the XUV was used to ionize neon in the pressence of an IR pulse, and sidebands and their angular distributions were studied.

1.4 Outline of this thesis

Chapter 2 describes the strong-field physics of IR and XUV pulses. Concepts such as ultra-short pulses, HHG and XUV non-linear ionization are introduced and discussed. Chapter 3 describes spectrometers used to measure electrons and ions after ionization, with focus on the DVMIS that I constructed for use at the Intense XUV Beamline in Lund. Chapter 4 describes the Intense XUV Beamline together with the experiments performed on this beamline, especially the non-linear experiments. The final chapter provides a summary and an outlook.

Chapter 2

Strong-field physics - from IR to XUV

The experiments described in this thesis all made use of intense IR and XUV light, so intense that the electric field could induce non-linear effects in a medium. An intense IR pulse is used to generate high-order harmonics of the driving field, and the experiment reported in Paper III shows that the XUV light generated in this process can be strong enough to in its turn non-linearly ionize a rare gas. The key to have intense light, at both IR and XUV wavelengths, is to be able to concentrate the generated photons in space and time. In space, the light can be focused tightly and in time, the energy is concentrated into ultra-short pulses.

This chapter introduces the concept of ultra-short pulses which is applicable to IR pulses generated in a laser cavity, XUV or X-ray pulses from free electron lasers, and attosecond pulses from high-order harmonic generation (HHG). HHG is then described with the help of the Three-Step Model. The chapter ends with a description of ionization, first with one XUV photon, and then XUV non-linear ionization involving more than one XUV photon.

2.1 Ultrashort pulses and pulse trains

Ultrashort IR and XUV pulses can be created when a broad range of frequencies with a fixed phase relation are combined, as explained later in this section. The mathematical description of the short pulses is the same for IR and XUV light, but the origin of the frequencies differs. In an IR laser cavity the bandwidth of the lasing medium together with the modes of the oscillator give rise to a comb of frequencies, and when the laser is mode-locked the result is a train of short pulses in the temporal domain. In HHG this comb of frequencies is instead generated by focusing a short, intense IR pulse into a gas, where odd harmonic orders of the driving frequency are created. Figure 2.1 shows frequency combs generated in an IR laser cavity and by HHG. The width of the frequency comb determines the shortest possible duration of the individual pulses, and the spacing between the frequencies involved determines the time between the pulses.

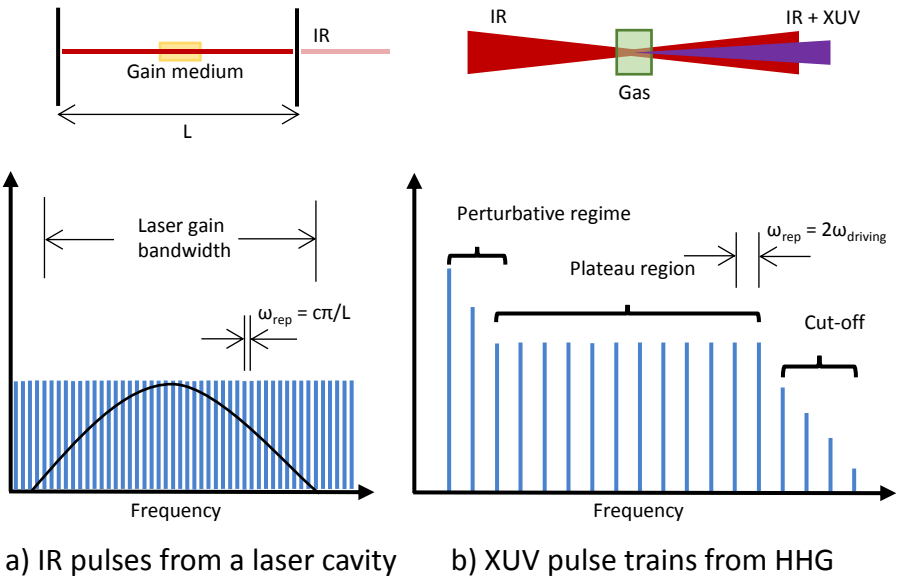

Figure 2.1: Frequency combs generated in a laser cavity (a) and by HHG (b) resulting in short IR pulses and short XUV pulses, respectively, if they are phase locked. The difference in frequency between two components is denoted ω_{rep}. Note that the frequency scale is different in the two illustrations.

While mode-locked oscillators have been used since the 1960s, HHG was accidentally discovered in 1986, in an experiment intended to study fluorescence from rare gases [6, 23]. They were surprised by the finding of high harmonic orders, and by the fact that the intensity did not decrease as rapidly as expected for a non-linear process, but was rather constant over many consecutive orders. It was early predicted that this broadband radiation could lead to very short, attosecond, pulses if the high-order harmonics were phase locked. Fifteen years after the discovery of HHG, evidence for single attosecond pulses was demonstrated [24, 25].

2.1.1 Mathematical description

Neglecting the magnetic field, which is small compared to the electric field, a monochromatic wave can be written as:

$$\widetilde{E}(t) = A_0 e^{i\omega t}, \tag{2.1}$$

where ω is the angular frequency and A_0 the amplitude. This is the complex representation, and the real part, $\mathbb{R}(\widetilde{E}(t))$, gives the physical electric field. In the case of pulses from a laser cavity and from HHG, monochromatic waves with equaly spaced frequencies ω_q are coherently added together, each with an amplitude A_q, and a phase ϕ_q.

$$\widetilde{E}(t) = \sum_q A_q e^{i\phi_q} e^{i\omega_q t}. \tag{2.2}$$

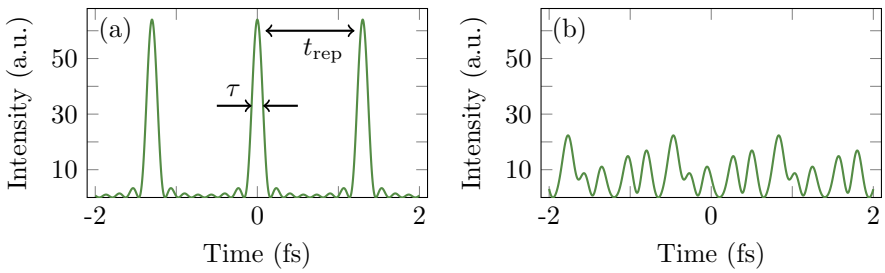

Figure 2.2: Harmonic orders with q = 15-25 of the 800 nm driving laser added up with (a) same phases and (b) random phases and attosecond pulses are formed in the first case.

This leads to a train of pulses where the time between the pulses, t_{rep}, depends on the frequency spacing, $\omega_{\text{rep}} = \omega_q - \omega_{q-1}$, and the width of the individual pulses, τ, is proportional to the total bandwidth of the frequencies involved, $\Delta\omega$:

$$t_{rep} = 2\pi/\omega_{rep}, \tag{2.3}$$

$$\tau \propto 2\pi/\Delta\omega. \tag{2.4}$$

Both IR and XUV pulse trains are described by the sum in Equation 2.2, but the results differ considerably, as shown in the following example. For IR laser pulses, the frequencies defined by the lasing medium and the oscillator, form the pulse train (Figure 2.1a). In a 1 m long laser cavity, the frequency spacing $\nu_{\text{rep}} = \omega_{\text{rep}}/2\pi$ is given by $c/2L = 1.5 \cdot 10^8$ Hz, resulting in a spacing between the pulses of about 1 ns. For XUV pulses, the pulse train is made up of the odd harmonics of the IR driving field (Figure 2.1b), and the frequency spacing is $2\omega/2\pi = 3.6 \cdot 10^{14}$ Hz for a 800 nm driving field. This corresponds to a time between the pulses of 1.3 fs.

Figure 2.2 shows the results of adding odd harmonics of the orders 15-25 of an 800 nm driving field when they have the same phase, ϕ_q, in (a) and when they have random phases in (b). It can be seen that a train of attosecond pulses is created when the harmonics have the same phase.

If a train of pulses is reduced to a single pulse, the corresponding frequency comb becomes a continuum. A train of pulses from an oscillator is typically reduced to a few pulses per second, using a pulse picker, before amplification for high energy lasers. In HHG it is possible to generate a single attosecond pulse (SAP) by manipulating the laser pulse, used for generation, in various ways together with selecting a spectral region of the light generated [26–29].

In the case of a single pulse, the sum over the frequencies (Equation 2.2) is instead written as an integral:

$$\widetilde{E}(t) = \int_{-\infty}^{+\infty} \widetilde{A}(\omega) e^{i\omega t} d\omega = \int_{-\infty}^{+\infty} A(\omega) e^{i\phi(\omega)} e^{i\omega t} d\omega. \tag{2.5}$$

This is recognized as the Fourier integral where $\widetilde{A}(\omega)$ is the Fourier transform of $\widetilde{E}(t)$ and $\phi(\omega)$ is the spectral phase. The spectral phase is important since it affects the shape of the pulse in the time domain. In the time domain, the pulse can be written as:

$$\widetilde{E}(t) = \widetilde{A}(t)e^{i\omega_0 t} = A(t)e^{i\omega_0 t}e^{i\phi(t)}, \tag{2.6}$$

where $\widetilde{A}(t)$ is the complex envelope, $\phi(t)$ its phase and ω_0 the central frequency. The instantaneous frequency, ω_i, of the pulse is given by:

$$\omega_i = \omega_0 + \frac{d\phi(t)}{dt}. \tag{2.7}$$

A pulse with a certain spectral intensity has the shortest pulse duration when the pulse is unchirped, meaning that the instantaneous frequency is the same throughout the pulse. This means that $\phi(t)$ in Equation 2.6 is constant or linear for an unchirped pulse, but in the latter case the central frequency of the pulse or the pulse train is shifted.

Taking $\phi(t) = bt^2$ as an example, the instantaneous frequency is $\omega_i = \omega_0 + 2bt$ and varies linearly in time, and the pulse is said to be linearly chirped. A pulse becomes chirped when travelling through a dispersive medium, meaning a medium in which the refractive index, n, is dependent on the wavelength, and thus different frequencies travel with different speeds, resulting in stretching of a short pulse. The shape and chirp of short pulses are important in the following discussion since chirped pulses allow the amplification of intense, ultrashort laser pulses, and also because the pulses generated in HHG are intrinsically chirped.

2.2 Generation of high-order harmonics

The XUV pulse trains described in the previous section and shown in Figure 2.2 were formed by combining odd frequencies of the driving laser field. High-order harmonics are generated by focusing a short, intense laser pulse into a gas target such that intensities on the order of 10^{14} W/cm^2 are achieved. The harmonic strength falls rapidly during the few first harmonic orders, followed by a plateau where the harmonics are of comparable strength. At a specific frequency, the cut-off frequency, the strength of the harmonics falls rapidly to zero (Figure 2.1b).

This phenomenon cannot be described using a perturbative description of the light-matter interaction. Figure 2.3 shows the potential of a hydrogen atom in an electric field corresponding to three different laser intensities. At low intensity (10^{13} W/cm^2) (a), the potential is barely distorted, and the dominating ionization mechanism is multiphoton ionization. At intermediate intensity ($5 \cdot 10^{14}$ W/cm^2) (b), a typical intensity where HHG takes place, a barrier is formed through which the electron can tunnel. At the highest intensity (10^{15} W/cm^2) (c), the barrier is suppressed, so the electron can leave the atom without tunnelling, and this is called over-the-barrier ionization.

The Three-Step Model (TSM) (also referred to as the semi-classical model or the simple man's model) provides a comprehensive understanding of the HHG process, and was first described in 1993 [30, 31]. The TSM combines concepts from both classical mechanics and quantum mechanics, and can explain many of the features of HHG such as the cut-off, the different trajectories and the intrinsic chirp of the attosecond pulses. Most importantly, it provides an intuitive picture, and this was an important step towards a more complete description that was presented in 1994 by Lewenstein

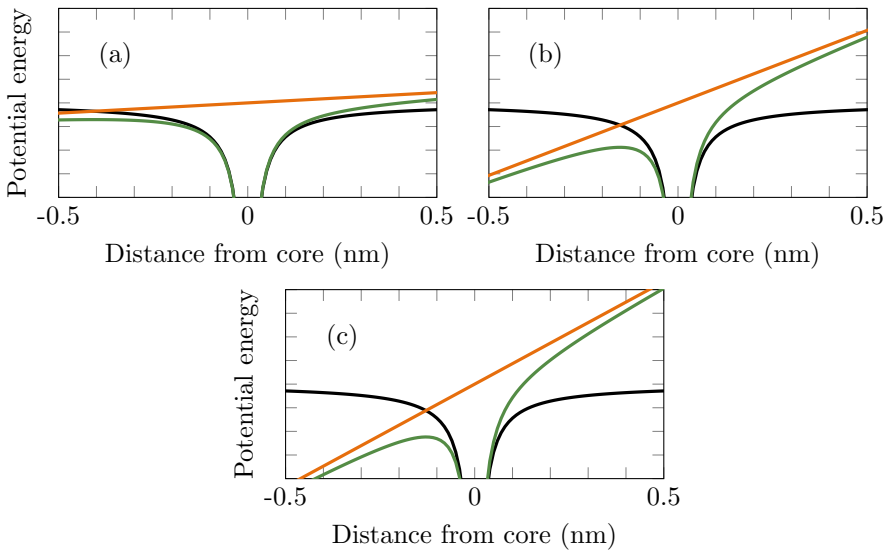

Figure 2.3: The unperturbed potential of hydrogen (black curve) and the potential of the driving field (orange) gives the resulting potential (green) for intensities of (a) $1 \cdot 10^{13}$ W/cm^2, (b) $5 \cdot 10^{14}$ W/cm^2 and (c) $1 \cdot 10^{15}$ W/cm^2. The dominant ionization mechanism in (a) is multiphoton ionization, in (b) tunnel ionization and in (c) over-the-barrier ionization.

and co-workers called the Strong Field Approximation (SFA) [32]. The SFA is a completely quantum mechanical approach where the time-dependent Schrödinger equation is solved under a number of assumptions. The description of HHG given in this thesis is based on the TSM. The SFA was used in the simulations presented in Paper VII, to describe XUV ionization in the presence of an IR field in an experiment performed with the Free-Electron Laser in Hamburg (FLASH).

2.2.1 The Three Step Model

In the TSM, the electron tunnels through the potential barrier in the first step, and is accelerated by the electric field of the light pulse in the second step. For certain tunnelling times, it is possible for the electron to be driven back to the ion where it has a small chance of recombining and emitting a high-energy photon, which constitutes the third step. Figure 2.4 illustrates the processes of tunnelling (1), acceleration (2) and recombination (3). In non-linear optics, the light is considered a perturbation, while here this is clearly not the case, as the potential barrier of the atom is strongly distorted. When the electron is free, the model neglects the potential of the ion and the electron is treated as a free electron in the electric field. The three steps are described briefly below for a monochromatic field, $E(t) = A_0 \sin(\omega t)$, polarized along z, where A_0 is the field amplitude and ω the laser angular frequency. A more detailed description can be found, for example, in Fundamentals of Attosecond Optics [33] and in the pioneering work of [30, 31].

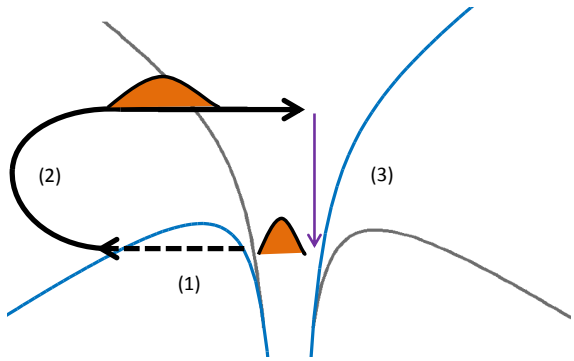

Figure 2.4: The three steps in the TSM: **(1)** The electron tunnels out through the barrier created by the laser field. **(2)** The electron wave packet gets accelerated (and dispersed) in the electric field. **(3)** The electron recombines with the ion and a light pulse is sent out.

Step 1: Tunnelling

The size of an atom is ≈ 0.1 nm, while the length of an oscillation is 800 nm, and the electric field can therefore be treated as constant over the atom and varying only in time. The potential of the electric field is given by integration of the electric field over space, z, which gives a function of space and time. $V_{\text{laser}}(z,t) = A_0 z \sin(\omega t)$. The potential to which the bound electron is exposed is a sum of the Coulomb potential and the electric field potential. (The resulting potential is illustrated in Figure 2.3b for an intensity of 10^{14} W/cm^2). The width of the barrier is a few Ångström and there is a small probability for the electron to tunnel out from the atom.

Step 2: Propagation in free space

After tunnelling, the electron is treated as a classical particle in the oscillating electric field. The force on the electron is $F(t) = -eE(t)$ and the position of the electron at time t can be found using the relation $F = \mathrm{m}\ddot{z}$:

$$z(t) = \frac{eA_0}{m\omega^2}[\sin(\omega t) - \sin(\omega t_i) - \omega(t - t_i)\cos(\omega t_i)], \tag{2.8}$$

where t_i is the time of ionization and m is the mass of the electron. Figure 2.5a shows the trajectories of electrons tunnelling out from the atom at different times. Electrons tunnelling between 0 and 0.25 T, where T is the period of the laser, will drift away from the ion and only electrons leaving the atom between 0.25 T and 0.5 T will be driven back to the ion and have the chance of recombining. The process is symmetric; thus, electrons leaving between 0.75 T and T will also return to the ion and two bursts of light will be emitted for every laser cycle, with a π phase shift between successive bursts. These bursts of light form the attosecond pulse train. The electrons acquire a phase in the continuum which is referred to as the dipole phase [34]. The phase acquired depends on the intensity of the field and the trajectory of the electron. Is it a valid assumption to neglect the atomic potential once the electron is in the continuum? Note that the maximum distance from the ion is no more than

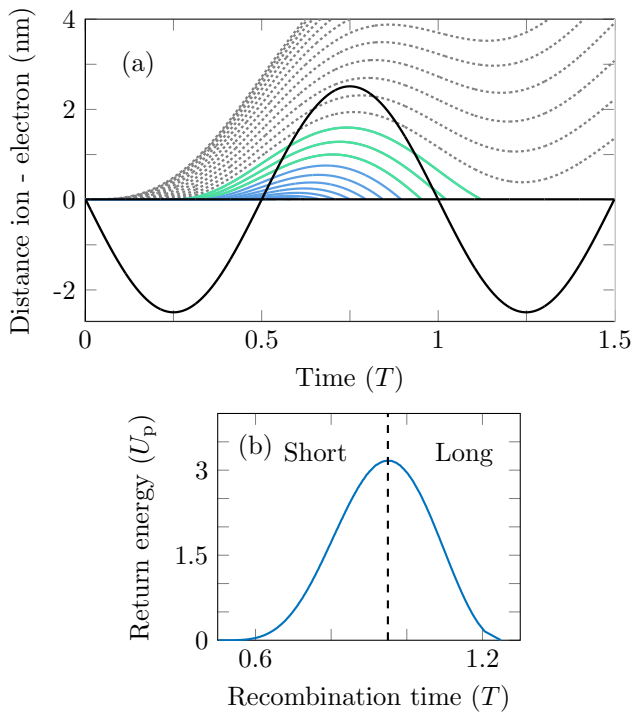

Figure 2.5: (a) Trajectories of electrons for different times of ionization. Electrons tunnelling between 0 and $T/4$ drift away from the ion (grey dotted line). Electrons that tunnel between $T/4$ and $T/2$ leave the ion but have a chance to recombine. The long trajectories are marked green and the short trajectories blue. (b) The return energy of the electrons as a function of their recombination time. The electron trajectories returning to the ion before the time corresponding to the maximum recombination energy are referred to as the short trajectories while the others are referred to as the long trajectories. The energy of the emitted light is dependent on the recombination time, and the emitted light pulses are thus intrinsically chirped: a positive chirp for the short trajectories and a negative chirp for the long trajectories.

2 nm for the long trajectories and well below 1 nm for the short trajectories at an intensity of 10^{14} W/cm^2 and 800 nm. This should be compared to the barrier, which is of the order of a few ångström, as can be seen in Figure 2.3b. The free electron is definitely affected by the Coulomb potential which must be taken into account in a more exact analysis.

Step 3: Recombination

The probability of the electron tunnelling through the barrier is highest at the maximum of the electric field, but only the electrons tunnelling between times 0.25 T and 0.5 T can recombine with the atom and contribute to HHG. Electrons tunnelling between 0 and 0.25 T increase the degree of ionization of the medium, which is an unavoidable effect (see Section 2.2.2). The short trajectories, shown in blue in Figure 2.5a, are formed from 0.3 T where the ionization rate is significantly lower. It is of

interest to enhance HHG from the short trajectories as they are most useful in experiments. The shape of the fundamental field can be altered by adding lower-order harmonics. This improves the ionization rate of the short trajectories as described in Paper I, and further discussed in Chapter 4.

The emitted photon energy, E_{ph}, is given by the sum of the ionization potential (Ip) and the kinetic energy of the electron at the time of recombination:

$$E_{\mathrm{ph}} = Ip + \frac{1}{2}mv^2(t) = Ip + 2U_{\mathrm{p}}[\cos(\omega t) - \cos(\omega t_i)]^2, \tag{2.9}$$

where U_{p} is the mean energy of a free electron in an oscillating field, and is given by $U_{\mathrm{p}} = e^2A_0^2/4m\omega^2$. The return energy depends on the time of recombination (see Figure 2.5b). Different return times (and therefore different tunnelling times since they come in pairs) result in photons with different energies. The maximum energy of a returning electron is $3.17U_{\mathrm{p}}$ which gives the characteristic cut-off energy of $Ip+3.17U_{\mathrm{p}}$ which is in good agreement with experimental observations. The trajectories that recombine before the recombination time for the cut-off harmonics are referred to as the short trajectories (shown in blue in Figure 2.5a) while the trajectories returning later are called the long trajectories (green in Figure 2.5a). Since the recombination time (and therefore the emission time of the radiation) depends on the photon energy, the pulses are intrinsically chirped. The pulses produced from the short trajectories are positively chirped while the long trajectories are negatively chirped.

2.2.2 Phase matching and reabsorption

The TSM describes HHG from the perspective of a single atom. In experiments, XUV light is emitted by atoms in a volume defined by the intersection of the laser beam at which a sufficient intensity is reached, and the gas medium. To maximize the XUV flux, all the atoms should radiate in phase, and this is referred to as phase matching. A short description of phase matching is given below since it is important to understand phase matching and scaling of the phase matching parameters when discussing the generation of a sufficiently intense HH beam to study non-linear XUV ionization, as described in Chapter 4.

The wave vector mismatch between the harmonic field and the fundamental field is defined by:

$$\Delta\mathbf{k} = q\mathbf{k}_{\mathrm{f}} - \mathbf{k}_q, \tag{2.10}$$

where q is the harmonic order, $\mathbf{k}_{\mathrm{f}}$ the wave vector of the fundamental field and $\mathbf{k}_q$ the wave vector of the harmonic order q. In the following short overview of phase matching, the vector notation will be omitted, and only phase matching along the propagation axis will be considered. The wave vector is related to the refractive index, n, through $k = n\omega/c_0$. For second harmonic generation in a birefringent crystal, the reason for a phase mismatch is the frequency dependence of the refractive index. This problem can be solved by using different polarizations of the fundamental and the second harmonic. If the incomming light impinges on the crystal at a certain angle to the crystal axis, the refractive index of the fundamental can be matched to that of the second harmonic, and Δk can be minimized. The phase mismatch in HHG originates from the frequency-dependent dispersion in the medium (from gas and free

electrons) as well as from the focusing geometry and the intrinsic phase acquired in the continuum during HHG [35–39]. The different contributions are described below.

$\Delta k_{\mathbf{n}}$ The refractive index for the harmonic order q, n_q, is in general lower (<1 for rare gases) than the refractive index for the fundamental beam, $n_{\mathrm{f}} > 1$. The wave vector mismatch is $\Delta k_n = qk_{\mathrm{f}} - k_q = q\omega(n_{\mathrm{f}} - n_q)/c_0$ and the contribution is positive.

$\Delta k_{\mathbf{p}}$ The strong fundamental ionizes the medium and creates a plasma of free electrons. This gives a negative contribution to the wave vector mismatch due to the change in refractive index (mainly for the fundamental).

$\Delta k_{\mathbf{g}}$ The phase of a focused beam, the Gouy phase, differs from that of a plane wave and the total change over the focus along the propagation direction is π. This leads to a maximum wave vector mismatch in the focus of $-q/z_0$, where z_0 is the Rayleigh length. If HHG takes place out of focus the geometrical contribution is minimized. The Gouy phase shift gives a negative contribution.

$\Delta k_{\mathbf{d}}$ The electron wave packet accumulates a phase during propagation, which is proportional to the intensity of the driving field (as mentioned in Section 2.2.1). The wave vector mismatch is therefore proportional to the gradient of the intensity, and makes a negative contribution before the focus and a positive contribution after the focus.

In the long focusing regime used in the presented work, Δk_d is small for the short trajectories and the total wave-vector mismatch (see Equation 2.11) can be minimized by balancing the neutral dispersion, Δk_{n}, with the Gouy phase, Δk_{g}, and the plasma dispersion, Δk_{p}.

$$\Delta k = \Delta k_{\mathrm{n}} + \Delta k_{\mathrm{p}} + \Delta k_{\mathrm{g}}. \tag{2.11}$$

In an experiment, the typical knobs to turn are the gas pressure in the generation cell, the intensity of the driving field, and the position of the focus relative to the generation cell. In the set-up described in Papers I and II the gas cell could be moved along the beam propagation axis while in that described in Paper III even looser focusing was used, making it more convenient to move the focusing optics. Changing the gas density affects Δk_{n} and Δk_{p}, and changing the intensity of the fundamental affects Δk_{p} due to the change in the number of free electrons. Changing the position of the focus affects Δk_{g}, Δk_{d} and Δk_{p}.

The discussion here concerns phase matching along the z-axis, but it is important to bear in mind that phase matching also may change transversally to the beam propagation direction due to change in intensity (and therefore a change in the number of free electrons and the dipole phase) and Gouy phase. Phase matching also changes during the pulse, since an intense pulse can create a large amount of free electrons in the leading edge of the pulse. The conversion efficiency is also limited by reabsorption of the harmonics. A discussion on how the conversion efficiency is related to the coherence length $\pi/\Delta k$ (over which phase matching is achieved), the absorption length and the medium length is found in [37].

The generation of high-order harmonics is a complex process and the optimum generation conditions must be determined experimentally in each case. However, a

theoretical understanding of the different parameters involved in phase matching is important as a guide.

2.2.3 Scaling

Intensities of about 10^{14} W/cm^2 to 10^{15} W/cm^2 are typically used in HHG, depending on the gas. The single atom response can be increased by increasing the intensity, but this also leads to a higher degree of ionization in the medium, which deteriorates phase matching. A higher degree of ionization requires an increase in the gas pressure to balance the wave vector mismatch arising from the free electrons, and there is a degree of ionization, $r_{\mathrm{ion}}^{\mathrm{max}}$, above which phase-matched generation conditions can no longer be found. As discussed in Paper II, a rule of thumb is to use $r_{\mathrm{ion}}^{\mathrm{max}}/2$ as the optimum degree of ionization which is typically a few percent.

The volume in which the high-order harmonics are generated is increased by using loose focusing geometry, i.e. a large f-number ($f_{\#} = f/D$, where f is the focal length and D the beam diameter befor focusing). To keep the same intensity in the focus, this requires using a higher pulse energy, which is posible with the laser used for the experiments presented in Papers I to V. It has been shown previously [38, 40] and in Paper II that, if the laser energy, the f-number, the gas pressure, p, and the medium length, L, are scaled according to Equations 2.12-2.14, the conversion efficiency can be maintained and the XUV pulse energy scales linearly with the laser pulse energy (Equation 2.15).

$$E_{\mathrm{laser}} \propto f_{\#}^2, \tag{2.12}$$

$$p \propto 1/f_{\#}^2, \tag{2.13}$$

$$L \propto f_{\#}^2, \tag{2.14}$$

$$E_{\mathrm{XUV}} \propto f_{\#}^2. \tag{2.15}$$

2.3 Ionization with XUV light

Studying the resulting electrons and ions after ionization provides insight into the structure of atoms and molecules. Ideally, this should be done while disturbing the system as little as possible. For XUV light (often defined as energies between 10 and 124 eV corresponding to wavelengths between 10 and 124 nm) one photon can ionize most neutral atoms and molecules, while, for example, 14 IR photons are required to overcome the ionization potential of neon (25.6 eV).

Using XUV light as a probe is favourable for two reasons. First, lower intensities can be used since ionization can be a linear process and, secondly, the ponderomotive force scales as $U_{\mathrm{p}} \propto 1/\omega^2$. U_{p} is a measure of the mean energy of a *free* electron in the light field, but also provides a good indication of how much the bound outer electrons are affected by the light field. For example, in a light field with an intensity of 10^{13} W/cm^2 the ponderomotive energy is $U_{\mathrm{p}} = 0.6$ eV for a wavelength of 800 nm (1.55 eV) but only 0.6 meV for harmonic order 31 (48 eV).

We here give a brief introduction of XUV ionization by absorption of one and two photons. Single-photon XUV ionization is briefly introduced in Section 2.3.1 and a more detailed description of two-photon double ionization, where the rate equations

are set up for the sequential and the direct case, is presented in Section 2.3.2. The result of a brief literature review on non-linear ionization with XUV light from HHG sources is also given.

2.3.1 Single-photon XUV ionization

The transition amplitude from the ground state to the final continuum state can be calculated by solving the TDSE. For moderately intense fields, first-order perturbation theory can be used and this, together with the single active electron approximation, allows the transition amplitude after the pulse has passed, $a_{\mathbf{p}}$, to be written [41]:

$$a_{\mathbf{p}} = -i \int_{-\infty}^{+\infty} \mathbf{d}_{\mathbf{p}} \cdot \mathbf{E}_{\mathrm{XUV}}(t) e^{\frac{i}{\hbar}(\mathbf{p}^2/2m + Ip)t} dt, \tag{2.16}$$

where $\mathbf{d}_{\mathbf{p}}$ is the dipole transition matrix element from the ground state to the final state, $\mathbf{E}_{\mathrm{XUV}}(t)$ is the electric field of the XUV pulse and $\mathbf{p}$ is the momentum of the final state. The probability to measure an electron in the final state with momentum $\mathbf{p}$ is given by $|a_{\mathbf{p}}|^2$. In the case of an atom or an unaligned molecule, the measured photoelectron angular distribution of the photoelectrons can be written as [42, 43]:

$$\frac{d\sigma}{d\Omega} = \frac{\sigma_{\mathrm{tot}}}{4\pi}(1 + \beta P_2(\cos\theta)), \tag{2.17}$$

$$P_2(\cos\theta) = \frac{1}{2}(3\cos^2\theta - 1), \tag{2.18}$$

where P_2 is the Legendre polynomial of order 2, and σ_{tot} is the total cross section. β is referred to as the asymmetry parameter. The differential cross section is positive, and β takes values between -1 and 2.

2.3.2 Two-photon XUV ionization

XUV photons can doubly ionize an atom in three ways, as is depicted Figure 2.6. One photon can doubly ionize an atom if the photon energy is greater than $Ip_1 + Ip_2$. Two-photon ionization can be either a sequential process (SP) or a direct process (DP). The first step in the sequential process is a one-photon single ionization of the neutral atom, and the second step is one-photon single ionization of the singly charged ion. In the direct process, however, two photons are simultaneously absorbed via a virtual state. The yield of doubly ionized ions depends quadratically on the intensity for two-photon double ionization, regardless of the process, but linearly for single-photon double ionization. However, the electron energies are different in the direct and sequential processes as shown in Figure 2.6. It is possible to distinguish the processes by recording the electron energy distribution.

The first report of non-linear ionization with HHG using harmonic orders above the 9th harmonic of 800 nm was in 2003 [10]. Harmonic orders 7 to 13 were generated in xenon and two-photon single ionization of helium was observed. Shortly after, the same group showed that it is possible to split the pulse and perform second-order autocorrelation of the APT using the non-linear interaction in helium [13].

Table 2.1 lists some examples of the early results of non-linear ionization using HHG. Xenon is often used as a generation gas due to the high conversion efficiency,

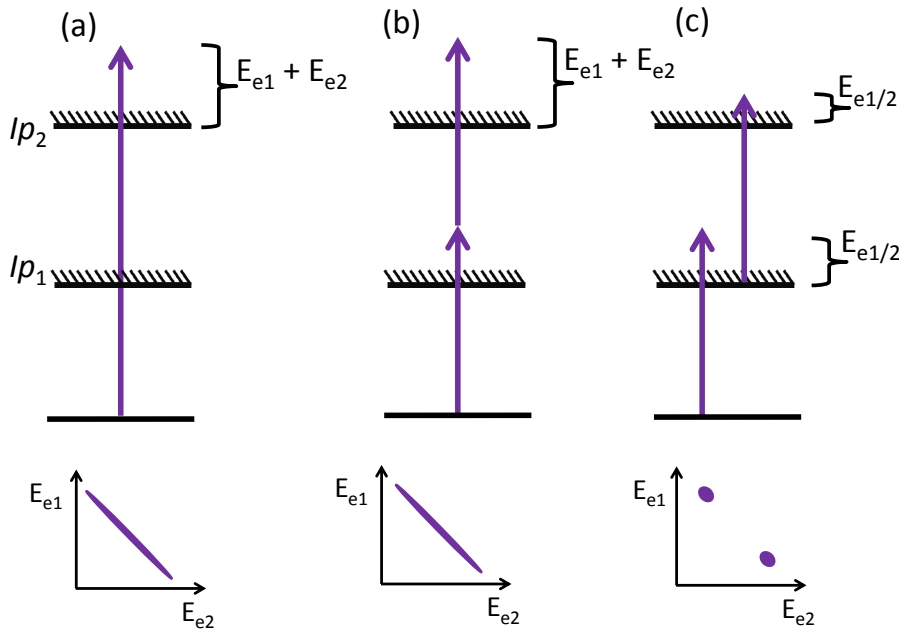

Figure 2.6: Three possible ways to create a doubly charged ion. (a) Absorption of one photon with an energy of $E_{\mathrm{ph}} > Ip_1 + Ip_2$. (b) Absorption of two photons that together have energy $2E_{\mathrm{ph}} > Ip_1 + Ip_2$. (c) Absorption of two photons with $E_{\mathrm{ph1}} > Ip_1$, $E_{\mathrm{ph2}} > Ip_2$

but a limitation is the lower cut-off for the harmonics generated [10, 13, 44–46]. In some of the experiments listed in the table, direct two-photon double ionization was studied, in which case it was necessary to use sufficiently low harmonic orders that the sequential channel required three photons and therefore was negligible, while the direct process was a two-photon process [46, 47]. In other experiments single ionization was studied, in which case only the direct channel exists. In most experiments, ions were observed but in one of the studies electrons were measured [45]. The use of filters to limit the bandwidth is common, and all the experiments uses close to normal-incidence optics to focus and, in some cases split, the XUV pulse. Multilayer coatings are commonly used, which limits the possible XUV bandwidth in experiments. In Chapter 4, the Intense XUV Beamline in Lund is described. As grazing incidence optics are used, together with generation in argon, energies between 20 and 50 eV are available for experiments, and both the sequential and the direct channel in, for example, neon can be accessed.

Below, two-photon double ionization is discussed and the rate equations are set up for the direct and the sequential cases. This helps to understand which parameters affect the number of doubly charged ions in the direct and the sequential cases and provides useful background for the equations presented in Paper III. Depletion of the ground state is not taken into account, which is a reasonable assumption for the available XUV intensities [49].

Within lowest order perturbation theory, the rate of a direct n-photon process

Table 2.1: A compilation of some of the early results on non-linear ionization using HHG. Xenon is often used as generation gas and harmonic orders up to 15 are most commonly used.

Year	Gen. gas	Harmonic order	Process	Comment	Reference
2003	Xenon	7-15	$He \rightarrow He^+$	Autocorrelation	[10, 13, 44]
2005	Argon	27 (42 eV)	$He \rightarrow He^{2+}$	Autocorrelation	[47]
2006	Xenon	7-15	$He \rightarrow He^+$	Electrons	[45]
2006	Xenon	11-15	$Ar \rightarrow Ar^{2+}$		[46]
			$Kr \rightarrow Kr^{2+}$		
2006	Xenon	9-19	$N_2 \rightarrow N^+ + N^+$	Autocorrelation	[48]

($\mathcal{N}_{\mathrm{d}}^{(n)}$) is described by the rate equation [49, 50]:

$$\frac{d\mathcal{N}_{\mathrm{d}}^{(n)}}{dt} = \mathcal{N}\sigma_{\mathrm{d}}^{(n)}F(t)^n, \tag{2.19}$$

where $\mathcal{N}$ is the number of neutral atoms, $\sigma^{(n)}$ the n-photon direct ionization cross section and $F(t)$ is the photon flux (photons $\cdot$ cm^{-2}s^{-1}).

For two-photon direct double ionization, assuming a square pulse with duration τ, we have:

$$\mathcal{N}_{\mathrm{d}}^{(2)} = \int_0^\tau \mathcal{N}\sigma_{\mathrm{d}}^{(2)}F^2dt = \mathcal{N}\sigma_{\mathrm{d}}^{(2)}F^2\tau = \frac{\rho L\sigma_d^{(2)}N_{\mathrm{ph}}^2}{\tau A}, \tag{2.20}$$

where N_{ph} is the total number of photons per pulse, L the length of the gas volume, ρ the gas density, τ the pulse length and A the focus spot size.

In the sequential two photon process, the single-photon process is repeated. In the first step, a singly ionized atom is created and the number of singly charged ions is given by:

$$\mathcal{N}^{(1)} = \int_0^\tau \mathcal{N}\sigma_I^{(1)}Fdt = \mathcal{N}\sigma_I^{(1)}F\tau = \rho LA\sigma_I^{(1)}\frac{N_{\mathrm{ph}}}{A\tau}\tau = \rho L\sigma_I^{(1)}N_{\mathrm{ph}}, \tag{2.21}$$

where $\sigma_I^{(1)}$ is the ionization cross section for the creation of a singly charged ion from a neutral atom. The number of doubly charged ions is given by applying the same equation again and changing the cross section to the cross section from singly charged to doubly charged, $\sigma_{II}^{(1)}$. The number of singly charged ions is not constant, as the number of neutral atoms was considered to be, but increases linearly during the pulse, so it is necessary to set up an integral giving the number of singly charged ions:

$$\mathcal{N}^{(1)}(t) = \int_0^t \mathcal{N}\sigma_I^{(1)}Fdt' = \mathcal{N}\sigma_I^{(1)}Ft. \tag{2.22}$$

This gives the number of doubly charged ions:

$$\mathcal{N}_{\mathrm{s}}^{(2)} = \int_0^\tau \mathcal{N}^{(1)}(t)\sigma_{II}^{(1)}Fdt = \int_0^\tau \mathcal{N}\sigma_I^{(1)}\sigma_{II}^{(1)}F^2tdt = \frac{\mathcal{N}\sigma_I^{(1)}\sigma_{II}^{(1)}F^2\tau^2}{2} = \frac{\rho L\sigma_I^{(1)}\sigma_{II}^{(1)}N_{\mathrm{ph}}^2}{2A}. \tag{2.23}$$

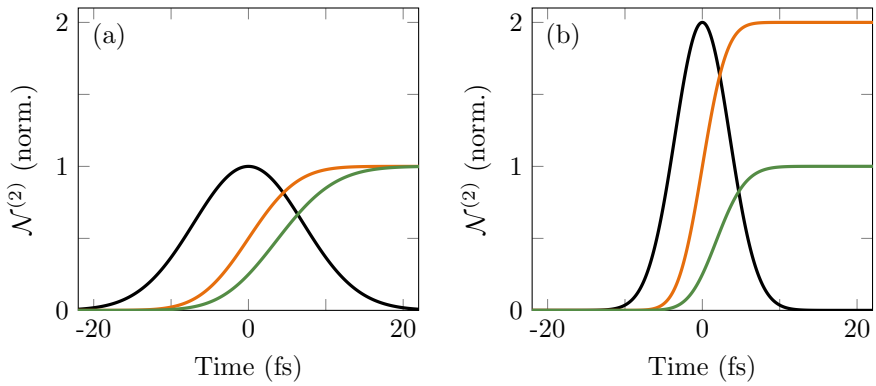

Figure 2.7: Yields of doubly charged ions for the sequential process (green) and the direct process (orange) for a Gaussian pulse (black), for a pulse length of (a) 20 fs and (b) 10 fs. The final yield of the doubly charged ion for the SP is not dependent on the pulse duration and is the same in (a) and in (b) while the final yield of doubly charged ions for the direct process is doubled in (b).

Comparing Equations 2.20 and 2.23 reveals a few interesting insights. For a constant number of XUV photons, the number of doubly charged ions in both the sequential process and the direct process is inversely proportional to the area of the focal spot; a smaller focus gives a higher number of doubly charged ions. The number of doubly charged ions also depends quadratically on N_{ph} for both processes. What differs between the direct and the sequential processes is their dependence on the pulse duration (τ). The sequential process is not dependent on the pulse duration, while the number of doubly charged ions produced in the direct process is inversely proportional to τ. In the sequential process the intermediate state is long-lived and it does not matter how far away the photons are in time, the probability of creating a doubly charged ion from the neutral atom remains the same. This reasoning is, of course, only valid at times when the ions have not yet moved out of the interaction region. In the direct process, the confinement in time is important because the photons must interact with the atom simultaneously. Figure 2.7 shows a simulation of the growth of $\mathcal{N}_s^{(2)}$ and $\mathcal{N}_d^{(2)}$ during the interaction with an XUV pulse for two different pulse lengths. The yields are normalized to the yields in (a), and the result shows that the doubly charged yield is doubled for the direct process, when the pulse length is reduced by a factor of two, but independent on the pulse duration for the sequetial process.

To determine which process is dominating, it is interesting to compare their yields:

$$\frac{\mathcal{N}_{\mathrm{s}}^{(2)}}{\mathcal{N}_{\mathrm{d}}^{(2)}} = \frac{\mathcal{N}\sigma_I\sigma_{II}F^2\tau^2}{2\mathcal{N}\sigma_{\mathrm{d}}^{(2)}F^2\tau} = \frac{\sigma_I\sigma_{II}}{2\sigma_{\mathrm{d}}^{(2)}}\tau. \tag{2.24}$$

A short pulse thus favours the direct process. Taking neon as an example, and using measured and calculated values for the cross sections [51–53], the approximate pulse duration for which the yields are similar can be calculated, and is found to be about 0.5 fs. Strictly speaking, the rate equations should not be used for very short pulses, and this value is thus only a rough estimate. For short very pulses, there is no clear distinction between the direct and sequential processes since the ion does not have

time to relax into the singly charged state before it is ionized again. The transition between the long and the short pulse regimes, and especially regarding the electron correlation and angular distributions, has been discussed in many theoretical papers (see, for example, Ref. [54] and references therein). While studies of the two-photon processes induced by a single pulse are interesting in their own right, splitting the pulse to perform XUV pump-XUV probe studies provides insight into electron correlations, dynamics in molecules and makes it possible to perform autocorrelation measurements of the XUV pulse.

Chapter 3

Particle spectrometers for experiments using intense XUV pulses

To understand matter we need to examine it, which means we need to interact with it in some way. In the macroscopic world, the photons emitted by the sun are reflected by objects around us, and by detecting these photons, i.e. seeing them, we can say what colour and shape objects have. Atoms and molecules can be investigated by directing beams of photons or electrons onto a target containing the material of interest, and by detecting and analysing the scattered photons or electrons, or the fragments resulting from ionization. Irradiating a sample with light and studying the diffracted photons gives insight into the structure of molecules that have the same size as the wavelength of the light. The structure of a virus, for example, has been studied in FEL experiments from diffracted X-ray photons using a wavelength of 7 Å [55]. Using longer wavelengths, such as XUV light, the typical observables are instead the momentum of the electrons and the ions formed after an ionization event. These measurements provide information on the energy levels of the system and the mass and charge of the fragments created, while molecular structures can be revealed by electron interference [22, 56].

A reaction microscope (REMI) is a spectrometer that can measure the momentum of ions and electrons simultaneously by directing the charged fragments, using electric and magnetic fields, onto detectors that are sensitive to both impact position, x and y, and arrival time, t [57]. If the number of events taking place is reduced to less than one per laser shot, e.g. by reducing the medium density or the XUV flux, the electrons and ions derived from the same ionization event can be measured in coincidence. The initial momentum vectors (p_{x}, p_{y} and p_{z}) can be derived from the measured parameters. If all the impact parameters of all the fragments are measured, the experiment is kinematically complete, and the molecular-frame photoelectron angular distribution (MFPAD) can be obtained. This technique has been extremely successful, especially for investigating the dynamics of molecules, but it is also challenging due to the requirement of high vacuum and the need for a source with a high repetition rate

to obtain sufficient statistics. Intense XUV pulses, sufficiently intense to induce non-linear effects, generated by HHG and FELs typically have repetition rates between 10 and 1000 Hz, and many ionization events may take place during each pulse. Most of the events are the result of linear processes, and reducing the gas pressure, to obtain experimental conditions suitable for coincidence measurements, leads to extremely low average count rates in the non-linear signal, making it difficult to get sufficient statistics. This gives rise to the need for detection techniques that can record many events per shot.

A velocity map imaging spectrometer (VMIS) records the x and y impact positions, but not the arrival time of the particles [58]. The fact that the arrival time of each individual fragment is not measured allows for detection of many events per laser shot. Instead of measuring the arrival time, strong field gradients are applied along the spectrometer axis, z, which means that the measurements of x and y are independent of p_z, resulting in a 2D projection of the 3D initial momentum distribution. If there is a symmetry axis in the ionization, which is the case when a linearly polarized laser pulse is used, perpendicular to the spectrometer axis, the 3D momentum distribution can be retrieved by processing the data using different methods [59, 60]. Measuring many events makes it impossible to assign two fragments to the same ionization event and instead of studying coincidences, the correlation between the ionization fragments has to be studied with statistical methods.

During the course of this work, I have designed and built two spectrometers for use at the Intense XUV Beamline in Lund. The first was a two-stage ion time-of-flight (TOF) spectrometer constructed and used in the first experiments on non-linear ionization presented in Paper III, and the second was a double-sided VMIS (DVMIS), which allowed simultaneous measurements of both electrons and ions on every single shot. The construction of the DVMIS is described in Paper VIII, together with the simulated energy resolution. The first results for synchronously acquired angular distributions of electrons and ions are also presented in the paper.

The velocity map imaging (VMI) technique was also used in Paper VII where the angular distribution of sidebands was studied using XUV light from the free-electron laser in Hamburg (FLASH).

This chapter is divided into three sections. The first describes charged particles in electric fields. The simplest possible spectrometer, using one acceleration region together with a drift region, is presented as an instructive example of how the masses or the momentum of charged particles are measured. The resolution in mass and momentum can be significantly improved by small modifications to this simple design, and such spectrometers are known as the Wiley-McLaren TOF spectrometer and the VMIS. The second section describes single shot analysis, and in particular covariance techniques, while the final section presents the construction, simulations and the first tests of the designed DVMIS.

3.1 Charged particle imaging

After an ionization event, the electrons and ions move in specific directions, with a certain kinetic energy and mass-to-charge ratio, all of which provide information about the system at the time of ionization. The charged particles can be directed towards a detector using magnetic fields, electric fields, or a combination of both, in a

way that makes it possible to reconstruct the initial momentum of the electrons, ions, and/or the ion mass spectrum. The spectrometers presented in this chapter make use of electric fields to accelerate ions or electrons along the detector axis z towards the detector.

The acceleration, $\mathbf{a}$, of a charged particle depends on the strength of the electric field, $\mathbf{E}$ (V/m), the mass, m, and the charge, q, of the particle:

$$\mathbf{a} = \frac{q\mathbf{E}}{m} \tag{3.1}$$

In the following, unless stated otherwise, only the z-direction is considered, and the vector notation is omitted. The velocity, v, is found by integrating Equation 3.1 with respect to time and, integrating once more, gives the equation for the z-position:

$$v_z(t) = \frac{qE_z}{m}t + v_0 \tag{3.2}$$

$$z(t) = \frac{E_z q t^2}{2m} + v_0 t + z_0, \tag{3.3}$$

where v_0 and z_0 are the initial velocity in the z-direction and the initial position, respectively. Assuming $v_0 = 0$ and $z_0 = 0$, the flight time, t, is given by:

$$t = \sqrt{\frac{2mz}{qE_z}}. \tag{3.4}$$

These equations describe the motion of a charged particle in an electric field, and will be used to describe the properties of the spectrometers discussed below.

The simplest form of spectrometer is illustrated in Figure 3.1. Ionization takes place between two plates, the first at a voltage, V_R, and the second grounded, $V_\mathrm{F} = 0$, resulting in an electric field directed along the axis of the spectrometer in the acceleration region. A grid in the second plate allows the particles to pass into the field-free drift tube, and the particles are detected by a detector that can record time and position. Figure 3.1a shows the time-of-flight detection of ions with zero kinetic energy, the same charge, but different masses. The sketch shows that ions with different masses, generated in a small volume, arrive at the detector at different times, and that the peaks have a small spread. An expression for the total flight time, t, is found by using Equations 3.1 to 3.4 and setting up an expression for the flight time in the acceleration region, where the acceleration is constant, and for the drift region where the velocity is constant:

$$t = \sqrt{\frac{m}{qE_z}}\left(\sqrt{2L_1} + \sqrt{\frac{L_2^2}{2L_1}}\right), \tag{3.5}$$

where L_1 is the distance the particle travels in the acceleration region and L_2 is the length of the drift region. Since the ions have zero initial kinetic energy, the width of the peaks is due to their different initial starting positions, i.e. different values of L_1. A particle further away from the detector travels a longer distance to the detector, but is also accelerated over a greater distance, and will thus have a higher velocity in

the drift tube. Two particles, starting at $L_1 + \Delta z/2$ and at $L_1 - \Delta z/2$ have the same flight time if L_2 is chosen to be:

$$L_2 = 2\sqrt{L_1^2 - (\Delta z/2)^2}. \tag{3.6}$$

If the source size, Δz, is assumed to be small compared to L_1, the detector must be placed at $L_2 = 2L_1$ to minimize the difference in flight time. This requirement can be relaxed if two acceleration regions are used as described below [61].

Figure 3.1b illustrates the same spectrometer, but the particles are instead assumed to have the same mass but different initial kinetic energies. These particles may be electrons resulting from ionization, or ions after, for example, a subsequent Coulomb explosion. The typical kinetic energy of electrons is below 100 eV and for ions below 10 eV when using XUV light.

Assuming that the field gradient in the z-direction is sufficiently strong, so that p_z can be neglected, the impact radius on the detector, r, for a particle with initial kinetic energy, E_{kin}, and the corresponding momentum component, p_{xy}, is given by:

$$r = v \cdot t = \sqrt{\frac{2E_{\text{kin}}}{m}} \cdot t, \tag{3.7}$$

where t is the time of flight defined in Equation 3.5. Combining Equation 3.5 and Equation 3.7 gives the impact radius:

$$r = \sqrt{x^2 + y^2} = \sqrt{\frac{2E_{\text{kin}}}{qE_z}} \left(\sqrt{2L_1} + \sqrt{\frac{L_2^2}{2L_1}} \right) = k\sqrt{E_{\text{kin}}} = k\frac{p_{xy}}{\sqrt{2m}}, \tag{3.8}$$

where k is a proportionality constant that depends on the geometry and the electric field. It is interesting to note that the radius is proportional to the square root of the kinetic energy but independent of the mass. In fact, it is the projection of the momentum vector divided by $\sqrt{m}$ in the xy-plane that is imaged. The image is thus a 2D projection of the 3D momentum distribution, which leads to rings, corresponding to particles with their initial directions in the xy plane, and a decreasing signal towards the centre of the image, corresponding to particles with an increasingly large component along the z-axis. The drawback of this simple design is that the resolution is poor if the source has a spread.

The spectrometers constructed and designed as part of this work are based on the principles described above.

3.1.1 Wiley-McLaren TOF spectrometer

The introduction of a second acceleration region was suggested by Wiley and McLaren in 1955 [61]. Compared to a single acceleration region, the distance where two particles starting at different L_1 arrive at the same time, can be tuned and the requirement of $L_2 = 2L_1$ is relaxed. Figure 3.2a shows an illustration of a two-stage Wiley-McLaren TOF spectrometer where the first plate is called the repeller plate and the second, extractor plate. The two particles depicted have the same mass but different starting positions and the voltage on the repeller and extractor, V_{R} and V_{E}, are set so that they arrive at the same time at the detector. A spectrometer of this type was designed and constructed, and used in the experiments presented in Paper III.

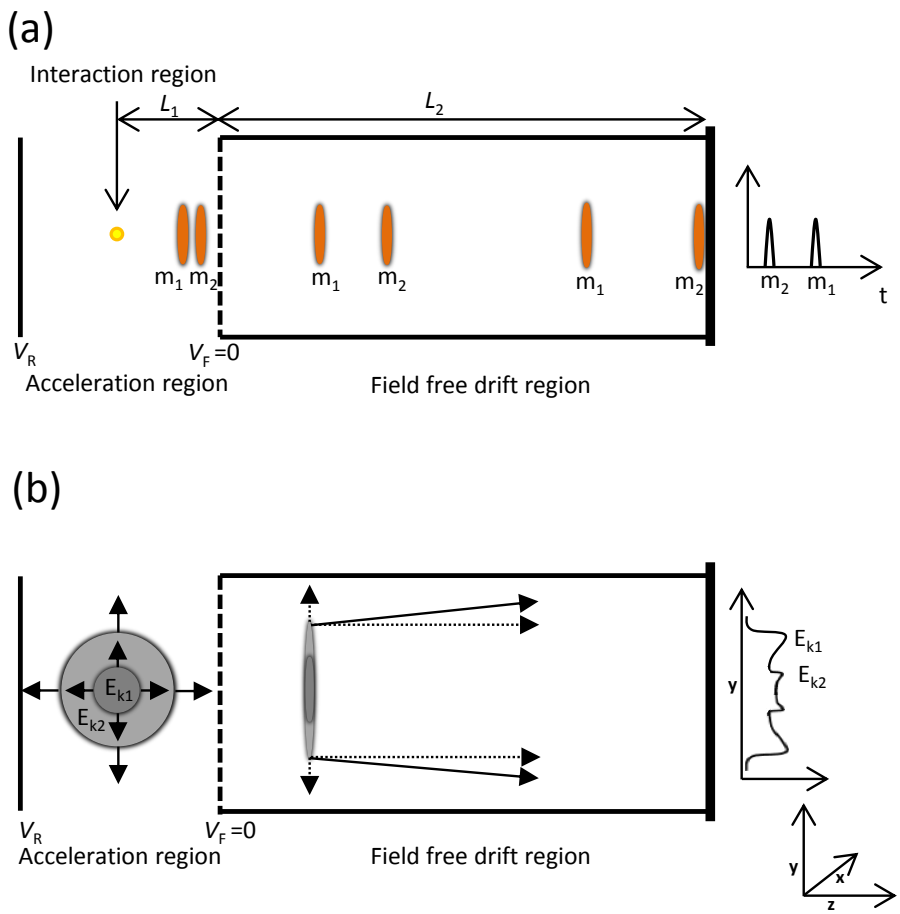

Figure 3.1: A simple spectrometer using a single acceleration region and a drift region, separated by a grid. (a) shows how ions with two different masses (m_1 and m_2), but zero kinetic energy, arrive at the detector at different times and have a small spread due to the initial spread along the z-axis. (b) shows the path of charged particles (ions or electrons) with two initial kinetic energies (E_{k1} and E_{k2}), but the same mass. The initial momentum in the xy-plane determines the impact radius at the detector. The result is two rings corresponding to the two energies when the momentum is completely in the xy-plane and a decreasing distribution towards the centre.

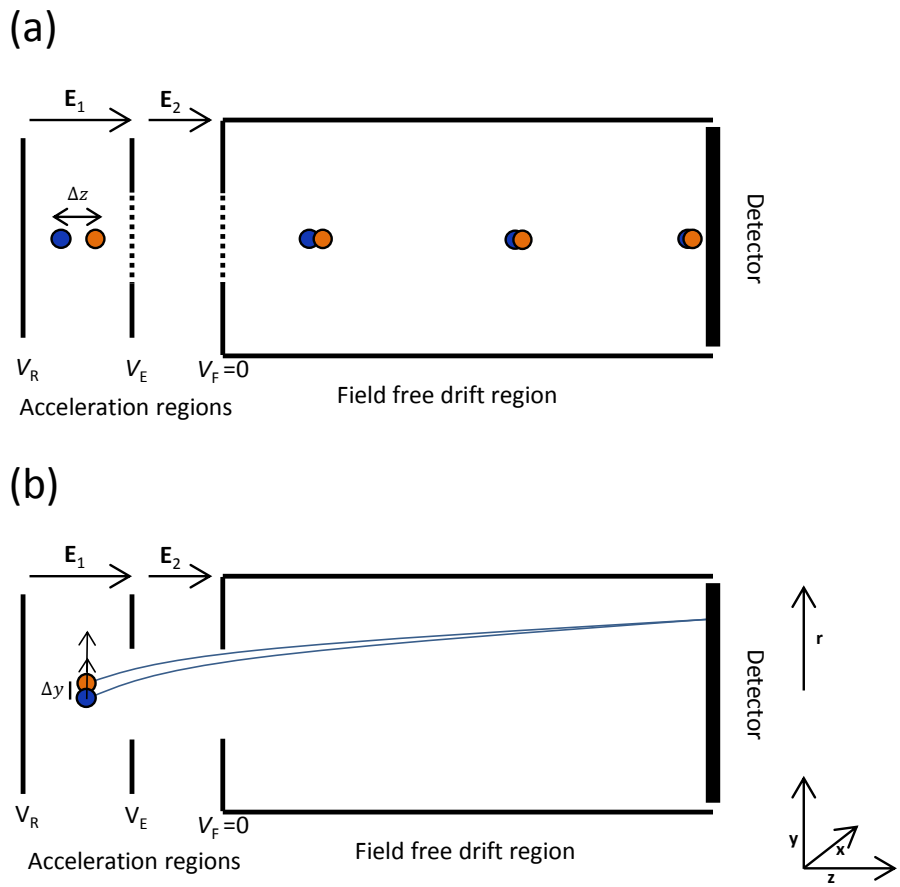

Figure 3.2: (a) An ion TOF operated in Wiley-McLaren conditions where two fragments generated at different positions arrive at the same time at the detector. By tuning V_{E} the distance where the blue particle catch up with the orange is changed. (b) A VMIS where the position on the detector depends only on the initial momentum in the xy-plane and not on the starting position along the y-axis. By tuning V_{E} the curvature, and therefore the acceleration in the xy-plane, is adjusted to compensate for the initial spread of the starting positions.

3.1.2 Velocity map imaging spectrometer

A velocity map imaging spectrometer, is based on the same design as the Wiley-McLaren TOF spectrometer, but has open electrodes instead of grids [58], as illustrated in Figure 3.2b. As in the simple spectrometer described above, the high electric field along the z-axis eliminates the dependence on the p_z component and allowing the 2D projection of the 3D momentum distribution to be measured. The 3D momentum can be reconstructed for a momentum distribution that is rotationally symmetric around the x- or y-axis, i.e. a distribution that can be described in two dimensions. The 3D distribution can be reconstructed using various methods, for example, the Abel inversion [59], onion peeling [62] or iterative methods [60].

The advantage of open electrodes is that the field lines are curved in the first and the second acceleration region, and the charged particles are subjected to a force in the xy-plane. It is possible to find a set of voltages (V_R, V_E and V_F) for which the particles experience an acceleration in the xy-plane that compensates for the initial spread in the xy-plane. Figure 3.3 shows simulated images from a spectrometer using grids (a) and with open electrodes (b). The corresponding inverted images are seen in (c) and (d) and the two resulting photoelectron spectra are shown in (e). The resolution is greatly improved in the case with open electrodes.

Operation modes

In a standard VMIS design three voltages can be set, V_R, V_E and V_F. For simplicity, V_F is commonly set to ground but can, in principle, also be varied if the mechanical and electrical design allow for it, as will be seen in the section where the DVMIS is described. The mode of operation is then determined by the ratio $\eta = V_\mathrm{E}/V_\mathrm{R}$, and the absolute voltage of the repeller and extractor decides the proportionality constant, k, in the relation between the initial kinetic energy (in the xy-plane) of the particle and the impact radius on the detector, calculated for a single acceleration region in Equation 3.8. Higher voltages lead to a greater velocity component in the z-direction, and thus a smaller radius. The higher the initial kinetic energy, the higher voltages are required to collect the particles on the detector. A VMIS can be operated in three different modes described below, where the velocity map imaging mode is the standard mode of operation. The voltage ratios presented are dependent on the exact design of the spectrometer, and the values given here are those used for the electron side of the DVMIS which is presented in Section 3.3.

Velocity map imaging mode (VMI mode): The transverse velocities are mapped onto the detector and the influence of the source size in the xy-plane is minimized. The voltage ratio is $\eta \approx 0.76$.

Spatial mode: A magnified image of the interaction region is projected onto the detector. In VMI mode, the influence of the initial position is minimized while in spatial mode, the effect of the initial energy distribution is minimized. This is a useful mode when aligning the spectrometer, to ensure that the laser beam is centred in the spectrometer, that all the beams (in pump-probe experiments) are aligned in the xy-plane, that the laser is overlaps with the gas, and to ensure that the laser focus is at the centre of the spectrometer [63]. The spatial mode is found for $\eta \approx 0.97$.

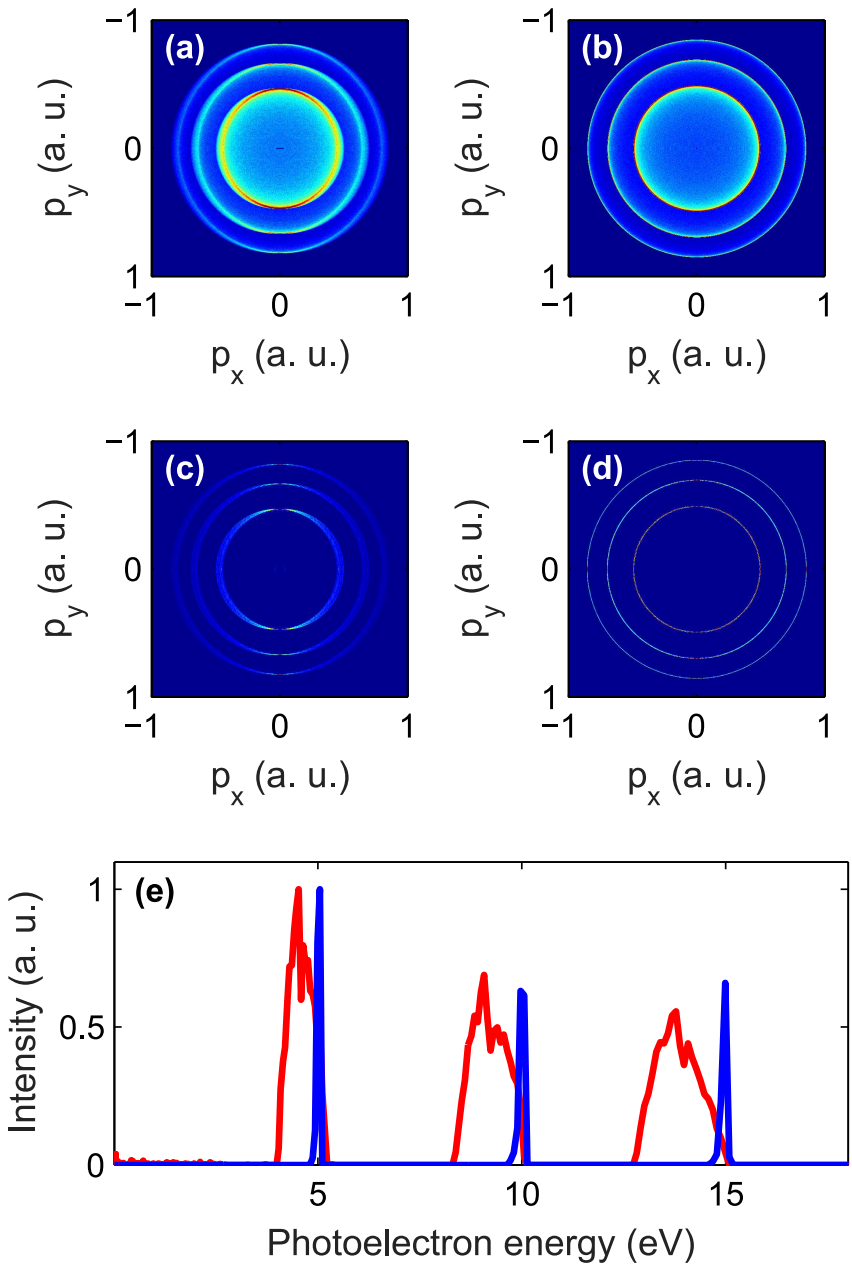

Figure 3.3: Simulation of 10 million charged particles with energies equally distributed between 5, 10 and 15 eV are emitted in random directions from an interaction region with the dimensions 20 µm× 20 µm × 1 mm. In (a) and (b) images are shown where grids and open electrodes are used, respectively. (c) and (d) show the corresponding inverted images and in (e) the photoelectron spectrum is shown in red for the geometry with grids and in blue for the open electrodes. The resolution is strongly improved for the open electrode geometry.

TOF mode: The Wiley-McLaren condition can also be met with open electrodes. The voltage ratio is $\eta \approx 0.78$. This is close to the settings of the VMIS mode, and it is thus possible to obtain a TOF trace and a VMIS image simultaneously, with only slightly degraded mass resolution.

3.2 Single shot analysis

In intense XUV experiments, which usually use sources with a lower repetition rate and where many events are recorded on every shot, coincidence analysis is not possible. Instead, single shot data can be acquired and correlations studied in various ways.

One example of a simple approach to retrieve correlations was described in Paper VII, where photoelectrons resulting from two-color (XUV+IR) ionization of neon were recorded on every single shot. When ionization takes place in the presence of an IR field, sidebands with an IR intensity dependent angular distribution are created by absorption or emission of IR photons. Due to the time jitter between the XUV FEL pulse and the IR pulse, the IR intensity seen by the ionized electrons varied strongly from shot to shot. Photoelectrons with high kinetic energies are created for shots where the spatial and temporal overlap is good, due to the absorption of a large number of IR photons. By sorting the single shots on the high energy photoelectron contribution, bins corresponding to different IR intensities seen by the XUV pulse can be formed and the sidebands and their angular distributions can be studied as a function of the IR intensity.

A more elaborate method is to study the relation between two signals using statistical methods. It is possible to study how two variables, $\mathbf{X} = (x_1, x_2, x_3, ...)$ and $\mathbf{Y} = (y_1, y_2, y_3, ...)$, sampled for the same shots, are correlated by calculating their covariance:

$$\mathrm{cov}(\mathbf{X}, \mathbf{Y}) \quad = \langle (\mathbf{X} - \langle \mathbf{X} \rangle)\,(\mathbf{Y} - \langle \mathbf{Y} \rangle) \rangle\,, \tag{3.9}$$

where $\langle \mathbf{X} \rangle$ denotes the expectation value of the variable $\mathbf{X}$. From Equation 3.9 it is easy to understand that if the two variables, $\mathbf{X}$ and $\mathbf{Y}$, are not correlated the expectation value will be close to zero. Two highly correlated events, for example two ion fragments created through Coulomb explosion, will have a high covariance since the two variables $\mathbf{X}$ and $\mathbf{Y}$ increase and decrease in the same way. If the variables are anti-correlated (meaning that an increase in $\mathbf{X}$ leads to a decrease in $\mathbf{Y}$), the products will have different signs and the covariance will be negative. While covariance is conceptually simple, its use on data from fluctuating sources becomes complicated. By using a source that fluctuates, all variables will be correlated due to the fact that all the signals vary with laser intensity. A technique called partial covariance has been suggested, where the measured shot-to-shot variations of the laser intensity are taken into account [64, 65]. Partial covariance mapping was for example used in Ref. [66], to study Coulomb explosion of diatomic molecules, and the contrast in the results were greatly improved. Covariance techniques are widely used for measurements, but its use in combination with a VMIS has only been reported in a few experiments studying ions with a single-sided VMIS. For example, a VMIS was used to calculate the covariance maps for the ion fragments resulting from Coulomb explosion [67, 68]. A recent review of covariance mapping techniques can be found in Ref. [69].

3.3 Design, construction and testing of a DVMIS

The VMI technique for single-sided spectrometers is well established, and the idea behind the DVMIS was to add a second side for the ions, while using the well tested, standard, electrode design for the electron side [70]. Apart from adding the ion side, the only change to the standard single-sided VMIS was the addition of a grid in the repeller plate. This resulted in good VMI conditions for the ion side, but the resolution is slightly compromised. There were three reasons for prioritizing the electron side.

(i) More features are expected for the electrons, requiring high resolution.

(ii) It is possible to use the electron side only and by swapping polarities, ions can be recorded with good resolution. It is not possible to record electrons on the ion side, since that side is not shielded from external magnetic fields.

(iii) Introducing a grid means that the electron side is not affected by the voltages on the ion side, and iteration is not necessary to find the optimum conditions for both sides.

A few experiments using a DVMIS have been reported [71–74] but with few exceptions [75], the spectrometers were combined with a delay line detector, and the electrons and ions detected in coincidence. To the best of the author's knowledge, there are to date no reports from experiments where a DVMIS has been used for correlated studies in the multi-event regime. In this section, the design and the simulated performance of the DVMIS are presented together with some of the first results, obtained from tests using light from the Max-Lab Synchrotron Facility.

3.3.1 Design

The DVMIS has two separate parts, the electron side and the ion side as shown in Figure 3.4a. The ion side and the electron side both consist of a mounting tube on which the flight tube and the electrode package are mounted. The mounting tube is attached to a CF200-CF160 reducer flange, which is attached to the vacuum chamber. An MCP-phosphor screen assembly is mounted on the reducer flange. A more detailed illustration of the electrode package is shown in Figure 3.4b, where the voltages on the electrodes are defined. A number of requirements must be taken into account in the design of the DMVIS. These include vacuum levels, the precision of alignment of the electrodes, stability properties and ease of installation. Some of the most important design requirements are discussed below, and these are followed by a description of the components chosen to fulfil these requirements.

Alignment between the ion and the electron side: The two sides must be precisely aligned.

Parallel electrodes: To ensure good image quality, the electrodes must be exactly parallel placing high demands on the spacers used.

Ultra-high vacuum: Vacuum levels as low as 10^{-9} mbar are needed, especially when studying larger molecules from which it is difficult to produce high gas jet pressures. When using high-intensity XUV beams, the residual gas leads to an

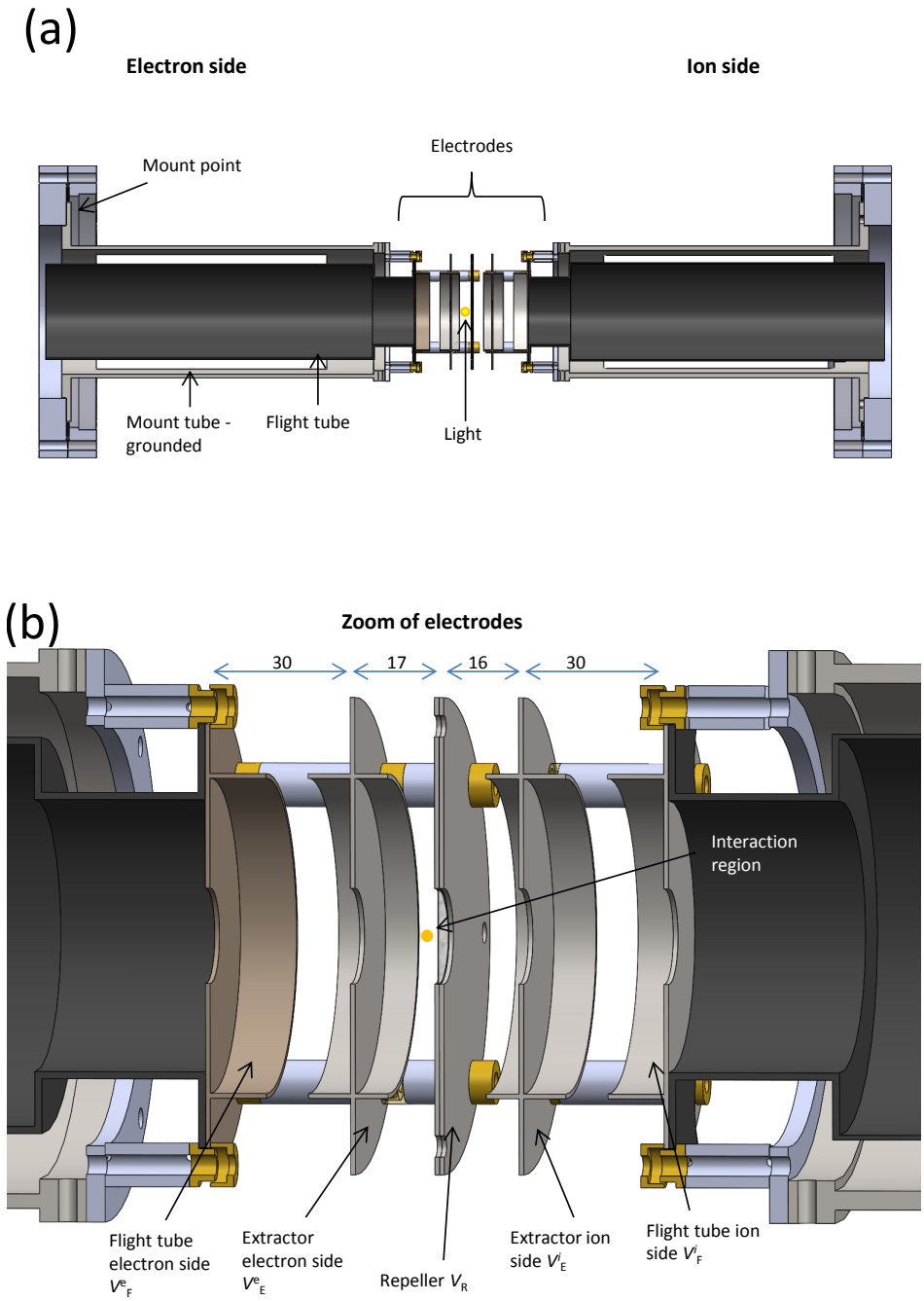

Figure 3.4: DVMIS model created by a 3D CAD program. In (a) the full DVMIS is shown and the electron side, the ion side and the electrode package are seen. In (b) a zoom of the electrodes is seen where the different electrodes are marked.

increase in the linear ionization signal, which conceals the weaker non-linear signal.

Voltages on all electrodes including flight tubes: In an ordinary VMIS design the flight tube is often attached to a flange on the chamber and must be grounded. To detect ions and electrons, the two flight tubes must have different voltages and, in order to use the maximum voltage range over the spectrometer, the two flight tubes will typically not be grounded, which places new demands on the design compared to the case of a single-sided VMIS.

High-voltage differences: The design must allow for high voltage differences. The distances between the electrodes and grounded parts must be at least 10 mm to allow a voltage difference of 10 kV, and the edges must not be sharp to avoid sparking.

Easy installation: The DVMIS must be easy to mount and unmount, and the electrode package must be replaceable.

The above-mentioned requirements were taken into account in the overall design and when designing the separate parts. The use of two parts simplifies both the construction and the mounting. As can be seen in Figure 3.4b, the repeller, is mounted on the electron side so as not to compromise the resolution on the electron side, as discussed above. The various components of the DVMIS are described below.

Flight tube: To allow for arbitrary voltages on the flight tubes, it is constructed as a tube with a rim and the rim is attached to the mounting tube by electrically insulating spacers. The flight tube on the electron side is made out of μ-metal to provide shielding from external magnetic fields. No μ-metal shielding is needed on the ion side as the ions are hardly affected by external magnetic fields, since the force exerted on a particle is proportional to the velocity of the particle, and the ions are slower due to their bigger mass.

Mounting tube: The mounting tube is made of non-magnetic stainless steel and is attached to a CF200 to CF160 reducer by four M6 screws. Four holes have been cut out of the tube to reduce the weight of the spectrometer, and to improve the pumping speed. The flight tube is attached to the top of the mounting tube.

Electrodes: The electrodes are made of non-magnetic steel (316L) and are 1.5 mm thick (Figure 3.4b). The central hole is 20 mm in diameter. A rim is used to shield from external electric fields. The edges are smooth to avoid sparking.

Spacers, bushings and threaded rods: The electrodes are positioned with respect to each other using spacers, bushings and threaded rods. The spacers determine the distance between the electrodes and the bushings are used to avoid contact between the rod and the electrode, to allow for the use of metallic rods. The spacers are sturdy and, together with the bushings ensure that the electrodes are parallel. The spacers and the bushings are made out of aluminium oxide (Al_2O_3), and are shown in white and yellow, respectively, in Figure 3.4b. The rods currently being used in the spectrometer are made of polyether ether ketone (PEEK), which does not accumulate charge and is compatible with ultra-high vacuum.

3.3.2 Modes of operation

The DVMIS can be operated as a single-sided VMIS, in which case the electron side is used, or both sides can be used for the simultaneous detection of ions and electrons. Using both sides, the ion side can be set to optimize the resolution for VMI mode or for the TOF mode. The possible ion/electron modes of operation are listed below:

1. High resolution ion modes (using only the electron side)
   (a) Ion TOF
   (b) Ion VMI
2. High resolution electron modes (using both sides)
   (a) Electron VMI, ion TOF
   (b) Electron VMI, ion VMI

In addition to the modes listed above it is possible to use spatial imaging (as described in Section 3.1.2) to optimize the focus and find the overlap with the gas jet.

When operated in double-sided mode, the total voltage difference available is divided between the electron and the ion side. A high voltage difference between the repeller and the front of the MCP allows the detection of particles with high kinetic energies. The voltage is mainly limited by the feedthroughs on the MCPs, which are limited to $\pm$ 10 kV. The phosphor screens have to be biased at 5 kV over the front of the MCP and the resulting voltage difference over the spectrometer is thus 15 kV. In most experiments with XUV light, the electrons are more energetic than the ions, and the greatest voltage difference must be applied to the electron side. When the voltage differences have been set (i.e., $V_{\mathrm{F}}^{\mathrm{e}}$, V_{R} and $V_{\mathrm{F}}^{\mathrm{i}}$ are set), the extractor voltage can be tuned on the electron side, and subsequently on the ion side, to determine the mode of operation.

3.3.3 Simulations

The four different modes of operation described above have been simulated to study the energy and time resolution. The simulations of the VMI modes (1(b) and 2(b)) are presented in this thesis while the full result of the TOF simulations (1(a) and 2(a)) are found in Paper VIII. Simulations were performed using the software SIMION, which calculates the trajectories of charged particles in static electric fields. Two different types of simulations were performed. In the first, 27 particles were defined, with initial positions in the corners of a box having the same size as the interaction region, all with an initial velocity perpendicular to the detector axis. In the second, a large number of particles were generated in the interaction volume with random positions and directions. The image generated is then treated as an experimental VMIS image and can be inverted [76], and the resolution is achieved by fitting a Gaussian curve to the peaks in the spectrum . This is referred to as the Monte Carlo method.

The boundary conditions given for the simulations were to use voltages such that electrons with $E_{\mathrm{kin}} \leq 90$ eV and ions with $E_{\mathrm{kin}} \leq 10$ eV could be measured. The first method, involving 27 particles, is fast and therefore convenient for finding the voltages giving optimum energy resolution for charged particles of different kinetic

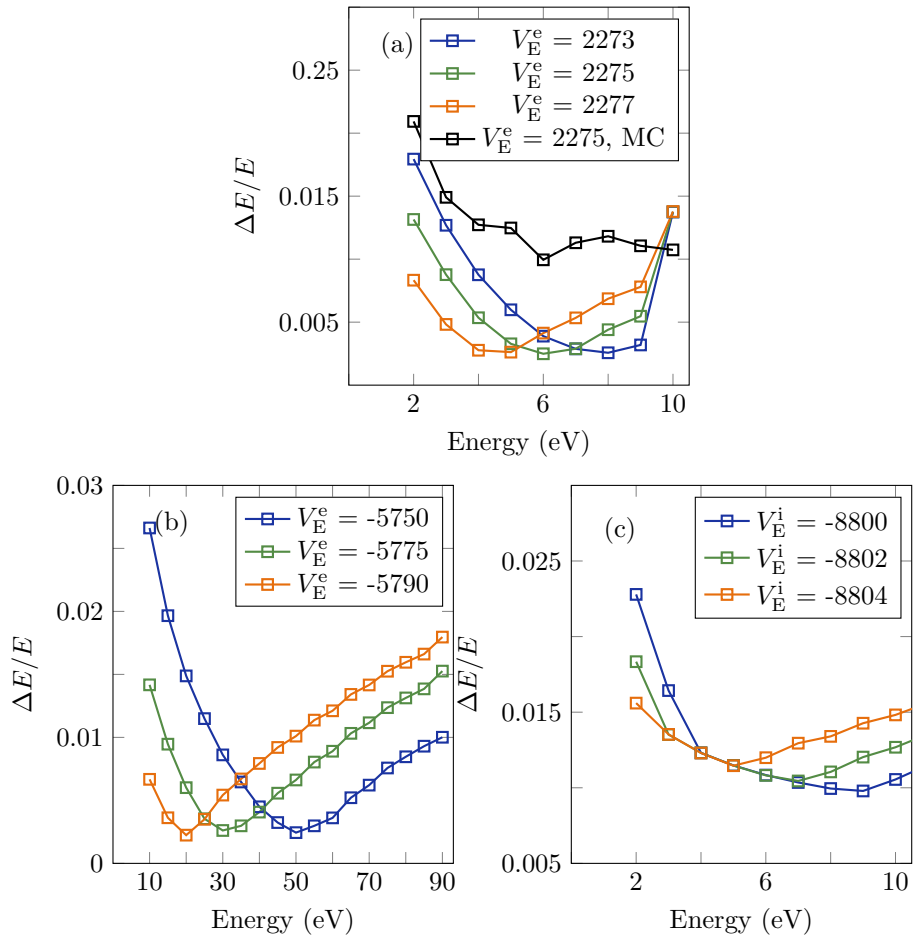

Figure 3.5: Simulations of charged particles emitted from the corners of a box with $\Delta x = \Delta z = 100$ µm and $\Delta y = 2000$ µm, and initial velocities between 2 and 10 eV, in 1 eV steps, for ions and between 10 and 90 eV, in 10 eV steps, for electrons. In (a) the high-resolution ion mode is simulated and in (b) and (c) the high-resolution electron mode using both sides. (b) shows the resolution of the electrons and (c) the ions. The green, blue and orange curves are found by using the 27 particle model while the black curve is from using the Monte Carlo method.

energies. The method is known to overestimate the resolution, and the Monte Carlo method was used for comparison. The size of the box was set to $\Delta x = \Delta z = 100$µm and $\Delta y = 2000$µm. Electron energies from 10 to 90 eV in steps of 10 eV and ion energies between 2 and 10 eV in steps of 1 eV were used. The voltages resulting in optimum resolution for 30 eV electrons and 6 eV ions are given in Table 3.1. For each mode, the resolution was simulated for two additional extractor voltages (above and below the optimum voltages), which shifts the energy for which the optimum resolution is achieved.

Table 3.1: Simulated voltages for the different modes of operation.

Operation mode	V_{F}^{e} (kV)	V_{E}^{e} (kV)	V_{R} (kV)	V_{E}^{i} (kV)	V_{F}^{i} (kV)
1(a) Ion TOF	0	2.354	3.000	not used	not used
1(b) Ion VMI	0	2.275	3.000	not used	not used
2(a) Electron VMI + ion TOF	5.000	-5.775	-9.200	-10.000	-10.000
2(b) Electron VMI + ion VMI	5.000	-5.775	-9.200	-8.802	-10.000

Figure 3.5 shows the results of the simulations of the resolution of the DVMIS for modes 1(b) (panel (a) in the figure) and 2(b) (panel (b) and (c) in the figure for electrons and ions, respectively). The energy resolution is defined as $\Delta E/E$ and is found to be below 2% for all ion energies, using mode 1(b). Simulating the same ion energies but on the ion side (mode 2(b)) shows that the resolution is slightly compromised. In (b) it can be seen that the electrons have an energy resolution of about 1% around the optimum electron energy and about 2% for the electron energies far from the optimum. The result from a Monte Carlo simulation is shown for mode 1(b) and the resolution is a factor two worse, but still reasonable.

3.3.4 First experimental results

The DVMIS was first tested using photons with an energy of 420 eV generated at the Max-Lab Synchrotron facility in Lund. Nitrogen (N_2) was used as the target gas delivered by an Even-Lavie pulsed gas jet (described in Chapter 4). The 1s ionization threshold of N_2 is 409.9 eV. After the removal of the core 1s electron, the ion can relax via Auger processes emitting a highly energetic electron. The resulting doubly charged ion can undergo Coulomb explosion, and the angle and kinetic energy of the resulting fragments can be detected. Figure 3.6 shows raw and inverted images for electrons and ions, together with the related photoelectron and photoion spectra. A fit of the angular distributions gives an asymmetry parameter (defined in Chapter 2) of 0.8 for the direct photoelectrons which agrees with previously published values [77].

Covariance analysis

The electron and ion images in the above mentioned data set consist of 20000 acquisitions. The synchrotron light source has a repetition rate of 100 MHz, which means that the light bunches are spaced by 10 ns, and the light can therefore be regarded as continuous compared with the shortest shutter time of the camera (50 µs) and the pulse length of the gas jet (50 µs). The repetition rate in the experiment is therefore determined by the repetition rate of the gas jet and camera frame rate. An acquisition consists of the electrons and ions hitting the detectors after the ionization events

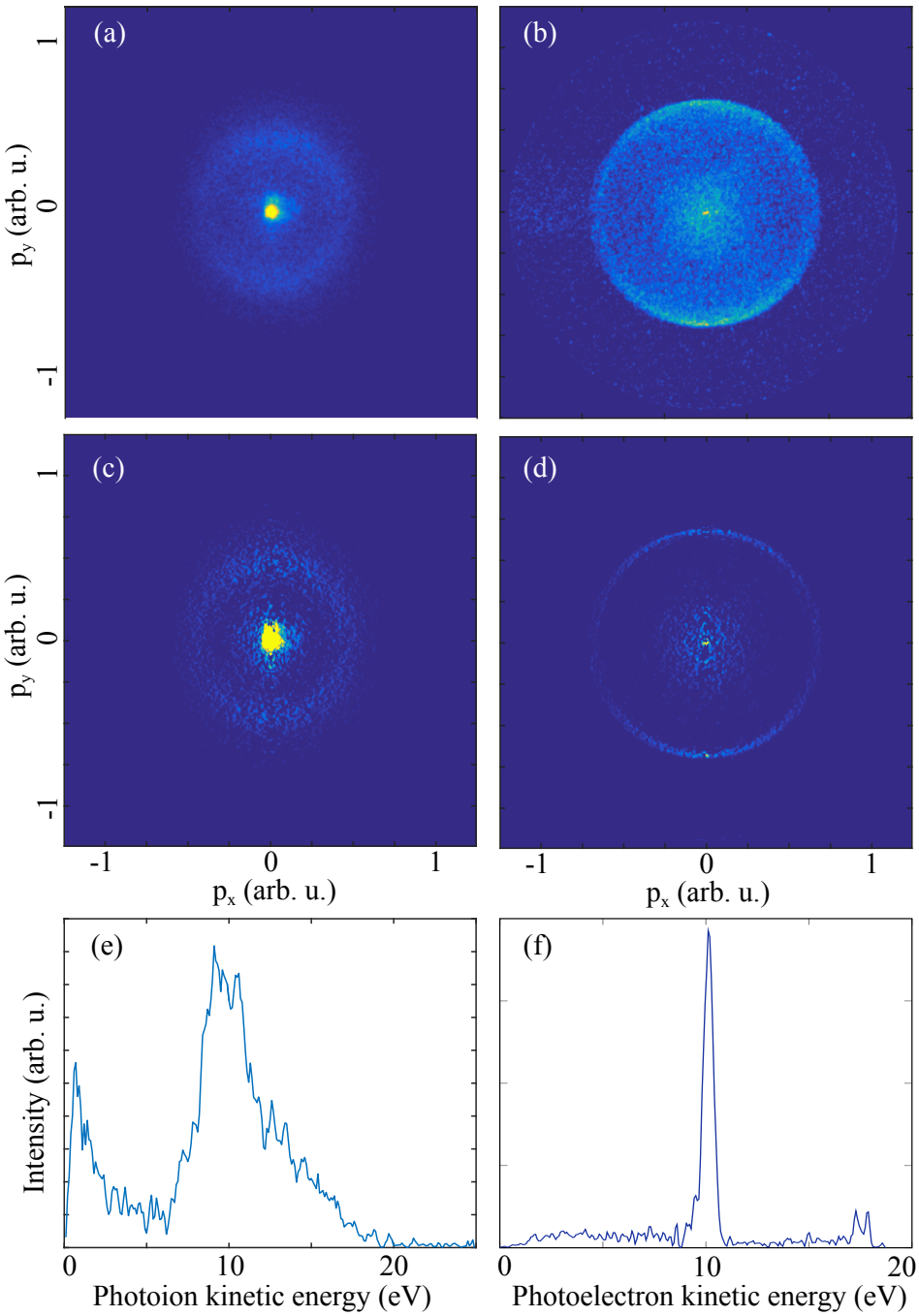

Figure 3.6: Raw (panel (a) and (b)) and inverted images (panel (c) and (d)) from the DVMIS when N_2 is ionized with photons with $E_{\mathrm{ph}} = 420$ eV. The ions resulting from Coulomb explosion are seen in the left column and electrons with energy of $E_{\mathrm{ph}} - Ip$ are seen in the left column. Panel (e) and (f) show the photoion and photoelectron spectrum, respectively.

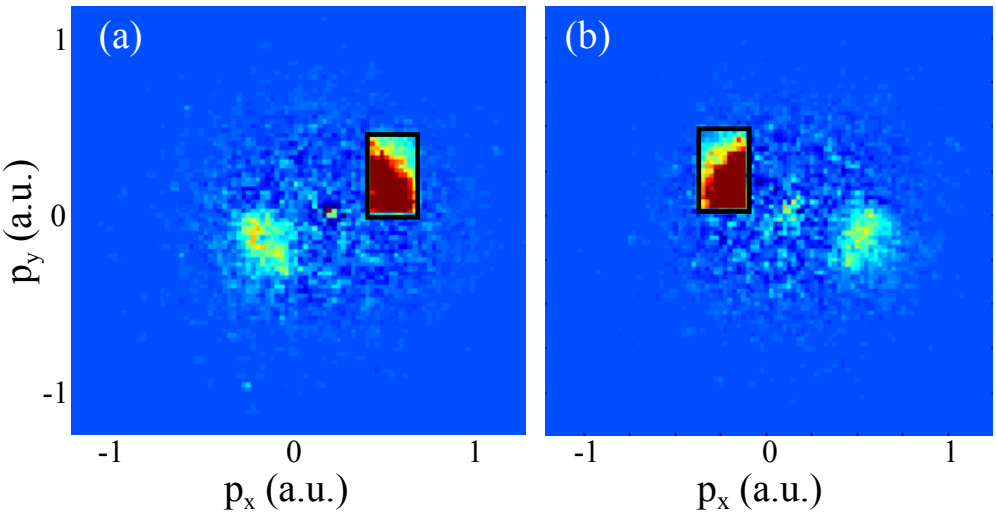

Figure 3.7: Covariance maps of the ion image, for two different areas in (a) and (b). The area choosen is highly correlated to itself, but also to an area with opposite momentum, as expected for Coulomb explosion.

taking place during the gas pulse. To ensure that only the events originating from the gas pulse are detected, and not those from the background gas, a short shutter time is used.

Covariance analysis was used to study the ion images. The number of counts in one area of the raw image are summed for every shot, forming $\mathbf{X}$, a stochastic variable. The covariance is calculated between $\mathbf{X}$ and every pixel in the binned (by 5×5 pixels) ion image to form a covariance map. Two covariance maps are shown in Figure 3.7, where two distinct regions can be observed. The region marked by a black rectangle is the area used to form $\mathbf{X}$, and that area is, not surprisingly, highly correlated to itself. The other area showing high correlation (dominated by light blue), tells us that the ions emitted in that direction are correlated to the ions in the area marked by a black rectangle. This is the signature of the Coulomb explosion, where every ionization event result in two fragments, sent out in opposite directions with the same energy.

The final goal is to reveal correlations between ions and electrons by the covariance technique and a first analysis has been attempted. The total signals from the ion and electron side are correlated, which proves a successful synchronization of the ion and electron images. By the use of covariance, the correlation between ions ejected in a specific direction and the electrons should, in principle, allow us to extract information on the MFPADs, even in multi-event experiments. Such an analysis is ongoing, but has not yet revealed any clear correlations and a possible reason is the need of more statistics.

Chapter 4

Experiments with intense XUV pulses

The generation of intense HHG light is challenging due to the inherent low conversion efficiency (typically 10^{-6} to 10^{-5} for argon). By using intense driving lasers with short pulses and low repetition rates, XUV light sufficiently intense to induce non-linear processes is being generated in a few laboratories around the world, for example, at FORTH in Greece [14, 16], RIKEN, in Japan [29, 78] and in Lund (see Paper III). However, the intensity of high-order harmonics can be increased in three ways, all of which have been employed in this work when developing the Intense XUV Beamline at the Lund Laser Centre.

HHG microscopic response: Increasing the probability that an atom will emit XUV light. This can be achieved by changing the driving field by adding another colour. In the study described in Paper I, high-order harmonics were generated in two gas cells placed one after the other, and the low-order harmonics generated in the first gas cell were found to enhance HHG in the second gas cell.

HHG macroscopic response: Phase matching of the harmonics generated. Scaling of the generation conditions to maintain phase matching, and therefore the conversion efficiency, while increasing the input energy. In this work, the optimum phase matching conditions were found by systematically scanning the generation parameters, and a scaling model for loose focusing of the IR beam was proposed (Paper II). The loose focusing was then extended to 9 m focal length, and a 6 cm long gas cell was used for HHG (Paper III).

XUV low loss propagation and tight focusing: Low-loss transport of the XUV beam to the experimental chamber and tight focusing in the interaction region. This was implemented in the experiments reported in Paper III. The resulting XUV intensity in the interaction region was sufficiently high to induce non-linear ionization in neon.

The Intense XUV Beamline in Lund was rebuilt during the course of this work to allow studies of non-linear processes in matter with intense attosecond pulse trains

(APTs). The beamline was extended to accommodate longer focal lengths, and an experimental chamber was added in which the XUV pulses can be tightly focused in a pulsed gas jet.

This chapter gives a description of the techniques used at the Intense XUV Beamline in Lund to generate and characterize intense XUV pulses and presents the first non-linear ionization results which were milestones in the development of the beamline. The experiments presented in Papers I-VI are introduced.

The Intense XUV beamline is described in Section 4.1. In Section 4.2, the methods used to measure the number of XUV photons are described, and the estimated intensity at the focus is discussed together with the challenges associated with absolute XUV pulse energy measurements. In Section 4.3 the results for non-linear ionization of neon are presented, together with a discussion on whether the underlying process is sequential or direct. Estimation of the non-linear ionization cross section is also outlined.

This chapter concludes with a discussion on the possibility of using the observed non-linear process for autocorrelation of the XUV pulse. This is of interest since the first tests of the XUV-XUV split-and-delay unit described in Paper IV are being performed at the time of writing.

4.1 The Intense XUV Beamline in Lund

The Intense XUV Beamline is driven by a Ti:sapphire laser delivering 225 mJ, 35 fs pulses at 10 Hz. Figure 4.1 shows flowcharts of the Ti:sapphire laser and the Intense XUV Beamline. After compression, the IR beam is focused into a gas cell where HHG takes place. After HHG, the fundamental is filtered away, and the beam can either be directed towards diagnostic equipment or passed straight into the experimental chamber where it is tightly focused in the gas under study. The charged fragments from ionization are detected in a spectrometer. Grazing incidence optics is used to split and focus the XUV beam, and together with generation in argon leads to an available bandwidth for experiments that spans HO 15-35. The bandwidth is limited on the low-energy side by the transmission of the aluminium filter, and on the high energy side by the generation gas. The bandwidth can be extended if necessary by performing HHG in, for example, neon. The use of broadband radiation allows both the direct and sequential two photon ionization channels in, for example, neon, to be accessed. So far, the beamline generates APTs, and the large bandwidth leads to shorter pulses in the train if they are correctly compressed (see discussion in Section 2.1). If single attosecond pulses (SAPs) are achieved in the future, a beamline that transmit a large bandwidth will allow shorter SAPs.

4.1.1 The terawatt laser system at the Lund Laser Centre

The laser system used for HHG delivers uncompressed pulses ($\approx$ 300 ps) with an energy of 225 mJ and a wavelength of 800 nm at a 10 Hz repetition rate. The system was installed in its original configuration in 1992 and is based on chirped pulse amplification (CPA) which was first used for laser pulse amplification in 1985 [79]. A flowchart of the laser chain is shown in Figure 4.1a. The chain starts with a mode-locked oscillator, which generates pulses of 50 nm bandwidth at an 80 MHz repetition rate using

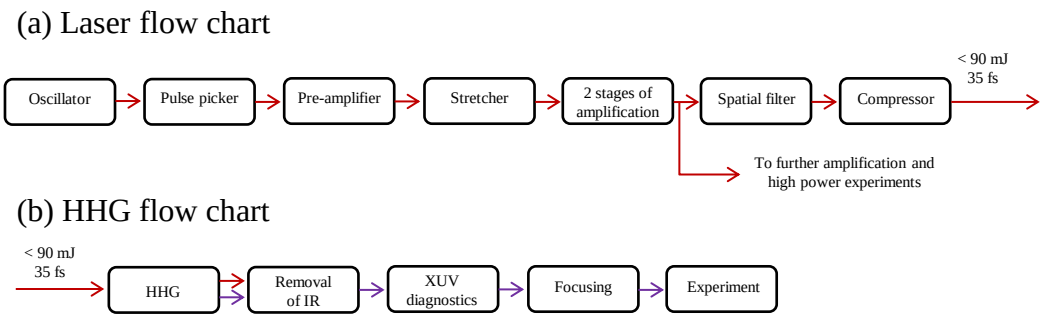

Figure 4.1: Flowchart for: (a) the terawatt Ti:sapphire laser, and (b) the Intense XUV Beamline in Lund. The colours of the arrows indicate whether an IR beam (red) or an XUV beam (violet) propagates between the steps.

Ti:sapphire as the gain medium [80]. When the frequencies are mode-locked, a short intense pulse travels in the cavity causing the Ti:sapphire crystal to act like a lens due to the non-linear Kerr effect [81]. The laser cavity is designed to be stable when the lensing effect is present, which favours mode-locking. A pulse picker reduces the repetition rate to 10 Hz before the beam is amplified in three stages. The main purpose of the first stage, pre-amplification, is to improve the contrast. About 1 µJ is sent to the stretcher which stretches the pulse to ≈450 ps before the two final amplification stages consisting of a regenerative amplifier and a multipass amplifier. The bandwidth is reduced during amplification, mainly due to gain narrowing in the amplifier crystals. The output has an energy of 450 mJ and is split into two 225 mJ parts, one of which is sent through the wall into the Intense XUV Laboratory. The other part of the beam is further amplified, and is used in proton and electron acceleration experiments, which are not covered in this thesis.

Before compression, the pulse is focused into a spatial filter, which is a small conical pinhole. Higher spatial frequencies are removed which improves the spatial profile. In the Intense XUV Laboratory, the beam is compressed in a grating compressor which adds a linear chirp with the opposite sign to the chirp added by the stretcher. After compression, the pulse length is less than 40 fs and the energy may be up to 90 mJ, and the pulse can now be used to generate intense APTs.

4.1.2 Generation of high flux XUV pulses in a loose focusing regime

As mentioned in the introduction of this chapter, the microscopic and macroscopic response must be optimized to generate a high-flux XUV beam. A higher generation intensity increases the microscopic response due to the higher probability of ionization in the first step in the TSM (see Chapter 2). The drawback is that a high degree of ionization of the medium leads to poorer phase matching conditions due to the dispersion in the plasma, as discussed in Paper II and Section 2.2. Typically, an ionization degree of a few percent is optimal which corresponds to $\approx 2{\cdot}10^{14}$ W/cm^2 for

argon, but the optimum intensity can be higher or lower depending on the ionization potential of the generation gas.

The microscopic response can instead be increased by altering the fundamental field in such a way that ionization is enhanced during the part of the fundamental period that leads to the generation of short trajectories. This idea was tested in an experiment at the beamline where HH were generated in two gas cells placed one after the other. The low-order harmonics generated in argon in the first cell increased the generation of HH in neon in the second cell due to reshaping of the fundamental generating field (Paper I). Figure 4.2 shows an overview of the two-cell experiment. Calculations show that by adding the third harmonic with the appropriate phase, the ionization step in TSM can be suppressed for ionization times that do not lead to the generation of HH through the short trajectories. A typical result showing the harmonic spatial profile as a function of wavelength, obtained using only the fundamental field focused in a neon-filled gas cell is compared with a result where the fundamental is combined with the low-order harmonics generated in the argon-filled seeding cell (4.2c).

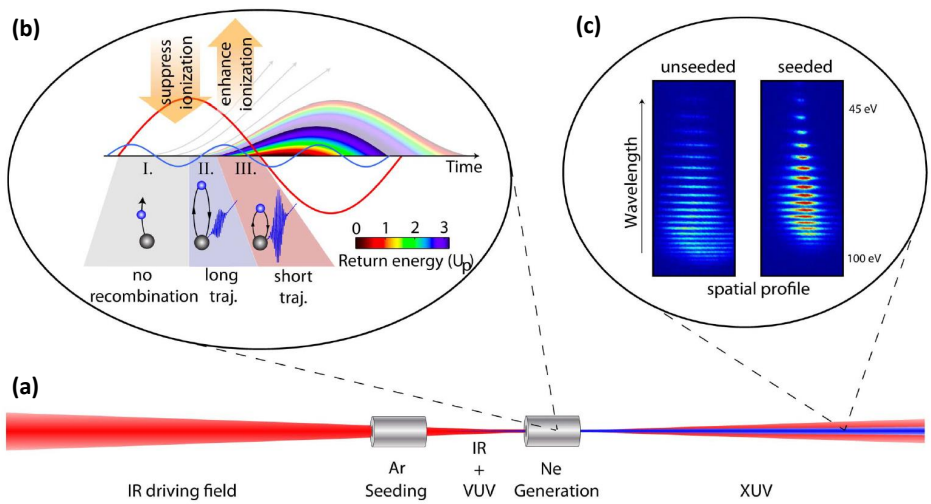

Figure 4.2: Overview of the two-cell HHG scheme described in Paper I. (a) A schematic overview of the experimental set-up. (b) A sketch showing which regions are suppressed and which are enhanced when adding the third harmonic. (c) Neon spectrum for the seeded and the non-seeded cases. Reproduced from Paper I.

To improve the macroscopic response, the generation should be phase matched, as discussed in Chapter 2, and the medium should have an appropriate length which is a trade-off between the quasi-coherent build-up of the harmonic radiation and re-absorption in the medium [37]. It is possible to use higher driving pulse energies if the f-number is increased so that the intensity at the focus remains the same. By changing the other generation parameters according to Equation 2.15 in Chapter 2 phase matching, and therefore the conversion efficiency, will be unchanged and the same increase in XUV pulse energy can be achieved. For example, if the f-number is

doubled, by doubling the focal length, the input energy can be increased by a factor 4, while maintaining the same intensity at focus. If the pressure and the length of the generation medium is scaled according to Equation 2.15 (by factors of 0.25 and 4, respectively), the conversion efficiency will be preserved and the XUV flux can be increased four times.

To be able to use up to 90 mJ after compression, the Intense XUV Laboratory was rebuilt to allow for long focusing (up to 10 m if the beam is folded once). The IR beam is now focused by a lens with 9 m focal length into vacuum and the HH are generated in a 6 cm long gas cell. The intensity is controlled by an attenuator and the beam size is adjusted by varying an aperture before the entrance to vacuum chambers. The aperture changes the f-number but also the intensity. The generation parameters used for HHG in argon (Paper III) are given in table 4.1:

Table 4.1: Generation parameters used in Paper III. The intensity at the focus is too high for HHG and the best generation conditions are found out of focus.

Pulse energy	80 mJ
Pulse length	35 fs
Aperture size	30 mm
Focus size	≈ 300 µm
Intensity in focus	$3 \cdot 10^{15}$ W/cm^2
Pressure	13 mbar

The intensity at the focus is estimated to be higher than the typical intensity used for HHG in argon ($2 \cdot 10^{14}$ W/cm^2) and this is the reason why the best generation position was found to be 0.5 to 1 m before the focus (Paper III). The intensity of the HH pulse generated was estimated to be 0.8 µJ for HO 15 and above. If HH are to be generated closer to the focus, the intensity must be decreased by changing the f-number. This means using an even longer focal length or a smaller beam diameter.

4.1.3 IR beam removal

The XUV and IR beams co-propagate after HHG, and before sending the XUV beam to the diagnostic chamber and the experimental chamber, the IR beam must be removed. Figure 4.3 shows an overview of the part of the beamline after HHG and before the experimental chamber. The XUV and IR beams are first reflected by a silica plate and then passed through a metal filter, which removes the IR beam. The XUV beam then enters the diagnostic chamber. The silica plate can be replaced by a split plate, which splits the XUV pulse into two parts for the XUV pump-XUV probe experiments presented in Section 4.4.1. Metallic filters have 0% transmittance for IR, but can have fairly high transmittance for XUV. If the metal filters were placed directly in the full IR beam they would be damaged after a few shots. This was avoided by first removing 90% of the IR-beam using the silica plate. The plate is coated with alternating layers of silica (SiO_2) and titanium oxide (TiO_2). The thickness of the layers is matched so that the coating is non-reflective for IR. The XUV is reflected by the outermost layer of silica. The most commonly used metal filter in the beamline is a 200 nm aluminium filter that has $\approx 20\%$ transmittance for 30 eV photons. A layer of aluminium oxide is formed on the filter when it is exposed to air, which reduces the transmittance of XUV

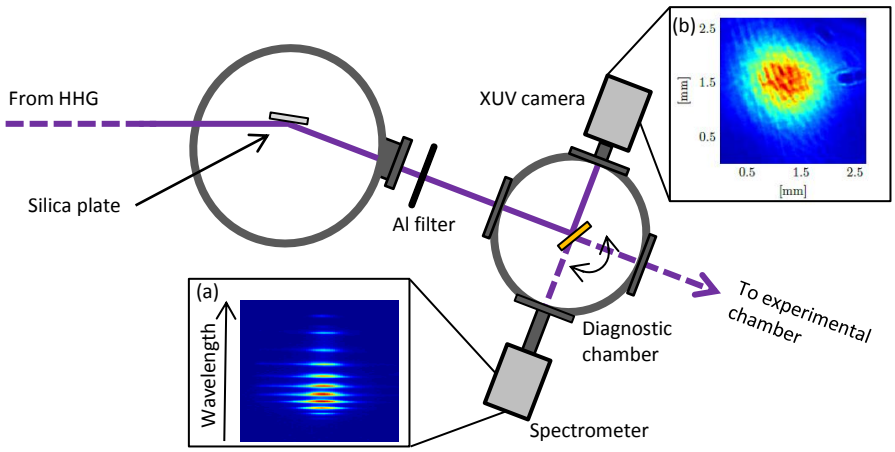

Figure 4.3: Overview of the part of the beamline between the generation and the experimental chamber. Inset (a) shows a HHG spectrum when argon is used as a generation gas and inset (b) shows a beam profile taken by the XUV CCD camera. The silica plate can be replaced by a split plate for XUV pump-XUV probe experiments.

light. The thickness of the oxide, and its effect on the transmittance of the filters is further discussed in Section 4.2.

4.1.4 XUV diagnostics

After removing the IR beam, the XUV beam enters the diagnostic chamber, as shown in Figure 4.3. The beam can be directed to a calibrated XUV camera or to an XUV spectrometer by a rotatable gold mirror, or it can be sent straight to the experimental chamber. Figure 4.3 also shows examples of a spectrum from HHG in argon and a beam profile taken obtained with the XUV CCD camera. The flux can also be measured with a calibrated XUV diode (not shown in the figure). It is difficult to measure the absolute XUV flux, and the possible sources of error are discussed in Section 4.2.

XUV spectrometer

The XUV spectrometer is a flat-field spectrometer and an MCP/phosphor assembly, imaged by a CCD camera, is used to record the diffracted harmonics. Figure 4.4 shows a spectrum from HHG in argon corrected for the grating response and the correction factor due to the variable change from wavelength to photon energy. An alternative to the XUV spectrometer is to allow the XUV beam to ionize a gas in the experimental chamber, and retrieve an XUV spectrum from the energy of the photoelectrons. Since the ionization potential of the gas is known, the assignment of harmonic orders is straight-forward and the spectrum can be corrected for the photoionization cross section, which is well known for single photon XUV ionization of all rare gases.

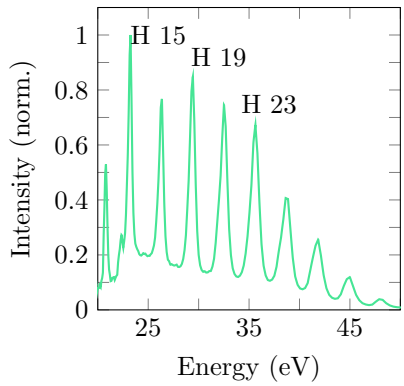

Figure 4.4: An example of a HH spectrum generated in argon.

The XUV CCD camera

An XUV-CCD camera (Andor iKon-L) is used to measure the XUV pulse energy and the beam profile. The XUV photons are absorbed in a layer of silicon and create electron-hole pairs. The electrons and holes are separated by the applied internal electric field, and the electrons are amplified and read out. The quantum efficiency is dependent on the photon energy, and in order to calculate the energy of the XUV-pulse, its spectrum must be known. A step-by-step description of the calculation of the XUV flux using the XUV CCD camera is given in Section 4.2. A typical beam profile can be seen in inset (b) in the sketch of the diagnostics set-up in Figure 4.3, where the size of the beam is approximately 1 mm.

Photodiode

A calibrated XUV photodiode can be used at different locations in the beamline. It can be installed in front of the XUV CCD camera on a push-pull device to allow comparison of the flux measured by the XUV CCD camera and the photodiode. The photodiode can also be installed directly after the focus in the experimental chamber to record the flux for single XUV shots. This is necessary when the intensity fluctuations between shots must be taken into account in the data processing, for example when partial covariance methods are used as is discussed in Section 3.2.

4.1.5 The experimental chamber

The XUV beam is focused into the centre of the experimental chamber, where it is overlapped with the pulsed gas jet, entering from the top of the chamber, and the ions and electrons can be recorded simultaneously by the double sided VMIS (described in Chapter 3). Figure 4.5 shows a sketch of the experimental chamber, the focusing optics and the DVMIS and in Figure 4.6 a photograph is seen.

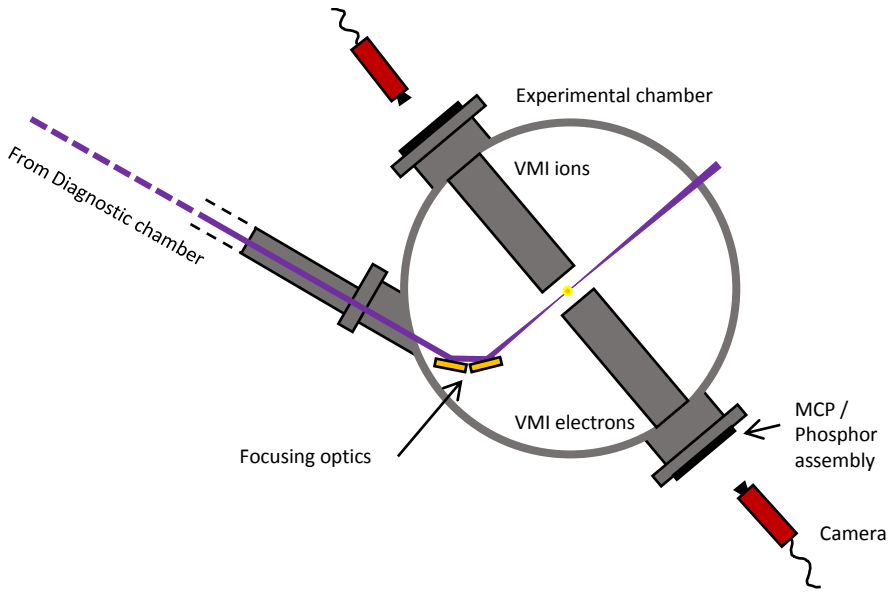

Figure 4.5: Sketch of the experimental chamber

Wolter optics

The XUV beam diverges for 6 m after generation, before being focused by two toroidal gold mirrors, which are mounted on a five-axis optical mount which can be seen in Figure 4.7a. To achieve a high XUV reflectivity, a grazing angle of incidence must be used. The angle between the first mirror and the incident beam is 15°, which results in a total deviation of 60° after two reflections. The mirrors are arranged in a so-called Wolter configuration [82], where the combination of two toroidal mirrors with different radii gives an almost aberration free focus. Theoretically, the best focus is achieved by focusing with an elliptical mirror. However, it is difficult to manufacture elliptical mirrors with high precision, and a toroidal mirror is therefore a better and cheaper alternative in practice.

The pulsed gas source

An electro-magnetically actuated Even-Lavie valve is used to create short, dense gas pulses [83, 84]. A photograph of the valve mounted on its flange can be seen in Figure 4.7b. It is possible to perform experiments on molecules in solid or liquid form by heating them and allowing them to be carried into the interaction region by a carrier gas. The valve has been used successfully with, for example, ferrocene, which is an organometallic compound in solid form, and with 1,3-cyclohexadiene, which is a liquid.

4.2 XUV pulse energy measurements

It is important to measure the energy of the XUV pulses generated as well as the resulting intensity in the experimental chamber. Knowing these quantities enables to

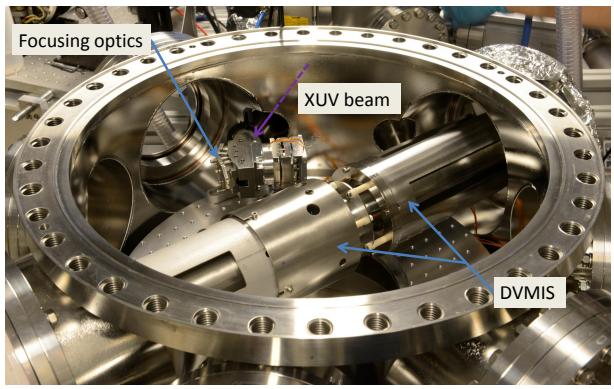

Figure 4.6: Experimental chamber where the focusing optics and the DVMIS are seen

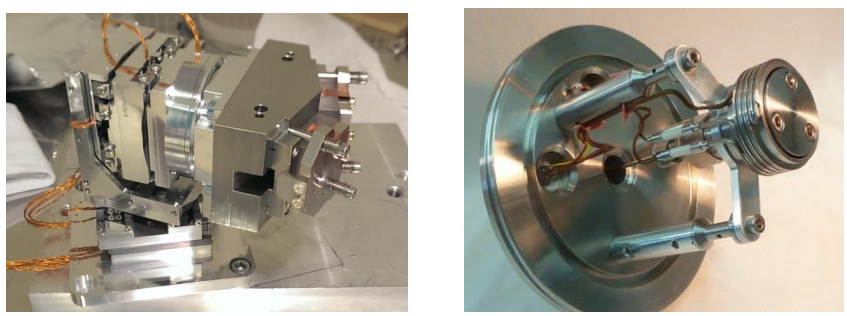

(a) **(b)**

Figure 4.7: (a) Focusing optics mounted in a five-axis mount, and (b) the Even-Lavie valve mounted on a flange.

determine the HHG conversion efficiency, the cross section for the non-linear ionization process, as well as the energy throughput of the beamline. Measuring the absolute number of photons is difficult since it requires knowing the spectrum at the point of measurement due to the large bandwidth of the HH combined with an often non-flat spectral response of the XUV detector. Measurements are typically conducted at one, or a few, positions in the beamline and the number of photons at another point can be calculated if the transmittance between the points is known. This section describes how the XUV pulse energy is calculated using the XUV spectrometer and the calibrated XUV CCD camera together, and discusses the sources of error and the challenges encountered in these measurements.

4.2.1 The XUV CCD camera

The calibrated XUV CCD camera was used to measure the XUV pulse energy. The flowchart in Figure 4.8 explains how photons impinging on the chip in the camera are transformed in three steps into the counts read out by the user. Below is a description

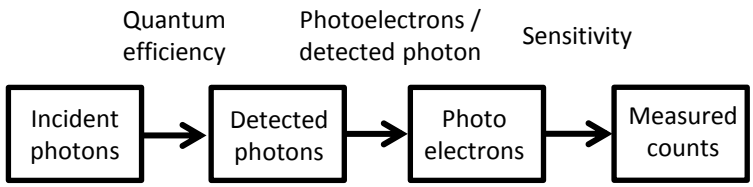

Figure 4.8: Flow chart of the different steps from incident photons to measured counts for the XUV CCD camera used to measure the XUV energy in the experiment reported in Paper III.

of the three steps, and the variables used in Equation 4.3 to calculate the total number of photons are introduced.

Incoming photons → detected photons: The quantum efficiency (QE) is the probability of detecting an incoming photon, i.e., absorption of the incident photon in the silicon layer where it creates electron-hole pairs. For low-energy photons, the probability of absorption in the electrode structure or the oxide layer on top of the silicon layer, instead of *in* the silicon layer, is rather high resulting in a low QE for energies of about 10-20 eV. The QE-curve for the energies relevant for this work is shown in Figure 4.9.

Detected photons → photoelectrons: The number of e-h pairs ($N_{\text{e-h}}$) generated is dependent on the energy of the incident photon (E_{ph}), and is given by $N_{\text{e-h}} = E_{\text{ph}}(eV)/3.65$ [85]. The number of photoelectrons is given by the number of detected photons multiplied by $N_{\text{e-h}}$.

Photoelectrons → counts: The number of photoelectrons divided by the sensitivity number (SN) gives the number of counts in the detector (N_{counts}) from the XUV pulse. The sensitivity depends on the settings on the camera (rate, pre-amplifier setting, high sensitivity mode or high capacity mode), but is independent of the energy of the incoming photon [86, 87].

The total number of XUV photons, assuming one frequency, is given by:

$$N_{\text{ph}} = \frac{N_{\text{counts}} \cdot SN}{N_{\text{e-h}} \cdot \text{QE}}, \tag{4.1}$$

and the XUV pulse energy is given by:

$$E_{XUV} = N_{\text{ph}} \cdot E_{\text{ph}}. \tag{4.2}$$

For light consisting of several harmonic orders, k, the energy dependence of QE, $N_{\text{e-h}}$ and E_{ph} must be taken into account, and the total number of XUV photons is given by:

$$N_{\text{ph}} = \frac{N_{\text{counts}} \cdot SN}{\sum_k W_k \cdot \text{QE}_k \cdot N_{\text{e-h,k}}}. \tag{4.3}$$

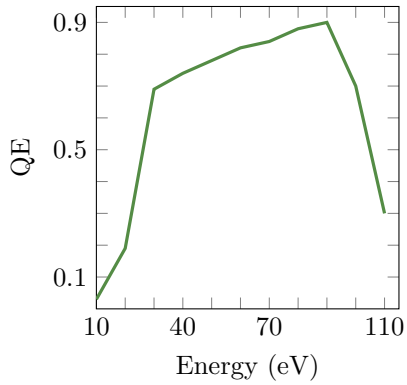

Figure 4.9: QE-curve for ANDOR iKon-L CCD camera. The low quantum efficiency for low energies is due to absoption of the photons before reaching the silicon layer where electron-hole pairs are created.

The energy-dependent factors are multiplied by a weight factor, W_k, and summed over k. W_k is the relative strength of the harmonic order k, given by the XUV spectrometer and $\sum W_k = 1$. The total XUV energy can then be written as:

$$E_{\mathrm{XUV}} = \sum N_{\mathrm{ph}} W_k E_{\mathrm{ph}}. \tag{4.4}$$

4.2.2 The XUV intensity on target

Once the number of photons per harmonic order at the position of the XUV camera is known, the generated pulse energy and the pulse energy in the interaction region can be calculated, if the energy-dependent transmission of the beamline is known. The transmission of the beamline includes reflection from the silica plate, the transmission of the filters used and the reflectivity of the focusing optics. These are calculated using the Handbook of Optical Constants [88]. To calculate the intensity at the focus, the energy dependent transmission of the beamline from the camera to the interaction region must be combined with the estimated duration of the individual attosecond pulses, the duration of the pulse train and the measured size of the focus. In the experiment reported in Paper III, the pulse energy generated was found to be ≈ 0.8 µJ and using an estimate of 15 attosecond pulses, each with a pulse length of 300 as, and a focal spot size of 10×15 µm, we obtain an intensity of $\sim 3 \cdot 10^{12}$ W/cm^2 at the focus.

4.2.3 Experimental challenges

Measurements of XUV pulse energy may appear to be simple, but during the process of learning how to measure XUV pulse energies, several sources of error were identified that are easily overlooked. The non-linearity of the spectrometer and the transmission of the metallic filters are two important factors, which will be discussed below.

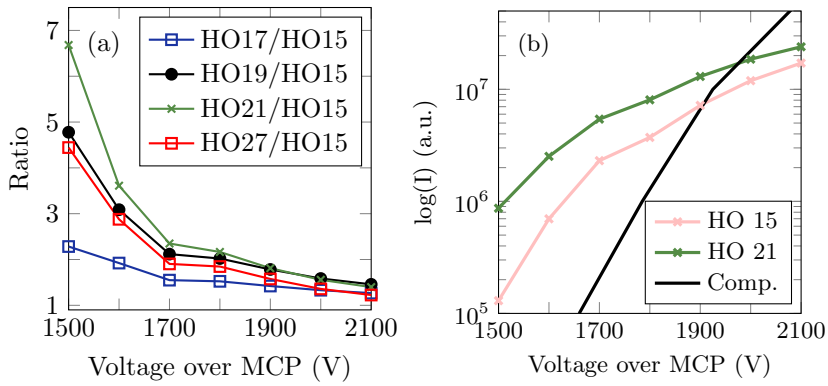

Figure 4.10: Indications of saturation of the MCP. (a) HO 17 to 23 normalized to HO 15 for different voltages over the MCP. The spectrometer is not linear since the ratio between the harmonic orders is voltage dependent. (b) The logarithm of the signal of HO 21 for 1500-2100 V together with the slope given by the manufacturer of the MCP. Observe that only the slope can be compared and not the absolute intensity. The slope for HO 21 is smaller than expected, which indicates saturation.

Non-linearity of the spectrometer

Non-linarites of the MCP were first suspected when unreasonable values of the filter transmission were obtained when measuring two spectra, one after a metallic filter and one without a filter, with the XUV spectrometer. To study the MCP response, spectra were collected at different voltages over the MCP. In Figure 4.10a the signals of HO 17-21 and HO 27 normalized to HO 15 are shown for voltages between 1500 and 2100 V, and it can be seen that the relative strength of the harmonics is dependent on the voltage on the MCP. At low voltages, HO 21 (which is the most intense HO) is seven times stronger than HO 15, but when applying a voltage of 2000 V they are almost equal in strength. Figure 4.10b shows the logarithm of the intensity of HO 15 and HO 21 as a function of voltage. The gain of the MCP is exponentially related to the voltage, and is expected to be a straight line in absence of saturation effects. The black line is the relation provided by the manufacturer of the MCP. The scale on the vertical axis is arbitrary, but the gradient is comparable to the measured gradient for a voltage of 1500-1600 V, indicating that saturation occurs around a voltage of 1700 for HO 15 but already at the lowest voltages used for HO 21. This problem could be solved by reducing the flux and instead using longer acquisition times, but it is difficult to reduce the flux without changing the spectrum. Another option is to replace the MCP with an XUV CCD camera, which has a better linearity.

Transmission of filters

When aluminium comes into contact with air, a layer of aluminium oxide (Al_2O_3) a few nm thick is formed on the surface, this affects significantly the filter transmission. Measurements of the XUV flux were performed with one and two filters, and the thickness of the Al_2O_3 layer was found to be 4 nm per side (Paper III). The XUV transmission of 8 nm Al_2O_3, 200 nm aluminium and the combination of both is shown

in Figure 4.11. The graphs shows two curves each, using data from the CXRO database [89, 90] and the Handbook of Optical Constants [88].

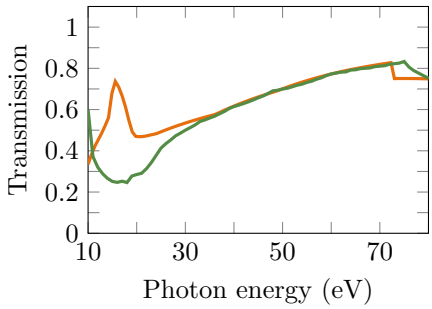

(a) Transmission for 8 nm Al_2O_3

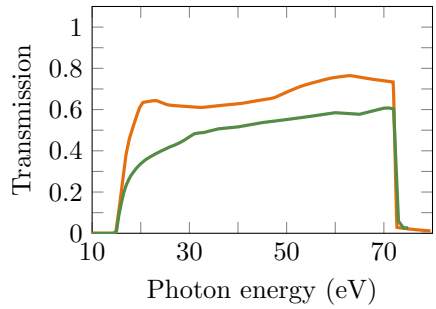

(b) Transmission for 200 nm Aluminium

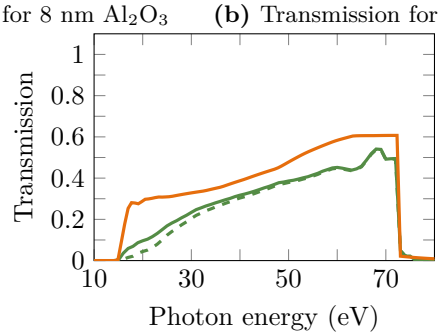

(c) Total transmission of 200 nm aluminium and 8 nm Al_2O_3

Figure 4.11: Transmission curves calculated from data from the CXRO database (orange) and from the Handbook of Optical Constants (green). (a) XUV light transmission through 8 nm Al_2O_3. (b) XUV light transmission through 200 nm aluminium. (c) XUV light transmission through 8 nm Al_2O_3 and 200 nm aluminium. For the dotted line, the reflections between the layers have been taken into acount.

The values in the CXRO data base are based upon photoabsorption measurements of elements in their elemental state and the condensed matter is modelled as a collection of non-interacting atoms [89]. This is not a good model for energies close to absorption thresholds and is probably the reason to the differences observed in Figure 4.11 between the two databases. The lowest harmonic observed at the spectrometer when using an aluminium filter is harmonic 15, which indicates that the curve using the Handbook of Optical constants is more correct, since if using the other curve, harmonic 13 should also be visible. When calculating the XUV transmission for the filters in the beamline, the parameters found in the Handbook of Optical Constants were used.

4.3 Two-photon double ionization of neon

The beamline was designed to achieve intense, broadband XUV light, and Paper III describes an experiment in which the first non-linear ionization, two-photon double

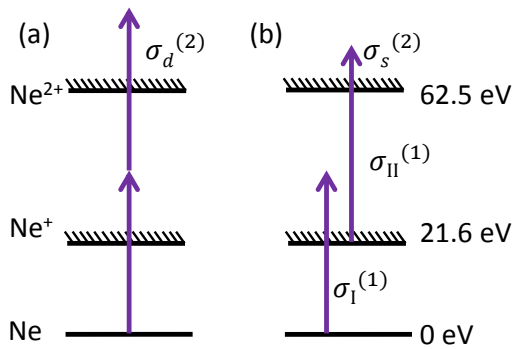

Figure 4.12: The two channels for two-photon double ionization, assuming a single harmonic order. (a) Direct channel, which requires $E_{\mathrm{ph}} > 31.25$ eV and where the resulting electrons share the excess energy. (b) Sequential channel, which requires $E_{\mathrm{ph}} > 40.9$ eV and where the resulting electrons have two discrete energies.

ionization of neon, was observed using this beamline. The two possible two-photon double ionization path-ways are illustrated in Figure 4.12. The XUV bandwidth allows access to both the direct and the sequential channel. The measurements provided strong indications that with these experimental conditions, two-photon double ionization is strongly dominated by the sequential channel.

Section 4.3.1 describes the observation of the non-linear signal, Section 4.3.2 describes the experiment carried out to deduce whether the nature of the non-linear process was mainly sequential or direct, while the estimation of the cross section going from a singly charged to a doubly charged neon ion is presented in Section 4.3.3.

4.3.1 Non-linear signal

The XUV beam was overlapped with the beam of neon atoms in the interaction region of an ion TOF spectrometer. The resulting mass spectrum is shown in Figure 4.13a and the peak at $m/q = 10$ arises from doubly ionized neon while the peak at $m/q = 20$ is from singly ionized neon. Approximately one Ne^{2+} ion was detected on every shot. To prove that the Ne^{2+} signal is due to two-photon ionization, and not from single-photon double ionization, the intensity of the harmonics was varied by changing the pressure in the generation gas cell, and the dependence of the intensity on the doubly charged ion yield was studied. Care was taken that the spectral distribution did not change notably. For a second-order process, a doubling of the intensity should lead to a four times higher yield, as discussed in Section 2.3.2. The peak seen at $m/q = 18$ is singly charged H_2O and this peak is considered to be proportional to the XUV flux, and was used to determine a relative XUV flux at each gas pressure. A plot showing the dependence of the Ne^{2+} peak on the XUV intensity is shown in Figure 4.13b. The slope is close to two, which proves that it is a two-photon process.

4.3.2 Identification of the ionization process

The shorter the pulses, the more likely it is that double ionization will take place through a direct process. The effective duration of the attosecond pulse train is defined

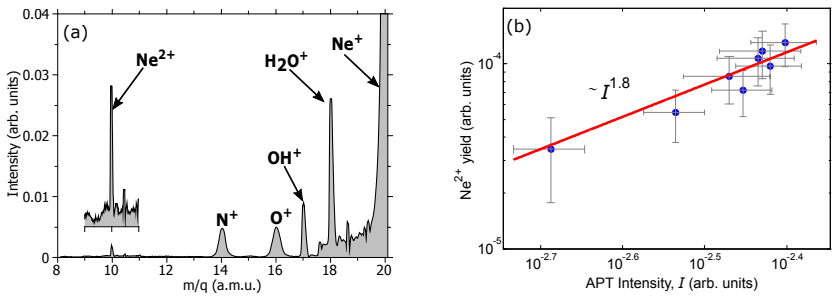

Figure 4.13: Two-photon double ionization of Neon. (a) A mass spectrum from the ion TOF showing the Ne^{2+} peak at $m/q = 10$. (b) The Ne^{2+} yield as a function of the intensity of the attosecond pulse train. The slope is close to two when using logarithmic scales. Reproduced from Paper III

as the sum of the individual pulse lengths, and was estimated to be 4.5 fs. According to theoretical calculations of the two-photon cross sections for the sequential and the direct process, the sequential process is expected to dominate for this pulse duration [54, 91]. To verify this, electrons should ideally be studied, as discussed in Chapter 2. In the sequential case, the electrons will have discrete energies given by:

$$E_1 = E_{\text{ph}} - 21.6, \tag{4.5}$$
$$E_2 = E_{\text{ph}} - (62.5 - 21.6) = E_{\text{ph}} - 40.9. \tag{4.6}$$

In the direct case, the electrons instead share the energy of the two photons that exceed the double ionization threshold [92–94]. At the time of the experiment, the set-up was designed to detect only ions, and to obtain an indication of which process dominates, experiments were performed with two high-order harmonic spectra with different cut-offs; one that allowed for sequential and direct two-photon double ionization, and one that only allows double ionization through the direct channel. The high-order harmonics were generated in krypton and the cut-off was changed by aperturing the beam before HHG. To maintain the same overall intensity in the XUV radiation used for the double ionization process in the two cases, argon gas was introduced in a part of the beamline to adjust the flux. Using a spectrum with a cut-off below the sequential threshold led to no Ne^{2+} signal, indicating that non-linear ionization is strongly dominated by the sequential channel, as is further discussed in Paper III.

4.3.3 Experimental estimation of $\sigma_{II}^{(1)}$

The cross sections involved in two-photon sequential double ionization of neon are denoted in Figure 4.12. Both $\sigma_I^{(1)}$ and $\sigma_{II}^{(1)}$ can be measured with a synchrotron light source [49, 51]. The rate equations for the sequential process were introduced in Chapter 2. The number of doubly charged neon ions is thus given by:

$$\mathcal{N}_{\text{s}}^{(2)} = \frac{\rho L \sigma_I^{(1)} \sigma_{II}^{(1)} N_{\text{ph}}^2}{2A}, \tag{4.7}$$

where ρ is the density of gas, L the length of the interaction region, A the area of the focal spot, and N_{ph} the number of photons, all of which must be known to calculate $\sigma_{II}^{(1)}$. By instead considering the ratio of the number of Ne^{2+} ions to Ne^{+} ions, the influence of the gas density can be eliminated, and only the area of the focus and the number of photons for the relevant harmonics are required to obtain an estimate of $\sigma_{II}^{(1)}$.

$$\frac{\mathcal{N}_{\mathrm{s}}^{(2)}}{\mathcal{N}^{(1)}} = \frac{\sigma_{II}^{(1)} N_{\mathrm{ph}}}{2A}. \tag{4.8}$$

Here, N_{ph} is the number of photons for the harmonic orders that can contribute to the second step in the sequential process. This ratio was experimentally determined to be 0.35%, and the cross section for single photon ionization of Ne^{+} to Ne^{2+} was found to be:

$$\sigma_{II}^{(1)} \approx 7 \cdot 10^{-18}\mathrm{cm}^2. \tag{4.9}$$

The uncertainty in the measurement of this cross section arises from the uncertainty in the number of photons, and focal spot size measurements. The cross section found is in very good agreement with previosly reported values of $6 \pm 1 \cdot\ 10^{-18}\mathrm{cm}^2$ [51] and $7 \pm 1 \cdot\ 10^{-18}\mathrm{cm}^2$ [49].

4.4 On-going developments

Since the proof-of-principle experiment, where intensities sufficiently high to observe non-linear ionization were achieved in the beamline as reported in Paper III, several developments to improve the beamline and the experimental chamber have been launched and some of them, as the DVMIS and the Even-Lavie gasjet, are described above. In this section, two ongoing developments are presented.

Section 4.4.1 presents the on-going experiment where the split-and-delay unit (described in Paper IV) is used for the first time in the beamline. The current experimental goal is to perform an autocorrelation of the APT and the discussion here is focused on the question on how the use of the sequential process, described in the last section, affects the autocorrelation trace.

Two strategies for generating shorter XUV pulses have been tested at the beamline and are discussed in Section 4.4.2. In the first experiment, a planar hollow waveguide is used to compress the IR pulse before generation. In the second experiment, two non-collinear IR pulses are used for HHG and the time structure in the train is mapped to different angles allowing for spatially choosing a short part of the APT.

4.4.1 XUV autocorrelation using a sequential process

The XUV pulse generated in the beamline is sufficiently intense to ionize neon with two photons. It is of great interest to split the XUV pulse into two pulses that can be delayed with respect to each other in order to study ultrafast processes and to perform an auto-correlation of the XUV pulse.

In the optical regime, an IR pulse can be split into two by amplitude splitting using a beam splitter, and the non-linear signal can be generated, for example, in a crystal. However, in the XUV region, the pulse must be split using reflective optics, and a gas

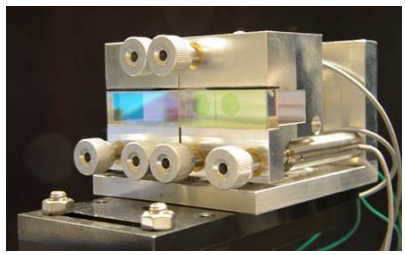

Figure 4.14: Photograph of the split-and-delay unit. One plate is movable by piezoelectric acctuators to introduce a delay in half of the XUV beam.

is used as the non-linear medium instead of a crystal. The first XUV autocorrelation was performed on APTs using two-photon single ionization of helium in 2003 [13], and has been followed by autocorrelation measurements using, for example, nitrogen [12, 48]. Autocorrelation measurements have also been performed on SAPs [29, 95]. To the best of the author's knowledge, autocorrelation measurements using a sequential process have not yet been reported.

The split-and-delay unit, consisting of a split plate and its mount, is shown in Figure 4.14. The XUV beam is reflected from a silica plate which is split into two parts, one of which can be moved to delay half the beam. A stabilization system using an external diode laser is used to ensure that the two beams are overlapped at the focus, and to control the delay. Further details can be found in Paper IV. The split-and-delay unit has recently been installed at the Intense XUV Beamline in Lund, and experiments are on-going where the sequential double ionization of neon, presented in Paper III, will be used to perform autocorrelation of the pulse.

This section deals with second-order autocorrelation of the APT in an attempt to understand how the autocorrelation trace is affected by the use of a sequential or a direct process. The simulations were carried out using both a linear process, and a direct and a sequential non-linear process. Calculations were performed for a single point in space.

A pulse with intensity $I \propto \left|\widetilde{A}(t)\right|^2$ and central frequency ω is described by:

$$\widetilde{E}(t) = \widetilde{A}(t)e^{i\omega t}. \tag{4.10}$$

The total intensity of two pulses that are delayed with respect to each other is found by adding the electric fields of the pulse and its delayed replica. In the following, τ denotes the *delay* between the two split pulses. In the case of a single harmonic order, and assuming that the intensity of the two pulses is the same, $I(t)$, the total intensity is given by:

$$\begin{aligned} I_{\text{tot}}(t,\tau) &\propto |E(t) + E(t-\tau)|^2 = |\widetilde{A}(t)|^2 + |\widetilde{A}(t-\tau)|^2 + 2|\widetilde{A}(t)||\widetilde{A}(t-\tau)|\cos(\omega\tau) \\ &= I(t) + I(t-\tau) + 2\sqrt{I(t)I(t-\tau)}\cos(\omega\tau). \end{aligned} \tag{4.11}$$

In a more realistic case a set of harmonic orders is used, and the electric field of the pulse train formed is the sum of the electric fields for single harmonic orders, as is

described in Equation 2.2. This electric field, and that of its replica, are used to find $I_{\mathrm{tot}}(t,\tau)$ for every delay, τ.

The ion yields for a given delay, τ, for the different processes are:

$$\mathcal{N}^{(1)}(\tau) \propto \int_{-\infty}^{\infty} I_{\mathrm{tot}}(t,\tau)dt, \qquad \text{One-photon}$$

$$\mathcal{N}_{\mathrm{d}}^{(2)}(\tau) \propto \int_{-\infty}^{\infty} I_{\mathrm{tot}}^{2}(t,\tau)dt, \qquad \text{Two-photon direct ionization}$$

$$\mathcal{N}_{\mathrm{s}}^{(2)}(\tau) \propto \int_{-\infty}^{\infty} I_{\mathrm{tot}}(t,\tau)\int_{-\infty}^{t} I_{\mathrm{tot}}(t',\tau)dt'dt. \qquad \text{Two-photon sequential ionization}$$

Using the above equations, the autocorrelation traces can be calculated numerically.

Figure 4.15 shows the autocorrelation results for the single ionization yield, $\mathcal{N}^{1}$, and the double-ionization yield, $\mathcal{N}_{\mathrm{d,s}}^{(2)}$ (direct and sequential). Calculations were performed for a single harmonic order (left column) and for an APT consisting of HO 21-33 (right column). When using neon as the gas, all combinations of HO can doubly ionize the atoms through the direct process, but in the sequential case, only HO 31-33 can contribute to the second step. Since not all the harmonic orders contribute to both ionization steps, the total intensity I_{tot} used in the above equation is thus formed from different sets of HO in the first and second step in the integral.

Looking at the autocorrelation trace using a single harmonic order (left column), it can be seen that for large positive or negative delays the pulses are separated in time and do not interfere. The envelope of the trace varies between 0 and 2 for the linear process, between 0 and 8 for the direct process and between 0 and 4 for the sequential process. The ratio between the case of two separated pulses and two fully overlapped pulses is referred to as the contrast, and has the values 2:1, 8:1 and 4:1, for the linear process and direct and the sequential non-linear processes, respectively. In the case of an APT (right column), the envelope is the same, but there are underlying structures separated by 1.3 fs. Note that the broader peaks in the trace formed by the sequential process are due to fewer contributing HO for the second step.

The result presented above would be obtained if the ions from only one point in space were detected and the delay between the pulses can be set exact. In the experimental situation, all the ions generated in a volume, defined by the intersection of the gas jet and the parts of the XUV beam that are sufficiently intense to induce non-linear ionization, contribute. In addition, the delay between the pulses cannot be set more exact than 50 as as mentioned in Paper IV. Due to the wavefront splitting of the XUV pulse, there is a π phaseshift over the focus for each beam, but with the opposite sign [96]. To obtain an approximate understanding of the volume effect and the limited time resolution, the simulated result is Fourier transformed and frequencies corresponding to HO 21 and above are set to zero before doing an inverse Fourier transform. These results are indicated by the black line in Figure 4.15. If a linear process is assumed, the yield is no longer dependent on the delay and this process cannot be used to retrieve information about the XUV pulse. In the sequential case, the 4:1 contrast is reduced to 1.5:1 and in the direct case the 8:1 contrast is reduced to 3:1. It is interesting to note that the contrast is not dependent on whether a single harmonic or an APT is used, and if the contrast can be measured accurately, it will

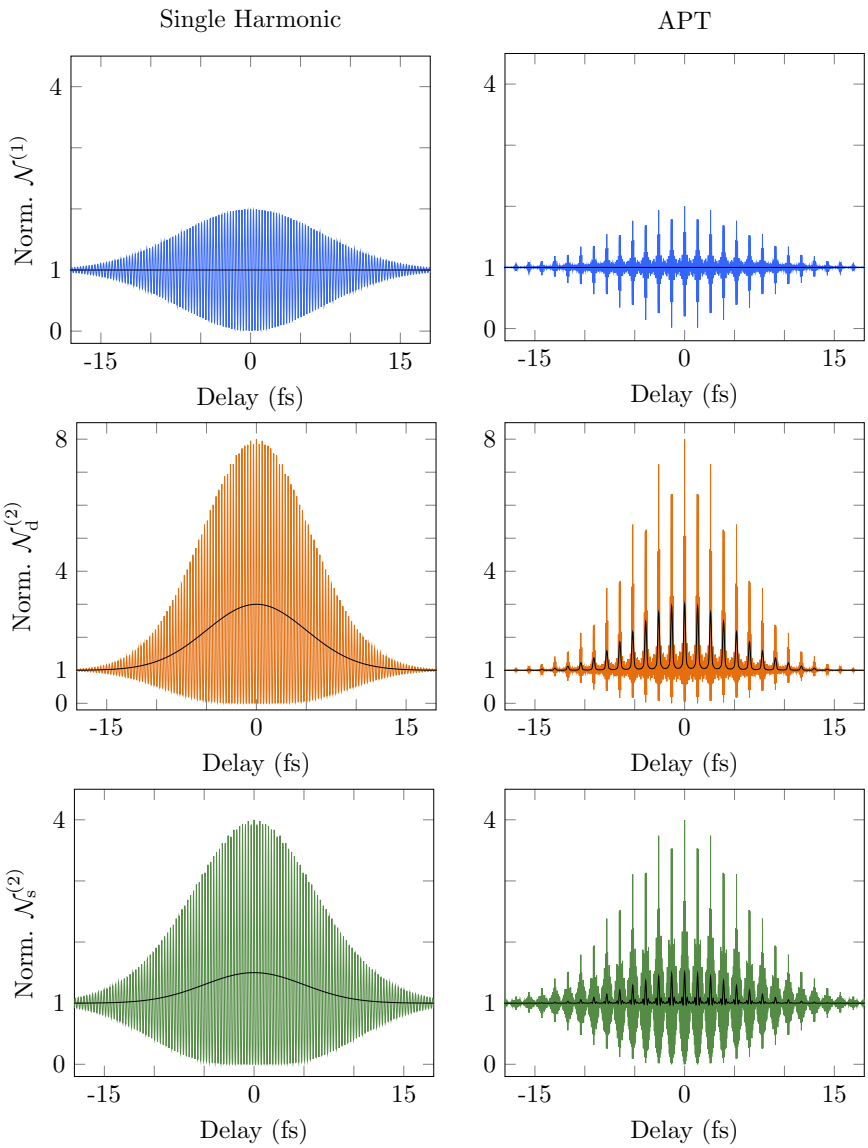

Figure 4.15: Autocorrelation traces for a single harmonic order (left column) and for an APT (right column). The pulse duration is 10 fs. The delay-dependent yields are shown, and all yields are normalized to 1 when the pulses are separated in time. The blue curves show the linear autocorrelation, and the orange and green curves show the second-order autocorrelation using a direct process and a sequential process, respectively. The black line is a first estimate of the yield when the interaction volume and the limited time resolution are taken into account, which means that high frequencies are not resolved.

contain information about whether the process is dominated by the sequential or the direct process.

4.4.2 Towards single attosecond pulses

For many experiments it is desirable to generate a single attosecond pulse (SAP), for example to improve the time resolution in the experiment. Most of the common techniques for generating SAPs are dependent on the use of a few cycle IR pulse, but to achieve such a short pulse is difficult with high energy laser systems. In the following, two experiments are presented that are both examining possible routes for generation of SAPs using laser systems with IR pulse energies of several tens of mJ.

Planar hollow waveguide

Laser pulses with a pulse energy of a few mJ can be compressed using the well known techniques where new frequencies are generated through non-linear processes in either gas filled hollow capillaries [97], or by using self-guided filaments [98]. These techniques do not allow for compression of pulses with higher pulse energies due to, for example, ionization of the medium if too high intensities are reached. In an experiment performed at the Intense XUV beamline in Lund and reported in Paper V the beam was post-compressed by focusing the beam with a cylindrica lens in a gas filled planar hollow waveguide and pulse durations down to sub 15 fs were achieved after compression. By using planar hollow waveguides higher input pulse energies can be accepted as compared to the normal compression techniques since one dimension can be scaled to keep the intensity at the desired level. The post-compressed beam was used for HHG and an increase in the cut-off, together with a broadening of the individual pulses, was observed. Both effects can be attributed to the use of a shorter driving pulse.

Noncollinear optical gating (NOG)

By using two noncollinear IR pulses for HHG, the attosecond pulse train can be angularly streaked and lead to the generation of SAPs separated in space. This can be understood by studying the wavefront in focus as a function of time. By delaying one of the pulses in respect to the other, the resulting wavefronts in focus will rotate during the duration of the two pulses. On the leading edge of the pulse, the high-order harmonics are generated in the direction of the first IR pulse and on the trailing edge the generation direction is that of the delayed pulse. In between, the IR wavefront rotates and if the rotation is sufficiently fast, SAPs separated in space, are generated. The idea was first tested in the Intense XUV beamline in Lund using pulses with a pulse duration of 40 fs. Angular streaking was observed and the spectrum was broadened but the IR pulse duration was too long to seperate the single attosecond pulses. In a follow up experiment, reported in Paper VI, high-order harmonics were generated using this technique with post-compressed laser pulses (3.2 fs) from a 1 kHz Ti:sapphire laser and SAPs seperated in angle were demonstrated.

In conclusion, NOG is an interesting technique even for high energy laser system if it is combined with IR pulse compression techniques, such as the planar hollow waveguide technique presented above.

Chapter 5

Summary and outlook

The experiments described in this thesis are separate experiments, interesting in themselves, but they also constitute important steps towards an experimental setup allowing processes taking place in atoms and molecules on the few femtosecond time scale to be studied. In large molecules, the rapid change in the charge distribution following ionization is interesting since this provides insight into the ensuing dynamics. Such experiments would strongly benefit from having XUV pulses that are only a few femtoseconds long, and that are sufficiently intense to be used in pump-probe studies. To study systems of biological interest, ideally both the electrons and the positively charged fragments should be detected in order to obtain information about the correlations and to interpret the, most likely, very complex signals [99, 100]. Below I describe five experimental challenges, important for studying processes on the few femtosecond timescale, that have all been addressed in this thesis. For each of these I will summarize how far we have come and also mention ongoing development and future plans.

Intense XUV pulses

XUV pulses with energies just below 1 µJ were produced at the Intense XUV Beamline in Lund (Paper II and III). These pulses were focused with a double toroidal mirror down to a focal spot size of 11 µm × 16 µm. The high intensity was confirmed by the observation of two-photon double ionization of neon. Work to further increase the intensity is on-going. In particular, a deformable mirror is now being used in the beamline to increase the XUV flux generated by improving the quality of the IR focus.

Short XUV pulses

The IR pulses used to generate the XUV pulses have a pulse duration of 35 fs, resulting in an attosecond pulse train. The train is assumed to have an effective pulse length of $\approx$ 15 fs, allowing us to study dynamics on the timescale of a few tens of femtoseconds, and possibly on the 1 fs timescale if the individual pulses in the train can be used, using e.g. stroboscopic approaches [101]. By generating SAPs, pulses with a duration of a few hundred attoseconds can be achieved. Conventional SAP generation techniques,

such as optical gating [26, 27] or intensity gating [28], require IR pulses with a duration of less than ten femtoseconds, which is difficult to achieve for IR pulses with energies of about 100 mJ. Different gating techniques, e.g. generalized double optical gating (GDOG) [102], allow slightly longer pulses, $\approx$ 20 fs, which is still challenging to reach for the pulse energies needed. In this work, a planar hollow waveguide has been used to post-compress IR pulses with an energy of 50 mJ and pulses with sub 15 fs duration and an energy of 20 mJ were achieved (Paper V). If short, energetic IR pulses can be generated, non-collinear optical gating (NOG), reported in Paper VI, could be a possible way towards intense SAPs. Another promising scheme for the generation of SAPs with energetic IR pulses has been presented in Ref. [29]. The 800 nm driving field is combined with a weak 1300 nm pulse, generated from the 800 nm field, which alters the field resulting in the generation of a SAP. This technique will be implemented in the Intense XUV Beamline in Lund in the near future.

XUV pump-XUV probe schemes

The XUV split-and-delay unit was tested off-line (Paper IV), and has now been installed in the beamline. Autocorrelation measurements of the IR pulse have been successfully performed using above-threshold ionization in neon, and efforts are being made to measure the autocorrelation of the XUV pulse. Simulations show that it is possible to perform an autocorrelation using the sequential process. At a single point in space, the contrast is 4:1, which can be compared to the well-known factor of 8:1 for a direct process. Simulations in which the effects of focus geometry and the volume effect are completely taken into account are on-going. XUV autocorrelation measurements are challenging, the overlap in time and space must be ensured, the pointing of the XUV beam needs to be stable and it is difficult to achieve good statistics due to the weak two-photon signal.

Sample delivery

The sample to be studied must be delivered into the vacuum and at the focus of the XUV beam. When studying non-linear ionization, the dominating linear ionization signal results in a massive background. The undesired linear signal scales with the number of photons, and is generated all along the laser beam, while the desired non-linear signal is predominantly generated at the focus. A gas jet that is confined to the XUV focus maximizes the ratio between the non-linear signal and the linear signal. An Even-Lavie valve is used in the beamline to produce short pulses of gas, and together with two skimmers an interaction length of about 1 mm has been achieved. A solid sample can be heated up in the Even-Lavie valve and transported into the interaction region by a carrier gas. It is difficult to heat the sample without it getting fragmented and this becomes even more challenging when using large molecules. Another challenge is to obtain a sufficient number of molecules in the interaction region.

Detection of electrons and ions

In the experiment presented in Paper III, where the first observation of non-linear ionization was reported, an ion TOF spectrometer was used. A simple spectrometer such as this allowed us to verify the non-linearity of the process, and estimate the cross section. However, to obtain better insight into the process, the electrons should

be studied. To be able to measure the momentum of the electrons and ions simultaneously, and to detect a large number of events per shot, a double-sided velocity imaging spectrometer (DVMIS) was designed and built (Paper VIII). Momentum images for both electrons and ions have been measured and the covariance technique has been used to verify Coulomb explosion of N_2 after ionization of a 1s electron using synchrotron radiation. The DVMIS has been installed in the Intense XUV Beamline at Lund, and initial synchronized data sets have been collected. Our goal for the near future is to record synchronized TOF signals and electron VMI images for non-linear ionization of neon, aiming to discern the weak electron signal from non-linear ionization by identifying the signals that are correlated with the Ne^{2+} ion.

Studies of ultrafast dynamics in large molecules using XUV pulses are extremely demanding experiments since all the above issues must be addressed and solved in the same experiment. Many experiments have been performed where some of these are addressed, but to date an experiment addressing all of them have not been performed. High XUV intensities can be generated in FELs which has allowed the study of highly non-linear processes [49] as well as detailed studies of correlations in few-photon ionization of atoms and diatomic molecules [19]. XUV pump-XUV probe studies have been performed on small molecules (see for example Ref. [19, 103]), but although shorter and shorter pulses can be generated, the comparably long pulses do not allow processes on the few femtosecond timescale to be studied. HHG can provide SAPs with sub-femtosecond time durations, but due to the limited flux, the short XUV pulse is in most cases combined with a few-femtoseconds IR pulse for pump-probe studies. This method has been successfully used to study, for example, charge migration in large molecules [9], but a drawback is the IR pulse duration which limits the time resolution and that it is hard to disentangle the intrinsic dynamics from those induced by the IR pulse. A few research groups are generating intense ultrashort XUV pulses, and have shown that it is possible to perform XUV pump - XUV probe studies, but the experiments have so far been limited to atoms or diatomic molecules such as Xe [15, 16] or H_2 [14]. In the near future, the development of new, ultra-broadband, lasers together with HHG in extremely loose focusing regimes, will allow even more intense SAPs to be generated. This, together with improved sample delivery techniques, is expected to result in better statistics in XUV pump-XUV probe experiments which will allow the study of ultrafast dynamics on the sub-femtosecond timescale in atoms and molecules. An interesting outlook is the possibility to not only observe, but to also control the dynamics, and the following fragmentation process, by shaping the attosecond pulse that initiates dynamics in the system [104]. Attosecond molecular dynamics is a very active field of research, both on the experimental side and the theory side. I believe that we will soon see experiments in which the five above mentioned challenges are solved, and I am sure that these will bring us exciting new knowledge, some in areas we cannot now foresee.

The author's contribution

I **Efficient high-order harmonic generation boosted by below-threshold harmonics**
I took part in the experiments at the start of my PhD and in the discussion of the manuscript. I did not perform any of the simulations.

II **A high-flux high-order harmonic source**
I played a major role in building up the new beamline and in the experiments performed on the new beamline. I did not perform the phase matching calculations.

III **Two-photon double ionization of neon using an intense attosecond pulse train**
I had a major role in building up the beamline and coordinated the setting up of the experimental chamber. I designed and built the ion TOF spectrometer used. I was one of the two main drivers of the experiment. I analyzed the flux measurements and some of the TOF measurements. I wrote large parts of the manuscript. I did not participate in the focal spot measurements.

IV **Design and test of a broadband split-and-delay unit for attosecond XUV-XUV pump-probe experiments**
I took part in the discussions from the start of the project but not in the experiments.

V **Compression of TW class laser pulses in a planar hollow waveguide for applications in strong-field physics**
I took part in the build-up of the HHG beamline that was used for the experiments but not in the planar hollow waveguide experiment.

VI **Gating attosecond pulses in a noncollinear geometry**
I took an active part in the experiments at the intense XUV beamline where the idea of noncollinear HHG was first tested.

VII **Interference in the angular distribution of photoelectrons in superimposed XUV and optical laser fields**
I took part in the experiment and in the preparations. I analyzed the data and wrote a major part of the manuscript. I did not perform the SFA simulations.

VIII **A versatile velocity map ion-electron covariance imaging spectrometer for high intensity XUV experiments**
I simulated, designed and built the spectrometer. I was a main driver in the experiments at MAX-lab where the first data was acquired. I analyzed the VMIS data, implemented the covariance analysis and wrote the first draft of the manuscript.

Acknowledgements

I think it is amazing to have had the chance to work at a place with people from all over the world. I realized that Atomic Physics is just 450 m from where I was born, but thanks to all of you people, I have still met the world!

There are so many people that I would like to thank, and after struggling to write a thesis in English, I would like to thank all of you, at least partly, in my own language. If you are not so into Swedish, now you have the chance for some practice!

Först av allt så vill jag tacka Per Johnsson för att du, efter en viss förvåning över att någon knackade på din dörr för att söka jobb, berättade inlevelsefullt om alla spännande projekt du hade på gång. Det var din entusiasm som gjorde att jag började doktorera på atomfysik. Du är en av de mest ambitiösa människorna jag känner, vilket har fått mig att alltid vilja göra mitt bästa. Dessutom har du en förmåga att komma med idéer som är så bra att jag alltid är lite avundsjuk på att inte ha kommit på dem själv!

Jag vill även tacka min biträdande handledare, Anne L'Huillier, för ditt genuina intresse för fysik och för att ha delat med dig av din kunskap. Jag minns speciellt en dag när jag precis hade börjat som doktorand och ett experiment i attolabbet visade spännande resultat. Någon från labbet kom upp för att hämta dig och du nästan småhoppade av nyfikenhet genom hela korridoren på väg till labbet, det minnet gör mig fortfarande glad.

The work in this thesis would not have been possible (and especially not fun at all) without all you people that have helped me in various ways. When starting as a PhD student, the "old" 10 Hz team was the best help to get going. Stort tack Fernando, Piotr och Christoph för trevliga stunder i labbet, och tack Christoph för tysklektioner, spelkvällar och cykelturer. A bit later came Filippo, Bastian and Byunghoon. Thank you for the company during all these days in the lab when we fought with leaking vacuum chambers and screaming pumps, in the end we made it all work! Filippo, grazie per aver cantato, non siamo stati mangiati del orso. About two years ago, a new 10 Hz generation started. Tack! Danke! Merci! To Sylvain, Hélène, Hampus, Jan and Jasper for bringing in a great spirit and a lot of fun, I wish I would have had a bit more time with you in (and outside) the lab. Thank you Jasper and Jan for the nice office atmosphere and an extra thank to you Jan for always making me feel included, even at stressful times. Many thanks to you Anders, for keeping an eye (or two) at the laser, and for always beeing so friendly and helpful.

I would also like to thank the big atto group, you are the best! I had so much fun with all of you at many many PhD parties (and other parties), at conferences, summer schools and during the, at least, 1000 cups of coffee I had during my years here. I

will not try to mentioned you all by name, since I am too afraid to forget someone. But there are a few people I would like to especially mention. David och Ello, för att ni var mina trogna kontorskompisar. Diego, för att du är så kittlig och för att du gav mig det bästa (på flera sätt) skvallret någonsin. Esben och Cord, för att ni är så kul. Stefanos, för att vi kommer att ha världens bästa disputationsfest. Neven, för att du gav mig inspiration till introduktionen. Post-Doc Anne, för att du har ett stort hjärta och för att jag blir klokare på livet när jag pratar med dig. Du kommer bli en superfysiker, jag tror på dig! Mathieu, för att du är en glad prick som är grym på att prata (franska) och på molekyler. Ello, för att du gör mig trygg. Marija, för många skratt. Jana, för allt sällskap när vi var föräldralediga samtidigt.

Jag vill också passa på att rikta ett stort tack till er som gör atomfysik till den trevliga arbetsplats det är. Tack avdelningsföreståndare Claes-Göran samt Anne, Jakob och Åke.

På atomfysik har jag också haft turen att ha två av mina bästa vänner, Jenny och Lovisa. Lovisa, tack för alla goa stunder och oavsett om det har varit i bergen i Italien, i kafferummet på fysikum med avhandlingsångest, på en golunch på stan eller innan klockan sju en lördagsmorgon med urpigga småungar, så har jag varit glad att du har varit där! Jenny, tänkt att vi lärde känna varandra på första fysikkursen, och att det är mer än tio år sedan, helt galet! Tack för att jag i dig har en glad, lugn, smart, pålitlig och fundersam vän. Välkommen tillbaka! Jag, Algot och många andra har saknat dig.

Jag vill tacka alla vänner som aldrig har satt sin fot på atomfysik och som har fått mig att tänka på annat än jobbet, framför allt stort tack till alla er i mitt kära Matlaget!

Många varma tack till mina föräldrar och till min syster. Pappa, du har inspirerat mig till att alltid vilja lära mig och förstå mera. Mamma, tack för att du alltid bryr dig och för att du får mig att våga. Hanna, du får mig att se världen utanför min egen bubbla. Stort tack för all hjälp med Algot, speciellt till dig mamma, det har gett oss ett ovärderligt andrum i vardagen.

Till sist vill jag tacka mina två allra bästa vänner i hela världen, Johan och Algot. Algot, ingen får mig att bli så glad som du! Ett “Mamma mera bus! Algot upp och ner!” får mig att glömma all stress och minnas vad som är viktigast i livet. Johan, ett stort tack för att du sa “skriv du din avhandling, så sköter jag resten”, och för att du verkligen menade det. Älskade Johan, du har lärt mig att det ska vara gött att leva.

References

1. R. Shimelmitz, S. Kuhn, A. J. Jelinek, A. Ronen, A. E. Clark and M. Weinstein-Evron. *Fire at wil: The emergence of habitual fire use 350,000 years ago.* J. Hum. Evol. **77**, 196–203 (2014).

2. A. Einstein. *Über einen die Erzeugung und Verwandlung des Lichtes betreffenden heuristischen Gesichtspunkt.* Annalen der Physik **322**, 132–148 (1905).

3. P. A. Franken, A. E. Hill, C. W. Peters and G. Weinreich. *Generation of optical harmonics.* Phys. Rev. Lett. **7**, 118–119 (1961).

4. G. S. Voronov and N. B. Delone. *Ionization of the xenon atom by the electric field of ruby laser emission.* J. Exp. Theo. Phys. Lett. **1**, 66 (1965).

5. P. Agostini, F. Fabre, G. Mainfray, G. Petite and N. K. Rahman. *Free-free transitions following six-photon ionization of xenon atoms.* Phys. Rev. Lett. **42**, 1127–1130 (1979).

6. M. Ferray, A. L'Huillier, X. F. Li, L. A. Lompre, G. Mainfray and C. Manus. *Multiple-harmonic conversion of 1064 nm radiation in rare gases.* J. Phys. B. **21**, 31–35 (1988).

7. L. S. Cederbaum and J. Zobeley. *Ultrafast charge migration by electron correlation.* Chem. Phys. Lett. **307**, 205–210 (1999).

8. K. Zhao, Q. Zhang, M. Chini, Y. Wu, X. Wang and Z. Chang. *Tailoring a 67 attosecond pulse through advantageous phase-mismatch.* Opt. Lett. **37**, 3891 (2012).

9. F. Calegari, D. Ayuso, A. Trabattoni, L. Belshaw, S. De Camillis, S. Anumula, F. Frassetto, L. Poletto, A. Palacios, P. Decleva et al. *Ultrafast electron dynamics in phenylalanine initiated by attosecond pulses.* Science **346**, 336–339 (2014).

10. N. A. Papadogiannis, L. A. A. Nikolopoulos, D. Charalambidis, G. D. Tsakiris, P. Tzallas and K. Witte. *Two-photon ionization of he through a superposition of higher harmonics.* Phys. Rev. Lett. **90** (2003).

11. L. A. A. Nikolopoulos, E. P. Benis, P. Tzallas, D. Charalambidis, K. Witte and G. D. Tsakiris. *Second order autocorrelation of an XUV attosecond pulse train.* Phys. Rev. Lett. **94** (2005).

12. T. Shimizu, T. Okino, K. Furusawa, H. Hasegawa, Y. Nabekawa, K. Yamanouchi and K. Midorikawa. *Observation and analysis of an interferometric autocorrelation trace of an attosecond pulse train.* Phys. Rev. A. **75** (2007).

13. P. Tzallas, D. Charalambidis, N. A. Papadogiannis, K. Witte and G. D. Tsakiris. *Direct observation of attosecond light bunching.* Nature **426**, 267–271 (2003).

14. P. A. Carpeggiani, P. Tzallas, A. Palacios, D. Gray, F. Martín and D. Charalambidis. *Disclosing intrinsic molecular dynamics on the 1-fs scale through extreme-ultraviolet pump-probe measurements.* Physical Review A **89**, 023420 (2014).

15. E. Skantzakis, P. Tzallas, J. E. Kruse, C. Kalpouzos, O. Faucher, G. D. Tsakiris and D. Charalambidis. *Tracking autoionizing-wave-packet dynamics at the 1-fs temporal scale.* Phys. Rev. Lett. **105** (2010).

16. P. Tzallas, E. Skantzakis, L. A. A. Nikolopoulos, G. D. Tsakiris and D. Charalambidis. *Extreme-ultraviolet pump-probe studies of one-femtosecond-scale electron dynamics.* Nature Phys. **7**, 781–784 (2011).

17. B. W. J. McNeil and N. R. Thompson. *X-ray free-electron lasers.* Nature Phot. **4**, 814–821 (2010).

18. A. A. Sorokin, S. V. Bobashev, T. Feigl, K. Tiedtke, H. Wabnitz and M. Richter. *Photoelectric effect at ultrahigh intensities.* Phys. Rev. Lett. **99**, 213002 (2007).

19. A. Rudenko, Y. H. Jiang, M. Kurka, K. U. Kühnel, L. Foucar, O. Herrwerth, M. Lezius, M. F. Kling, C. D. Schröter, R. Moshammer and J. Ullrich. *Exploring few-photon, few-electron reactions at FLASH: from ion yield and momentum measurements to time-resolved and kinematically complete experiments.* J. Phys. B. **43**, 194004 (2010).

20. V. Ayvazyan et al. *First operation of a free-electron laser generating GW power radiation at 32 nm wavelength.* Eur. Phys. J. D. **37**, 297–303 (2005).

21. K. Schnorr, A. Senftleben, M. Kurka, A. Rudenko, G. Schmid, T. Pfeifer, K. Meyer, M. Kübel, M. F. Kling, Y. H. Jiang et al. *Electron rearrangement dynamics in dissociating I_2^{n+} molecules accessed by extreme ultraviolet pump-probe experiments.* Phys. Rev. Lett. **113** (2014).

22. A. Rouzée, P. Johnsson, L. Rading, A. Hundertmark, W. Siu, Y. Huismans, S. Düsterer, H. Redlin, F. Tavella, N. Stojanovic et al. *Towards imaging of ultrafast molecular dynamics using FELs.* J. Phys. B. **46**, 164029 (2013).

23. A. McPherson, G. Gibson, H. Jara, U. Johann, T. S. Luk, I. A. McIntyre, K. Boyer and C. K. Rhodes. *Studies of multiphoton production of vacuum-ultraviolet radiation in the rare gases.* J. Opt. Soc. Am. B **4**, 595 (1987).

24. N. A. Papadogiannis, B. Witzel, C. Kalpouzos and D. Charalambidis. *Observation of attosecond light localization in higher order harmonic generation.* Phys. Rev. Lett. **83**, 4289–4292 (1999).

25. P. M. Paul, E. S. Toma, P. Breger, G. Mullot, F. Augé, P. Balcou, H. G. Muller and P. Agostini. *Observation of a train of attosecond pulses from high harmonic generation.* Science **292**, 1689–1692 (2001).

26. P. B. Corkum, N. H. Burnett and M. Y. Ivanov. *Subfemtosecond pulses.* Opt. Lett. **19**, 1870 (1994).

27. O. Tcherbakoff, E. Mével, D. Descamps, J. Plumridge and E. Constant. *Time-gated high-order harmonic generation.* Phys. Rev. A. **68** (2003).

28. F. Ferrari, F. Calegari, M. Lucchini, C. Vozzi, S. Stagira, G. Sansone and M. Nisoli. *High-energy isolated attosecond pulses generated by above-saturation few-cycle fields.* Nat. Photonics **4**, 875–879 (2010).

29. E. J. Takahashi, P. Lan, O. D. Mücke, Y. Nabekawa and K. Midorikawa. *Attosecond nonlinear optics using gigawatt-scale isolated attosecond pulses.* Nat. Commun. **4** (2013).

30. P. B. Corkum. *Plasma perspective on strong field multiphoton ionization.* Phys. Rev. Lett. **71**, 1994–1997 (1993).

31. K. J. Schafer, B. Yang, L. F. DiMauro and K. C. Kulander. *Above threshold ionization beyond the high harmonic cutoff.* Phys. Rev. Lett. **70**, 1599–1602 (1993).

32. M. Lewenstein, Ph. Balcou, M. Yu. Ivanov, A. L'Huillier and P. B. Corkum. *Theory of high-harmonic generation by low-frequency laser fields.* Phys. Rev. A. **49**, 2117–2132 (1994).

33. Z. Chang. *Fundamentals of Attosecond Optics.* CRC Press 1 edition (2011). ISBN 9781420089370.

34. M. Lewenstein, P. Salières and A. L'Huillier. *Phase of the atomic polarization in high-order harmonic generation.* Phys. Rev. A. **52**, 4747–4754 (1995).

35. P. Balcou, P. Salières, A. L'Huillier and M. Lewenstein. *Generalized phase-matching conditions for high harmonics: The role of field-gradient forces.* Phys. Rev. A. **55**, 3204–3210 (1997).

36. A. L'Huillier, X. F. Li and L. A. Lompré. *Propagation effects in high-order harmonic generation in rare gases.* J. Opt. Soc. Am. B. **7**, 527 (1990).

37. E. Constant, D. Garzella, P. Breger, E. Mével, Ch. Dorrer, C. Le Blanc, F. Salin and P. Agostini. *Optimizing high harmonic generation in absorbing gases: model and experiment.* Phys. Rev. Lett. **82**, 1668–1671 (1999).

38. C. M. Heyl, H. Coudert-Alteirac, M. Miranda, M. Louisy, K. Kovacs, V. Tosa, E. Balogh, K. Varjù, A. L'Huillier, A. Couairon and C. L. Arnold. *Scale-invariant nonlinear optics in gases.* Optica **3**, 75 (2016).

39. A. L'Huillier, P. Balcou, S. Candel, K. J. Schafer and K. C. Kulander. *Calculations of high-order harmonic-generation processes in xenon at 1064 nm.* Phys. Rev. A. **46**, 2778–2790 (1992).

40. K. Midorikawa, Y. Nabekawa and A. Suda. *XUV multiphoton processes with intense high-order harmonics.* Prog. Quant. Elec. **32**, 43–88 (2008).

41. F. Quéré, Y. Mairesse and J. Itatani. *Temporal characterization of attosecond XUV fields.* J. Mod. Opt. **52**, 339–360 (2005).

42. D. J. Kennedy and S. T. Manson. *Photoionization of the noble gases: cross sections and angular distributions.* Phys. Rev. A. **5**, 227–247 (1972).

43. S. Thorin. Design and construction of a velocity map imaging spectrometer. Master's thesis Lund university (2004).

44. N. A. Papadogiannis, L. A. A. Nikolopoulos, D. Charalambidis, G. D. Tsakiris, P. Tzallas and K. Witte. *On the feasibility of performing non-linear autocorrelation with attosecond pulse trains.* Appl. Phys. B. **76**, 721–727 (2003).

45. E. P. Benis, P. Tzallas, L. A. A. Nikolopoulos, M. Kovačev, C. Kalpouzos, D. Charalambidis and G. D. Tsakiris. *Frequency-resolved photoelectron spectra of two-photon ionization of He by an attosecond pulse train.* New. J. Phys. **8** (2006).

46. E. P. Benis, D. Charalambidis, T. N. Kitsopoulos, G. D. Tsakiris and P. Tzallas. *Two-photon double ionization of rare gases by a superposition of harmonics.* Phys. Rev. A. **74**, 051402 (2006).

47. Y. Nabekawa, H. Hasegawa, E. J. Takahashi and K. Midorikawa. *Production of doubly charged helium ions by two-photon absorption of an intense sub-10-fs soft X-ray pulse at 42 eV photon energy.* Phys. Rev. Lett. **94**, 043001 (2005).

48. Y. Nabekawa, T. Shimizu, T. Okino, K. Furusawa, H. Hasegawa, K. Yamanouchi and K. Midorikawa. *Interferometric autocorrelation of an attosecond pulse train in the single-cycle regime.* Phys. Rev. Lett. **97**, 153904 (2006).

49. A. A. Sorokin, M. Wellhofer, S. V. Bobashev, K. Tiedtke and M. Richter. *X-ray-laser interaction with matter and the role of multiphoton ionization: Free-electron-laser studies on neon and helium.* Phys. Rev. A. **75**, 051402 (2007).

50. M. Protopapas, C. H. Keitel and P. L. Knight. *Atomic physics with super-high intensity lasers.* Rep. Prog. Phys. **60**, 389 (1997).

51. A. M. Covington, A. Aguilar, I. R. Covington, M. F. Gharaibeh, G. Hinojosa, C. A. Shirley, R. A. Phaneuf, I. Álvarez, C. Cisneros, I. Dominguez-Lopez and et al. *Photoionization of Ne^+ using synchrotron radiation.* Phys. Rev. A. **66** (2002).

52. M. Førre, S. Selstø and R. Nepstad. *Nonsequential two-photon double ionization of atoms: identifying the mechanism.* Phys. Rev. Lett. **105** (2010).

53. J. B. West and G. V. Marr. *The absolute photoionization cross sections of helium, neon, argon and krypton in the extreme vacuum ultraviolet region of the spectrum.* Proceedings of the Royal Society A **349**, 397–421 (1976).

54. A. Palacios, D. A. Horner, T. N. Rescigno and C. W. McCurdy. *Two-photon double ionization of the helium atom by ultrashort pulses.* J. Phys. B. **43**, 194003 (2010).

55. M. M. Seibert et al. *Single mimivirus particles intercepted and imaged with an X-ray laser.* Nature **470**, 78–81 (2011).

56. A. Landers, Th. Weber, I. Ali, A. Cassimi, M. Hattass, O. Jagutzki, A. Nauert, T. Osipov, A. Staudte, M. H. Prior and et al. *Photoelectron diffraction mapping: molecules illuminated from within.* Phys. Rev. Lett. **87** (2001).

57. J. Ullrich, R. Moshammer, A. Dorn, R. Dörner, L. Ph. H. Schmidt and H. Schmidt-Böcking. *Recoil-ion and electron momentum spectroscopy: reaction-microscopes.* Rep. Prog. Phys. **66**, 1463–1545 (2003).

58. A. T. J. B. Eppink and D. H. Parker. *Velocity map imaging of ions and electrons using electrostatic lenses: Application in photoelectron and photofragment ion imaging of molecular oxygen.* Rev. Sci. Instrum. **68**, 3477 (1997).

59. L. M. Smith, Keefer D. R. and S.I. Sudharsanan. *Abel inversion using transform techniques.* Journ. Quant. Spectr. Rad. Trans. **39**, 367–373 (1988).

60. M. J. J. Vrakking. *An iterative procedure for the inversion of two-dimensional ion/photoelectron imaging experiments.* Rev. Sci. Instrum. **72**, 4084 (2001).

61. W. C. Wiley and I. H. McLaren. *Time-of-flight mass spectrometer with improved resolution.* Rev. Sci. Instrum. **26**, 1150 (1955).

62. C. J. Cameron. *One-dimensional tomography: a comparison of Abel, onion-peeling, and filtered backprojection methods.* Appl. Opt. **31**, 1146 (1992).

63. P. Johnsson, A. Rouzée, W. Siu, Y. Huismans, F. Lépine, T. Marchenko, S. Düsterer, F. Tavella, N. Stojanovic, H. Redlin and et al. *Characterization of a two-color pump-probe setup at FLASH using a velocity map imaging spectrometer.* Opt. Lett. **35**, 4163 (2010).

64. L. Frasinski, K. Colding and P. A. Hatherly. *Covariance mapping: a correlation method applied to multiphoton multiple ionization.* Science **246**, 1029–1031 (1989).

65. L. J. Frasinski, A. J. Giles, P. A. Hatherly, J. H. Posthumus, M. R. Thompson and K Codling. *Covariance mapping and triple coincidence techniques applied to multielectron dissociative ionization.* J. Electron. Spectrosc. Relat. Phenom. **79**, 367–371 (1996).

66. O. Kornilov, M. Eckstein, M. Rosenblatt, C. P. Schulz, K. Motomura, A. Rouzée, J. Klei, L. Foucar, M. Siano, A. Lübcke et al. *Coulomb explosion of diatomic molecules in intense XUV fields mapped by partial covariance.* J. Phys. B. **46**, 164028 (2013).

67. J. L. Hansen, J. H. Nielsen, C. B. Madsen, A. T. Lindhardt, M. P. Johansson, T. Skrydstrup, L. B. Madsen and H. Stapelfeldt. *Control and femtosecond time-resolved imaging of torsion in a chiral molecule.* J. Chem. Phys. **136**, 204310 (2012).

68. C. S. Slater et al. *Covariance imaging experiments using a pixel-imaging mass-spectrometry camera.* Phys. Rev. A. **89** (2014).

69. L. J. Frasinski. *Covariance mapping techniques.* J. Phys. B. **49**, 152004 (2016).

70. F. Rosca-Pruna. *Alignment of diatomic molecules induced by intense laser fields.* PhD thesis VU University of Amsterdam (2001).

71. Y. Liu, T. Gerber, C. Qin, F. Jin and G. Knopp. *Visualizing competing inter-system crossing and internal conversion with a complementary measurement.* J. Chem. Phys. **144**, 084201 (2016).

72. A. Bodi, P. Hemberger, T. Gerber and B. Sztáray. *A new double imaging velocity focusing coincidence experiment: i^2PEPICO.* Rev. Sci. Instrum. **83**, 083105 (2012).

73. A. Vredenborg, W. G. Roeterdink and M. H. M. Janssen. *A photoelectron-photoion coincidence imaging apparatus for femtosecond time-resolved molecular dynamics with electron time-of-flight resolution of =18 ps and energy resolution $\Delta E/E$=3.5%.* Rev. Sci. Instrum. **79**, 063108 (2008).

74. M. Takahashi, J. P. Cave and J. H. D. Eland. *Velocity imaging photoionization coincidence apparatus for the study of angular correlations between electrons and fragment ions.* Rev. Sci. Instrum. **71**, 1337 (2000).

75. R. Boll, D. Anielski, C. Bostedt, J. D. Bozek, L. Christensen, R. Coffee, S. De, P. Decleva, S. W. Epp, B. Erk et al. *Femtosecond photoelectron diffraction on laser-aligned molecules: Towards time-resolved imaging of molecular structure.* Phys. Rev. A. **88** (2013).

76. O. Ghafur, W. Siu, P. Johnsson, M. F. Kling, M. Drescher and M. J. J. Vrakking. *A velocity map imaging detector with an integrated gas injection system.* Rev. Sci. Instrum. **80**, 033110 (2009).

77. B. Kempgens, A. Kivimäki, M. Neeb, H. M. Köppe, A. M. Bradshaw and J. Feldhaus. *A high-resolution N 1s photoionization study of the N_2 molecule in the near-threshold region.* J. Phys. **29**, 5389–5402 (1996).

78. T. Okino, Y. Furukawa, Y. Nabekawa, S. Miyabe, A. Amani Eilanlou, E. J. Takahashi, K. Yamanouchi and K. Midorikawa. *Direct observation of an attosecond electron wave packet in a nitrogen molecule.* Sci. Adv. **1**, 1500356–1500356 (2015).

79. D. Strickland and G. Mourou. *Compression of amplified chirped optical pulses.* Opt. Com. **55**, 447–449 (1985).

80. P. F. Moulton. *Spectroscopic and laser characteristics of Ti:Al_2O_3.* J. Opt. Soc. Am. B **3**, 125 (1986).

81. D. E. Spence, P. N. Kean and W. Sibbett. *60-fsec pulse generation from a self-mode-locked Ti:sapphire laser.* Opt. Lett. **16**, 42 (1991).

82. H. Wolter. *Spiegelsysteme streifenden Einfalls als abbildende Optiken für Röntgenstrahlen.* Annalen der Physik **445**, 94–114 (1952).

83. U. Even. *The Even-Lavie valve as a source for high intensity supersonic beam.* EPJ Techn. Instrum. **2** (2015).

84. U. Even. *Pulsed supersonic beams from high pressure source: Simulation results and experimental measurements.* Adv. Chem. Phys. pages 1–11 (2014).

85. ANDOR. *ANDOR - High energy detection brochure* (2014).

86. ANDOR. *Technical solutions - conversion of counts to photoelectrons / incoming photons* (2014).

87. ANDOR. *CCD performance* (2009).

88. Edward D. Palik, editor. *Handbook of optical constants of solids II.* Academic Press (1991).

89. http://henke.lbl.gov/opticalconstants/ (2016).

90. B.L. Henke, E. M. Gullikson and J.C. Davis. *X-ray interactions: photoabsorption, scattering, transmission, and reflection at E=50-30000 eV, Z=1-92.* Atomic Data and Nuclear Data Tables **54**, 181–342 (1993).

91. G. Sansone, T. Pfeifer, K. Simeonidis and A. I. Kuleff. *Electron correlation in real time.* Chem. Phys. Chem. **13**, 661–680 (2011).

92. J. S. Parker, L. R. Moore, K. J. Meharg, D. Dundas and K. T. Taylor. *Double-electron above threshold ionization of helium.* J. Phys. B. **34**, L69–L78 (2001).

93. L. Peng, Z. Zhang, W. Jiang, G. Zhang and Q. Gong. *Probe of the electron correlation in sequential double ionization of helium by two-color attosecond pulses.* Phys. Rev. A. **86** (2012).

94. X. Guan, K. Bartschat and B. I. Schneider. *Dynamics of two-photon double ionization of helium in short intense xuv laser pulses.* Phys. Rev. A. **77** (2008).

95. P. Tzallas, E. Skantzakis and D. Charalambidis. *Direct two-XUV-photon double ionization in xenon.* J. Phys. B. **45**, 074007 (2012).

96. H. Mashiko, A. Suda and K. Midorikawa. *All-reflective interferometric autocorrelator for the measurement of ultra-short optical pulses.* Appl. P **76**, 525–530 (2003).

97. M. Nisoli, S. De Silvestri, O. Svelto, R. Szipöcs, K. Ferencz, Ch. Spielmann, S. Sartania and F. Krausz. *Compression of high-energy laser pulses below 5 fs.* Opt. Lett. **22**, 522 (1997).

98. C.P. Hauri, W. Kornelis, F.W. Helbing, A. Heinrich, A. Couairon, A. Mysyrowicz, J. Biegert and U. Keller. *Generation of intense, carrier-envelope phase-locked few-cycle laser pulses through filamentation.* Appl. Phys. B. **79**, 673–677 (2004).

99. F. Lépine, M. Y. Ivanov and M. J. J. Vrakking. *Attosecond molecular dynamics: fact or fiction?* Nat. Phot. **8**, 195–204 (2014).

100. S. R. Leone et al. *What will it take to observe processes in real time?* Nat. Phot. **8**, 162–166 (2014).

101. J. Mauritsson, T. Remetter, M. Swoboda, K. Klünder, A. L'Huillier, K. J. Schafer, O. Ghafur, F. Kelkensberg, W. Siu, P. Johnsson and et al. *Attosecond electron spectroscopy using a novel interferometric pump-probe technique.* Phys. Rev. Lett. **105** (2010).

102. X. Feng, S. Gilbertson, H. Mashiko, H. Wang, S. D. Khan, M. Chini, Y. Wu, K. Zhao and Z. Chang. *Generation of isolated attosecond pulses with 20 to 28 femtosecond lasers.* Phys. Rev. Lett. **103** (2009).

103. Y. H. Jiang, A. Rudenko, J. F. Pérez-Torres, O. Herrwerth, L. Foucar, M. Kurka, K. U. Kühnel, M. Toppin, E. Plésiat, F. Morales and et al. *Investigating two-photon double ionization of D_2 by XUV-pump-XUV-probe experiments.* Phys. Rev. A. **81** (2010).

104. M. Lara-Astiaso, D. Ayuso, I. Tavernelli, P. Decleva, A. Palacios and F. Martín. *Decoherence, control and attosecond probing of xuv-induced charge migration in biomolecules. A theoretical outlook.* Faraday Discussions (2016).

Papers

Paper I

Efficient high-order harmonic generation boosted by below-threshold harmonics

F. Brizuela, C. M. Heyl, P. Rudawski, D. Kroon, L. Rading,
J. M. Dahlström, J. Mauritsson, P. Johnsson, C. L. Arnold and A. L'Huillier.

Sci. Rep. **3**, 1410 (2013).

SCIENTIFIC REPORTS

OPEN

SUBJECT AREAS:
ATTOSECOND SCIENCE
NONLINEAR OPTICS
APPLIED PHYSICS
X-RAYS

Received
12 February 2013

Accepted
13 February 2013

Published
11 March 2013

Correspondence and requests for materials should be addressed to A.L. (anne.lhuillier@fysik.lth.se)

Efficient high-order harmonic generation boosted by below-threshold harmonics

F. Brizuela[1], C. M. Heyl[1], P. Rudawski[1], D. Kroon[1], L. Rading[1], J. M. Dahlström[2], J. Mauritsson[1], P. Johnsson[1], C. L. Arnold[1] & A. L'Huillier[1]

[1]Department of Physics, Lund University, P. O. Box 118, SE-22100 Lund, Sweden, [2]Atomic Physics, Fysikum, Stockholm University, AlbaNova University Center, SE-10691 Stockholm, Sweden.

High-order harmonic generation (HHG) in gases has been established as an important technique for the generation of coherent extreme ultraviolet (XUV) pulses at ultrashort time scales. Its main drawback, however, is the low conversion efficiency, setting limits for many applications, such as ultrafast coherent imaging, nonlinear processes in the XUV range, or seeded free electron lasers. Here we introduce a novel scheme based on using below-threshold harmonics, generated in a "seeding cell", to boost the HHG process in a "generation cell", placed further downstream in the focused laser beam. By modifying the fundamental driving field, these low-order harmonics alter the ionization step of the nonlinear HHG process. Our dual-cell scheme enhances the conversion efficiency of HHG, opening the path for the realization of robust intense attosecond XUV sources.

The interaction of intense laser pulses with atomic or molecular gas media leads to the generation of harmonics of the laser light, up to very high orders[1]. These harmonics are locked in phase, giving rise to attosecond bursts of XUV light. The simplicity of the experimental technique, together with the progress in ultrafast laser technology, has promoted HHG sources as essential tools in many laboratories; opening, in particular, the field of attosecond science[2]. However, HHG suffers from low conversion efficiency, owing partly to phase mismatches in the nonlinear medium that prevent efficient build up of the macroscopic field[3–6], but mostly to the weak response of the individual atoms to the field.

The atomic response to an external driving field can be described by a three-step model [Fig. 1(a)]: First, a bound electron tunnel-ionizes into the continuum; second, it is accelerated by the laser field; and finally, it recombines with the parent ion upon field reversal, emitting an XUV photon[7,8]. The electron trajectories can be grouped in two families, named the long and the short, depending on the excursion time of the electron and generated in intervals II and III of Fig. 1(a), respectively. The most interesting from a practical point-of-view are the short trajectories, which lead to collimated and spectrally narrow emission. Unfortunately, these trajectories start at times close to the zero-crossings of the driving electric field, suffering from very low quantum-tunneling probability.

Altering the driving electric field at the subcycle level[9] provides a way of modifying the single atom response. This has been investigated mainly by adding the second harmonic field[10–13], thus breaking the symmetry between consecutive half cycles. In contrast, odd-order harmonics modify the HHG process while maintaining the half-cycle symmetry. In a pioneering work, Watanabe and coworkers[14] investigated the influence of the third harmonic (TH) on single ionization and HHG in Ar, obtaining an enhancement of up to a factor of ten for the 27–31 harmonics. Also, a few theoretical works discuss the influence of the TH on the enhancement of the yield[15,16] and/or the extension of the cutoff energy[17–19]. Another approach to enhance the signal by modify the single atom response is to control the time of ionization by using attosecond pulse trains to initialize the three-step process via single photon absorption[20–23].

In this letter, we demonstrate a simple and robust, yet powerful enhancement scheme based on a dual gas-cell setup [Fig. 1(b)]. We study HHG in neon using a high-energy (~20 mJ), near-infrared fundamental field, loosely focused in a long gas cell, resulting in high-order harmonics in the 40–100 eV range, with a typical energy of 10 nJ per harmonic order. The addition of a high-pressure Ar gas cell before the generation cell produces a large enhancement in the Ne signal, as seen in Fig. 1(c). We experimentally and theoretically show that the observed enhancement is due to below-threshold, low-order harmonics which modify the fundamental field in such a way that the contribution of the short trajectories is increased.

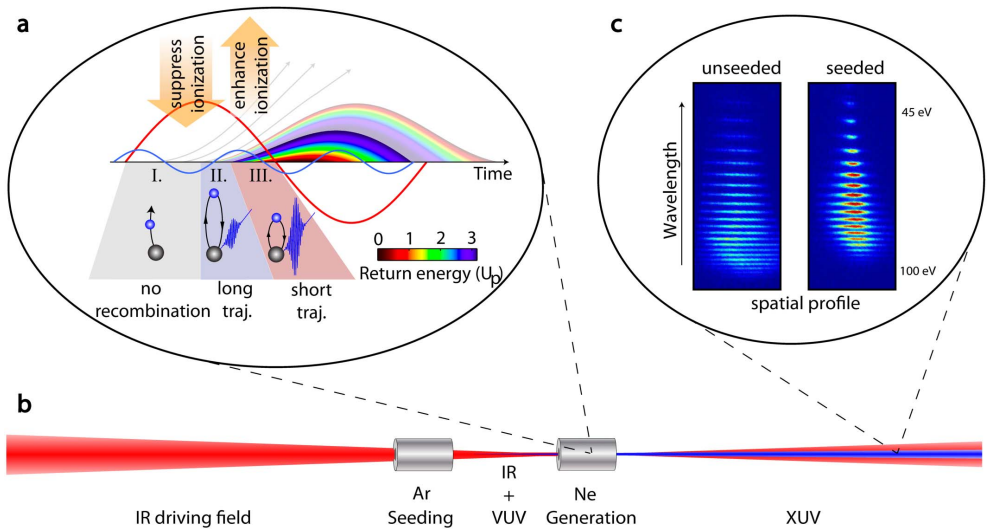

Figure 1 | **HHG in a dual gas-cell.** (a) Schematic classical trajectories for a sinusoidal driving field (red line). The colors indicate the return energy of the electrons in units of the ponderomotive energy U_p. Modifying the driving field by adding an odd harmonic field (blue line) can lead to an enhanced ionization probability for short trajectories (interval III) while suppressing the ionization of non-contributing electrons (intervals I and II), as indicated by the arrows. (b) Schematic experimental setup. Low-order harmonics generated in the seeding cell co-propagate with the fundamental into the generation cell and modify the HHG process. (c) Comparison of a typical HHG spectrum from a neon-filled generation cell obtained using only the fundamental field; and a spectrum obtained combining the fundamental field with low-order harmonics generated in the argon-filled seeding cell. In the latter case, the harmonic yield for the plateau harmonics is enhanced while the cutoff energy and the divergence are reduced.

Results

In our experiment, the generation cell is placed approximately at the laser focus while the seeding cell is located a few centimeters before (see Methods). The gas pressures in the cells can be independently adjusted and are typically a few mbar in the generation cell (Ne) and up to tens of mbar in the seeding cell (Ar). In Fig. 2(a–c), HHG spectra from neon are plotted as a function of the seeding pressure for three different driving intensities. When no gas is present in the seeding cell, standard Ne spectra are obtained. As the seeding pressure increases, the signal from the neon cell decreases until it is almost completely suppressed. At higher pressures, the neon spectra reappear and are significantly enhanced in the 50 – 80 eV region while the maximum photon energy slightly shifts to lower harmonic orders.

Figure 2(d) shows harmonics generated in the seeding cell. Harmonics with energies above the ionization threshold are not present at pressures where the enhancement in the generation cell occurs, and therefore are not responsible for the signal boost through single-photon ionization[20–23]. At these pressures, only low-order harmonics are efficiently generated in the seeding cell, indicating that they are responsible for the seeding process.

In order to validate our interpretation, we performed numerical simulations for both cells. In the generation cell, we simulated the seeded HHG process using the strong-field approximation

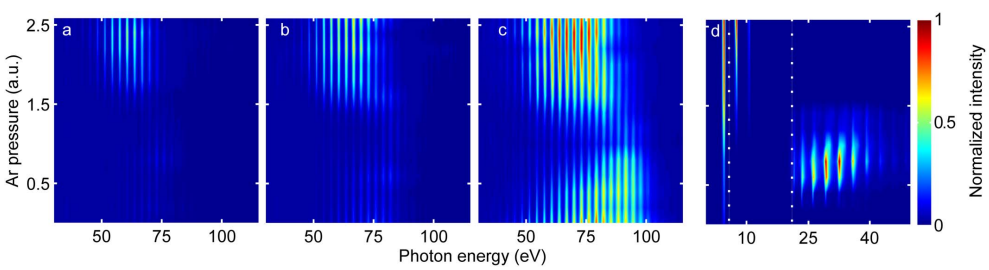

Figure 2 | **Experimental HHG spectra.** (a-c) Spectra from the generation cell as a function of the pressure in the seeding cell at three driving intensities 2.7, 3.5, and 4.4×10^{14} W/cm^2, respectively. The spectra were obtained using argon in the seeding cell and neon, at a fixed pressure, in the generation cell. The data were normalized to the most intense enhanced neon spectrum. (d) Low- (3–7) and high-order harmonics from the seeding cell as a function of Ar pressure. The dotted lines indicate regions measured independently with different detectors. Each region was normalized to the highest intensity in the corresponding spectral range.

(SFA)[15,16,24,25] (see Methods). The total field can be written as

$$E(t) = E_0 \left[\sin(\omega t) + \sum_{q\omega < I_p} r_q \sin\left(q\omega t + \Delta\varphi_q\right) \right], \qquad (1)$$

where E_0 is the amplitude of the fundamental field, ω its frequency, I_p the ionization energy, r_q the ratio between the fundamental and qth harmonic field, and $\Delta\varphi_q$ their relative phase. Although all harmonics below the ionization threshold of Ar may influence the enhancement phenomenon, we considered only the TH, which is the most intense one (we omit the subscript 3 below). A simulated HHG spectrum in neon with $|r|^2 = 0.01$, is shown in Fig. 3(a) as a function of $\Delta\varphi$. A relative phase of ~1 rad leads to an enhanced ionization probability, since the electrical field is increased at the time where the short electron trajectories are born [interval III in Fig. 1(a)]. Furthermore, the electric field amplitude is reduced around the peak of the fundamental field leading to suppressed probability for non-contributing trajectories (intervals I, II) and to an improved macroscopic situation since plasma dispersion and depletion effects are minimized[4,5]. When $\Delta\varphi \approx 1 \pm \pi$, the situation is reversed and HHG is suppressed compared to the unseeded case.

We experimentally confirmed the dependence of the HHG signal on $\Delta\varphi$ by studying HHG using a combination of the fundamental and the TH generated in a crystal[14]. To control the delay between the two fields, we used a Michelson interferometer with the TH produced in one arm. Our results, plotted in Fig. 3(b), show a strong delay dependence of the harmonic yield. However, we could not increase the overall HHG efficiency compared to the dual-cell scheme, since a large fraction of the fundamental field was needed for the TH generation and consequently lost for HHG.

In the seeding cell, we examined the pressure dependence of both low-order and high-order harmonic generation. Our calculations[26] confirm the experimental observation that HHG in Ar peaks at a certain pressure (~10 mbar) which corresponds to optimized phase matching[27], while below-threshold harmonics continue to increase up to pressures as high as 100 mbar. We also investigated the propagation of the fundamental and TH fields in a high pressure cell[28] (see Methods). This allowed us to examine their phase relation after the seeding cell and to eliminate the relatively weak reshaping of the fundamental field in our experimental conditions as possible cause for the enhancement. As Fig. 3(c) shows, for high enough seeding pressures, $\Delta\varphi$ will be between 0 and 2 radians during part of the laser pulse, leading to a gated enhancement mechanism.

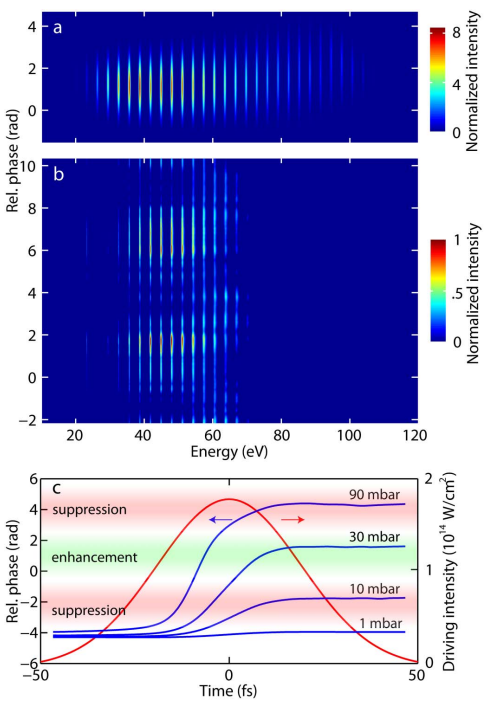

Figure 3 | Influence of the relative (ω, 3ω) phase in HHG. (a) SFA spectra as a function of $\Delta\varphi$ in the generation cell, normalized to the unseeded spectrum. Only the contribution of the short trajectory is considered. An effective grating response is included to mimic the experimental conditions. (b) Experimental results with the TH generated in a crystal, normalized to the highest signal. (c) Propagation simulations in the seeding cell: $\Delta\varphi$ at the exit of the cell as a function of time for different pressures.

Discussion

As in any enhancement scheme, a key question is whether our method is advantageous over "usual" HHG optimization, which can be achieved for example by using looser focusing, optimizing the position of the focus in the cell, or adjusting the pressure in the gas cell[4,29,30]. Ideally, one would like to compare optimized HHG and optimized seeded HHG for a given fundamental pulse energy. This is not easy to realize experimentally, so we choose to benchmark seeded HHG against optimized unseeded HHG, with ~10 nJ at 63 eV (41st harmonic).

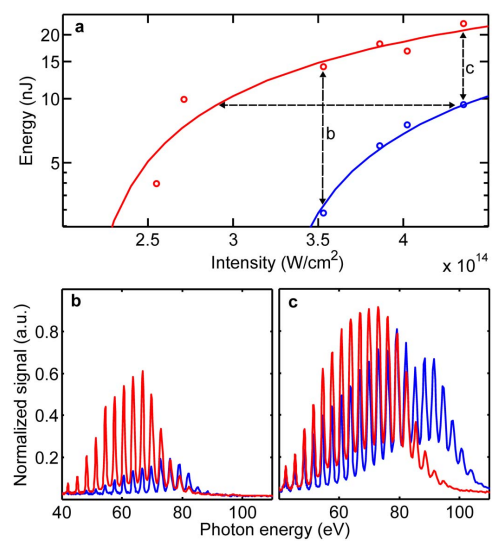

Figure 4 | Optimization of HHG. (a) 41st harmonic energy as a function of the driving intensity for seeded (red) and unseeded (blue) HHG. Unseeded HHG is optimized at the maximum intensity. (b, c) Corresponding experimental spectra at 3.5 and 4.4 × 10^{14} W/cm^2, respectively.

Figure 4(a) compares the 41st harmonic signal in the seeded and unseeded cases as a function of the driving intensity. The intensity required for saturating seeded HHG is only half that needed for unseeded HHG. This explains the reduction of the cutoff energy and the lower divergence for the harmonics. The enhancement factor depends on the driving intensity [Fig. 4(b,c)]. For the 41st harmonic, it varies from five at 3.5×10^{14} W/cm^2 (and even higher at lower intensity) to two at 4.4×10^{14} W/cm^2. By further optimizing seeded HHG (e.g. by changing the focusing conditions) one should be able to obtain an even larger increase compared to unseeded HHG. The higher efficiency together with the lower divergence leads to a brighter source of XUV light.

In summary, we have studied the effect of seeding HHG using harmonics generated in a separate gas cell and showed that low-order harmonics are responsible for the resulting enhancement. The combined electric field preferentially enhances the short trajectories while suppressing depletion and plasma dispersion effects. The required phase difference between the fundamental and the low-order harmonics is obtained by adjusting the pressure in the seeding cell, thus modifying the free-electron dispersion. Our method is not limited to the gas combination presented here. Experimentally we have observed an increased harmonic yield for a variety of gas combinations, and even when the same gas is used in both cells. Our simulations show that the enhancement can be scaled far above one order of magnitude by increasing the low-order harmonic intensity, for example by using longer cells, higher pressures or gases with higher nonlinearities. This also leads to a shorter temporal gate, of interest for single attosecond pulse generation.

Methods

Experimental setup. The harmonics were generated using 45 fs pulses, centered at 800 nm. The gas cells used in this setup were 1 cm long with a diameter of 1 mm. The injection of gas into the cell was synchronized with the laser repetition rate (10 Hz) and the delay between the gas injection and the laser pulse was optimized for each cell. In the experiments, seeding cell pressure and pulse energy were the parameters investigated. The generation cell pressure was set for the best phase-matching conditions for Ne at the highest laser intensity intensity (4.4×10^{14} W/cm^2), corresponding to less than 10 mbar. The focus position was adjusted in order to optimize HHG in the generation cell. The cell separation was 15 mm with the generation-cell located at focus (f = 4 m). Nevertheless, larger separations, up to 50 mm yielded similar results. The cells were mounted on motor-controlled XYZ stages with motorized XY tilt capabilities. The cells could be removed completely from the IR field. A CCD camera was used to align each cell to the laser and observation of the spectra at the best phase-matching conditions were used to evaluate the tilt of each cell. The same Ne spectra from the generation cell could be obtained though the evacuated seeding cell or with the seeding cell removed from the beam path. The same was true for the seeding cell where Ar spectra could be obtained under both conditions. The pressure and intensity controls were automated to scan the region of interest. At each experimental condition 10 single-shot spectra were measured and averaged. The harmonic orders were calibrated using the absorption edge of an Al-foil filter. The fundamental intensity was estimated from the cutoff of the unseeded Ne spectra.

Numerical simulations. *Generation cell.* The influence of a weak third harmonic field on the HHG process was simulated by solving the time dependent Schrödinger Equation within the strong field approximation. The quasi-classical action for the electron motion in the continuum

$$S(\vec{p},t,t_0) = \int_{t_0}^{t} dt' \left(\frac{\left[\vec{p} - e\vec{A}(t')\right]^2}{2m} + I_p \right) \tag{2}$$

is calculated for a combined vector potential of the fundamental field and a weak parallel auxiliary field consistent with the field definition in Eq. (1). t_0 and t correspond to the tunneling and recombination times for an electron with canonical momentum $\vec{p}$, I_p is the ionization potential, and $\vec{A}$ the vector potential of the field. We approximate the HHG dipole as[24]

$$\begin{aligned} x(t) = i \int_0^{\infty} d\tau \left(\frac{\pi}{\epsilon + i\tau/2} \right)^{3/2} & d_x^*(p_{st}(t,\tau) - A_x(t)) \\ & \times d_x(p_{st}(t,\tau) - A_x(t-\tau)) E(t-\tau) \\ & \times \exp[-iS_{st}(t,\tau)] F(\tau) + c.c., \end{aligned} \tag{3}$$

where a stationary phase approximation is performed over momentum, with $p_{st}(t,\tau) = [E(t) - E(t-\tau)]/\tau$, where $\tau = t - t_0$ is the excursion time in the continuum. We also insert a filter function $F(\tau)$ to select the short trajectory: $F(\tau) \approx 1$ for $\tau < 0.65T$ and $F(\tau) \approx 0$ for $\tau > 0.65T$, where $0.65T$ corresponds to the position of the cutoff. The integral in Eq. (3) is then evaluated numerically on a finite grid followed by a numerical Fourier transform for the dipole emission.

Seeding cell. We performed calculations which combine the solution of the time-dependent Schrödinger equation in a single-active electron approximation and propagation in a partially ionized medium[26,5] using a slowly-varying envelope approximation. Our main goal was to examine the influence of the pressure both for low-order and high-order harmonic generation in conditions mimicking the experiment. We found a maximum for HHG at around 10 mbar, while below-threshold, low-order harmonics which are not reabsorbed in the medium continue to increase up to very high pressures (100 mbar).

The generation of the third harmonic in the seeding cell was simulated using a (3 + 1)-dimensional, unidirectional, nonlinear envelope equation[28]. The complete frequency dependent dispersion relation is considered, enabling to propagate the fundamental and the third harmonic simultaneously. It is numerically integrated using a split-step technique, where the linear contributions, such as dispersion and diffraction are treated in k-transverse frequency space, while the nonlinear part, taking into account the Kerr effect, third-harmonic generation as well as plasma dispersion and plasma defocusing is treated in normal space. The method is described in detail in[28]. The calculated phase variation is mainly due to plasma dispersion effects. There are also small contributions from the geometrical phase acquired along the seeding cell as well pressure-dependent third harmonic phase matching.

1. Popmintchev, T. *et al.* Bright Coherent Ultrahigh Harmonics in the keV X-ray Regime from Mid-Infrared Femtosecond Lasers. *Science* **336**, 1287–1291 (2012).
2. Krausz, F. & Ivanov, M. Attosecond Physics. *Rev. Mod. Phys.* **81**, 163 (2009).
3. Constant, E. *et al.* Optimizing High Harmonic Generation in Absorbing Gases: Model and Experiment. *Phys. Rev. Lett.* **82**, 1668 (1999).
4. Kazamias, S. *et al.* Global Optimization of High Harmonic Generation. *Phys. Rev. Lett.* **90**, 193901 (2003).
5. Gaarde, M. B., Tate, J. L. & Schafer, K. J. Macroscopic aspects of attosecond pulse generation. *J. Phys. B* **41**, 132001 (2008).
6. Willner, A. *et al.* Efficient control of quantum paths via dual-gas high harmonic generation. *New J. Phys.* **13**, 113001 (2011).
7. Corkum, P. B. Plasma perspective on strong field multiphoton ionization. *Phys. Rev. Lett.* **71**, 1994–1997 (1993).
8. Schafer, K. J., Yang, B., DiMauro, L. F. & Kulander, K. C. Above threshold ionization beyond the high harmonic cutoff. *Phys. Rev. Lett.* **70**, 1599 (1993).
9. Wirth, A. *et al.* Synthesized Light Transients. *Science* **334**, 195–200 (2011).
10. Eichmann, H. *et al.* Polarization-dependent high-order two-color mixing. *Phys. Rev. A* **51**, R3414 (1995).
11. Mauritsson, J. *et al.* Attosecond Pulse Trains Generated Using Two Color Laser Fields. *Phys. Rev. Lett.* **97**, 013001 (2006).
12. Kim, I. J. *et al.* Highly Efficient High-Harmonic Generation in an Orthogonally Polarized Two-Color Laser Field. *Phys. Rev. Lett.* **94**, 243901 (2005).
13. Raz, O., Pedatzur, O., Bruner, B. D. & Dudovich, N. Spectral caustics in attosecond science. *Nat. Phot.* **6**, 170 (2012).
14. Watanabe, S., Kondo, K., Nabekawa, Y., Sagisaka, A. & Kobayashi, Y. Two-Color Phase Control in Tunneling Ionization and Harmonic Generation by a Strong Laser Field and Its Third Harmonic. *Phys. Rev. Lett.* **73**, 2692 (1994).
15. Kondo, K., Kobayashi, Y., Sagisaka, A., Nabekawa, Y. & Watanabe, S. Tunneling ionization and harmonic generation in two-color fields. *J. Opt. Soc. Am. B* **13**, 424–429 (1996).
16. Pi, L. W., Shi, T. Y. & Qiao, H. X. Enhancement of Bichromatic High-Order Harmonic Generation by a Strong Laser Field and Its Third Harmonic. *Chin. Phys. Lett.* **23**, 1490 (2006).
17. Ishikawa, K. Photoemission and Ionization of He^+ under Simultaneous Irradiation of Fundamental Laser and High-Order Harmonic Pulses. *Phys. Rev. Lett.* **91**, 043002 (2003).
18. Ivanov, I. A. & Kheifets, A. S. Tailoring the waveforms to extend the high-order harmonic generation cutoff. *Phys. Rev. A* **80**, 023809 (2009).
19. Chipperfield, L. E., Robinson, J. S., Tisch, J. W. G. & Marangos, J. P. Ideal waveform to generate the maximum possible electron recollision energy for any given oscillation period. *Phys. Rev. Lett.* **102**, 063003 (2009).
20. Schafer, K. J., Gaarde, M. B., Heinrich, A., Biegert, J. & Keller, U. Strong Field Quantum Path Control Using Attosecond Pulse Trains. *Phys. Rev. Lett.* **92**, 23003 (2004).
21. Gaarde, M. B., Schafer, K. J., Heinrich, A., Biegert, J. & Keller, U. Large enhancement of macroscopic yield in attosecond pulse train-assisted harmonic generation. *Phys. Rev. A* **72**, 013411 (2005).
22. Heinrich, A. *et al.* Enhanced VUV-assisted high harmonic generation. *J. Phys. B* **39**, S275 (2006).
23. Takahashi, E. J., Kanai, T., Ishikawa, K. L., Nabekawa, Y. & Midorikawa, K. Dramatic Enhancement of High-Order Harmonic Generation. *Phys. Rev. Lett.* **99**, 053904 (2007).
24. Lewenstein, M., Salières, P. & L'Huillier, A. Phase of the atomic polarization in high-order harmonic generation. *Phys. Rev. A* **52**, 4747 (1995).

25. Dahlström, J. M., L'Huillier, A. & Mauritsson, J. Quantum mechanical approach to probing the birth of attosecond pulses using a two-colour field. *J. Phys. B* **44**, 095602 (2011).
26. Erny, C. *et al.* Metrology of high-order harmonics for free-electron laser seeding. *New J. Phys.* **13**, 073035 (2011).
27. Heyl, C. M., Güdde, J., L'Huillier, A. & Höfer, U. High-order harmonic generation with μJ laser pulses at high repetition rates. *J. Phys. B* **45**, 074020 (2012).
28. Arnold, C. L. *et al.* Pulse compression with planar hollow waveguides: a pathway towards relativistic intensity with table-top lasers. *N. J. Phys.* **12**, 073015 (2010).
29. Takahashi, E., Nabekawa, Y. & Midorikawa, K. Generation of 10-μJ coherent extreme-ultraviolet light by use of high-order harmonics. *Opt. Lett.* **27**, 1920 (2002).
30. Salières, P., L'Huillier, A. & Lewenstein, M. Coherence control of high-order harmonics. *Phys. Rev. Lett.* **74**, 3776 (1995).

Acknowledgements

We thank Erik Mansten, Jörg Schwenke, and Rafal Rakowski for their early contribution to the project, and Byunghoon Kim for his contribution to the $\omega/3\omega$ measurements. This research was supported by the Marie Curie program ATTOFEL (ITN), the European Research Council (ALMA), the Joint Research Programme ALADIN of Laserlab-Europe II, the Swedish Research Council, the Swedish Foundation for Strategic Research, the Knut and Alice Wallenberg Foundation.

Author contributions

F.B., C.M.H. and P.R. contributed equally to this work. F.B., C.M.H., P.R. and L.R. performed the experiments. D.K. and C.L.A. performed the propagation calculations. C.M.H. and J.M.D. performed the SFA calculations. J.M, P.J., A.L. and all the other authors helped with the interpretation and the writing of the article.

Additional information

Competing financial interests: The authors declare no competing financial interests.

How to cite this article: Brizuela, F. *et al.* Efficient high-order harmonic generation boosted by below-threshold harmonics. *Sci. Rep.* **3**, 1410; DOI:10.1038/srep01410 (2013).

Paper II

A high-flux high-order harmonic source

P. Rudawski, C. M. Heyl, F. Brizuela, J. Schwenke, A. Persson, E. Mansten, R. Rakowski, L. Rading, F. Campi, B. Kim, P. Johnsson, and A. L'Huillier.

Rev. Sci. Inst. **84**, 073103 (2013).

REVIEW OF SCIENTIFIC INSTRUMENTS **84**, 073103 (2013)

A high-flux high-order harmonic source

P. Rudawski,[1,a)] C. M. Heyl,[1] F. Brizuela,[1] J. Schwenke,[1] A. Persson,[1] E. Mansten,[2] R. Rakowski,[1] L. Rading,[1] F. Campi,[1] B. Kim,[1] P. Johnsson,[1] and A. L'Huillier[1]
[1]*Department of Physics, Lund University, P.O. Box 118, SE-221 00 Lund, Sweden*
[2]*MAX-lab, Lunds Universitet, P.O. Box 118, SE-221 00 Lund, Sweden*

(Received 12 March 2013; accepted 11 June 2013; published online 9 July 2013)

We develop and implement an experimental strategy for the generation of high-energy high-order harmonics (HHG) in gases for studies of nonlinear processes in the soft x-ray region. We generate high-order harmonics by focusing a high energy Ti:Sapphire laser into a gas cell filled with argon or neon. The energy per pulse is optimized by an automated control of the multiple parameters that influence the generation process. This optimization procedure allows us to obtain energies per pulse and harmonic order as high as 200 nJ in argon and 20 nJ in neon, with good spatial properties, using a loose focusing geometry ($f_{\#} \approx 400$) and a 20 mm long medium. We also theoretically examine the macroscopic conditions for absorption-limited conversion efficiency and optimization of the HHG pulse energy for high-energy laser systems. [http://dx.doi.org/10.1063/1.4812266]

I. INTRODUCTION

High-order harmonics generated by the nonlinear interaction of an intense ultrashort laser pulse with atoms or molecules are now used in many fields of physics. The interest in the generated radiation results from unique features like tunability over the extreme ultraviolet (XUV) and soft x-ray (SXR) spectral regions (reaching several keV[1,2]), excellent beam quality,[3] and ultrashort pulse duration down to the attosecond range.[4] High-order harmonic generation (HHG) sources are well established in many research areas such as attosecond science[5] or femtosecond spectroscopy[6] and have become interesting for high-resolution imaging,[7,8] free-electron-laser seeding,[9] and nonlinear optics in the XUV range.[10,11]

Most applications of HHG sources benefit from harmonic pulses with high pulse energy. This requirement is difficult to achieve due to the low conversion efficiency of the generation process. Since the discovery of the HHG process over two decades ago,[12,13] its conversion efficiency has been progressively improved by optimizing the macroscopic phase-matching conditions and the microscopic single atom response. High-order harmonic generation has been carried out in different conditions, such as high-pressure jets,[14] gas cells,[15] semi-infinite media, and capillaries.[16] Phase-matching optimization using loosely focused (possibly self-guided) fundamental fields has led to conversion efficiencies of $\sim 10^{-7}$ in neon,[15] $\sim 10^{-5}$ in argon,[17] and slightly below 10^{-4} in xenon.[18,19] By modifying the generation field, e.g., by combining the fundamental field with one or more of its harmonics, the microscopic single atom response has been controlled on the subcycle level leading to enhanced HHG signals and/or generation of even-order harmonics.[20–22]

In this article, we describe a high-flux HHG source operating in the photon energy range up to 100 eV. The HHG setup is designed to work in a loose focusing geometry (up to 5 m focal length) and is driven by a high energy femtosecond laser system delivering up to 100 mJ per pulse. The optimization of the signal is performed using an automated scan of the main parameters that contribute to phase-matching (e.g., driving pulse intensity, gas pressure, etc.). Using this technique we have obtained a total energy per pulse in argon of a microjoule and a few hundred nJ in neon, in a geometry with an f-number $f_{\#} = f/D \approx 400$ and $f_{\#} \approx 133$, respectively, and a 20 mm long gas cell. Beam profiles were measured using an XUV-camera and the coherence properties were estimated in a Young's double-slit experiment. The article is organized as follows. Section II presents theoretical considerations for HHG under loose focusing. The HHG setup together with the methods for characterization and optimization are described in Sec. III. Results obtained with the high-energy, ultrashort laser system at the Lund Laser Centre are presented in Sec. IV. Section V presents a summary of the work and a discussion about scaling to extremely long focal lengths.

II. MODEL FOR LOOSE FOCUSING HHG

High-order harmonic generation with high conversion efficiency requires optimization of both the microscopic and macroscopic properties of the process. The microscopic response is well described by a semi-classical three-step model.[23,24] In every half-cycle of the driving wave, electrons can tunnel through the distorted atomic potential barrier, being then accelerated in the intense laser field. Depending on the release time into the continuum, the electrons may return to the parent ion and recombine, emitting an XUV photon. The trajectories of these electrons can be divided into two groups called short and long, depending on the excursion time in the continuum. HHG requires laser intensities in the range of 10^{14} W/cm^2–10^{15} W/cm^2 depending on the selected gas.

a)Electronic mail: piotr.rudawski@fysik.lth.se

Macroscopically, the total HHG signal is a coherent sum of the photons emitted from different atoms in the medium. For a given harmonic order q, constructive addition occurs along the propagation direction over the so-called coherence length $L_{\text{coh}} = \pi/\Delta k$. Here, $\Delta k = qk_1 - k_q$ is the wave-vector mismatch along the propagation direction between the generated field and the laser-induced polarization at frequency $q\omega$. In order to maximize the coherence length, the wave-vector mismatch must be minimized. In a non-guiding focus geometry this can be done through the interplay between the four sources of wave-vector mismatch,

$$\Delta k = \underbrace{\Delta k_g}_{<0} + \underbrace{\Delta k_n}_{>0} + \underbrace{\Delta k_p}_{<0} + \underbrace{\Delta k_d}_{\substack{<0 \text{ for } z<0 \\ >0 \text{ for } z>0}} . \quad (1)$$

The negative contribution Δk_g originates from the Gaussian beam phase gradient along the propagation direction (z). Δk_n and Δk_p describe the neutral and free-electron dispersion which have opposite sign and are proportional to the gas pressure. To explicitly outline this linear dependence, we write $\Delta k_{n,p} = p\,\partial(\Delta k_{n,p})/\partial p$, where the partial derivative is now pressure independent in the following. Δk_d is the gradient of the so-called dipole phase which is proportional to the intensity gradient and is small for the short trajectories but large for the long ones.[25]

Under our experimental conditions, the short trajectories dominate the HHG process. If only these trajectories are considered in Eq. (1), the dipole phase contribution can be neglected and the wave-vector mismatch can be minimized by canceling the plasma dispersion and Gaussian beam phase gradient with the neutral dispersion. For a fixed generation geometry, the degree of ionization in the medium determines the pressure, p_{match}, for which the system is phase matched.[26,27] For each harmonic order, p_{match} is defined as

$$p_{\text{match}} = -\frac{\Delta k_g}{\frac{\partial(\Delta k_n)}{\partial p} + \frac{\partial(\Delta k_p)}{\partial p}}. \quad (2)$$

For a given medium, harmonic order, and focal length, the only variable parameter is the free-electron contribution which is proportional to the degree of ionization ($\partial\Delta k_p/\partial p \propto r_{\text{ion}}$), and consequently can be adjusted by changing the laser intensity. The equation requires the intensity to be low enough so that the contribution due to neutral dispersion dominates over the free-electron dispersion. This defines a maximum ionization degree ($r_{\text{ion}}^{\text{max}}$), typically a few percent, above which phase-matched generation is not possible.

Figure 1 shows the variation of p_{match} in argon as a function of the degree of ionization for three harmonic orders and two different focusing geometries. p_{match} tends towards infinity when r_{ion} reaches $r_{\text{ion}}^{\text{max}}$. At low degree of ionization, the phase-matching pressure varies little both with pressure and with harmonic order. Considering that the dipole response is highest at the highest intensity, one could assume that the most efficient generation is possible at high pressures and at intensities that support an ionization degree around $r_{\text{ion}}^{\text{max}}$. High intensities, however, lead to steep gradients of r_{ion} in the longitudinal and radial directions within the generation volume, confining phase-matched generation to a small volume and leading to transient phase-matching.[27] In spite of a higher single atom response at high intensity, those effects can reduce the overall efficiency. An optimum ionization degree should assure phase-matched HHG over a broad bandwidth and a large volume. The ionization level should be such that the phase-matching pressure is approximately constant for a broad range of high-order harmonics, potentially leading to short and intense attosecond pulses. This phase-matching bandwidth increases with decreasing ionization degree yet at the same time the single atom response as well as the conversion efficiency decrease. As a rule of thumb, the optimum value for the ionization degree can be taken as $\sim r_{\text{ion}}^{\text{max}}/2$ for the highest harmonic in the considered HHG bandwidth. Under the conditions of Figure 1, this corresponds to ~2% ionization and a laser intensity of $\sim 1.1 \times 10^{14}$ W/cm^2.

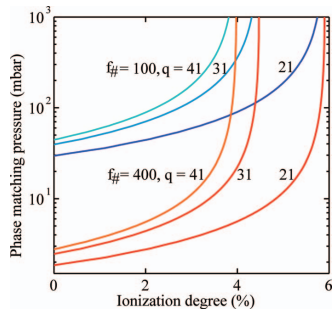

FIG. 1. Phase matching pressure in Ar as a function of ionization degree for different harmonic orders, q, and different focus geometries $f_\# = 100$, blue, and $f_\# = 400$, red. The central wavelength is 800 nm and the generation cell is placed at the focus of the fundamental beam.

When the coherence length, L_{coh}, is maximized, the harmonic emission is limited by re-absorption in the generation gas. The absorption length, L_{abs}, is defined by

$$L_{\text{abs}}(p) = \frac{kT}{p\sigma_{\text{ion}}}, \quad (3)$$

where k is the Boltzmann constant, T the temperature, and σ_{ion} the ionization cross-section. Following the argumentation of Constant *et al.*,[28] the harmonic yield is then maximized when the medium length, L_{med}, is at least three times the absorption length. This allows to define an optimum medium length under phase-matched conditions, $L_{\text{med}}^{\text{opt}} = 3L_{\text{abs}}(p_{\text{match}})$. For example for the 21st harmonic in Ar, and $f_\# = 400$, $T = 300$ K, $\sigma_{\text{ion}} = 2 \times 10^{-21}$ m^2, $p_{\text{match}} \approx 5$ mbar, and consequently $L_{\text{med}}^{\text{opt}}$ should be chosen to be at least 12 mm.

For high-energy laser systems, an increase of the absorption-limited HHG intensity can be achieved by scaling up the $f_\#$, i.e., by increasing the focal length for a certain initial beam diameter. The conversion efficiency can be held constant when changing the focal length if the laser pulse energy, the gas pressure, and the medium length are scaled appropriately. Using Gaussian optics and Eqs. (2) and (3), we derive the following scaling relations: E_f (laser energy) $\propto f^2$ in order to keep the same intensity at focus, $p_{\text{match}} \propto 1/f^2$ since $\Delta k_g \propto 1/f^2$, and $L_{\text{med}} \propto f^2$. This ensures constant conversion

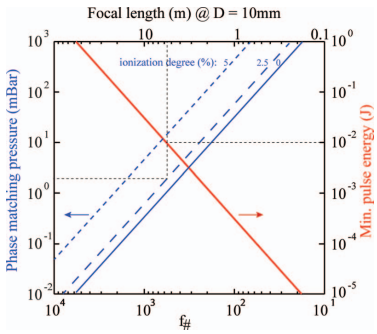

FIG. 2. Scaling of the phase matching pressure and the required laser pulse energy with focal length (or $f_\#$) for different ionization levels in argon. The corresponding minimum laser pulse energy required is shown in red. For the simulations, the following parameters were used: beam diameter before focusing: $D = 10$ mm, gas cell position: at the focus, central wavelength of 800 nm, harmonic order $q = 21$. The required pulse energy was calculated assuming a peak intensity of 1.5×10^{14} W/cm^2 and a pulse length of 45 fs.

efficiency, independent of the focusing geometry,[27] and the harmonic energy $E_h \propto f^2$.

Figure 2 illustrates these scaling relations in the case of argon, with the following parameters: 800 nm wavelength, a 45 fs pulse duration, an intensity of 1.5×10^{14} W/cm^2 at focus, and an initial beam diameter of 10 mm. A laser pulse energy of 10 mJ requires a focal length of approximately 5 m and a generation pressure of a few mbar to efficiently generate harmonics.

III. HIGH-ORDER HARMONIC EXPERIMENTAL SETUP

Our HHG setup consists of three sections: generation, diagnostics, and application (see Figure 3). The sections are connected by vacuum tubes with a diameter $\phi = 40$ mm. The generation section is mounted on stiffly connected optical tables. The diagnostics section together with the application chamber are mounted on a rail system. This allows us to adjust the distance between the vacuum chambers depending on the focusing geometry in order to avoid damage of optical elements placed after the generation by the fundamental laser field. It also provides vibration isolation and high stability.

High-order harmonics are generated by loosely focusing a high energy laser beam into a noble gas. The fundamental laser beam is apertured down by a variable diameter iris (I), typically between 9 and 30 mm and focused by a lens (L). Control of the beam size allows for re-adjustments of the focusing geometry ($f_\#$) as well as laser energy and intensity distribution at focus. Thus it allows us to optimize phase-matching in a simple way. Directly after the focusing optics, the beam enters the generation chamber. The entrance UV fused silica window is mounted at a small angle to avoid back propagation of the reflected light to the laser system. The beam propagates inside a 100 mm diameter vacuum tube and is folded by mirrors (M) mounted on small breadboards placed in 6-way crosses. Alternatively, the laser beam can be focused by a mirror at near-normal incidence placed in one of the vacuum crosses. The focused beam interacts with the noble gas confined in a cell (PGC). The cylindrical cell has a diameter of typically 0.5 mm and a length between 3 mm and 20 mm. The gas is released at the repetition rate of the laser by a valve[29] driven by a piezo-electric actuator and synchronized with the laser pulse. The opening and closing times are optimized for maximum harmonic signal. Simulating the gas distribution in the cell, we found a small pressure gradient from the middle of the cell, where the gas is injected, towards the ends of the cell, where the pressure abruptly drops. The cell is mounted on an XY motorized stage. Additionally, two motorized actuators control the tilt of the cell with respect to the incoming beam. In order to optimize the position of the cell relative to the laser focus the gas cell is additionally placed on a 6 cm long-range translation stage moving along the propagation direction (Z).

The generation chamber is designed to work simultaneously with up to two gas cells. The cells can be mounted in parallel or in series. The parallel configuration allows for the generation of two independent harmonic beams[30] while the serial configuration can be used for the enhancement of the HHG process using low-order harmonics generated in the first cell.[22] In both configurations, the generated harmonic beam propagates collinearly with the fundamental radiation in vacuum (10^{-6} mbar) to the diagnostics chamber. Elimination

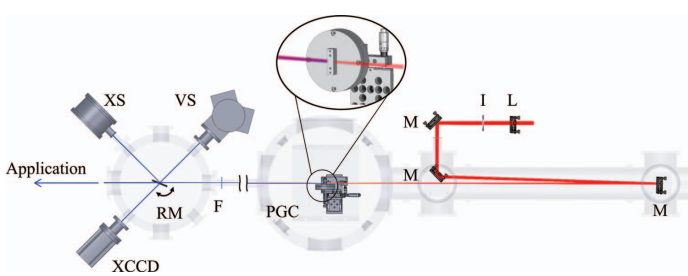

FIG. 3. HHG setup in the 4 m focusing configuration; L - focusing lens, I - iris, M - folding mirrors, PGC - pulsed gas cell, F - aluminum filters, RM - rotating mirror, XS - XUV spectrometer, VS - VUV spectrometer, and XCCD - XUV CCD camera.

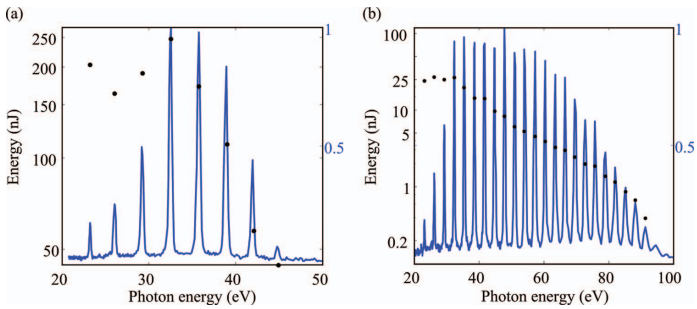

FIG. 4. High-order harmonic spectra in argon (a) and neon (b) gas. The pulse energy per individual harmonics, shown as dots, was obtained by combining total energy measurements with the spectral response from the XUV spectrometer.

of the fundamental is achieved by using 200 nm thick aluminum filters (F). The filters are mounted on a manual translation stage placed at the entrance of the diagnostics chamber, and controlled from the outside of the vacuum chamber.

The alignment of the setup is based on the beam position at the entrance iris and a reference point inside the diagnostics chamber. The precise alignment of the gas cell with respect to the laser beam is done by motorized control of the cell's four axes (XY and two tilts). The reference point and gas cell are monitored by cameras equipped with variable focal length objectives.

At the center of the diagnostics chamber, a gold-coated flat mirror (RM) mounted on a rotation stage is used to send the XUV beam to the different instruments or, when the mirror is removed, towards the application chamber (Fig. 3). The HHG spectra are measured by a flat-field grating spectrometer (XS, Jobin-Yvon PGM-PGS 200). The spectrometer detects spectrally-resolved far-field spatial profiles of individual high-order harmonics in the XUV spectral range. Low-order harmonics are detected using a vacuum ultraviolet monochromator (VS, McPherson 234/302). The vacuum ultraviolet spectrometer is equipped with an MCP detector coated with CsI allowing HHG diagnostics in a range from 50 to 250 nm. Additionally, spatial profiles and energy measurements are carried out using a back-illuminated XUV-CCD (Andor iKon-L) camera (XCCD). To attenuate the HHG beam for these measurements we use one or two 200 nm thick aluminum filters.

IV. RESULTS

This section presents measurements of high-order harmonics generated in argon and neon. The driving laser system is a high-power Ti:Sapphire chirped-pulse-amplification-based laser system delivering 45 fs pulses with up to 100 mJ energy at 10 Hz repetition rate. Before compression, the laser beam is spatially filtered with a conical pinhole mounted in a vacuum chamber. The pinhole waist, approximately 500 μm, is placed in a focal plane of a 1.7 m focal length lens. The laser beam diameter is 30 mm at the entrance to the harmonic setup. The laser beam position and angle are actively stabilized.

Figure 4 presents typical integrated harmonic spectra for (a) argon and (b) neon, recorded by the XUV spectrometer. The driving laser beam, with 20 mJ energy in case of argon and 24 mJ in case of neon, was focused by a 4 m lens in a 20 mm long cell. The HHG cut-off energy is 45 eV (29th harmonic) in argon whereas in neon it reaches 91.5 eV (59th harmonic). Under these conditions the total measured harmonic energy per laser shot is 1.15 μJ for argon and 0.23 μJ for neon. These values correspond to conversion efficiencies of 5×10^{-5} for argon and 8×10^{-6} for neon. Due to the high sensitivity of the XUV camera to the infrared radiation, the harmonic beam energy is measured within the aluminum filter's transmission window, i.e., between 14 eV and 71 eV, corresponding to harmonic orders between 11 and 45. The measurement procedure, similar to the one described by Erny *et al.*,[31] is based on XUV-CCD recorded background-subtracted images. The images are integrated to obtain the total number of counts. The total number of photons is estimated based on a calibration curve from the manufacturer. The individual harmonic energy is obtained by multiplying the total HHG beam energy with the relative intensity of each harmonic measured by the spectrometer. The spectrum is corrected for the folding mirror reflection (based on data from Henke *et al.*[32]), the grating efficiency, and the measured aluminum filter transmission. The estimated pulse energy per harmonic is shown as dots in Figure 4. The most prominent harmonic, both in argon and neon is the 21st harmonic (32.5 eV). Its energy is 250 nJ in argon and 30 nJ in neon. These values are comparable to previous results obtained by Takahashi *et al.*[15,17]

To find the optimum high-order harmonic energies an automated optimization procedure was carried out. This procedure is briefly summarized here. The important parameters to control are: fundamental beam energy and diameter (before focusing), gas pressure, and gas cell position relative to the laser focus. The energy of the fundamental beam is varied by an attenuator consisting of a half-wave plate mounted on a motorized rotation stage and a polarizer. We use a motorized

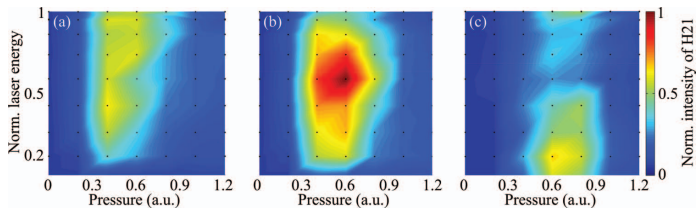

FIG. 5. Intensity of the 21st harmonic generated in argon as a function of driving laser energy and generation gas pressure. The measurements were carried out for a gas cell placed at the laser focus for three iris sizes: (a) $\phi = 22$ mm, (b) $\phi = 24$ mm, and (c) $\phi = 32$ mm. The values of a harmonic intensity between the measured points, shown as black dots, were interpolated.

variable iris to change the diameter of the fundamental beam before focusing. The distance between the center of the cell and the fundamental beam waist is varied by moving the cell. Finally, the gas pressure in the cell is adjusted by controlling a voltage applied to the cell nozzle's piezoelectric disks. We record a set of harmonic spectra while varying these four parameters in an automated way. Either the total HHG energy or the energy of a single harmonic can be optimized. Our optimization procedure allows us to routinely obtain HHG energies at the level of several hundred nJ in argon and a few tens of nJ in neon.

An example of the automated optimization is presented in Figure 5, where we investigated the dependence of the intensity of the 21st harmonic generated in argon as a function of the laser energy and gas pressure for three iris diameters. The signal is normalized to the maximum obtained for 21st harmonic. The recorded data show that for increasing iris size (decreasing $f_{\#}$), the required laser energy decreases and the phase matching pressure increases in agreement with our model prediction (see Fig. 1). Similar optimization in neon shows, as expected, a higher p_{match}. The optimum iris diameter corresponds to the longest Rayleigh range (the highest $f_{\#}$) for which the phase-matching conditions can be achieved, while keeping a high enough intensity at focus. It assures the highest HHG beam energy as is shown in Sec. II.

Figure 6(a) shows the spatial profile of high-order harmonics generated in argon and transmitted through an aluminum filter. The corresponding orders are between 11 and 45. The back-panel shows that the intensity distribution is almost perfectly Gaussian. Similar high quality Gaussian beams were generated in neon. The high spatial quality of the generated beams is due partly to the spatial quality of the driving beam, and partly to optimized phase-matching along the propagation axis. In our conditions, IR and XUV beams distortion due to nonlinear and plasma effects are negligible.

The generated beams divergence carries information about the contribution from the electronic trajectories. The divergence of the "short trajectory" harmonic beam is usually much smaller than for the "long trajectory" harmonics. For the 21st harmonic generated in argon, the divergence of the beam resulting from the long trajectory is 14 times higher than that from the short trajectory.[36] The different divergence is a consequence of a larger accumulated phase on the long trajectories. The analysis of the harmonic beam divergence shows that the main contribution to HHG in our conditions comes from the short trajectories. The contribution from the long trajectories is visible on the analyzed CCD images as a weak background.[30]

To estimate the spatial coherence of the HH beam, we performed a double-slit experiment. The degree of coherence of the HHG beam can be estimated from the fringe contrast in the diffraction pattern.[33,34] The slits used in this experiment had a width of 40 μm, a slit separation of 400 μm, and were located 1.5 m from the source. Figure 6(b) shows a cross-section of the double-slit diffraction pattern obtained with a single shot exposure. The experimental data were fitted with

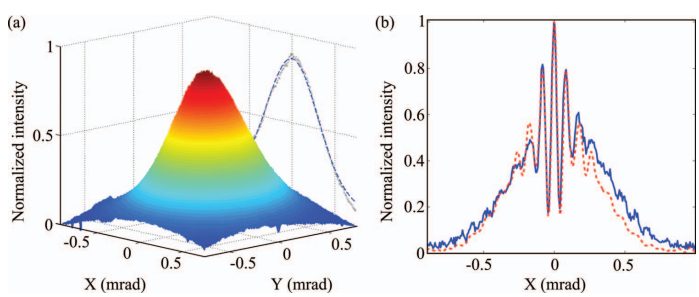

FIG. 6. (a) Spatial profile of the harmonic beam generated in Ar by focusing fundamental radiation with 2 m focal length lens into a 10 mm long cell, recorded with an x-ray CCD camera. The back-panel shows the cross-section of the beam (gray, dotted line), and a fitted intensity distribution (blue, dashed line), (b) Diffraction pattern created in a double-slit experiment, experimental data (blue, solid line), and fitted intensity distribution (red, dashed line).

a theoretical intensity function formed by the sum of diffraction patterns of the different harmonic wavelengths within the transmission window of the filter. The best fit was found with a degree of coherence of 0.8, in good agreement with previous measurements.[35]

V. SUMMARY AND OUTLOOK

We have developed a high-energy HHG setup, working in a loose focusing geometry, generating a total energy per laser pulse of a microjoule in argon and a few hundred nJ in neon. The source is designed for future studies of nonlinear processes in the XUV spectral range. The high harmonic pulse energies together with their high spatial coherence allow us to reach high peak intensities. For example, an intensity of 2×10^{14} W/cm^2 per harmonic pulse could be reached by focusing the HHG beam generated in argon using a broadband grazing-incident mirror, assuming a 3 μm focal spot size, 20 fs duration, and 30% transmission after reflection and filtering by an Al filter.

Our theoretical analysis of phase-matching in the absorption-limited case provides a simple guide for scaling HHG properties to high laser energies. For example we estimate that with $E_t = 1$ J, $f = 50$ m, $p = 0.01$ mbar, and $L_{med} = 6$ m, harmonic pulses with energy as high as 70 μJ could be reached.

Further increase in energy could be achieved by modifying the single atom response, e.g., using a double-cell scheme.[22] Our current beam line includes the option to drive the HHG process with two cells or to use an interferometric setup in order to combine the fundamental with itself, its second or third harmonic (ω/ω, $\omega/2\omega$, and $\omega/3\omega$), thus providing a large range of options for modifying the driving field.

Our experimental results combined with the above considerations show that HHG has the potential to provide intense ultrashort pulses reaching the intensity levels required for nonlinear experiments in the XUV spectral range.

ACKNOWLEDGMENTS

This research was supported by the Marie Curie program ATTOFEL (ITN), the European Research Council (ALMA), the Joint Research Programme ALADIN of Laserlab-Europe II, the Swedish Research Council, the Swedish Foundation for Strategic Research, and the Knut and Alice Wallenberg Foundation.

[1]C. Spielmann, N. H. Burnett, S. Sartania, R. Koppitsch, M. Schnürer, C. Kan, M. Lenzner, P. Wobrauschek, and F. Krausz, "Generation of coherent x-rays in the water window using 5-femtosecond laser pulses" Science **278**, 661 (1997).
[2]T. Popmintchev, M.-C. Chen, D. Popmintchev, P. Arpin, S. Brown, S. Ališauskas, G. Andriukaitis, T. Balciunas, O. D. Mücke, A. Pugzlys, A. Baltuska, B. Shim, S. E. Schrauth, A. Gaeta, C. Hernández-García, L. Plaja, A. Becker, A. Jaron-Becker, M. M. Murnane, and H. C. Kapteyn, "Bright coherent ultrahigh harmonics in the keV x-ray regime from mid-infrared femtosecond lasers," Science **336**, 1287–1291 (2012).
[3]Y. Tamaki, J. Itatani, M. Obara, and K. Midorikawa, "Highly coherent soft x-ray generation by macroscopic phase matching of high-order harmonics," Jpn. J. Appl. Phys. **40**, L1154–L1156 (2001).
[4]E. Goulielmakis, M. Schultze, M. Hofstetter, V. S. Yakovlev, J. Gagnon, M. Uiberacker, A. L. Aquila, E. M. Gullikson, D. T. Attwood, R. Kienberger, F. Krausz, and U. Kleineberg, "Single-cycle nonlinear optics," Science **320**, 1614 (2008).
[5]F. Krausz and M. Ivanov, "Attosecond physics," Rev. Mod. Phys. **81**, 163–234 (2009).
[6]S. L. Sorensen, O. Bjorneholm, I. Hjelte, T. Kihlgren, G. Ohrwall, S. Sundin, S. Svensson, S. Buil, D. Descamps, and A. L'Huillier, "Femtosecond pump-probe photoelectron spectroscopy of predissociative states in acetylen," J. Chem. Phys. **112**, 8038 (2000).
[7]R. L. Sandberg, C. Song, P. W. Wachulak, D. A. Raymondson, A. Paul, B. Amirbekian, E. Lee, A. E. Sakdinawat, C. La-O-Vorakiat, M. C. Marconi, C. S. Menoni, M. M. Murnane, J. J. Rocca, H. C. Kapteyn, and J. Miao, "High numerical aperture tabletop soft x-ray diffraction microscopy with 70-nm resolution," Proc. Natl. Acad. Sci. U.S.A. **105**, 24–27 (2008).
[8]J. Schwenke, E. Lorek, R. Rakowski, X. He, A. Kvennefors, A. Mikkelsen, P. Rudawski, C. M. Heyl, I. Maximov, S.-G. Pettersson, A. Persson, and A. L'Huillier, "Digital in-line holography on amplitude and phase objects prepared with electron beam lithography," J. Microsc. **247**, 196–201 (2012).
[9]G. Lambert, T. Hara, D. Garzella, T. Tanikawa, M. Labat, B. Carre, H. Kitamura, T. Shintake, M. Bougeard, S. Inoue, Y. Tanaka, P. Salieres, H. Merdji, O. Chubar, O. Gobert, K. Tahara, and M.-E. Couprie, "Injection of harmonics generated in gas in a free-electron laser providing intense and coherent extreme-ultraviolet light," Nat. Phys. **4**, 296–300 (2008).
[10]E. P. Benis, D. Charalambidis, T. N. Kitsopoulos, G. D. Tsakiris, and P. Tzallas, "Two-photon double ionization of rare gases by a superposition of harmonics," Phys. Rev. A **74**, 051402(R) (2006).
[11]K. Ishikawa and K. Midorikawa, "Two-photon ionization of He^+ as a nonlinear optical effect in the soft-x-ray region," Phys. Rev. A **65**, 043405 (2002).
[12]M. Ferray, A. L'Huillier, X. F. Li, G. Mainfray, and C. Manus, "Multiple-harmonic conversion of 1064 nm radiation in rare gases," J. Phys. B **21**, L31 (1988).
[13]A. McPherson, G. Gibson, H. Jara, U. Johann, T. S. Luk, I. A. McIntyre, K. Boyer, and C. K. Rhodes, "Studies of multiphoton production of vacuum-ultraviolet radiation in the rare gases," J. Opt. Soc. Am. B **4**, 595 (1987).
[14]T. Brabec and F. Krausz, "Intense few-cycle laser fields: Frontiers of nonlinear optics," Rev. Mod. Phys. **72**, 545 (2000).
[15]E. J. Takahashi, Y. Nabekawa, and K. Midorikawa, "Low-divergence coherent soft x-ray source at 13 nm by high-order harmonics," Appl. Phys. Lett. **84**, 4–6 (2004).
[16]T. Popmintchev, M. C. Chen, P. Arpin, M. M. Murnane, and H. C. Kapteyn, "The attosecond nonlinear optics of bright coherent x-ray generation," Nat. Photonics **4**, 822–832 (2010).
[17]E. Takahashi, Y. Nabekawa, T. Otsuka, M. Obara, and K. Midorikawa, "Generation of highly coherent submicrojoule soft x rays by high-order harmonics," Phys. Rev. A **66**, 021802(R) (2002).
[18]E. Takahashi, Y. Nabekawa, and K. Midorikawa, "Generation of 10-μJ coherent extreme-ultraviolet light by use of high-order harmonics," Opt. Lett. **27**, 1920 (2002).
[19]J.-F. Hergott, M. Kovacev, H. Merdji, C. Hubert, Y. Mairesse, E. Jean, P. Breger, P. Agostini, B. Carré, and P. Salières, "Extreme-ultraviolet high-order harmonic pulses in the microjoule range," Phys. Rev. A **66**, 021801(R) (2002).
[20]J. Mauritsson, P. Johnsson, E. Gustafsson, A. L'Huillier, K. J. Schafer, and M. B. Gaarde, "Attosecond pulse trains generated using two color laser fields," Phys. Rev. Lett. **97**, 013001 (2006).
[21]D. Shafir, H. Soifer, B. D. Bruner, M. Dagan, Y. Mairesse, S. Patchkovskii, M. Yu. Ivanov, O. Smirnova, and N. Dudovich, "Resolving the time when an electron exits a tunneling barrier," Nature (London) **485**, 343–346 (2012).
[22]F. Brizuela, C. M. Heyl, P. Rudawski, D. Kroon, L. Rading, J. M. Dahlström, J. Mauritsson, P. Johnsson, C. L. Arnold, and A. L'Huillier, "Efficient high-order harmonic generation boosted by below-threshold harmonics," Sci. Rep. **3**, 1410 (2013).
[23]P. B. Corkum, "Plasma perspective on strong-field multiphoton ionization," Phys. Rev. Lett. **71**, 1994 (1993).
[24]K. J. Schafer, B. Yang, L. F. DiMauro, and K. C. Kulander, "Above threshold ionization beyond the high harmonic cutoff," Phys. Rev. Lett. **70**, 1599 (1993).
[25]P. Salières, A. L'Huillier, and M. Lewenstein, "Coherence control of high-order harmonics," Phys. Rev. Lett. **74**, 3776 (1995).
[26]S. Kazamias, D. Douillet, F. Weihe, C. Valentin, A. Rousse, S. Sebban, G. Grillon, F. Augé, D. Hulin, and P. Balcou, "Global optimization of high harmonic generation," Phys. Rev. Lett. **90**, 193901 (2003).

[27]C. M. Heyl, J. Güdde, A. L'Huillier, and U. Höfer, "High-order harmonic generation with μJ laser pulses at high repetition rates," J. Phys. B **45**, 074020 (2012).
[28]E. Constant, D. Garzella, P. Breger, E. Mével, C. Dorrer, C. L. Blanc, F. Salin, and P. Agostini, "Optimizing high harmonic generation in absorbing gases: Model and experiment," Phys. Rev. Lett. **82**, 1668 (1999).
[29]Attotech HB.
[30]C. Lyngå, M. B. Gaarde, C. Delfin, M. Bellini, A. L'Huillier, T. W. Hänsch, and C.-G. Wahlström, "Studies of the temporal coherence of high-order harmonics," Phys. Rev. A **60**, 4823 (1999).
[31]C. Erny, E. Mansten, M. Gisselbrecht, J. Schwenke, R. Rakowski, X. He, M. B. Gaarde, S. Werin, and A. L'Huillier, "Metrology of high-order harmonics for free-electron laser seeding," New J. Phys. **13**, 073035 (2011).
[32]B. L. Henke, E. M. Gullikson, and J. C. Davis, "X-ray interactions: Photoabsorption, scattering, transmission, and reflection at $E = 50$-30000 ev, $Z = 1$–92," At. Data Nucl. Data Tables **54**, 181–342 (1993).
[33]M. Born and E. Wolf, *Principles of Optics* (Cambridge University Press, 1999).
[34]B. E. A. Saleh and M. C. Teich, *Fundamentals of Photonics* (John Wiley and Sons, 2007).
[35]R. A. Bartels, A. Paul, H. Green, H. C. Kapteyn, M. M. Murnane, S. Backus, I. P. Christov, Y. Liu, D. Attwood, and C. Jacobsen, "Generation of spatially coherent light at extreme ultraviolet wavelengths," Science **297**, 376 (2002).
[36]X. He, M. Miranda, J. Schwenke, O. Guilbaud, T. Ruchon, C. Heyl, E. Georgadiou, R. Rakowski, A. Persson, M. B. Gaarde, and A. L'Huillier, "Spatial and spectral properties of the high-order harmonic emission in argon for seeding applications," Phys. Rev. A **79**, 063829 (2009).

Paper III

Two-photon double ionization of neon using an intense attosecond pulse train

B. Manschwetus*, L. Rading*, F. Campi, S. Maclot, H. Coudert-Alteirac, J. Lahl, H. Wikmark, P. Rudawski, C. M. Heyl, B. Farkas, T. Mohamed, A. L'Huillier, and P. Johnsson. (*Both authors contributed equally).

Phys. Rev. A **93**, 061402 (2016).

RAPID COMMUNICATI

PHYSICAL REVIEW A **93**, 061402(R) (2016)

Two-photon double ionization of neon using an intense attosecond pulse train

B. Manschwetus,[1] L. Rading,[1] F. Campi,[1] S. Maclot,[1] H. Coudert-Alteirac,[1] J. Lahl,[1] H. Wikmark,[1] P. Rudawski,[1] C. M. Heyl,[1] B. Farkas,[2] T. Mohamed,[2,3] A. L'Huillier,[1] and P. Johnsson[1,*]

[1]*Department of Physics, Lund University, P.O. Box 118, 22100 Lund, Sweden*

[2]*ELI-HU Non-profit Ltd., Dugonics ter 13, Szeged 6720, Hungary*

[3]*Physics Department, Faculty of Science, Beni-Suef University, Beni-Suef 62511, Egypt*

(Received 9 February 2016; published 21 June 2016)

We present a demonstration of two-photon double ionization of neon using an intense extreme ultraviolet (XUV) attosecond pulse train (APT) in a photon energy regime where both direct and sequential mechanisms are allowed. For an APT generated through high-order harmonic generation (HHG) in argon we achieve a total pulse energy close to 1 μJ, a central energy of 35 eV, and a total bandwidth of $\sim$30 eV. The APT is focused by broadband optics in a neon gas target to an intensity of 3×10^{12} W cm^{-2}. By tuning the photon energy across the threshold for the sequential process the double ionization signal can be turned on and off, indicating that the two-photon double ionization predominantly occurs through a sequential process. The demonstrated performance opens up possibilities for future XUV-XUV pump-probe experiments with attosecond temporal resolution in a photon energy range where it is possible to unravel the dynamics behind direct versus sequential double ionization and the associated electron correlation effects.

DOI: 10.1103/PhysRevA.93.061402

Double photoionization of atoms or molecules can occur through the absorption of either a single energetic photon or several less energetic photons. Single-photon multiple ionization is typically studied at synchrotron facilities where the photon energies can be high but the achievable peak intensities are low. Such experiments have led to an increased understanding of electron-electron correlation and have also provided an important tool to benchmark the theory of fundamental two-electron systems like He and H_2 [1,2]. At lower photon energies and high peak intensities, two or more photons can be used for ionization. In this regime, nonlinear processes in atoms and molecules can be studied and pump-probe experiments become possible. While multiphoton ionization using ultrashort intense infrared (IR) or visible laser pulses in the strong-field regime has been extensively studied [3], very few studies have been performed in the vacuum ultraviolet (VUV) and extreme ultraviolet (XUV) regimes, where absorption of one or two photons is sufficient to overcome the ionization thresholds [4–6]. Double ionization by absorption of more than one photon may occur either through a direct process where the photons are absorbed simultaneously or through a sequential process where the electrons are removed one at a time from the atom or ion, as depicted in Fig. 1. For pulse durations comparable to the time it takes for the system to relax to the ionic ground state, typically below 1 fs, the distinction between the two mechanisms becomes meaningless [7]. The development of experimental tools with the ability to carry out time-resolved measurements at such short time scales will thus open up an intriguing regime where charge rearrangement and electron correlation can be studied on their natural time scale.

The intensities required to induce multielectron, few-photon processes in the VUV or XUV photon energy regime have so far mainly been available at free electron lasers (FELs), where the dependence on intensity and wavelength for multiphoton ionization and the competition between direct and sequential two-photon double ionization have been studied [4,8,9], with pulse durations in the 10- to 100-fs regime. During recent years, laser-driven high-order harmonic generation (HHG) sources with potential to produce pulses in the attosecond regime have started to reach the intensity levels needed for studying nonlinear phenomena. However, to date only a few HHG-based experiments have been reported where two-photon double ionization in the XUV regime was studied [10–13], since the approach still presents a formidable experimental challenge due to the inherently low conversion efficiency of the generation process. These studies use xenon as the generation medium in order to reach sufficient XUV intensities, thus limiting the highest available photon energy to regions where the direct two-photon double-ionization channel dominates, since three photons are needed to access the sequential channel.

In this Rapid Communication we present a demonstration of two-photon double ionization of neon using an attosecond pulse train (APT) generated in argon with individual pulse durations of $\approx$300 as. The APT has a total pulse energy around 1 μJ and is focused to an intensity of 3×10^{12} W cm^{-2}. With a central energy of 35 eV and a total bandwidth of $\sim$30 eV the APT covers the spectral ranges of both the direct and the sequential two-photon double-ionization channels in neon. When tuning the photon energy below the threshold for the sequential channel, the double-ionization signal disappears, indicating that the two-photon double ionization predominantly occurs through a sequential process. In addition, we experimentally determine the single-photon ionization cross section for Ne^+ and find good agreement with earlier measurements [4,14].

*per.johnsson@fysik.lth.se

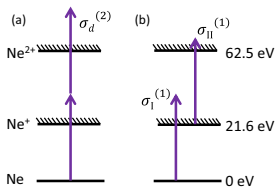

FIG. 1. Possible pathways when a neon atom is doubly ionized by two photons in a direct (a) or sequential (b) process. The relevant photoionization cross sections are indicated in the figure.

Figure 1 shows the possible outcomes when a neon atom is doubly ionized by two photons either in a direct or in a sequential process as shown in Figs. 1(a) and 1(b), respectively. While the direct and the sequential processes cannot be distinguished by measuring doubly charged ion yields, as they both involve absorption of two photons and depend quadratically on the intensity, they behave differently in two ways. First, for the direct channel the electrons share the total excess energy continuously and are preferentially emitted back to back [15]. For the sequential channel the electrons have discrete energies corresponding to the excess energy in each ionization step since they are removed one at a time. Despite this, a certain degree of angular correlation, possibly due to the coherent superposition of the $^2P_{3/2}$ and $^2P_{1/2}$ states of the Ne^+ ion, has been observed both experimentally and theoretically [9,16,17]. Second, the direct and sequential ionization channels have different temporal behavior as the intermediate ionic state in the sequential channel has a long lifetime. Within lowest order perturbation theory, for a given photon flux, F [photons cm^{-2} s^{-1}], and pulse duration, τ, the ratio between the sequential and direct double ionization yields, may be approximated as

$$\frac{\mathcal{N}_s^{2+}}{\mathcal{N}_d^{2+}} = \frac{\left(\sigma_{\rm I}^{(1)} F\tau\right)\left(\sigma_{\rm II}^{(1)} F\tau\right)}{2\sigma_d^{(2)} F^2 \tau} = \frac{\sigma_{\rm I}^{(1)}\sigma_{\rm II}^{(1)}}{2\sigma_d^{(2)}}\tau, \qquad (1)$$

where $\sigma_d^{(2)}$ is the two-photon double-ionization cross section for the direct process and $\sigma_{\rm I,II}^{(1)}$ is the one-photon single-ionization cross sections for Ne and Ne^+, respectively. The factor of two in the denominator is due to the time ordering of the ionization events in the sequential process.

As shown in Eq. (1), the branching ratio between the sequential and the direct process will depend on the pulse duration. Using measured [14,18] and calculated [19] values for the cross sections close to the threshold for two-photon sequential double ionization, Eq. (1) predicts that the yield of the direct process will become comparable to that of the sequential one at pulse durations below ~500 as. As stated in the introduction, the distinction between the two mechanisms becomes meaningless for sub-fs pulses, and thus the model in Eq. (1) is strictly not valid in this regime. The result above should therefore be regarded as a very coarse estimate of the regime where the transition occurs. Detailed theoretical calculations indicate that in helium the transition between the two regimes occurs for pulse durations just below 1 fs [15].

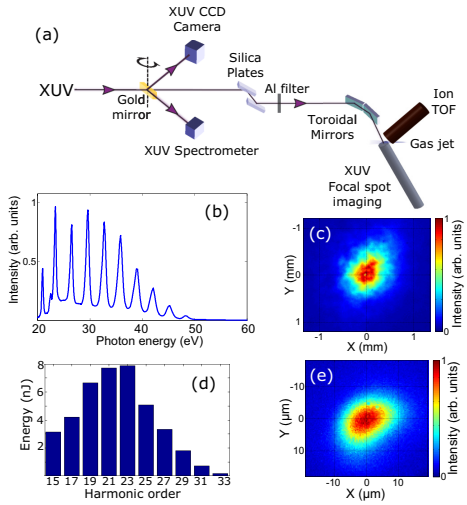

FIG. 2. Experimental setup and XUV pulse characterization results for HHG in argon. (a) Schematic experimental setup. (b) Generated XUV spectrum. The peak at 20.5 eV is due to second-order diffraction from the grating. (c) Far-field XUV beam profile. (d) Energy per harmonic on target. (e) XUV focal spot image.

Due to the requirement of attosecond pulse durations, so far two-photon direct double ionization has only been observed experimentally for photon energies below the threshold of the sequential channel, [4,10–13].

The principle of the experiment as well as the characteristics of the HHG source are shown in Fig. 2, with a schematic drawing of the experimental setup in Fig. 2(a). The HHG is driven by a high-power Ti:Sapphire chirped pulse amplification laser which delivers pulses at a central wavelength of 800 nm with a temporal duration of 35 fs at 10-Hz repetition rate and with a pulse energy of up to 80 mJ after compression. The IR pulses, with a beam diameter of 30 mm, are loosely focused by a $f = 9$ m lens into the generation chamber, where HHG takes place in a 6-cm-long static gas cell (not shown in the figure) [20,21]. After the HHG a rotatable gold mirror can be used to send the generated XUV pulses to different diagnostic devices. The spectrum, measured by a flat-field grating spectrometer, is shown in Fig. 2(b) and harmonics from order 15 (23.3 eV) up to order 33 (51.2 eV) can be seen. Based on the properties of the generating IR pulses, the HHG spectrum and previous APT measurements performed in our laboratory [22,23], the duration of the individual harmonics is estimated to 20 fs, and the APT thus contains ≈15 attosecond pulses with estimated individual pulse durations of ≈300 as, leading to an equivalent pulse duration of 4.5 fs. The far-field XUV beam profile, measured with a calibrated XUV CCD camera, is shown in Fig. 2(c). The total energy above 20 eV of the generated APT in argon was estimated to 0.8 ± 0.3 μJ.

To eliminate the IR field before the experiment, we use two grazing incidence silica plates, antireflection coated for the IR, together with a 200-nm-thick Al filter. The XUV pulses are then focused using two toroidal mirrors with a total focal length of 17 cm. The two mirrors, arranged in a Wolter configuration to minimize coma aberration [24], are gold coated and designed for a grazing angle of 15°, which allows for a theoretical reflectivity of 46% after two reflections for the full bandwidth of the APT. By taking into account the transmission of all elements of the beamline, we estimate a total APT energy in focus of 40 nJ for generation in argon. In Fig. 2(d) the calculated energy per harmonic on target is shown.

The focal spot is characterized by positioning a Ce:YAG scintillation crystal in the focus and imaging its surface using a long-working-distance optical microscope. The measured spot is shown in Fig. 2(e). It is slightly elliptical with 11 μm × 16 μm FWHM. This is 2–3 times larger than predicted by the ray-tracing simulations, which we attribute to the remaining aberrations manifested in the elliptical shape of the focal spot. Using a pulse energy of 40 nJ in the focus and assuming an APT with 15 pulses with individual durations of 300 as, we estimate the APT peak intensity in the focus to 3×10^{12} W cm^{-2}.

To perform the nonlinear ionization experiment, the Ce:YAG crystal was replaced with an ion time-of-flight (TOF) spectrometer and a pulsed neon gas jet. The TOF spectrometer was operated in Wiley-McLaren conditions, allowing for good time focusing over a large interaction volume [25]. Two microchannel plates followed by a phosphor screen were used to detect the ions. A mass spectrum from neon is shown in Fig. 3(a). Apart from the neon ionic species, the spectrum contains a few peaks due to residual gas and water contamination of the gas line. At $m/q = 20$ a.m.u., the main Ne^+ peak is visible, although heavily saturated in the plot. The peak at $m/q = 10$ a.m.u. corresponds to the doubly charged neon ion Ne^{2+} with a ratio between the yields of Ne^{2+} and Ne^+ of 0.35%. For double ionization of neon with a single photon, photon energies larger than 62.5 eV are required, which are not available in the experimental spectrum [see Fig. 2(b)]. This implies that the observed double ionization involves the absorption of more than one photon.

To confirm this we studied the nonlinearity of the Ne^{2+} yield as a function of the APT intensity. The XUV flux was adjusted by changing the gas pressure in the HHG gas cell, which had no major effect on the spectrum of the APT. To monitor the APT intensity we used the photoionization yield of H_2O^+. Since the ionization potential of H_2O is 12.6 eV [26], all photon energies within the experimental spectrum are able to photoionize it with a single photon and the measured yield of singly charged water ions is therefore proportional to the APT intensity. The result is shown in Fig. 3(b) in a double logarithmic plot. A linear fit to the data retrieves a slope of 1.8, close to the expected slope of 2 for a two-photon process.

The on-target APT spectrum generated in Ar includes harmonics from 15 to 33, covering the whole spectral range from 20 to 50 eV [see Fig. 2(d)], and thus both direct and sequential two-photon double ionization are possible. The APT intensity dependence of the Ne^{2+} yield is quadratic for both processes and cannot be used to differentiate them. To identify the dominant ionization pathway, we generated APTs

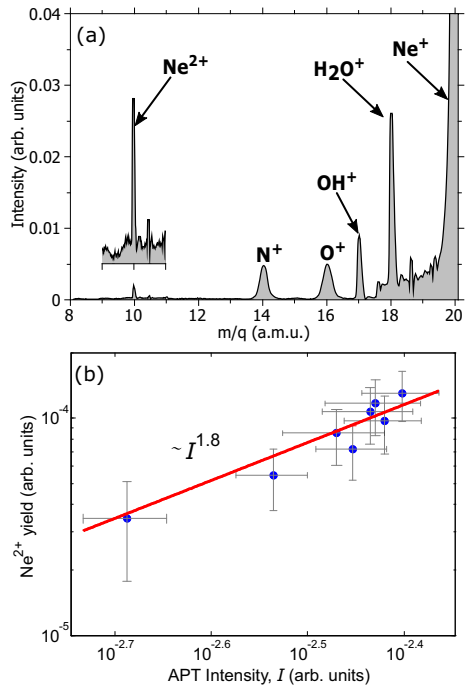

FIG. 3. Two-photon double ionization of neon using an APT generated in argon. (a) Ion mass spectra. For better visibility the signal between $m/q = 9$ and 11 a.m.u. is shown magnified. (b) Double logarithmic plot of the Ne^{2+} yield vs the APT intensity. The error bars indicate the standard deviation of the signal after integrating over 100 shots.

in krypton and varied the cutoff energy across the threshold for the sequential channel (40.9 eV) while maintaining an approximately constant APT energy on target (≈1 nJ). The use of Kr rather than Ar was motivated by the presence of a Cooper minimum in the Ar spectrum above the direct-sequential threshold, making difficult to identify the true cutoff energy. The position of the cutoff, which is a highly nonlinear function of the IR laser intensity, was changed by varying the laser energy focused in the generation cell. The APT pulse energy was kept constant by adjusting the pressure in an absorption cell filled with argon introduced in the beamline after HHG. The optimization of HHG for best cutoff tunability resulted in lower energy per harmonic on target than in Ar [compare Fig. 2(d) and Fig. 4(a)]. In order to obtain a sufficiently good signal-to-noise ratio, an ion-counting technique was applied to the single-shot TOF traces around the expected time of flight for Ne^{2+}. Figure 4(b) shows the extracted ion count rates for a cutoff below (blue bars) and above (red bars) 40.9 eV. The Ne^{2+} is only visible above the noise for the high-energy cutoff, indicating that the sequential channel is the dominant one in

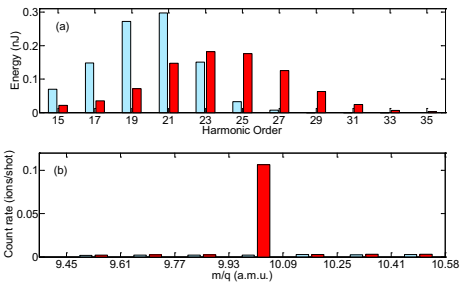

FIG. 4. Ionization of neon using APTs generated in krypton. (a) The energy per harmonic on target is shown for the low (blue bars) and high (red bars) cutoff case. (b) Ion count rates in the time-of-flight region around the Ne^{2+} signal ($m/q = 10$) for the low (blue bars) and high (red bars) cutoff case.

the current experiment. Using Eq. (1) and an equivalent pulse duration of $\tau = 4.5$ fs by assuming 15-as pulses, each with an individual duration of 300 as, we obtain a ratio of more than 20:1 between the expected ionization rates of the sequential and the direct channel [27], strengthening the conclusion that the sequential channel dominates, in agreement with the results of more sophisticated theoretical modeling [15,28].

We now return to the results shown in Fig. 3 and the measured ratio of 0.35% between the yields of Ne^{2+} and Ne^{+}. Using rate equations and assuming a sequential process, this ratio can be approximated as

$$\frac{\mathcal{N}_s^{2+}}{\mathcal{N}^{+}} = \frac{\sigma_{II}^{(1)} F_{II}}{2}\tau, \qquad (2)$$

where $\mathcal{N}^{+}$ is the yield of Ne^{+} ions and F_{II} is the photon flux [photons cm^{-2} s^{-1}] of photons with sufficiently high energy to ionize Ne^{+} (harmonics of order 27 and higher). Using the measured energies per harmonic pulse from Fig. 2(d) we obtain a value for the single-photon single-ionization cross section of Ne^{+}, $\sigma_{II}^{(1)} \approx 7 \times 10^{-18}$ cm^2, in good agreement with earlier experimental results measured at synchrotrons ($6 \pm 1 \times 10^{-18}$ cm^2) [14] and FELs ($7 \pm 1 \times 10^{-18}$ cm^2) [4], further supporting the conclusion that the sequential channel dominates.

In conclusion we have demonstrated two-photon double ionization of neon using an APT generated in argon with individual pulse durations of ∼300 as, a central energy of 35 eV, and a total bandwidth of ∼30 eV covering the spectral ranges of both the direct and the sequential double two-photon ionization channels. By generating APTs in krypton, we were able to tune the photon energy over the threshold of the sequential channel and could conclude that, in agreement with the estimation using a simple theoretical model, despite the attosecond pulse structure of the APT, the two-photon double ionization predominantly occurs through a sequential process. Finally, from the ratio of the measured ion yields we determine the single-photon ionization cross section for Ne^{+} is in good agreement with earlier measurements.

Our experimental setup allows us to make use of the full bandwidth of the XUV radiation through the use of grazing incident optics for focusing and filtering of the IR, imposing no lower limit on the achievable pulse duration in terms of the available bandwidth. The demonstrated performance opens up possibilities for future XUV-XUV pump-probe experiments with attosecond temporal resolution [29], with a potential to unravel, e.g., the dynamics behind direct versus sequential double ionization and associated electron correlation effects [15,28]. Further, pump-probe experiments with attosecond time resolution are expected to be a useful tool for studies of charge migration in molecules, where recent theoretical [30–32] and experimental [33] results have indicated the existence of dynamics on an attosecond time scale.

Acknowledgments. This research was supported by the Swedish Research Council, the Swedish Foundation for Strategic Research, the Knut and Alice Wallenberg Foundation, the European Research Council (PALP), the European COST Action CM1204 XLIC, and the Joint Research Programme INREX of Laserlab-Europe III. This project has received funding from the European Union's Horizon 2020 research and innovation program under Marie Sklodowska-Curie Grant Agreement No. 641789 MEDEA. B.F. and T.M. are financed by the project GOP-1.1.1.-12/B-2012-0001 (ELI-Hu).

B.M. and L.R. contributed equally to this work.

[1] A. Knapp, A. Kheifets, I. Bray, T. Weber, A. L. Landers, S. Schössler, T. Jahnke, J. Nickles, S. Kammer, O. Jagutzki, L. P. H. Schmidt, T. Osipov, J. Rösch, M. H. Prior, H. Schmidt-Böcking, C. L. Cocke, and R. Dörner, Phys. Rev. Lett. **89**, 033004 (2002).

[2] D. Akoury, K. Kreidi, T. Jahnke, T. Weber, A. Staudte, M. Schffler, N. Neumann, J. Titze, L. P. H. Schmidt, A. Czasch, O. Jagutzki, R. A. C. Fraga, R. E. Grisenti, R. D. Muio, N. A. Cherepkov, S. K. Semenov, P. Ranitovic, C. L. Cocke, T. Osipov, H. Adaniya, J. C. Thompson, M. H. Prior, A. Belkacem, A. L. Landers, H. Schmidt-Böcking, and R. Dörner, Science **318**, 949 (2007).

[3] P. Agostini, G. Barjot, G. Mainfray, C. Manus, and J. Thebault, IEEE J. Quantum Electron. **6**, 782 (1970).

[4] A. A. Sorokin, M. Wellhöfer, S. V. Bobashev, K. Tiedtke, and M. Richter, Phys. Rev. A **75**, 051402 (2007).

[5] N. A. Papadogiannis, L. A. A. Nikolopoulos, D. Charalambidis, G. D. Tsakiris, P. Tzallas, and K. Witte, Phys. Rev. Lett. **90**, 133902 (2003).

[6] K. Midorikawa, Y. Nabekawa, and A. Suda, Prog. Quantum Electron. **32**, 43 (2008).

[7] E. Foumouo, S. Laulan, B. Pireaux, and H. Bachau, J. Phys. B **39**, S427 (2006).

[8] R. Moshammer, Y. H. Jiang, L. Foucar, A. Rudenko, T. Ergler, C. D. Schröter, S. Lüdemann, K. Zrost, D. Fischer, J. Titze, T. Jahnke, M. Schöffler, T. Weber, R. Dörner, T. J. M. Zouros, A. Dorn, T. Ferger, K. U. Kühnel, S. Düsterer, R. Treusch,

P. Radcliffe, E. Plönjes, and J. Ullrich, Phys. Rev. Lett. **98**, 203001 (2007).

[9] M. Kurka, A. Rudenko, L. Foucar, K. Kühnel, Y. Jiang, T. Ergler, T. Havermeier, M. Smolarski, S. Schössler, K. Cole *et al.*, J. Phys. B **42**, 141002 (2009).

[10] P. Tzallas, D. Charalambidis, N. A. Papadogiannis, K. Witte, and G. D. Tsakiris, Nature (London) **426**, 267 (2003).

[11] Y. Nabekawa, H. Hasegawa, E. J. Takahashi, and K. Midorikawa, Phys. Rev. Lett. **94**, 043001 (2005).

[12] E. J. Takahashi, P. Lan, O. D. Mücke, Y. Nabekawa, and K. Midorikawa, Nat. Commun. **4**, 2691 (2013).

[13] P. Tzallas, E. Skantzakis, L. Nikolopoulos, G. Tsakiris, and D. Charalambidis, Nat. Phys. **7**, 781 (2011).

[14] A. Covington, A. Aguilar, I. Covington, M. Gharaibeh, G. Hinojosa, C. Shirley, R. Phaneuf, I. Alvarez, C. Cisneros, I. Dominguez-Lopez *et al.*, Phys. Rev. A **66**, 062710 (2002).

[15] J. Feist, S. Nagele, R. Pazourek, E. Persson, B. I. Schneider, L. A. Collins, and J. Burgdörfer, Phys. Rev. Lett. **103**, 063002 (2009).

[16] S. Fritzsche, A. Grum-Grzhimailo, E. Gryzlova, and N. Kabachnik, J. Phys. B **41**, 165601 (2008).

[17] L. A. A. Nikolopoulos, Phys. Rev. Lett. **111**, 093001 (2013).

[18] J. B. West and G. V. Marr, Proc. R. Soc. Lond. A **349**, 397 (1976).

[19] M. Førre, S. Selstø, and R. Nepstad, Phys. Rev. Lett. **105**, 163001 (2010).

[20] E. Takahashi, Y. Nabekawa, T. Otsuka, M. Obara, and K. Midorikawa, Phys. Rev. A **66**, 021802 (2002).

[21] P. Rudawski, C. M. Heyl, F. Brizuela, J. Schwenke, A. Persson, E. Mansten, R. Rakowski, L. Rading, F. Campi, B. Kim, P. Johnsson, and A. L'Huillier, Rev. Sci. Instrum. **84**, 073103 (2013).

[22] R. López-Martens, K. Varjú, P. Johnsson, J. Mauritsson, Y. Mairesse, P. Salières, M. B. Gaarde, K. J. Schafer, A. Persson, S. Svanberg, C.-G. Wahlström, and A. L'Huillier, Phys. Rev. Lett. **94**, 033001 (2005).

[23] K. Varjú, Y. Mairesse, B. Carre, M. B. Gaarde, P. Johnsson, S. Kazamias, R. Lopez-Martens, J. Mauritsson, K. J. Schafer, P. Balcou, A. L'Huillier, and P. Salières, J. Mod. Opt. **52**, 379 (2005).

[24] H. Wolter, Ann. Phys. **445**, 94 (1952).

[25] W. C. Wiley and I. H. McLaren, Rev. Sci. Instrum. **26**, 1150 (1955).

[26] S. Lias, in *Ionization Energy Evaluation*, edited by P. Linstrom and W. Mallard, NIST Standard Reference Database Number 69 (NIST Chemistry WebBook, National Institute of Standards and Technology, Gaithersburg, MD, 2014).

[27] Note that the used pulse duration is still much longer than the expected correlation time of the neon ground state (210 as), as defined in Ref. [7], motivating the use of the model in Eq. (1).

[28] A. Palacios, T. N. Rescigno, and C. W. McCurdy, Phys. Rev. A **79**, 033402 (2009).

[29] F. Campi, H. Coudert-Alteirac, M. Miranda, L. Rading, B. Manschwetus, P. Rudawski, A. L'Huillier, and P. Johnsson, Rev. Sci. Instrum. **87**, 023106 (2016).

[30] L. S. Cederbaum and J. Zobeley, Chem. Phys. Lett. **307**, 205 (1999).

[31] F. Remacle and R. D. Levine, PNAS **103**, 6793 (2006).

[32] A. I. Kuleff and L. S. Cederbaum, Chem. Phys. **338**, 320 (2007).

[33] F. Calegari, D. Ayuso, A. Trabattoni, L. Belshaw, S. De Camillis, S. Anumula, F. Frassetto, L. Poletto, A. Palacios, P. Decleva, J. B. Greenwood, F. Martin, and M. Nisoli, Science **346**, 336 (2014).

Paper IV

Design and test of a broadband split-and-delay unit for attosecond XUV-XUV pump-probe experiments

F. Campi, H. Coudert-Alteirac, M. Miranda, L. Rading, B. Manschwetus, P. Rudawski, A. L'Huillier, and P. Johnsson.

Rev. Sci. Inst. **87**, 023106 (2016).

REVIEW OF SCIENTIFIC INSTRUMENTS **87**, 023106 (2016)

Design and test of a broadband split-and-delay unit for attosecond XUV-XUV pump-probe experiments

F. Campi,[a] H. Coudert-Alteirac,[a] M. Miranda, L. Rading, B. Manschwetus, P. Rudawski, A. L'Huillier, and P. Johnsson[b]
Department of Physics, Lund University, P.O. Box 118, 22100 Lund, Sweden

(Received 6 August 2015; accepted 27 January 2016; published online 16 February 2016)

We present the design of a split-and-delay unit for the production of two delayed replicas of an incident extreme ultraviolet (XUV) pulse. The device features a single grazing incidence reflection in combination with attenuation of remaining infrared light co-propagating with the XUV beam, offering a high throughput without the need of introducing additional optics that would further decrease the XUV flux. To achieve the required spatial and temporal stabilities, the device is controlled by two PID-controllers monitoring the delay and the beam pointing using an optical reference laser beam, making collimation of the beam by additional optics unnecessary. Finally, we demonstrate the stability of the split-and-delay unit by performing all-reflective autocorrelation measurements on broadband few-cycle laser pulses. [http://dx.doi.org/10.1063/1.4941722]

I. INTRODUCTION

The ultrafast dynamics of ionized and excited molecular systems depend on fundamental processes such as charge transfer or charge migration,[1–3] leading to chemical reactions and dissociation through, for instance, intramolecular rearrangements.[4] To achieve a deeper knowledge of the interplay between charge and structural dynamics in molecules, it is necessary to simultaneously probe the dynamics in the molecule on femtosecond and attosecond time scales, as these are the ones on which nuclear motion and charge dynamics occur, respectively.

One route to access the attosecond time scales involved in the above-mentioned processes is to use High-order Harmonic Generation (HHG), in which an intense infrared (IR) femtosecond pulse is focused in a gas, leading to the generation of odd harmonics of the driving field in the extreme ultraviolet (XUV) region and pulse durations in the attosecond regime.[5,6] So far, most HHG pump-probe experiments have been based on a two-color XUV-pump IR-probe approach, with the drawback that the IR pulse might control the dynamics rather than probing them. An alternative approach is to perform XUV-XUV pump-probe experiments, with the added challenge that the XUV pulses then have to be sufficiently intense to allow for the absorption of two or more XUV photons. With photon energies of several tens of eVs the absorption of one photon often leads to single ionization of the target atom, while absorption of a second or more photons can lead to multiple ionization and excitation of the target. Previously, such experiments have been limited to free electron lasers,[7–9] a light source with very high intensity but, so far, reduced time resolution. In the last years intense HHG sources reaching pulse energies in the microjoule range have been developed at FORTH,[10] RIKEN,[11] and recently in our laboratory at the Lund Laser Centre (LLC),[12,13] which are intense enough to perform XUV-XUV pump-probe experiments. So far, only a few HHG-based XUV-XUV pump-probe experiments have been reported,[14–17] and the approach still presents a formidable experimental challenge, requiring simultaneously three critical conditions to be fulfilled: a high XUV intensity, a broad XUV bandwidth and an XUV interferometer with attosecond time resolution.

Here we present the design of a split-and-delay unit for the production of two delayed replicas of an incident XUV pulse. The device features a single grazing incidence reflection in combination with attenuation of remaining IR light co-propagating with the XUV beam, offering a high throughput without the need of introducing additional optics that would further decrease the XUV flux. To achieve the required spatial and temporal stabilities the device is controlled by two PID-controllers monitoring the delay and the beam pointing using an optical reference laser beam. This report is organized as follows: in Section II we present the mechanical design of the split-and-delay unit and discuss how the required specifications are met. In Section III we give details on the feedback and control scheme needed for reliable operation of the device and in Section IV we demonstrate the experimental performance of the unit through a series of tests using a broadband few-cycle IR laser. Finally, we conclude in Section V.

II. MECHANICAL DESIGN

As stated in the Introduction, the split-and-delay unit has to split the XUV pulse in two equal replicas and delay one of them with respect to the other with attosecond resolution, still being able to send them both to the same focusing optics. In addition, in order to guarantee high intensities and short attosecond pulses in the experimental region, the optical components of the device need to feature a high broadband reflectivity in the XUV region.

[a]F. Campi and H. Coudert-Alteirac contributed equally to this work.
[b]E-mail: per.johnsson@fysik.lth.se

To achieve a high broadband reflectivity, we use a single grazing incidence reflection on a silica (SiO_2) substrate, which allows for the transmission of the fundamental IR field. While other designs use collimation of the XUV beam before the split-and-delay unit in order to maintain the spatial overlap in the subsequent focus,[18] our design avoids the use of additional collimating optics which would lower the throughput by the implementation of an active feedback and control scheme, described in Section III. Further, the reflectivity for the IR is minimized by a multi-layer anti-reflection (AR) coating for the IR with *s*-polarization. The coating is designed for a grazing angle of 10° with alternating layers of SiO_2 and TiO_2, the top one being SiO_2, decreasing the IR reflectivity to below 10%. The thickness of the SiO_2 top layer is much larger than the penetration depth of the XUV radiation; therefore, the XUV reflectivity is unchanged by the applied AR coating. At the chosen grazing angle of 10°, the XUV reflectivity of SiO_2 for *s*-polarized light is larger than 50% for photon energies up to 70 eV.

Our mechanical design is based on wavefront splitting, whereas a standard beamsplitter performs the same function through amplitude splitting. In other words, the wave is sent to the edge of two aligned surfaces which are separately reflecting the two halves of the wavefront, creating two replicas of the incoming wave. While other designs usually align the surface edges parallel to the incidence plane (the plane defined by the incoming beam and the surface normal),[16,18] our unit has the surface edges aligned perpendicular to the incidence plane, in order to minimize the fraction of the beam lost between the edges of the plates, ensuring maximum throughput. A similar but less compact design with femtosecond resolution and without the here described PID loop stabilization has recently been implemented for X-rays at the Linac Coherent Light Source free electron laser.[19] The size of the silica plates is 40×14 mm each, so that the combination of the two plates can accommodate a beam diameter of 10 mm at 10° grazing incidence.

The high-intensity HHG beamline is described in detail elsewhere[12,13] but a sketch of the intended inclusion of the split-and-delay unit in the beamline is shown in Fig. 1(a). Briefly, the high-flux XUV pulses together with the generating IR pulses hit the split-and-delay unit at a 10° grazing angle. The IR that is still remaining is blocked completely by a metallic (e.g., aluminum) filter after the split-and-delay unit. The two XUV pulse replicas are finally focused by a short focal length double toroidal mirror in a Wolter configuration, allowing for focusing to a spot size of ~10 μm and intensities in excess of 10^{12} W/cm^2, as recently demonstrated.[13]

A 3D-model of the unit is shown in Fig. 1(b). The unit was designed to meet the requirements of functionality and stiffness, while keeping the maximum flexibility for future upgrades. With this intent the mount is symmetrical with respect to the interface between the two plates in order to be able to use it in different geometry configurations. It is constituted by a base plate (BP) mountable on standard optical posts and two movable parts (MPs), each of them holding one silica plate (SP). The assembly is equipped with three piezoelectric actuators (P-840.3 Physical Instruments, PAs) having a total travel range of 45 μm and three dummy actuators (DAs), which are replicas of the actuator casings without containing piezoelectric actuators. In this way either of the two movable mirror holders could be actuated from the computer, depending on how the split mirror is assembled. Furthermore, there is a possibility of upgrading the design installing six piezoelectric actuators, to have full control of the steering of both the reflected beams. All the real and dummy actuators are directly screwed on the base plate from the back side. The two movable parts are individually held back on the ball tips of the actuators by two extension springs and the contact is made in such a way that the ball tips are resting in the ball tip sockets of manual actuators for standard optics holders (MA). These manual actuators are very finely threaded differential screws, which allow for a pre-alignment of the entire assembly, to a very high precision (25 μm/rev). The actuators are positioned in an "L" shape, so that one of them can control the pivoting point, which can be preset to be right below the reflecting surface of the mirror. This minimizes the coupling between the horizontal and vertical tilt, which can be controlled by means of the other two actuators. The distances between the actuators are such that

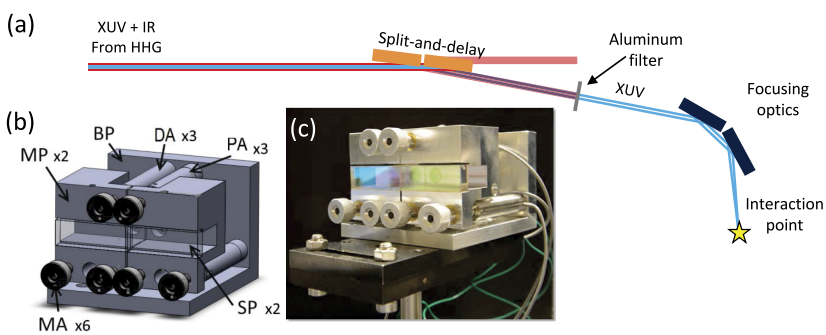

FIG. 1. (a) Sketch of the intended use of the split-and-delay unit in the existing high-intensity XUV beamline. (b) 3D-model of the split-and-delay unit with mounted silica plates. The two movable parts (MPs) are connected to the base plate (BP) by either real piezo-actuators (PA) or dummy actuators (DA), three for each MP. For each connection point there is also a manual actuator (MA) for coarse adjustments. The silica plates (SPs) are held in place by set screws from the top. (c) Photograph of the split-and-delay unit mounted on an optical post for the tests.

the maximum deflection angles are 1.7 mrad and 1.2 mrad in the horizontal and vertical directions, respectively. In our case the achievable delay is not limited by the dimensions of the silica plates since the XUV beam size is much smaller than the 10 mm aperture of the plates. Further, as discussed in Section III, the longitudinal movement of the focus can be neglected, and it is the 45 μm travel range of the piezoelectric actuators that limits the delay range of the device to 52 fs at 10° grazing incidence. Figure 1(c) shows a photo of the assembled device with the silica plates mounted.

III. FEEDBACK AND CONTROL SCHEME

When nonlinear experiments involving the two split replicas, e.g., autocorrelation or pump-probe experiments, have to be performed, not only the temporal delay has to be finely tunable and controlled but also the spatial overlap of the two beams has to be preserved. In the configuration the beamline is designed,[13] after the generation in the gas cell, the harmonic beam propagates over 6 m down to an application chamber. Along this path the beam is diverging before impinging on the split-and-delay unit and keeps diverging down to the application chamber, where the focusing apparatus is installed. Even if the silica plates could be displaced in a perfectly parallel manner not only the delay between the two replicas changes, but the source point of the XUV beam also moves, both laterally and longitudinally. The lateral movement is de-magnified by the focusing optics but, nevertheless, as confirmed by raytracing calculations, a translation of one of the silica plates through its full range (52 fs delay at 10° grazing incidence) leads to an 88 μm movement of the source point which corresponds to a 3 μm movement of the focal spot. This movement, being comparable to the focal spot size, would be detrimental for any pump-probe experiment. In earlier designs this has been remedied by collimating the beam before the split-and-delay unit.[18] In our design, in order to minimize the number of required optics and maintain a high throughput, we have chosen to actively stabilize the overlap of the two replicas in the focus. The longitudinal movement of the source also leads to a longitudinal movement of the focus, but this is so strongly de-magnified by the focusing optics that it becomes negligible. For a translation over the full delay range, as in the example above, the focus moves by less than 20 nm, which is much smaller than the Rayleigh length. Thus, much larger delays could be achieved by replacing the actuators for some with a larger travel.

The optical feedback system uses a green diode laser beam which is made to co-propagate with the main beam using a holey mirror, as illustrated in Fig. 2. After impinging on the split mirror the stabilization beam is constituted by two delayed replicas which are then picked out with another holey mirror and divided in two beams by a beamsplitter. One beam is focused on a camera (overlap control) to monitor the positions of the focal spots of the two replicas, as shown in the top inset of Fig. 2. In the other beam the two replicas are crossed at an angle on another camera (delay control) in order to create an interference pattern like the one shown in the bottom inset of Fig. 2. The phase of the fringes is extracted through Fourier analysis of the recorded image and, since the diode laser wavelength is well-known, from this the relative change in delay between the two replicas can be calculated and used as input to the PID-loop controlling the delay. Before the first holey mirror, a negative lens is used to match the divergence of the diode laser beam with that of the XUV beam, which is crucial for achieving proper control of the spatial overlap of the two replicas in the focus. This is in turn important for ensuring that the crossing angle of the two beams on the delay control camera stays constant. While the current version of the stabilization scheme does not allow for finding the zero delay, this could be achieved through e.g., the interference from a broadband white-light source. For the overlap control, the focal spot positions are recorded and the position of the delayed replica can be tracked by blocking the static replica. This change in the position with respect to the position of the other beam is used as an error function in the PID-loop controlling the two tilts to keep the two replicas overlapped in focus. Figure 3 shows a simplified block diagram of the PID loops implemented in the control software. Pointing and delay controls run asynchronously, each of them updating the piezo-voltages at different rates.

IV. PERFORMANCE TESTS

For the tests of the optical feedback system few-cycle IR pulses with pulse durations down to 5 fs were used instead of

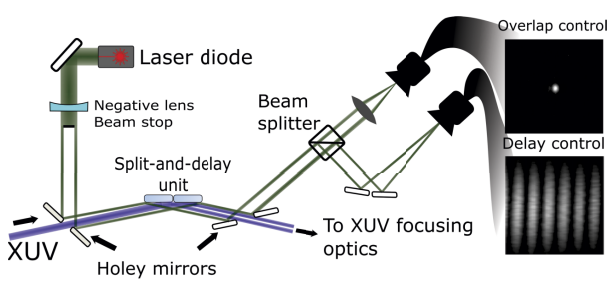

FIG. 2. Setup of the optical feedback system implemented for simultaneously stabilizing delay and overlap in the focus. The insets show images recorded by the overlap control camera (top inset) and the delay control camera (bottom inset).

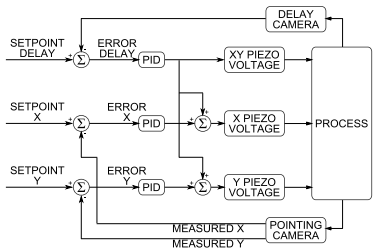

FIG. 3. Block diagram of the pointing and delay control PID loops. The fringes from the "delay camera" are used to measure the delay between the two arms by Fourier analysis, and a PID loop is used to calculate the voltage on the three piezos to get the desired delay. The focus spot from the "pointing camera" is used to monitor the beam position and two PID loops control the voltage applied to the horizontal and the vertical actuators piezos to correct for misalignment. The delay and pointing PID's run asynchronously and can update the piezos voltages at different rates.

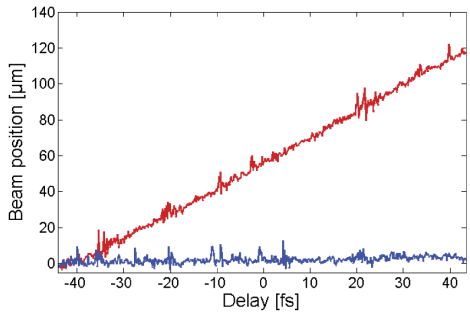

FIG. 4. Horizontal focus position as a function of delay with (blue line) and without (red line) the PID-loop for overlap control.

XUV pulses making it possible to perform the tests outside the vacuum chamber. The IR beam was made to diverge in order to create a virtual source point, and the divergence of the stabilization laser beam was matched to that of the IR. In addition, the unit was used at a larger grazing angle, ≈20°, to obtain a larger delay range. After the split-and-delay unit the IR pulses were focused by a lens with a focal distance of ≈1 m, leading to an IR focal spot of ≈100 μm.

First, the general performance of the feedback and control scheme was tested by placing a beam monitoring camera in the IR focus. The position of the IR focal spot was monitored while scanning over the full delay range. In Fig. 4 the horizontal focus position is shown as a function of delay, with the PID-loop off (red line) and on (blue line). Note that the total delay range in this case is ≈100 fs due to the larger grazing angle used in the test setup than in the XUV setup. Without the PID-loop for overlap control the horizontal position of the focused IR beam moves 120 μm over the full delay range. With the beam geometry used for the test, this corresponds to a movement of the source point of 75 μm, which is consistent with our raytracing simulations. As discussed in Section III, for a future XUV-XUV pump-probe experiment such a source point movement would be detrimental. The stability of the focus position with the PID-loop was 1.9 μm rms which, for the XUV beamline parameters correspond to a stability better than 0.3 μm rms, which is expected to be more than sufficient for future pump-probe experiments. We note that even when the PID loop is running, there are measurements for which the focal spot position deviates with as much as 10 μm from the nominal position. This is still well within the focal spot size of the IR laser, and the corresponding movement of the focal spot for the XUV beamline parameters would be below 2 μm, and thus below the XUV focal spot size.

Second, a pinhole followed by a photodiode was placed in the IR focus and a field autocorrelation scan was recorded. The pinhole was used to increase the contrast by looking only at a tiny portion of the pattern generated by the two replicas. In fact, a standard field autocorrelation is usually performed in a collinear configuration, and when the delay introduces a π phase shift in the relative phase, a minimum is recorded. In our configuration the two replicas have opposite wavefront tilts which produce a time-smearing that, if integrated over the focus, would reduce the contrast of the measurement. Figure 5(a) shows the measured field autocorrelation trace (blue line) and the predicted one (green line) calculated from the measured spectrum of the few-cycle IR pulse, shown in Fig. 5(b).[20] There is a fair agreement between the two, with a slightly lower oscillation frequency for the calculated trace. This is most likely due to the fact that the spectrum of the laser was measured before the setup and will differ slightly from the spectrum with which the trace was recorded, mainly due to the reflectivity of the anti-reflection coating of the silica plates, but possibly also due to the selection of a

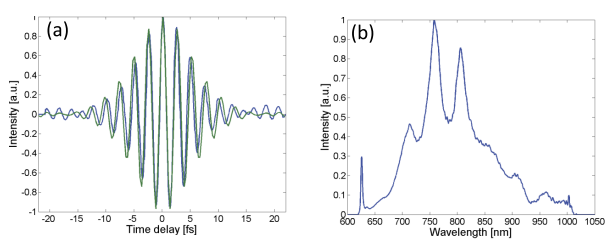

FIG. 5. Field autocorrelation measurement. In panel (a) the measured field autocorrelation trace (blue line) is shown together with the calculated field autocorrelation trace (green line) from the measured spectrum of the few-cycle IR pulse shown in panel (b).

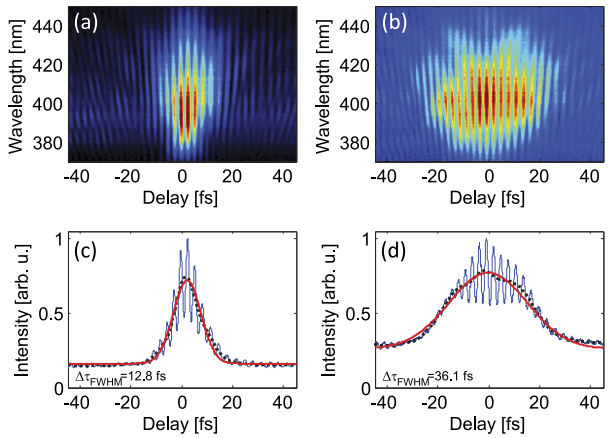

FIG. 6. All-reflective second-order autocorrelation measurement for two different pulse durations, 6.2 fs ((a) and (c)) and 30 fs ((b) and (d)). Panels (a) and (b) show the spectrally resolved measurement and panels (c) and (d) the spectrally integrated signal (blue solid line) and a Gaussian fit (red solid line) to its slowly varying component (black dotted line).

small part of the beam by the pinhole in combination with a small spatial chirp. During the test, the jitter of the PID-loop controlling the delay was estimated to be about 100 mrad rms, corresponding to a delay jitter of 28 as rms. At this point it is worth mentioning that, as discussed above, the actual time resolution obtained in a measurement might be limited by the time-smearing caused by integration over part of the focal plane in combination with the opposite wavefront tilts. If the measurement integrates over the whole focal volume the maximum phase difference will be close to 2π, meaning that the temporal smearing becomes similar to the period of the laser.

After confirming the performance of the feedback scheme, both for the overlap and for the delay, the final test consisted in performing an all-reflective second-order autocorrelation. While a field autocorrelation only contains information about the spectrum of the pulse and no information about the pulse duration, a second-order method allows for extraction of the temporal information. The bandwidth of the pulses used for the tests spans over 300 nm, supporting pulses down to a duration of 5.0 fs. Thus, they are not readily measured by a standard autocorrelation scheme due to intrinsic pulse broadening in the beamsplitter and an all-reflective scheme is necessary. To do this, the pinhole was replaced by a second harmonic generation crystal and a small beam stop was placed in the center of the beam after the crystal for suppressing the intensity autocorrelation component that is preferentially emitted in the forward direction, thus increasing the contrast of the measurement. The signal was then recorded using a fiber-coupled spectrometer for two different pulse durations, and the result is shown in Fig. 6. In Figs. 6(a) and 6(c), the pulses are fully compressed to a duration of 6.2 fs, measured using the d-scan technique,[21] and in Figs. 6(b) and 6(d) the pulse was stretched by material dispersion to a pulse duration of 30 fs. Figs. 6(a) and 6(b) show the spectrally resolved measurement and Figs. 6(c) and 6(d) the spectrally integrated signal.

The traces resemble typical interferometric autocorrelation results but the available scan range is too short compared to the pulse duration to apply a pulse reconstruction algorithm like frequency-resolved optical gating (FROG).[22] We note that the contrast is lower than the 8:1 contrast expected from a collinear second-order interferometric autocorrelation. This is expected since the opposite wavefront tilt of the two replicas, caused by the use of wavefront rather than amplitude division, causes a temporal smearing as the measurement is integrated over the whole focal plane.[23] A low pass frequency filter was applied to the spectrally integrated signal in order to extract the slowly varying signal component. Gaussian fits to this component and deconvolution assuming Gaussian pulse shapes yield pulse durations of 9.1 fs and 25.5 fs for the short and long pulse, respectively, which is in fair agreement with the known pulse durations of 6.2 fs and 30 fs. A possible explanation for the deviation is a narrowing of the bandwidth in the second-harmonic conversion process, which would cause a close to transform-limited pulse to stretch, and a chirped pulse to shorten. In addition, from the Gaussian fits it is clear that, at least the stretched pulse, is not well approximated by a Gaussian.

V. CONCLUSION AND OUTLOOK

In conclusion, we have reported on the design of an all-reflective, grazing incidence, split-and-delay unit for the creation of two time-delayed replicas of an incident XUV pulse. The device has a high broadband throughput, larger than 50% for photon energies up to 70 eV, using a single reflection and combining its function with attenuation of remaining IR light from the HHG process. The device uses two optical feedback loops to maintain spatial overlap and to reach a precise time-resolution. The device was tested using a broadband few-cycle IR laser to perform all-reflective

autocorrelation measurements, demonstrating a delay-jitter below 30 as rms and a spatial overlap stability below 0.3 μm rms. In the near future, the device will be incorporated in our high-intensity HHG beamline with the aim to perform XUV-XUV pump-probe experiments studying attosecond dynamics in atomic and molecular systems.

ACKNOWLEDGMENTS

This research was supported by the Swedish Research Council, the Swedish Foundation for Strategic Research, the Knut and Alice Wallenberg Foundation, the European COST Action CM1204 XLIC, and the European Research Council (PALP). This project has received funding from the European Union's Horizon 2020 research and innovation programme under the Marie Sklodowska-Curie Grant Agreement No. 641789 MEDEA.

[1]L. S. Cederbaum and J. Zobeley, Chem. Phys. Lett. **307**, 205 (1999).
[2]F. Remacle and R. D. Levine, Proc. Natl. Acad. Sci. U. S. A. **103**, 6793 (2006).
[3]F. Calegari, D. Ayuso, A. Trabattoni, L. Belshaw, S. De Camillis, S. Anumula, F. Frassetto, L. Poletto, A. Palacios, P. Decleva, J. B. Greenwood, F. Martin, and M. Nisoli, Science **346**, 336 (2014).
[4]Y. H. Jiang, A. Rudenko, O. Herrwerth, L. Foucar, M. Kurka, K. U. Kühnel, M. Lezius, M. F. Kling, J. van Tilborg, A. Belkacem, K. Ueda, S. Düsterer, R. Treusch, C. D. Schröter, R. Moshammer, and J. Ullrich, Phys. Rev. Lett. **105**, 263002 (2010).
[5]M. Ferray, A. L'Huillier, X. F. Li, L. A. Lompre, G. Mainfray, and C. Manus, J. Phys. B **21**, L31 (1988).
[6]P. Agostini and L. F. DiMauro, Rep. Prog. Phys. **67**, 813 (2004).
[7]N. Berrah, B. Langer, J. Bozek, T. Gorczyca, O. Hemmers, D. W. Lindle, and O. Toader, J. Phys. B **29**, 5351 (1996).
[8]A. Sorokin, M. Wellhöfer, S. Bobashev, K. Tiedtke, and M. Richter, Phys. Rev. A **75**, 051402 (2007).
[9]R. Moshammer, Y. H. Jiang, L. Foucar, A. Rudenko, T. Ergler, C. D. Schröter, S. Lüdemann, K. Zrost, D. Fischer, J. Titze, T. Jahnke, M. Schöffler, T. Weber, R. Dörner, T. J. M. Zouros, A. Dorn, T. Ferger, K. U. Kühnel, S. Düsterer, R. Treusch, P. Radcliffe, E. Plönjes, and J. Ullrich, Phys. Rev. Lett. **98**, 203001 (2007).
[10]N. A. Papadogiannis, L. A. A. Nikolopoulos, D. Charalambidis, G. D. Tsakiris, P. Tzallas, and K. Witte, Phys. Rev. Lett. **90**, 133902 (2003).
[11]E. Takahashi, Y. Nabekawa, and K. Midorikawa, Opt. Lett. **27**, 1920 (2002).
[12]P. Rudawski, C. M. Heyl, F. Brizuela, J. Schwenke, A. Persson, E. Mansten, R. Rakowski, L. Rading, F. Campi, B. Kim, P. Johnsson, and A. L'Huillier, Rev. Sci. Instrum. **84**, 073103 (2013).
[13]B. Manschwetus, L. Rading, F. Campi, S. Maclot, H. Coudert-Alteirac, J. Lahl, H. Wikmark, P. Rudawski, C. M. Heyl, B. Farkas, T. Mohamed, A. L'Huillier, and P. Johnsson, "Two-photon double ionization of neon using an intense attosecond pulse train" (unpublished).
[14]P. Tzallas, D. Charalambidis, N. A. Papadogiannis, K. Witte, and G. D. Tsakiris, Nature **426**, 267 (2003).
[15]Y. Nabekawa, H. Hasegawa, E. J. Takahashi, and K. Midorikawa, Phys. Rev. Lett. **94**, 043001 (2005).
[16]E. J. Takahashi, P. Lan, O. D. Mücke, Y. Nabekawa, and K. Midorikawa, Nat. Commun. **4**, 2691 (2013).
[17]P. Tzallas, E. Skantzakis, L. Nikolopoulos, G. Tsakiris, and D. Charalambidis, Nat. Phys. **7**, 781 (2011).
[18]F. Frassetto, A. Trabattoni, S. Anumula, G. Sansone, F. Calegari, M. Nisoli, and L. Poletto, Rev. Sci. Instrum. **85**, 103115 (2014).
[19]K. R. Ferguson, M. Bucher, J. D. Bozek, S. Carron, J.-C. Castagna, R. Coffee, I. Curiel, M. Holmes, J. Krzywinski, M. Messerschmidt, M. Minitti, A. Mitra, S. Moeller, P. Noonan, T. Osipov, S. Schorb, M. Swiggers, A. Wallace, J. Yina, and C. Bostedt, J. Synchrotron Radiat. **22**, 492 (2015).
[20]Due to the short temporal range of the autocorrelation scan, the acquired trace does not allow for a reconstruction of the spectrum.
[21]M. Miranda, C. L. Arnold, T. Fordell, F. Silva, B. Alonso, R. Weigand, A. L'Huillier, and H. Crespo, Opt. Express **20**, 18732 (2012).
[22]R. Trebino, K. W. DeLong, D. N. Fittinghoff, J. Sweetser, M. A. Krumbügel, and B. Richman, Rev. Sci. Instrum. **68**, 1 (1997).
[23]P. Tzallas, D. Charalambidis, N. A. Papadogiannis, K. Witte, and G. D. Tsakiris, J. Mod. Opt. **52**, 321 (2005).

Paper V

Compression of TW class laser pulses in a planar hollow waveguide for applications in strong-field physics

A. Jarnac, F. Brizuela, C. M. Heyl, P. Rudawski, F. Campi, B. Kim, L. Rading, P. Johnsson, A. Mysyrowicz, A. L'Huillier, A. Houard, and C. L. Arnold.

Optica **93**, 061402 (2015).

Eur. Phys. J. D (2014) 68: 373
DOI: 10.1140/epjd/e2014-50558-7

THE EUROPEAN PHYSICAL JOURNAL D

Regular Article

Compression of TW class laser pulses in a planar hollow waveguide for applications in strong-field physics*

Amélie Jarnac[2], Fernando Brizuela[1], Christoph M. Heyl[1], Piotr Rudawski[1], Filippo Campi[1], Byunghoon Kim[1], Linnea Rading[1], Per Johnsson[1], André Mysyrowicz[2], Anne L'Huillier[1], Aurélien Houard[2], and Cord L. Arnold[1,a]

[1] Department of Physics, Lund University, P.O. Box 118, 22100 Lund, Sweden
[2] Laboratoire d'Optique Appliquée, ENSTA Paristech, École Polytechnique, CNRS, 91762 Palaiseau, France

Received 28 July 2014 / Received in final form 21 August 2014
Published online 16 December 2014

Abstract. We demonstrate pulse post-compression of a TW class chirped pulse amplification laser employing a gas-filled planar hollow waveguide. A waveguide throughput of 80% is achieved for 50 mJ input pulse energy. Good focusability is found and after compression with chirped mirrors a pulse duration of sub-15 fs is measured in the beam center. Whereas a total energy efficiency of ≈70% should be achievable, our post-compressor currently delivers 20 mJ output pulse energy (≈40% efficiency), mostly limited by apertures of chirped mirrors and vacuum windows. The viability of the planar hollow waveguide compression scheme for applications in strong-field physics is demonstrated by generating high-order harmonics in a pulsed Ar gas cell.

1 Introduction

Few-cycle laser pulses, i.e. pulses so short that the pulse envelope encloses only a few cycles of the field, have become indispensable tools in optics and related sciences, such as High-order Harmonic Generation (HHG) [1], attosecond science [2], strong-field physics [3], and acceleration of particles [4]. While low-energy, few-cycle pulses can today routinely be obtained from Titanium:Sapphire (Ti:Saph) based ultrafast oscillators [5], the output of chirped pulse amplification (CPA) femtosecond lasers hardly reaches below 20 fs pulse duration, mostly due to gain-bandwidth-narrowing. Typical Ti:Saph based CPA lasers, found in research laboratories today, have pulse duration in the range of 25–100 fs and pulse energies in the mJ to hundreds of mJ range. Common pulse post-compression techniques can hardly handle more than 10 mJ input pulse energy. Thus, there is a strong need for post-compression of energetic laser pulses.

The two most prominent schemes for pulse compression to the few-cycle regime are based on strong spectral broadening due to nonlinear propagation in either a noble gas filled hollow capillary [6] or in a self-guided filament [7] and subsequent compression with chirped mirrors. Due to ionization inside the capillary and nonlinear coupling to higher order capillary modes with stronger attenuation the output pulse energy of a hollow capillary compressor rarely exceeds a few mJ. Attempts to increase the energy output require advanced optical [8] or capillary engineering [9,10], and may exhibit low efficiency [11].

The other scheme uses self-guiding in a laser filament, which forms as consequence of a dynamic equilibrium between self-focusing and plasma defocusing [12]. In certain conditions saturation of the Kerr-nonlinearity was suggested as an alternative effect to stabilize the filament [13]. Post-compression via filamentation in practice is limited to output pulse energies of about 1 mJ, mainly due to the onset of multiple filamentation, spatial chirp, and angular dispersion [14,15]. Hence, only the center of the output beam is spectrally homogeneous and can be recompressed to a few-cycle pulse.

As alternative to hollow capillaries and filamentation, self-compression in the relativistic self-focusing regime has been suggested and demonstrated [16,17]. Whereas this approach might work even up to the PW power level, the energy efficiency usually is around 20% [18].

A scheme that potentially scales to high pulse energy much more favorably than hollow capillaries and filamentation was proposed by Nurhuda et al. [19]. By use of gas-filled planar hollow waveguides for post-compression, the pulse energy can easily be up-scaled by increasing the beam size in one spatial direction, while keeping the intensity inside the waveguide at levels benefiting efficient self-phase modulation, but limiting ionization. In the first experimental realization it was recognized that modulational instability due to one-dimensional, small-scale self-focusing along the unguided waveguide direction could result in strong deterioration of the transverse beam profile

* Contribution to the Topical Issue "X-ray Generation from Ultrafast Lasers", edited by Germán J. de Valcárcel, Luis Roso and Amelle Zaïr.

[a] e-mail: cord.arnold@fysik.lth.se

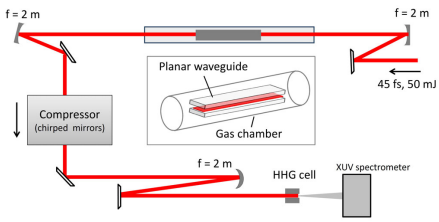

Fig. 1. Sketch of the experimental setup.

and in the extreme to break-up of the beam into several filaments [20]. Shortly after, some of the authors of this publication showed that by carefully controlling experimental parameters, such as gas pressure and waveguide length, a balance between spectral broadening and beam deterioration can be achieved and demonstrated compressed pulses at the 10 mJ level with good focusability [21,22]. Furthermore, a theoretical model describing a stability regime for energy up-scaling of the planar hollow waveguide compression scheme was introduced [23]. The results from these early experiments were summarized in an article [24], which discusses in detail how the detrimental transverse dynamics inside the waveguide can be balanced in order to support energies exceeding the current limitations in pulse post-compression with hollow capillaries and filamentation.

In the current work, we present pulse post-compression of a TW class CPA laser in a gas-filled planar hollow waveguide with up to 50 mJ input pulse energy. While the waveguide throughput can be as high as 80%, the total efficiency of the compression setup currently is ≈40% (20 mJ), mainly limited by the apertures of chirped mirrors and vacuum windows. The compressed pulses are characterized in terms of beam profile, focusability, and pulse duration. We demonstrate the suitability of such pulses for applications in high-field physics by performing HHG in a pulsed Ar gas cell. The harmonic cut-off is significantly increased compared to that obtained with longer driving pulses.

2 Experiments and discussion

2.1 Setup

The experimental setup is sketched in Figure 1. Pulses of up to 50 mJ pulse energy at 10 Hz repetition rate and duration of 45 fs, centered around 800 nm are focused with a cylindrical focusing mirror ($f = 2$ m) onto the input of the planar hollow waveguide. The pulse energy can be adjusted by a $\lambda/2$-plate and a polarizer installed before the grating compressor of the CPA chain. The beam size before focusing is ≈25 mm (FWHM). The waveguide consists of two parallel, highly polished glass slabs (Plan Optik) made of Borofloat with dimensions $500 \times 40 \times 10$ mm^3 with a gap of $2a = 127$ μm between them. A homogeneous gap size is achieved by putting narrow spacers, made of a polycarbonate foil (Precision Brand), along the long sides of the waveguide. This reduces the usable transverse aperture to ≈36 mm. The size of the gap is matched to the width of the line-shaped laser focus at the waveguide entrance $w_y \approx 0.735a$, where w_y is the Gaussian beam size ($1/e^2$); this condition facilitates maximum coupling efficiency into the fundamental waveguide mode. We make the arbitrary choice in the following to call the unguided (free) waveguide dimension the x-direction and the guided the y-direction. The waveguide is located inside a gas cell with thin (2.2 mm), broadband anti-reflection coated fused silica windows at both ends. The gas cell is approximately 3 m long in order to minimize detrimental nonlinear interaction with the windows. After the gas cell, the output beam of the waveguide is collimated with an identical cylindrical mirror and passed through a chirped mirror compressor. The beam is then sent to a HHG setup and harmonic spectra are recorded with a flat-field, XUV photon spectrometer [25].

The gas cell, in which the waveguide is located, can be filled with Ar at pressures up to one atmosphere. The waveguide throughput is higher than 80% in vacuum (86% in theory), proving good coupling to the fundamental mode. It does not decrease up to 400 mbar of Ar, indicating that losses due to ionization and nonlinear coupling to higher order modes are small. Beyond 500 mbar the transverse mode breaks up into a number of filaments, unusable for pulse compression. At the same time, the throughput drops, indicating increased losses due to stronger nonlinear propagation effects and stronger ionization.

2.2 Spectral broadening, beam profile, and focusability

Figure 2a shows the spectra observed at the input and output of the waveguide for pulse energy of 50 mJ in vacuum, at 200, and 400 mbar of Ar. For the evacuated gas cell, the spectrum slightly broadens, probably due to residual parasitic nonlinear interaction with the windows. When the gas cell is filled with 400 mbar of Ar, an about four-fold increase of the spectral width is observed with the spectral wings spanning from 700 to 900 nm. The broadening is only slightly blue-shifted, identifying self-phase modulation as the main source of spectral broadening with only small contribution from plasma related blue-shifting [26]. The spectrum obtained at 400 mbar supports a transform-limited pulse duration of 13 fs. The spectra were measured at the center of the output beam. It should be noted that along the unguided waveguide direction, spectral broadening is strongest at the beam center and weaker at the wings. Inhomogeneous spectral broadening leads to different transverse pulse duration after compression, with the shortest pulse obtained at the beam center and longer pulse duration at the wings. This effect was investigated in detail in reference [24].

Transverse beam profile and focusability are important criteria for pulse compression in planar hollow waveguides. If the waveguide output is not focusable to a small spot size, pulse post-compression will not result in an increase of the peak intensity. As was discussed in detail in reference [24], the focusability in the non-guided

Eur. Phys. J. D (2014) 68: 373

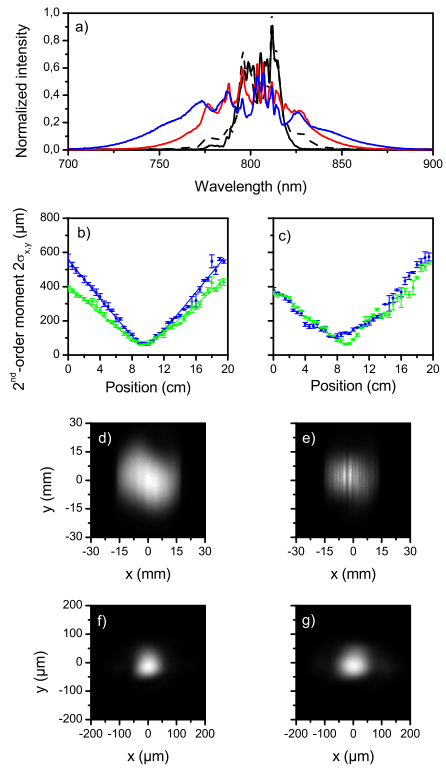

Fig. 2. (a) Spectra observed at the waveguide input (solid black) and output (dashed black) for vacuum and for 200 (red) and 400 mbar (blue) of Ar. (b) and (c) Focusability of the guided (green) and free (blue) waveguide directions, illustrated in terms of beam caustics for the waveguide under vacuum (b) and 400 mbar of Ar (c). M^2-fits are plotted in (b). The far-field output mode from the waveguide and the near-field focal spot after focusing with a $f = 2$ m lens are shown for the case of vacuum in panels (d) and (f) and for 400 mbar of Ar in panels (e) and (g).

waveguide direction inevitably diminishes; first, due to the transversely inhomogeneous spectrum and second, due to a pulse front deformation resulting from the beam center propagating slower (due to the Kerr-effect) than the wings. The second effect essentially introduces an astigmatism (to first-order approximation), which however can easily be compensated by translating the collimating cylindrical mirror [24]. Finally, modulational instability from one-dimensional self-focusing deteriorates the mode along the unguided waveguide direction.

The far-field output modes, recorded with a camera at the position of the collimating cylindrical mirror, are shown in Figures 2d and 2e for vacuum and 400 mbar of Ar, respectively. A modulation along the unguided waveguide direction is evident for the latter case (Fig. 2e). With increasing pressure of Ar the transverse mode further deteriorates and finally breaks up into a number of filaments at ≈500 mbar, unusable for pulse compression. As self-phase modulation and self-focusing are the spectral and spatial manifestations of the Kerr-nonlinearity, transverse beam break-up ultimately limits the maximum spectral broadening and thus the shortest achievable compressed pulse duration [24]. Modulational instability in principle results from noise, but in practice starts from small imperfections in the transverse beam profile. To delay the onset of break-up, the laser beam profile was spatially filtered before the grating compressor of our CPA chain. The sharp cuts at the sides of far-field output modes along the unguided waveguide direction (Figs. 2d and 2e) originate from clipping of the input beam at the waveguide spacers.

The focusability is investigated by focusing the beam, after careful attenuation with reflections from uncoated wedges, with a thin lens ($f = 2$ m) onto the chip of a CCD camera. The camera is moved along the optical axis to record the focal spot in the vicinity of the geometrical focus. The beam size is extracted from the images by computing second order moments $\sigma_{x,y}$. For Gaussian beams $2\sigma_{x,y} = w_{x,y}$, where $w_{x,y}$ is the Gaussian beam radius ($1/e^2$). Figures 2b and 2c show the beam size $2\sigma_{x,y}$ as a function of position for the guided and the free waveguide directions for the evacuated waveguide (b) and filled with 400 mbar of Ar (c). Indeed, the beam sizes obtained by moment theory are very close to those resulting from fitting a Gaussian profile (not shown), indicating that the focal spot is single-peaked and close to Gaussian shape. The focusability in terms of a M^2-parameter is obtained by fitting a parabola to the beam caustic (beam size vs. propagation distance) [27]. For the case of vacuum, $M_y^2 \approx 1.28$ and $M_x^2 \approx 1.32$ in the guided and free waveguide directions are obtained, respectively. For a filling pressure of 400 mbar of Ar, the focusability in the guided direction remains approximately unchanged, while in the free direction the minimum beam size increases by a factor of ≈1.6. At the same time, the focal position moves towards the lens, exhibiting a slight astigmatism, which however is easily removed by moving the collimation mirror [24]. The near-field focal spots for vacuum and 400 mbar are shown in Figures 2f and 2g, respectively. It can clearly be observed that the beam size remains approximately the same in the guided direction, while it increases slightly in the free waveguide direction. It is interesting to note that the transverse mode structure in the far-field (Fig. 2e) does not reduce the focusable intensity significantly, as was shown in reference [24].

2.3 Pulse duration measurement

The waveguide output is compressed using chirped mirrors from Layertec and Venteon, respectively.

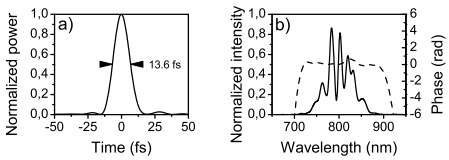

Fig. 3. Temporal pulse profile (a) and spectral intensity and phase (b) obtained from SPIDER measurement.

While ≈40 mJ pulses are obtained at the output of the waveguide (50 mJ at the input), the compressed pulse energy available for experiments is ≈20 mJ. The losses are mostly due to clipping at the limited apertures of vacuum windows and chirped mirrors. The compressed pulses are characterized with a commercial, few-cycle SPIDER (Venteon). Dispersion can be fine-tuned by transmitting the beam through a pair of anti-reflection coated fused silica wedges. Note that the wedges can only be put after strongly attenuating the beam, otherwise filaments form inside. Thus, for actual experiments with the waveguide output, dispersion has to be coarsely adjusted by the number of bounces from the chirped mirrors without fine dispersion control.

Figure 3 shows a SPIDER measurement in optimized conditions for 50 mJ pulse energy at the waveguide input and 400 mbar of Ar. Individual measurements exhibit a large spread in retrieved pulse duration due to shot-to-shot pulse energy fluctuations, typical for low repetition rate TW class lasers. We performed ten SPIDER measurements, with retrieved duration spreading from 13.4 fs to 17 fs; the average pulse duration was 14.3 fs. The retrieved spectral phase (Fig. 3b) is reasonably flat, indicating that the chirped mirror compressor is well suited to compress the waveguide output. The pulse duration was measured in the center of the beam. Due to less spectral broadening, the compressed pulse duration becomes longer towards the edges of the waveguide. It was shown before, both experimentally and numerically, that for a Gaussian transverse beam profile, about 70% of the compressed pulse energy falls within a pulse duration interval of 1.5 times the center pulse duration [24]. By translating the conclusions from [24] to our current data, we can estimate that the 20 mJ pulses available for experiments have an average pulse duration of ≈22 fs. By clipping the beam along the free direction, one can select shorter pulses with lower energy, e.g. ≈14 mJ with an average pulse duration of ≈17 fs.

2.4 High-order harmonic generation

After having demonstrated strong spectral broadening, high throughput, good focusability, and sub-15 fs center pulse duration, we used the compressed pulses to drive high-order harmonic generation. In particular, we compared the generated XUV spectrum with the one obtained with longer pulses, circumventing the planar hollow waveguide compressor, in similar conditions. HHG requires high field intensity (exceeding 10^{14} W cm^{-2}) and thus serves as a sensitive measure to demonstrate that post-compression with a planar hollow waveguide can provide short pulses, good focusability, and high field intensity. HHG essentially is a strong-field effect and is most easily explained by the semi-classical three-step model [28]. The HHG spectrum is comprised of discrete odd-order harmonics of the driving field frequency, whereas the spectral width of individual harmonics decreases with increasing number of half-cycles contributing to harmonic generation. In the single-atom response picture, the highest energy $E_{\max}$ in a HHG spectrum is related to the driving field intensity by the cut-off law $E_{\max} = 3.17U_P + I_P$ [29], where U_P is the ponderomotive energy (average energy of an electron in an AC field with $U_P \propto I_{\max}$), I_P is the ionization potential of the gas, and $I_{\max}$ is the peak intensity of the driving field. In our experimental conditions, the cut-off energy is rather determined by macroscopic phase-matching and propagation effects.

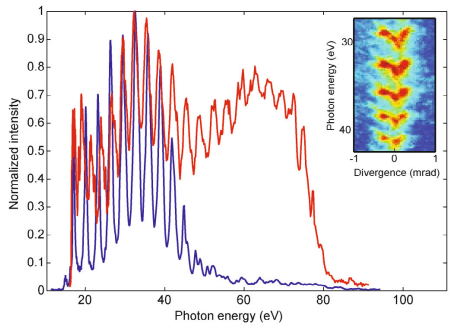

Fig. 4. HHG spectrum in Ar with (red) and without (blue) waveguide compressor at ≈20 mJ pulse energy. The inset shows the spatial shape for a range of harmonics generated from the waveguide compressed pulses.

Strong ionization of the gas medium leads both to reshaping of the fundamental field due to plasma-defocusing as well as to termination of HHG due to plasma-related unfavorable phase-matching conditions. Thus generating with shorter pulses, two main effects should be observed: first, a broadening of the individual harmonics due to fewer half-cycles contributing to the generation process and second, a higher cut-off energy due to higher peak intensity as well as due to plasma-related effects setting in later for shorter pulses.

The compressed waveguide output is loosely focused with a spherical mirror (f = 2 m) into an Ar gas cell. Figure 4 shows HHG spectra obtained in two different situations, using long pulses ≈45 fs, circumventing the waveguide setup (blue), or using the waveguide compressor with 400 mbar of Ar (red). The pulse energy in both cases is ≈20 mJ and the beam sizes before

focusing are comparable. With the waveguide compressor the individual harmonics become broader and the cut-off energy increases, indicating that the pulses are significantly shorter and more intense. Furthermore, the harmonics feature rich transverse spatial structure (see inset), where each of the harmonics exhibits a spectrally asymmetric 'V'-shape with higher central frequency on-axis as compared to the wings. Such behavior is not observed with the long pulses. It might result from blue-shifting of the fundamental on-axis due to high ionization yield [30]. In addition, the transversely varying spectrum and pulse duration of the waveguide output can potentially lead to complicated spatio-temporal couplings in combination with nonlinear propagation and the strongly nonlinear dynamics of the HHG process itself [31]. Although interesting in itself, a detailed interpretation of the particular shape of the harmonics is beyond the scope of this article.

3 Conclusion and outlook

In conclusion, we have demonstrated that planar hollow waveguides can be used to post-compress typical TW CPA lasers, which are currently operated in laboratories around the world. In this work 50 mJ input pulses could be compressed to a center pulse duration of sub-15 fs with a total pulse energy of 20 mJ. The viability of the scheme for applications in strong-field physics was proven by driving high-order harmonic generation with the compressed waveguide output. The total throughput is currently limited by the sizes of chirped mirrors and vacuum windows. A carefully designed chirped mirror compressor should in the future allow for 70% total energy efficiency (waveguide-input-to-compressed-output). Furthermore, considering the transverse variation in compressed pulse duration inherent to the planar hollow waveguide scheme [24], pulse duration shorter than 1.5 times the center pulse duration can be obtained with a total energy efficiency of ≈50%. Although we could not achieve pulse durations significantly below 15 fs, the pulse energy range presented here currently is and most likely will remain not easily accessible with competing compression schemes, such as hollow capillaries or filamentation. Furthermore, the planar hollow waveguide still bears great potential for energy up-scaling.

Up-scaling can most easily be discussed in terms of the B-integral acquired by the beam during nonlinear propagation inside the waveguide,

$$B = \int_{z=0}^{L} k_0 I(z)\, n_2 P z dz \approx k_0 I_0 n_2 P L \qquad (1)$$

where k_0 is the wavenumber at the carrier frequency, I_0 is the intensity at the waveguide input, n_2 is the nonlinear refractive index for Ar at atmospheric pressure, P is the gas pressure in atmospheres, and L is the length of the waveguide. For the current experiment, the B-integral accumulated in the waveguide is $B \approx 8$. While a higher B-integral would lead to stronger spectral broadening, inevitably the transverse beam profile would break into filaments, resulting in an unusable beam. Consequently, energy up-scaling must be achieved, while keeping the B-integral constant. Increasing the beam size in the unguided direction and using larger waveguides provides a trivial way to up-scale the pulse energy. Further control knobs are intensity, pressure, length of the waveguide, and type of gas. The intensity however should be kept below a level of strong ionization ($\approx 7\times10^{13}$ W cm^{-2} in the current experiment) to avoid plasma-related absorption and nonlinear coupling to higher waveguide modes. For Ne and He as filling gases the pulse energy can be increased by factors of ≈3 and ≈5, respectively, while keeping similar relative ionization [32]. The lower nonlinearity (≈7 times for Ne and ≈33 times for He) has to be compensated by higher pressure inside the waveguide. Considering the degrees of freedom sketched above, an up-scaling to input pulse energies in the range of hundreds of mJ seems feasible, offering a possibility to expand the concept of pulse post-compression to lasers with tens of TW peak power.

This research was supported by the European Research Council (ALMA, PALP), the Swedish Research Council, the Crafoord Foundation, the Knut and Alice Wallenberg Foundation, and the Swedish Foundation for Strategic Research. A.J. and A.H. acknowledge support from the French DGA, the European Science Foundation (SILMI), and the European Cooperation in Science and Technology (COST).

References

1. A. L'Huillier, T. Auguste, Ph. Balcou, B. Carre, P. Monot, P. Salieres, C. Altucci, M.B. Gaarde, J. Larsson, E. Mevel, T. Starczewski, S. Svanberg, C.G. Wahlstrom, R. Zerne, K.S. Budil, T. Ditmire, M.D. Perry, J. Nonlinear Opt. Phys. Mater. **4**, 647 (1995)
2. F. Krausz, M. Ivanov, Rev. Mod. Phys. **81**, 163 (2009)
3. T. Brabec, F. Krausz, Rev. Mod. Phys. **72**, 545 (2000)
4. E. Esarey, C.B. Schroeder, W.P. Leemans, Rev. Mod. Phys. **81**, 1229 (2009)
5. S. Rausch, T. Binhammer, A. Harth, E. Schulz, M. Siegel, U. Morgner, Opt. Express **17**, 20282 (2009)
6. M. Nisoli, S. De Silvestri, O. Svelto, R. Szipöcs, K. Ferencz, C. Spielmann, S. Sartania, F. Krausz, Opt. Lett. **22**, 522 (1997)
7. C. Hauri, W. Kornelis, F. Helbing, A. Heinrich, A. Couairon, A. Mysyrowicz, J. Biegert, U. Keller, Appl. Phys. B **79**, 673 (2004)
8. X. Chen, A. Malvache, A. Ricci, A. Jullien, R. Lopez-Martens, Fib. Opt. **21**, 198 (2011)
9. S. Bohman, A. Suda, M. Kaku, M. Nurhuda, T. Kanai, S. Yamaguchi, K. Midorikawa, Opt. Express **16**, 10684 (2008)
10. F. Böhle, M. Kretschmar, A. Jullien, M. Kovacs, M. Miranda, R. Romero, H. Crespo, U. Morgner, P. Simon, R. Lopez-Martens, T. Nagy, Las. Phys. Lett. **11**, 095401 (2014)
11. C. Fourcade Dutin, A. Dubrouil, S. Petit, E. Mével, E. Constant, D. Descamps, Opt. Lett. **35**, 253 (2010)
12. A. Couairon, A. Mysyrowicz, Phys. Rep. **441**, 47 (2007)

13. P. Béjot, E. Hertz, J. Kasparian, B. Lavorel, J.-P. Wolf, O. Faucher, Phys. Rev. Lett. **106**, 243902 (2011)
14. A. Couairon, J. Biegert, C.P. Hauri, W. Kornelis, F.W. Helbing, U. Keller, A. Mysyrowicz, J. Mod. Opt. **53**, 75 (2006)
15. A. Zair, A. Guandalini, F. Schapper, M. Holler, J. Biegert, L. Gallmann, A. Couairon, M. Franco, A. Mysyrowicz, U. Keller, Opt. Express **15**, 5394 (2007)
16. C. Ren, B.J. Duda, R.G. Hemker, W.B. Mori, T. Katsouleas, T. Antonsen, P. Mora, Phys. Rev. E **63**, 026411 (2001)
17. J. Faure, Y. Glinec, J.J. Santos, F. Ewald, J.-P. Rousseau, S. Kiselev, A. Pukhov, T. Hosokai, V. Malka, Phys. Rev. Lett. **95**, 205003 (2005)
18. A. Pipahl, E.A. Anashkina, M. Toncian, T. Toncian, S.A. Skobelev, A.V. Bashinov, A.A. Gonoskov, O. Willi, A.V. Kim, J. Phys.: Conf. Ser. **414**, 012011 (2013)
19. M. Nurhuda, A. Suda, S. Bohman, S. Yamaguchi, K. Midorikawa, Phys. Rev. Lett. **97**, 153902 (2006)
20. J. Chen, A. Suda, E.J. Takahashi, M. Nurhuda, K. Midorikawa, Opt. Lett. **33**, 2992 (2008)
21. S. Akturk, C.L. Arnold, B. Zhou, A. Mysyrowicz, Opt. Lett. **34**, 1462 (2009)
22. S. Chen, A. Jarnac, A. Houard, Y. Liu, C.L. Arnold, B. Zhou, B. Forestier, B. Prade, A. Mysyrowicz, J. Opt. Soc. Am. B **28**, 1009 (2011)
23. C.L. Arnold, S. Akturk, M. Franco, A. Couairon, A. Mysyrowicz, Opt. Express **17**, 11122 (2009)
24. C.L. Arnold, B. Zhou, S. Akturk, S. Chen, A. Couairon, A. Mysyrowicz, N. J. Phys. **12**, 073015 (2010)
25. P. Rudawski, C.M. Heyl, F. Brizuela, J. Schwenke, A. Persson, E. Mansten, R. Rakowski, L. Rading, F. Campi, B. Kim, P. Johnsson, A. L'Huillier, Rev. Sci. Instrum. **84**, 073103 (2013)
26. A. Brodeur, S.L. Chin, Phys. Rev. Lett. **80**, 4406 (1998)
27. A. Siegman, OSA TOPS **17**, 184 (1998)
28. P.B. Corkum, Phys. Rev. Lett. **71**, 1994 (1993)
29. J.L. Krause, K.J. Schafer, K.C. Kulander, Phys. Rev. Lett. **68**, 3535 (1992)
30. M.B. Gaarde, J.L. Tate, K.J. Schafer, J. Phys. B **41**, 132001 (2008)
31. A. Dubrouil, O. Hort, F. Catoire, D. Descamps, S. Petit, E. Mével, V.V. Strelkov, E. Constant, Nat. Commun. **5**, 4637 (2014)
32. A.M. Perelomov, V.S. Popov, M.V. Terent'ev, JETP **23**, 924 (1966)

Paper VI

Gating attosecond pulses in a noncollinear geometry

M. Louisy, C. L. Arnold, M. Miranda, E. W. Larsen, S. N. Bengtsson, D. Kroon, M. Kotur, D. Guenot, L. Rading, P. Rudawski, F. Brizuela, F. Campi, B. Kim, A. Jarnac, A. Houard, J. Mauritsson, P. Johnsson, A. L'Huillier, and C. M. Heyl.

Optica **93**, 061402 (2015).

Letter Vol. 2, No. 6 / June 2015 / Optica 563

optica

Gating attosecond pulses in a noncollinear geometry

M. Louisy,[1,†] C. L. Arnold,[1,†] M. Miranda,[1] E. W. Larsen,[1] S. N. Bengtsson,[1] D. Kroon,[1] M. Kotur,[1] D. Guénot,[1] L. Rading,[1] P. Rudawski,[1] F. Brizuela,[1] F. Campi,[1] B. Kim,[1] A. Jarnac,[2] A. Houard,[2] J. Mauritsson,[1] P. Johnsson,[1] A. L'Huillier,[1] and C. M. Heyl[1,*]

[1]Department of Physics, Lund University, P.O. Box 118, SE-221 00 Lund, Sweden
[2]Laboratoire d'Optique Appliquée, ENSTA Paristech, École Polytechnique, CNRS, FR-91762 Palaiseau, France
*Corresponding author: christoph.heyl@fysik.lth.se

Received 11 February 2015; revised 19 May 2015; accepted 27 May 2015 (Doc. ID 234123); published 17 June 2015

The efficient generation of isolated attosecond pulses (IAPs), giving access to ultrafast electron dynamics in various systems, is a key challenge in attosecond science. IAPs can be produced by confining the extreme ultraviolet emission generated by an intense laser pulse to a single field half-cycle or, as shown recently, by employing angular streaking methods. Here, we experimentally demonstrate the angular streaking of attosecond pulse trains in a noncollinear geometry, leading to the emission of angularly separated IAPs. The noncollinear geometry simplifies the separation of the fundamental laser field and the generated pulses, making this scheme promising for intracavity attosecond pulse generation, thus opening new possibilities for high-repetition-rate attosecond sources.

OCIS codes: (190.2620) Harmonic generation and mixing; (320.7110) Ultrafast nonlinear optics; (260.7200) Ultraviolet, extreme.

http://dx.doi.org/10.1364/OPTICA.2.000563

Table-top sources of coherent extreme ultraviolet (XUV) radiation are nowadays used in many laboratories, delivering pulses with attosecond duration. These sources are based on high-order harmonic generation (HHG), a process that requires intensities of around 10^{14} W/cm^2, thus setting stringent requirements on the driving laser. Ultrashort laser pulses with rather high pulse energy are typically employed, implicitly limiting the repetition rate to a few kilohertz. Many techniques, such as coincidence spectroscopy [1,2], photoelectron spectroscopy on surfaces [3], and time-resolved microscopy [4,5] would, however, benefit greatly from higher repetition rates. A promising route toward multimegahertz attosecond sources relies on HHG inside a passive enhancement cavity [6,7]. In such a scheme, subsequent laser pulses are coherently superimposed, leading to a total power enhancement of two to three orders of magnitude [8]. Although successfully demonstrated for attosecond pulse trains [6,7,9–11], the generation of isolated attosecond pulses (IAPs) inside a cavity remains an unsolved challenge, limited mainly by dispersion management [12,13] and outcoupling problems [14]. Traditional IAP gating concepts [15,16] usually imply severe manipulations of the laser field and cannot easily be brought in line with passive enhancement cavities. Especially dispersion control increases in complexity if shorter pulses and IAP gating schemes are considered. Recent attempts are however pointing towards intracavity gating and improved outcoupling [11,17].

We recently proposed a new gating concept for IAPs [18], noncollinear optical gating (NOG), which has the potential to facilitate intracavity gating and efficient outcoupling at once. Similar to the attosecond lighthouse [19], NOG employs angular streaking [20] and combines this concept with noncollinear HHG, proposed [21,22] as an outcoupling method for intracavity HHG. The noncollinear generation of several angularly separated synchronized IAPs includes the functionality of an all-optical broadband XUV beam splitter, offering new possibilities for IAP–pump–IAP–probe experiments [23,24] where the low photon flux of today's IAP sources is a severe limitation. Moreover, NOG can simplify the separation of the generated IAPs from the driving field, thus reducing XUV photon flux losses.

In this Letter, we provide, to the best of our knowledge, first experimental evidence that angular streaking of attosecond pulse trains can be realized in a noncollinear geometry (Fig. 1). We demonstrate a time-to-angle mapping of attosecond pulse trains, which leads to the emission of angularly separated spectral XUV continua, indicating the generation of several IAPs. We further investigate how the time-to-angle mapping process depends on the time delay between the driving laser pulses and on their carrier envelope phase (CEP), allowing us to control the number and emission direction of the generated XUV pulses.

Noncollinearly superimposing two identical laser pulses at the position of the geometrical focus results in a transverse intensity grating with a periodicity of $a \approx \lambda/2\gamma$ and a transverse envelope corresponding to the focal spot size (with beam radius w_0) of either pulse. Here λ is the carrier wavelength of the pulses and 2γ denotes a small noncollinear angle. For a sufficiently small γ, such that $a \approx w_0$ (all spatial beam dimensions are specified at $1/e^2$ of the intensity profile), the intensity grating collapses into a single

2334-2536/15/060563-04$15/0$15.00

Letter Vol. 2, No. 6 / June 2015 / Optica 564

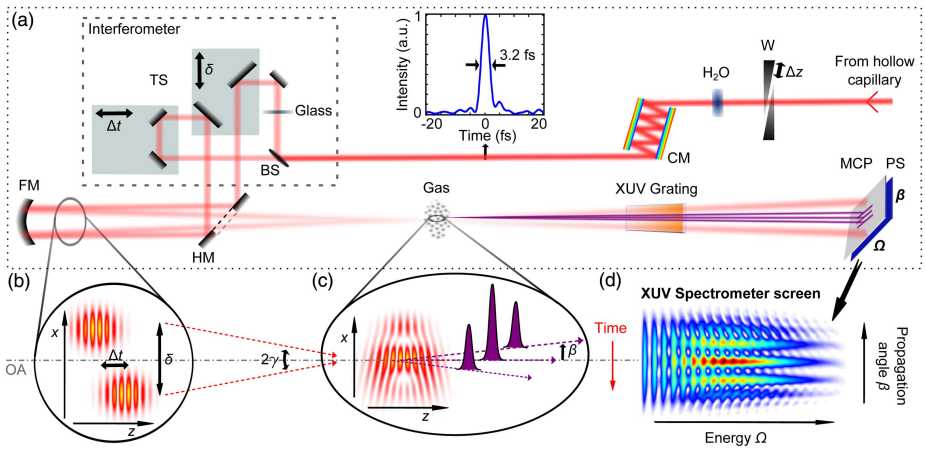

Fig. 1. (a) Schematic of the experimental setup. W, motorized pair of wedges; H_2O, water cell; CM, chirped mirrors; BS, beam splitter; TS, translation stages; HM, holey mirror; FM, focusing mirror ($f = 400$ mm); Gas, argon; MCP, multichannel plate; PS, phosphor screen; OA, optical axis. (b) Illustration of the IR laser pulses in the far-field before focusing ($\Delta t > 0$) and (c) at the position of the gas cell in gating conditions, and (d) of the angularly separated spectral XUV continua (simulation) showing the time-to-angle mapping.

maximum with weak satellites. In the far field (before focusing), this corresponds to a separation of the two beams by $\delta \approx \pi D/2$ (independent of focal length), where D is the diameter of either beam. For two identical pulses being focused noncollinearly with complete temporal overlap into a nonlinear medium, the attosecond pulses generated are emitted along the bisector angle of the two fundamental beams, i.e., the optical axis, the emission direction being defined by the wavefront orientation of the driving field. If a temporal delay (Δt) is introduced, the resulting temporal amplitude variation leads to an ultrafast wavefront rotation. If the rotation is fast enough, the XUV pulses originating from consecutive half-cycles are angularly separated from each other. This results in angularly streaked XUV emission, mapping time into spatial position in the far field. The wavefront orientation angle can be expressed as a function of the amplitude ratio $\xi(t, \Delta t) = \varepsilon_2/\varepsilon_1$ between the two driving field envelopes $\varepsilon_{1,2}$ [18]:

$$\beta(t, \Delta t) = \gamma \frac{1 - \xi(t, \Delta t)}{1 + \xi(t, \Delta t)}. \quad (1)$$

Figure 1 illustrates the experimental setup together with the principle of the gating technique. We use a Ti:sapphire-based chirped pulse amplification laser system, delivering CEP-stabilized pulses with a repetition rate of 1 kHz and energy of up to 5 mJ. Few-cycle pulses, centered around 720 nm, are obtained by post-compression using a hollow capillary in combination with a chirped mirror setup and a water cell [25] (see Supplement 1 for details). A pair of motorized fused silica wedges is used for dispersion fine control, temporal characterization [26], and scanning the CEP of the pulses. A change of 28.9 μm of the thickness of the fused silica corresponds to a CEP slip of π, i.e., we scan the CEP by multiple π without significantly influencing the pulse duration. After post-compression, pulses with duration of $\tau = 3.2$ fs (FWHM, Fourier limit of 2.9 fs) and ~0.5 mJ energy enter an interferometer setup (after passing through an aperture, less than 0.2 mJ per interferometer arm are available for HHG) consisting of a dispersion-balanced beam splitter and two translation stages to spatially (δ) and temporally (Δt) separate the pulses [Fig. 1(a)]. The laser pulses enter vacuum through a thin (0.5 mm) antireflective-coated fused silica window and are focused noncollinearly with a $f = 400$ mm spherical mirror into a pulsed Ar gas cell (length $L_{\text{med}} = 3$ mm). Figure 1(c) illustrates the wavefront rotation obtained at the focus in gating conditions. The XUV pulses are recorded in the far field with a flat-field XUV spectrometer [Fig. 1(d)].

Best gating can be achieved for $\Delta t \approx \tau$ [18], provided the phase delay between the two driving fields is 0 (modulo 2π) at the point of intersection. For the short pulse duration in our experiments, this condition is fulfilled best for $\Delta t \approx \pm T$, where T denotes the field cycle period. In this condition, the pulses overlap partially and the wavefront orientation of the total driving field changes rapidly in time. The attosecond pulse train is thus streaked across the angle sector $[-\gamma, \gamma]$ (with $\gamma = 7.3$ mrad), leading to a wide angular spread of the emitted XUV radiation [Fig. 2(a)]. Spatially, several emission maxima with almost continuous spectral composition are visible, indicating the emission of several IAPs. The angular streaking is illustrated in Fig. 2(b), which displays a simulation of the fundamental field distribution on the optical axis. The temporal field distribution $|\Re[E(t)]|$ is mapped onto the emission angle (giving $|\Re[E(\beta)]|$) via the mapping function $\beta(t)$. $E(\beta)$ is defined via Eq. (1) using the inverse function $t(\beta) = \beta^{-1}(t)$ such that $E(t) = E[t(\beta)]$.

Figure 3(a) displays the XUV spatial far-field profile, integrated over photon energy, as a function of the temporal delay. At delays much larger than the pulse duration, the two laser pulses do not interact, leading to angularly well-separated XUV emission

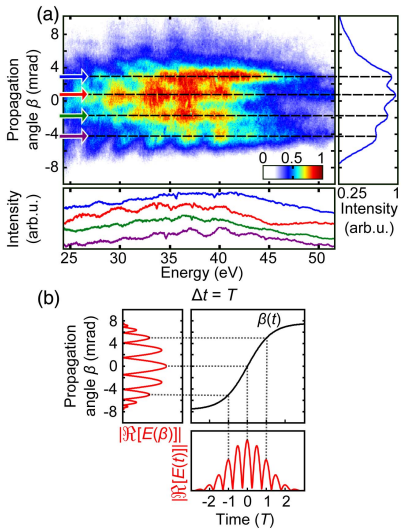

Fig. 2. (a) Measured angularly resolved far-field XUV spectrum in gating conditions ($\Delta t \approx T$). The side panels show the spectrally integrated spatial profile (right) and lineouts (emission angle indicated with arrows in the main panel) of the XUV emission spectra (bottom). (b) Illustration of the time-to-angle mapping of the IR field in gating conditions ($\Delta t = T$) for a CEP of both pulses equal to 0. The bottom panel shows $|\Re[E(t)]|$, the left panel shows the corresponding $|\Re[E(\beta)]|$, and the middle one shows the time-to-angle mapping function $\beta(t)$.

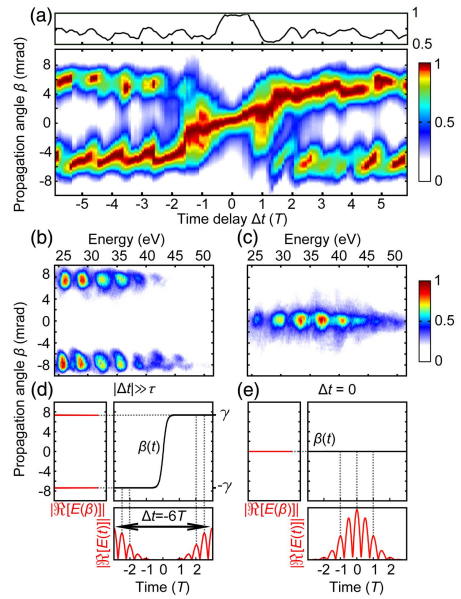

Fig. 3. (a) Measured spectrally integrated (25–50 eV) and at each time delay normalized XUV far-field profile versus time delay Δt. The panel at the top displays the normalization factor. Panels (b) and (c) show measured angularly resolved far-field XUV spectra for $|\Delta t| \gg \tau$ and $\Delta t = 0$, respectively. Panels (d) and (e) show illustrations of the corresponding time-to-angle mapping of the IR field for a CEP of both pulses equal to 0, analogous to Fig. 2(b).

at $\beta = \pm\gamma$ [see Figs. 3(b) and 3(d)]. In this condition, the XUV beams are co-propagating with the fundamental IR fields. The intensity modulations with delay can be explained by a spatial movement of the fundamental intensity grating in the focus [18]. Even for $|\Delta t| \gg \tau$, such modulations are visible, most likely due to the influence of weak temporal satellite pulses. The far-field XUV intensity distribution shows further a distinct asymmetry relative to the optical axis, which is inverted when the delay changes sign. For negative (positive) delays, the fundamental pulse generating the XUV beam in the lower part of the figure ($\beta \leq 0$) comes first (second) [see also Fig. 1(b)]. Because of ionization of the nonlinear medium, XUV generation is less efficient for the second IR pulse. For delays around $\pm T$, i.e., in gating conditions, several spatially separated IAPs are emitted across the angle sector $[-\gamma, \gamma]$ (see Fig. 2). The fundamental beams are still propagating at $-\gamma$ and γ, therefore, the XUV emission around $\beta = 0$ can be spatially separated from the fundamental field. Finally, at complete temporal overlap, the spatial emission profile is confined to a small angle sector around the optical axis [see Figs. 3(c) and 3(e)]. In this case, the amplitude ratio of the two fundamental fields does not change in time ($\beta = 0$).

The angular streaking process is strongly dependent on the CEP of the driving fields. Figure 4 shows the spatially resolved XUV signal integrated over photon energy as a function of CEP. A clear downward shift (toward negative β) of the XUV emission maxima is visible as the CEP decreases. For the experimental scan shown here, the beam splitter in the interferometer was replaced with a D-shaped mirror and the noncollinear angle was reduced, resulting in less divergent emission. In these conditions, fewer attosecond pulses were observed, most likely due to an even better compressed laser pulse. The angular shift of the XUV emission pattern with CEP arises due to the time-to-angle mapping process. A shift of the time of emission induced by changing the CEP of both driving fields results in a corresponding shift of the emission direction. If an aperture is placed on the optical axis and if the CEP is adjusted accordingly, one IAP can be selected.

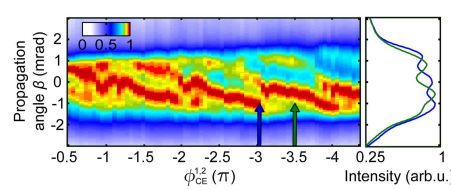

Fig. 4. Spectrally integrated (20–50 eV) spatial XUV far-field profile as a function of CEP (with arbitrary offset) for $\Delta t \approx -T$. In the right panel, two lineouts with a CEP offset of $\pi/2$ are shown. The lineout location is marked in the main panel.

Alternatively, two attosecond pulses can be selected off-axis for attosecond pump–probe experiments [27] if the CEP is changed by $\pi/2$.

Since the CEP strongly affects the gating process, the XUV emission direction becomes a sensitive probe for shot-to-shot CEP fluctuations on-target. In our measurements, the XUV signal was integrated over a few shots. The fluctuations visible in Fig. 4 correspond to a stability of ≈500 mrad (see Supplement 1 for details). The shot-to-shot CEP fluctuations result in a loss of contrast in the recorded spatiospectral patterns [see also Figs. 2(a) and 3(a)]. As predicted by simulations, a residual higher order chirp [see the pulse profile shown in the inset in Fig. 1(a)] can also reduce the contrast or even prevent IAP gating. Because of both effects, individual IAPs appear angularly less separated than predicted theoretically. Numerical simulations show a clear angular separation and thus IAP gating for pulse lengths exceeding 5 fs. A general pulse length limit of approximately four cycles can be derived analytically [18].

In conclusion, we have experimentally demonstrated noncollinear angular streaking of attosecond pulse trains. We have studied the streaking process as a function of temporal pulse separation and CEP, allowing us to control the direction and number of emitted IAPs. NOG does not require major manipulations of the driving laser pulses and allows a direct angular separation of XUV and laser fields. These aspects make NOG a promising candidate for intracavity IAP generation. Note that NOG can even be extended to the tight-focus regime as usually employed for intracavity HHG if γ, L_{med}, and gas pressure p are adjusted accordingly. For a typical intracavity configuration (see, e.g., Ref. [10]) and considering phase-matched generation, the required parameters would reach values in the range of $2\gamma \approx 50$ mrad, $L_{\mathrm{med}} \approx 250$ μm, and p approaching 1 bar [28]. In a cavity, the noncollinear geometry can be achieved by either synchronizing two independent enhancement cavities [29] or designing an enhancement cavity with two circulating pulses [21]. With elaborate dispersion management, such approaches promise IAPs at unprecedented repetition rates and power levels, as well as broadband XUV frequency combs.

†These authors contributed equally to this work.

European Cooperation in Science and Technology (COST) (MP1203); European Research Council (ERC) (111016); European Science Foundation (ESF) (5423); French DGA; Knut och Alice Wallenbergs Stiftelse (Knut and Alice Wallenberg Foundation); Marie Curie ITN (238362); Stiftelsen för Strategisk Forskning (Swedish Foundation for Strategic Research) (FFL09-0078, FFL12-0101); Vetenskapsrådet (Swedish Research Council) (2011-4236, 641-2013-8185, C0394301, C0394601, C0436501, C0675701).

See Supplement 1 for supporting content.

REFERENCES

1. J. Ullrich, R. Moshammer, A. Dorn, R. Dörner, L. Schmidt, and H. Schmidt-Böcking, Rep. Prog. Phys. **66**, 1463 (2003).
2. A. Sandhu, E. Gagnon, R. Santra, V. Sharma, W. Li, P. Ho, P. Ranitovic, C. Cocke, M. Murnane, and H. Kapteyn, Science **322**, 1081 (2008).
3. T. Haarlammert and H. Zacharias, Curr. Opin. Solid State Mater. Sci. **13**, 13 (2009).
4. M. I. Stockman, M. F. Kling, U. Kleineberg, and F. Krausz, Nat. Photonics **1**, 539 (2007).
5. E. Mårsell, C. L. Arnold, E. Lorek, D. Guenot, T. Fordell, M. Miranda, J. Mauritsson, H. Xu, A. L'Huillier, and A. Mikkelsen, Ann. Phys. **525**, 162 (2013).
6. R. Jones, K. Moll, M. Thorpe, and J. Ye, Phys. Rev. Lett. **94**, 193201 (2005).
7. C. Gohle, T. Udem, M. Herrmann, J. Rauschenberger, R. Holzwarth, H. Schuessler, F. Krausz, and T. Hänsch, Nature **436**, 234 (2005).
8. A. Mills, T. Hammond, M. Lam, and D. Jones, J. Phys. B **45**, 142001 (2012).
9. A. Ozawa, J. Rauschenberger, C. Gohle, M. Herrmann, D. Walker, V. Pervak, A. Fernandez, R. Graf, A. Apolonski, R. Holzwarth, F. Krausz, T. Hänsch, and T. Udem, Phys. Rev. Lett. **100**, 253901 (2008).
10. A. Cingöz, D. Yost, T. Allison, A. Ruehl, M. Fermann, I. Hartl, and J. Ye, Nature **482**, 68 (2012).
11. I. Pupeza, S. Holzberger, T. Eidam, H. Carstens, D. Esser, J. Weitenberg, P. Rußbüldt, J. Rauschenberger, J. Limpert, T. Udem, A. Tünnermann, T. Hänsch, A. Apolonski, F. Krausz, and E. Fill, Nat. Photonics **7**, 608 (2013).
12. A. Schliesser, C. Gohle, T. Udem, and T. Hänsch, Opt. Express **14**, 5975 (2006).
13. T. Hammond, A. Mills, and D. Jones, Opt. Express **17**, 8998 (2009).
14. I. Pupeza, E. Fill, and F. Krausz, Opt. Express **19**, 12108 (2011).
15. I. J. Sola, E. Mével, L. Elouga, E. Constant, V. Strelkov, L. Poletto, P. Villoresi, E. Benedetti, J.-P. Caumes, S. Stagira, C. Vozzi, G. Sansone, and M. Nisoli, Nat. Phys. **2**, 319 (2006).
16. F. Ferrari, F. Calegari, M. Lucchini, C. Vozzi, S. Stagira, and G. S. M. Nisoli, Nat. Photonics **4**, 875 (2010).
17. I. Pupeza, M. Högner, J. Weitenberg, S. Holzberger, D. Esser, T. Eidam, J. Limpert, A. Tünnermann, E. Fill, and V. Yakovlev, Phys. Rev. Lett. **112**, 103902 (2014).
18. C. M. Heyl, S. N. Bengtsson, S. Carlström, J. Mauritsson, C. L. Arnold, and A. L'Huillier, New J. Phys. **16**, 052001 (2014).
19. H. Vincenti and F. Quéré, Phys. Rev. Lett. **108**, 113904 (2012).
20. K. Kim, C. Zhang, T. Ruchon, J.-F. Hergott, T. Auguste, D. Villeneuve, P. Corkum, and F. Quéré, Nat. Photonics **7**, 651 (2013).
21. K. Moll, R. Jones, and J. Ye, Opt. Express **14**, 8189 (2006).
22. A. Ozawa, A. Vernaleken, W. Schneider, I. Gotlibovych, T. Udem, and T. Hänsch, Opt. Express **16**, 6233 (2008).
23. P. Tzallas, E. Skantzakis, L. Nikolopoulos, G. Tsakiris, and D. Charalambidis, Nat. Phys. **7**, 781 (2011).
24. E. Takahashi, P. Lan, O. Mücke, Y. Nabekawa, and K. Midorikawa, Nat. Commun. **4**, 2691 (2013).
25. F. Silva, M. Miranda, B. Alonso, J. Rauschenberger, V. Pervak, and H. Crespo, Opt. Express **22**, 10181 (2014).
26. M. Miranda, T. Fordell, C. Arnold, A. L'Huillier, and H. Crespo, Opt. Express **20**, 688 (2012).
27. F. Quéré, H. Vincenti, A. Borot, S. Monchoc, T. Hammond, K. Kim, J. Wheeler, C. Zhang, T. Ruchon, T. Auguste, J. Hergott, D. Villeneuve, P. Corkum, and R. Lopez-Martens, J. Phys. B **47**, 124004 (2014).
28. C. M. Heyl, J. Güdde, A. L'Huillier, and U. Höfer, J. Phys. B **45**, 074020 (2012).
29. C. Benko, T. Allison, A. Cingöz, L. Hua, F. Labaye, D. Yost, and J. Ye, Nat. Photonics **8**, 530 (2014).

Paper VII

Interference in the angular distribution of photoelectrons in superimposed XUV and optical laser fields

S. Düsterer, L. Rading, P. Johnsson, A. Rouzée, A. Hundertmark, M. J. J. Vrakking, P. Radcliffe, M. Meyer, A. K. Kazansky, and N. M. Kabachnik.

J. Phys. B: At., Mol. Opt. Phys. **46**, 164026 (2013).

IOP Publishing Journal of Physics B: Atomic, Molecular and Optical Physics
J. Phys. B: At. Mol. Opt. Phys. **46** (2013) 164026 (6pp) doi:10.1088/0953-4075/46/16/164026

Interference in the angular distribution of photoelectrons in superimposed XUV and optical laser fields

S Düsterer[1], L Rading[2], P Johnsson[2], A Rouzée[3], A Hundertmark[3], M J J Vrakking[3], P Radcliffe[4], M Meyer[4], A K Kazansky[5,6,7] and N M Kabachnik[4,8]

[1] Deutsches Elektronen-Synchrotron (DESY), Notkestrasse 85, D-22603 Hamburg, Germany
[2] Lund University, PO Box 118, SE-221 00 Lund, Sweden
[3] Max Born Institute, Max Born Strasse 2A, D-12489 Berlin, Germany
[4] European XFEL GmbH, Albert-Einstein-Ring 19, D-22761 Hamburg, Germany
[5] Departamento de Fisica de Materiales, University of the Basque Country UPV/EHU, E-20018 San Sebastian/Donostia, Spain
[6] Donostia International Physics Center (DIPC), E-20018 San Sebastian/Donostia, Basque Country, Spain
[7] IKERBASQUE, Basque Foundation for Science, E-48011 Bilbao, Spain
[8] Skobeltsyn Institute of Nuclear Physics, Lomonosov Moscow State University, Moscow 119991, Russia

E-mail: stefan.duesterer@desy.de

Received 14 February 2013, in final form 2 April 2013
Published 13 August 2013
Online at stacks.iop.org/JPhysB/46/164026

Abstract
The angular distribution of photoelectrons ejected during the ionization of Ne atoms by extreme ultraviolet (XUV) free-electron laser radiation in the presence of an intense near infrared (NIR) dressing field was investigated experimentally and theoretically. A highly nonlinear process with absorption and emission of more than ten NIR photons results in the formation of numerous sidebands. The amplitude of the sidebands varies strongly with the emission angle and the angular distribution pattern reveals clear signatures of interferences between the different angular momenta for the outgoing electron in the multi-photon process. As a specific feature, the central photoelectron line is characterized at the highest NIR fields by an angular distribution, which is peaked perpendicularly to both the XUV and NIR polarization directions. Experimental results are reproduced by a theoretical model based on the strong field approximation.

(Some figures may appear in colour only in the online journal)

Free-electron lasers (FELs) operating in the extreme ultraviolet (XUV) and x-ray regimes [1–3], featuring unrivalled high photon fluxes, have rapidly become important tools for investigating matter under extreme conditions [4–6]. These sources allow us to investigate atoms in strong fields with high photon energies. Combining XUV FELs with intense optical laser fields opens up a wide range of laser-assisted photoionization experiments as the control of the relaxation of resonant core hole states in either resonant or a normal Auger decay due to the influence of the optical field [7], or to study the time-resolved relaxation pathways in Auger cascades [8].

Photoelectrons emitted during the many cycles of a strong optical or NIR field experience the quantum nature of the dressing field and can be shifted in energy by an integer number of optical quanta, $\pm\hbar\omega_{\mathrm{NIR}}$. The central photo line is split into a multitude of lines—the so-called sidebands. In the quantum-mechanical picture, the appearance of sidebands is the result of interference between electron waves emitted at different periods of the optical laser pulse [9]. The corresponding experiments provide in this way a unique test ground for studying the fundamental multi-photon processes and for testing the validity of theoretical approaches aiming to describe these nonlinear phenomena.

Sidebands were extensively investigated using high-order harmonic generation (HHG) sources [10] and were proven to be an ideal tool to characterize the HHG emission on both femtosecond (fs) and attosecond timescales [11, 12]. Later, the approach was transferred to FEL experiments, for which, besides the characterization of the source, the nonlinear processes induced by the optical laser could be investigated more clearly. But so far these experiments have been relying mainly on angle-integrated measurements [13, 14]. More information on the photoionization process is obtained by angle-resolved experiments, which have been so far only performed at either low optical intensities with HHG sources (only one sideband) [15, 16] or for low energetic electrons in above-threshold ionization (ATI) [17–22]. In the latter case, the angular distribution of the ejected electrons was reported for the one-colour multi-photon case.

Theoretical studies of the angularly resolved photoelectron spectra in XUV-optical two-colour experiments at high optical intensities also show quantum-mechanical interference structures when more and more photons are involved. This results in oscillations in the angular distribution of the photo- and Auger electrons. The sideband amplitudes for a given emission angle exhibit variations as a function of the photoelectron kinetic energy, the so-called gross structure, due to the interference of electrons emitted within one optical cycle [9, 23–25]. These calculations were performed for ultra-short XUV or x-ray pulses with a duration comparable to the oscillation period of optical light, i.e. a few fs. Recently, the above-mentioned gross structure was experimentally observed in the laser-assisted Auger decay of Ne atoms [26] using x-ray FEL pulses of such short nature. In these experiments, the lifetime of the Auger process was on the timescale of the oscillation period of the optical laser.

In this paper, we report on the angle-resolved observation of sideband formation in the XUV direct photoionization of Ne atoms at high NIR intensities yielding up to ten sidebands. Here, the XUV pulse duration is much longer (∼30 optical cycles) than that discussed in the previous calculations. However, we still observed strong oscillations in the angular distribution as well as in the sideband amplitudes for given angles. In particular, there is a distinct asymmetry comparing the features occurring at the higher energetic side of the initial photoionization line and the corresponding lower energetic one. The oscillatory structures are altered by changing the peak field of the NIR dressing laser, but the interference is still present when the experimental data are integrated over many different intensities. The experimentally observed angular variations can be interpreted as interferences between many outgoing partial waves in the multi-photon ionization. The observations are reproduced by our theoretical model.

The experiments were performed at beam line BL2 of the Free-electron LASer in Hamburg (FLASH) [1]. FLASH was operated at a wavelength of 13.7 nm (90.5 eV) and a bandwidth of less than 1% (<0.9 eV). The pulse duration was ∼ 80 fs and the pulse energy was 30–40 μJ. For the two-colour experiments, we also used the optical laser system at FLASH [27]. The laser also delivered 80 fs pulses at a central wavelength of 800 nm; peak intensities of the order of 10^{13} W cm^{-2} could be reached in the focus. Both XUV and NIR pulses were linearly polarized in the horizontal plane. The optical laser and the FEL pulses were synchronized electronically to each other up to a remaining pulse–pulse jitter of ∼ 0.5 ps (FWHM) [27]. This jitter leads to significant shot-to-shot variations of the effective optical intensity seen by the ionized electrons. Thus, the recording of the electron spectra for each single FEL pulse and the subsequent resorting of the data as described below were essential for the success of the experiment.

In the experimental chamber, the FEL beam and the optical laser were combined using a 45° holey mirror and crossed with a pulsed gas jet. The resulting photoelectrons were detected with a velocity map imaging spectrometer (VMIS) [28]. The VMIS is ideally suited to perform momentum imaging of the charged particles resulting from the ionization by the high-flux FEL as it allows for very high count rates (10^4–10^5 events/shot). The image detected by the VMIS is a 2D projection of the 3D momentum photoelectron distribution in the interaction region, which can be retrieved by an inverse Abel transform [29]. In order to achieve the spatial and temporal overlap between the FEL pulses and the optical pulses, the capabilities of the VMIS setup were used [30].

Neon was used as the target gas and the main ionization channel for the 90.5 eV FEL pulses was Ne $2p^6 \rightarrow$ Ne^+ $2p^5$+ e^- (68.9 eV). The acquired data set consists of 10.000 single-shot images. To be able to study in more detail how the angular distribution changes with the NIR intensity seen by the photoelectrons, the single-shot images were sorted into ten bins depending on the amount of sideband signal, which increases with increasing intensity, compared to the total signal. The effective NIR intensity for each bin was retrieved from the ponderomotive energy shift of the photoelectron lines with respect to the line position without an NIR field [31]. Through an FFT analysis of the photolines, the subpixel resolution could be achieved and shifts in the order of 0.2 eV were found. The sorting resulted in about equidistant intensity windows of 0.8 × 10^{12} W cm^{-2} for each bin. The sample image shown in figure 1 displays the measured raw data of the VMIS with the FEL only as well as the FEL in combination with the strong NIR field (averaged and intensity-binned). The sidebands are separated by only ∼3 pixels, thus demonstrating the resolution capabilities of the VMIS. The inverted, angularly resolved photoelectron spectra of Ne are shown in figure 2 (upper panel) in the presence of a 6×10^{12} W cm^{-2} NIR field.

The experimental spectra bring out several interesting features (figure 2, upper panel). First, for each particular angle, the intensity of the sidebands clearly shows an oscillatory behaviour (gross structure). Furthermore, the low-order sidebands and the central line show strong modulations as a function of the emission angle. Higher order sidebands show less modulations and the angular distribution is peaked towards 0°. Thus, the highly accelerated and decelerated electrons are predominantly emitted along the polarization axis of the optical laser. Finally, the modulations are different for the sidebands of the same order on the high- and low-energy sides of the central peak.

A counter-intuitive result has been obtained for the angular distribution when the intensity of the optical laser is

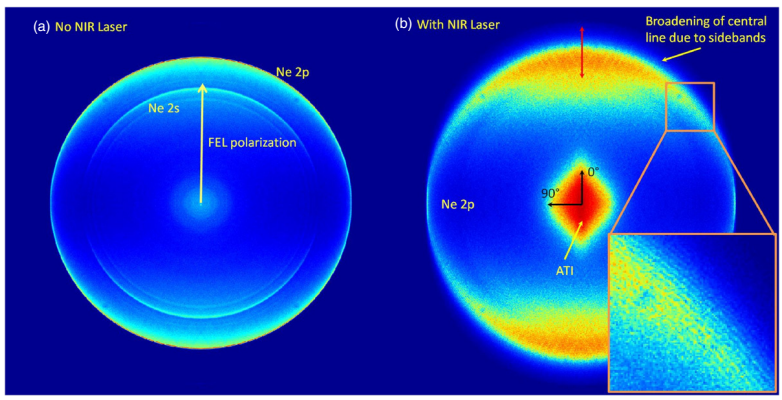

Figure 1. Experimentally recorded VMIS data for the Ne photoionization at 90.5 eV FEL photon energy is shown for the case with only FEL (a) and FEL in the presence of an NIR (800 nm) intensity of $\sim 3 \times 10^{12}$ W cm^{-2} (b). Shown is the angular dependence of the emitted photoelectrons (the polarization direction of FEL and NIR laser is vertical). In (a), the 2p as well as the 2s (inner ring) are clearly visible (the radius represents the electron momentum). In (b), the NIR laser broadens the central line substantially due to sideband formation. Thus, 2p and 2s contributions are not clearly visible anymore. The broadening decreases for larger angles with respect to the polarization until finally at 90°, there is almost no effect of the NIR laser on the photoelectrons. The red double arrow indicates the energy range shown in figure 2. The low kinetic energy feature in the centre results from NIR-generated ATI electrons in the rest gas. The data are binned according to the sideband amplitude (b) and averaged over several hundred single-shot images. The enlarged view of the data (inset) shows that successive sidebands are separated by only ∼3 pixels (corresponding to a separation of 1.5 eV), thus demonstrating the excellent resolution capabilities of the VMIS.

increased. This is illustrated in figure 3 (upper panel) where the angular distribution of the central emission line is displayed. The angular distribution in low NIR fields resembles the well-known dipole-type distribution of the Ne $2p^6 \rightarrow Ne^+2p^5 + e^-$ ionization, which has an emission maximum at 0° and 180° angles corresponding to the emission along the polarization direction of the FEL. In the presence of a stronger optical dressing field, the angular distribution changes dramatically and is characterized by several maxima. In particular, we obtain a distinctly stronger relative contribution to the emission of electrons perpendicular to the polarization of the ionizing radiation until, at the highest NIR intensity, the emission is almost entirely directed away from the polarization of the FEL and optical laser. This is in contrast to the known results for the angular distributions of photoelectrons in the one-colour multi-photon ionization where the photoelectrons are concentrated along the polarization vector of the laser field (see e.g. [32]).

To interpret the experimental results, simulations have been performed using a theoretical approach based on the strong-field approximation, which is described in detail in [9]. Namely, it is supposed that the ionization by the XUV pulse occurs in an 'undressed' free atom, but the emitted photoelectron, propagating from the atom to the detector, interacts with the strong IR field which changes the electron energy and scattering angle. In this approximation, the photoelectron is described by the Volkov wavefunction [33] which contains all partial waves with corresponding field-modified phases. This approach works surprisingly well when the photoelectron energy is sufficiently large (several tens of eV). Its comparison with the much more elaborate method of calculation based on numerically solving the time-dependent Schrödinger equation shows very good agreement [34]. In the present simulation, based on this approach, it is assumed that both the XUV and NIR pulses have fixed amplitudes and shapes. To simulate the temporal jitter of the FEL pulses, the relative position of the envelope maxima (relative delay) of the two pulses has been varied from 0 (maximum overlap) to ± 200 fs (practically no overlap). Naturally, this is a rather rough approximation since the XUV pulse has a very complicated temporal shape which differs from shot to shot. Therefore, one can only expect a qualitative agreement of the simulation with the experiment.

In the calculations presented here (figure 2, lower panel), the XUV and NIR pulse have the same pulse duration as in the experiment (80 fs FWHM). The NIR field has a peak intensity of 6×10^{12} W cm^{-2}. The necessary dipole matrix elements and phases have been calculated within the Hartree–Slater approximation [35, 36], which provides the angular distribution parameter for one-photon absorption and has previously showed good agreement with experiments. The calculated spectra for each particular relative delay of the two pulses have been associated with a certain effective NIR intensity by extracting the ponderomotive shift in the same way as for the experimental spectra.

The theoretical double-differential cross section is shown in figure 2 (lower panel) for the maximum overlap of the two pulses. The comparison with the experimental spectra in figure 2 (upper panel) shows a quite satisfactory agreement. In particular, the simulation also shows a different oscillatory structure for the sidebands of the same order on the high and

J. Phys. B: At. Mol. Opt. Phys. **46** (2013) 164026 S Düsterer *et al*

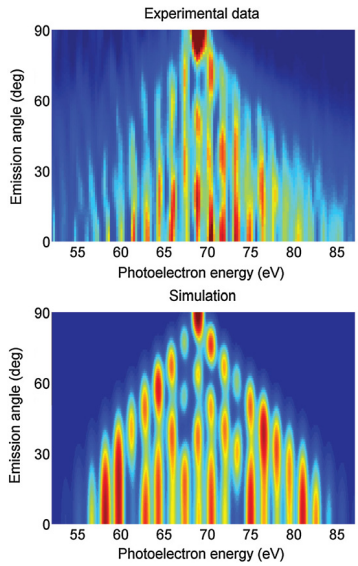

Figure 2. Upper panel: photoelectron angular distribution spectra retrieved from an Abel inversion of the measured 2D projection of the electron momentum distribution for the Ne $2p^6 \rightarrow Ne^+ 2p^5 + e^-$ photoionization at 90.5 eV FEL photon energy in the presence of an NIR (800 nm) intensity of 5–6×10^{12} W cm^{-2}. Shown are the inverted VMIS data. The emission angle is defined with respect to the XUV and the NIR polarization. Lower panel: calculated spectra for the same parameters as used in the experiment.

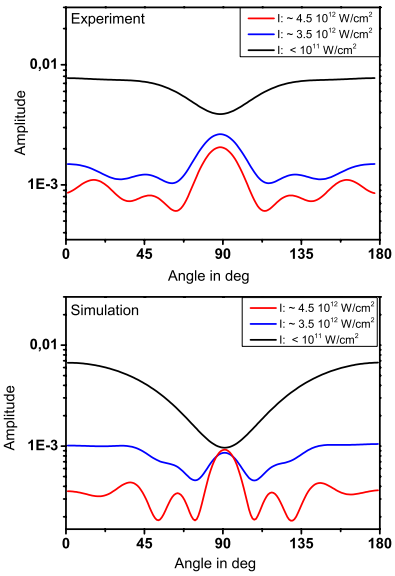

Figure 3. Angular dependence of the central line at a kinetic energy of about 68.9 eV shown for different effective NIR intensities (i.e. different temporal overlap). The experimental values are shown in the upper panel. The lower panel displays the corresponding simulated angular distribution.

low energetic side. This asymmetry between low-energy and high-energy sidebands of the same order might be explained by the additional phase acquired by the electron in the NIR field which is determined by its velocity or wave vector k (see expression (3) for the Volkov phase in [9]). On the other hand, the sidebands are situated on both sides of the central line symmetrically in energy $E_{SB} = E_0 \pm n\,\hbar\omega_{NIR}$. This leads to non-symmetrical values of $k = k_0 \pm \delta k$ and thus to a non-symmetrical Volkov phase which finally determines the intensity of the sidebands.

The number of sidebands decreases with an increase of the emission angle and turns to 0 at 90° (only the central line remains), in agreement with the experimental results. In addition, in both experiment and theory, the angular distribution of the high-order sidebands is concentrated at 0°, i.e. along the polarization vector of both the pulses.

The oscillatory behaviour of the central line at higher NIR intensities (see figure 3) can be, at least qualitatively, explained by our model. At low NIR intensity, when single-photon ionization dominates, the angular distribution has the well-known dipole character. With higher NIR intensity (i.e. better overlap of the pulses), an increasing number of NIR quanta are additionally absorbed and emitted, each quantum bringing in a unit of angular momentum. For the electron to end up in the central line, it has to absorb and emit the same number of NIR photons. Thus, for the photoionization from the Ne 2p ($\ell = 1$) shell, having a maximum angular momentum of $\ell = 2$ in XUV photoionization, the electron in the central line will progressively get maximum angular momenta of $\ell = 4$, $\ell = 6$, etc due to the absorption and emission of more and more NIR photons as the NIR intensity is increased. The oscillatory nature (additional maxima) in the angular distribution can thus be explained by the interference between the partial waves with different ℓ.

The strong maximum at 90° for the central line, at maximum NIR intensity, is also reproduced in the theoretical model (figure 3). Qualitatively, this feature can be explained by the fact that the NIR field, acting on the electrons emitted from the atom at 90°, practically does not change their direction of motion and energy for our experimental conditions. In contrast, the electron yield in the central line emitted at small angles around the FEL polarization axis is substantially depleted and redistributed between sidebands as the intensity of the NIR is increased, resulting in an angular distribution that peaks perpendicular to the laser polarization direction. This maximum at 90° remains the dominant feature also for much higher dressing fields. We note that although there is qualitative agreement between the

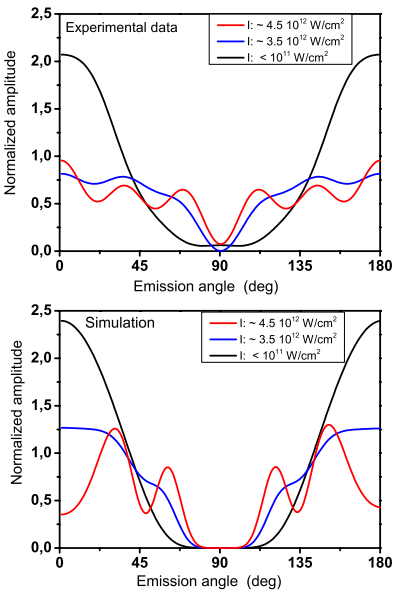

Figure 4. Angular dependence of the (high-energy side) second sideband (electron energy ∼71.9 eV) shown for different effective optical intensities (i.e. different delay times). The experimental results are shown in the upper panel. The lower panel displays the corresponding simulated angular distribution. For better comparison, the curves are normalized on the total amount of signal for the sideband.

experimental and theoretical angular distributions in figure 3, there are nevertheless some discrepancies, which can be explained by the roughness of the modelling, which ignores the variation of the XUV pulse structure from shot to shot, and by the relatively large error that can result from the sorting procedure. Further experiments, including more statistics and better time-resolution should lead to a better agreement.

A quite different angular distribution pattern is observed for the sidebands. In figure 4, the experimental (upper panel) and simulated (lower panel) angular distributions of the second sideband (electron energy ∼71.9 eV) on the high-energy side of the central line are shown for different NIR intensities. The modulation due to the multi-photon character of photo absorption is again clearly present. But in contrast to the central line, the angular distribution of the sideband is characterized by a deep minimum at 90°. The theoretical simulation agrees qualitatively with the experiment and reproduces the minimum and the modulation. The minimum at 90° is again easily explained by the fact that the electrons emitted perpendicular to the NIR field polarization undergo a momentum shift under the influence of the NIR field that is perpendicular to their original momentum, which does not change the absolute magnitude of the momentum very much, i.e. it does not contribute to the formation of sidebands.

For the discussion of experiments using an SASE (self-amplification of spontaneous emission) FEL, the low temporal coherence has to be taken into account. As already experimentally demonstrated in molecular dissociation experiments e.g. [37], the chaotic sub-pulse structure of an SASE FEL pulse shows different experimental signatures as expected from a fully coherent XUV pulse. The sub-pulse width (corresponding to the coherence time) was measured at FLASH by autocorrelation measurements to be within ∼1.6 and ∼8 fs depending on the XUV wavelength [38, 39]. For the parameters of the current experiment, a coherence time of about 3 fs is expected. As shown in [40], the sideband spectrum is also rather sensitive to the degree of temporal coherence of the XUV pulse. A smaller coherence time leads to an increase of the width of each sideband. The acquired sideband spectra are in good agreement with the expectation and support a coherence time >1.5 fs.

In conclusion, we have investigated the angular distribution of photoelectrons from Ne atoms created by XUV FEL radiation in the presence of a strong NIR dressing field using VMIS. Extended sideband structures with clear signatures of interferences in the energy spectra and in the angular distributions were observed, showing evidence of a gross structure. The measured oscillatory structures of the angular distributions of the sidebands as well as the central line are dominated by multi-photon processes in the NIR dressing field, which give rise to the formation of electrons with high angular momenta resulting in the oscillatory structures. Even after averaging over a range of NIR intensities, these structures are still present and demonstrate the universal character of the interference effects. The experimental results are qualitatively explained by the theoretical model based on the strong field approximation.

Acknowledgments

The authors wish to acknowledge the work of the scientific and technical team at FLASH, in particular N Gerasimova for the analysis of the FEL pulse duration by spectral correlations. NMK is grateful to European XFEL for hospitality and financial support. LR and PJ acknowledge the support from the Swedish Research Council and the Swedish Foundation for Strategic Research.

References

[1] Ackermann W *et al* 2007 *Nature Photon.* **1** 336
[2] Emma P *et al* 2010 *Nature Photon.* **4** 641
[3] Ishikawa T *et al* 2012 *Nature Photon.* **6** 540
[4] Sorokin A *et al* 2007 *Phys. Rev. Lett.* **99** 213002
[5] Young L *et al* 2010 *Nature* **466** 56
[6] Rohringer N *et al* 2012 *Nature* **481** 488
[7] Mazza T *et al* 2012 *J. Phys. B: At. Mol. Opt. Phys.* **45** 141001
[8] Krikunova M *et al* 2011 *J. Chem. Phys.* **134** 024313
[9] Kazansky A K, Sazhina I P and Kabachnik N M 2010 *Phys. Rev.* A **82** 033420
[10] Schins J M *et al* 1994 *Phys. Rev. Lett.* **73** 2180
Schins J M *et al* 1995 *Phys. Rev.* A **52** 1272

[11] Mauritsson J *et al* 2004 *Phys. Rev.* A **70** 021801
[12] Paul P M *et al* 2001 *Science* **292** 1689
[13] Meyer M *et al* 2008 *Phys. Rev. Lett.* **101** 193002
[14] Radcliffe P *et al* 2012 *New J. Phys.* **14** 043008
[15] Haber L H, Doughty B and Leone S R 2011 *Phys. Rev.* A **84** 013416
Haber L H, Doughty B and Leone S R 2009 *J. Phys. Chem.* A **113** 13152
[16] Aseyev S A 2003 *Phys. Rev. Lett.* **91** 223902
[17] Rudenko A *et al* 2004 *J. Phys. B: At. Mol. Opt. Phys.* **37** L407
[18] Morishita T *et al* 2007 *Phys. Rev.* A **75** 023407
[19] Kumarappan V *et al* 2008 *Phys. Rev. Lett.* **100** 093006
[20] Marchenko T *et al* 2010 *J. Phys. B: At. Mol. Opt. Phys.* **43** 185001
[21] Arbo D G *et al* 2010 *Phys. Rev.* A **81** 021403
Arbo D G *et al* 2010 *Phys. Rev.* A **82** 043426
[22] Arbo D G *et al* 2011 *Nucl. Instrum. Methods Phys. Res.* B **279** 24
[23] Kazansky A K and Kabachnik N M 2009 *J. Phys. B: At. Mol. Opt. Phys.* **42** 121002
[24] Kazansky A K, Sazhina I P and Kabachnik N M 2009 *J. Phys. B: At. Mol. Opt. Phys.* **42** 245601
[25] Kazansky A K and Kabachnik N M 2010 *J. Phys. B: At. Mol. Opt. Phys.* **43** 035601
[26] Meyer M *et al* 2012 *Phys. Rev. Lett.* **108** 063007
[27] Redlin H *et al* 2011 *Nucl. Instrum. Methods Phys. Res.* A **635** 88
[28] Eppink A T J B and Parker D H 1997 *Rev. Sci. Instrum.* **68** 3477
[29] Vrakking M J J 2001 *Rev. Sci. Instrum.* **72** 4084
[30] Johnsson P *et al* 2010 *Opt. Lett.* **35** 4163
[31] Agostini P *et al* 1979 *Phys. Rev. Lett.* **42** 1127
[32] Bauch S and Bonitz M 2008 *Phys. Rev.* A **78** 043403
[33] Volkov D B 1935 *Z. Phys.* **94** 250
[34] Kazansky A K and Kabachnik N M 2007 *J. Phys. B: At. Mol. Opt. Phys.* **40** 2163
[35] Herman F and Skillman S 1963 *Atomic Structure Calculations* (Englewood Cliffs, NJ: Prentice-Hall)
[36] Kennedy D J and Manson S T 1972 *Phys. Rev.* A **5** 227
[37] Jiang Y H *et al* 2010 *Phys. Rev.* A **82** 041403
[38] Roling S *et al* 2011 *Phys. Rev. Spec. Top. Accel. Beams* **14** 080701
[39] Schlotter W F *et al* 2010 *Opt. Lett.* **35** 372
[40] Kazansky A K, Sazhina I P and Kabachnik N M 2012 *Phys. Rev.* A **86** 033404

Paper VIII

A versatile velocity map ion-electron covariance imaging spectrometer for high intensity XUV experiments

L. Rading, S. Maclot, J. Lahl, F. Campi, H. Wikmark, B. Oostenrijk, M. Gisselbrecht, and P. Johnsson.

Manuscript in preparation.

A Versatile Velocity Map Ion-Electron Covariance Imaging Spectrometer for High Intensity XUV Experiments

L. Rading,[1, a)] S. Maclot,[1] J. Lahl,[1] F. Campi,[1] H. Wikmark,[1] B. Oostenrijk,[1] M. Gisselbrecht,[1] and P. Johnsson[1, b)]

Department of Physics, Lund University, P.O. Box 118, 22100 Lund, Sweden

(Dated: 18 December 2016)

We report on the design and performance of a velocity map imaging (VMI) spectrometer optimized for experiments using high-intensity extreme ultraviolet (XUV) sources such as laser-driven high-order harmonic generation (HHG) sources and free-electron lasers (FELs). Typically exhibiting low repetition rates and high single-shot count rates, such experiments do not easily lend themselves to coincident detection of photoelectrons and -ions and, in order to obtain molecular frame or reaction channel specific information, one has to rely on other correlation techniques, such as covariant detection schemes. Our device allows for combining different photoelectron and -ion detection modes for covariance analysis. We present the expected performance in the different detection modes, and present first results using an intense HHG source as well as synchrotron radiation.

I. INTRODUCTION

During recent years, emerging short pulse high-intensity extreme ultraviolet (XUV) and X-ray sources such as laser-driven high-order harmonic generation (HHG)[1,2] and free-electron lasers (FELs)[3–6] have opened up new fields of science. They have made it possible to study ultrafast dynamics induced and probed with wavelengths in the XUV/X-ray regime on femtosecond (FELs)[7] and even attosecond (HHG)[8] time scales. In addition, the associated high intensities enables the study of hitherto unknown ionization processes[9–12] as well as single shot imaging of molecular structure[13,14]. However, experiments using these sources operate in very different signal rate regimes than traditional laser or synchrotron experiments, and thus there is a large need for adapted detection schemes.

In experiments employing photo-induced ionization or fragmentation the information lies in the energy and angular distribution of the emitted photoelectrons and -ions. One way of getting this information is by means of the application of a reaction microscope (REMI)[15], where the initial three-dimensional momentum of particles is deduced from measurements of the spatial coordinates as well as the flight time by means of e.g. delay-line detectors. REMI gives access to complete, correlated, 3D velocity information of all particles as long as the count rates are sufficiently low ($<$ 1 event/laser shot) to avoid detecting fragments from more than one target atom or molecule on the same shot.

With high-intensity sources, the repetition rates are typically low while the single-shot count rates can be very high, which in many cases makes it difficult to apply REMI techniques. Another approach is to use the so-called velocity map imaging (VMI) technique[16]. VMI uses an extraction field configuration that makes the impact coordinates on the detector independent of the location of the ionization event within the interaction volume, thus allowing for the use of a phosphor screen where the impact of a large number of particles can be accumulated on every shot. Under certain conditions, the initial velocity and angular distribution of the particles can be recovered from the measured two-dimensional projection using numerical inversion procedures[17,18].

An obvious drawback of traditional VMI compared to to REMI is that, due to the high count rates, one can not rely on coincidence detection for extracting information about different electrons or ions coming from the same target molecule. An elegant way to overcome this lack of correlated information in VMI, without sacrificing the high count rates, is to use covariance mapping[19]. Briefly, for any two variables sampled synchronously in a repetitive measurement one can calculate the covariance which is a measure on how well correlated the variation of the two variables is. Covariance mapping has since then successfully been used in several laser and FEL experiments for different detection schemes demonstrating ion-ion, electron-electron, and ion-electron covariance mapping[20]. There are also a few examples where not only the mass or energy but also the momentum of the particles has been studied through so-called covariance imaging[21].

Here we present the design and performance of a double VMI spectrometer (VMIS) for covariance imaging of electrons and ions, optimized for experiments using high-intensity XUV and X-ray sources. The instrument is versatile and allows for combining photoelectron and -ion detection modes, such as ion time-of-flight (TOF), ion VMI and electron VMI, in different ways, depending on the required information and the process under study. The performance for the different detection modes is estimated using simulations, which are finally compared with the first experimental results from an intense HHG source and synchrotron radiation.

In Section II we describe the design of the apparatus based on the requirements, and discuss the motiva-

[a)] E-mail: linnea.rading@fysik.lth.se
[b)] E-mail: per.johnsson@fysik.lth.se

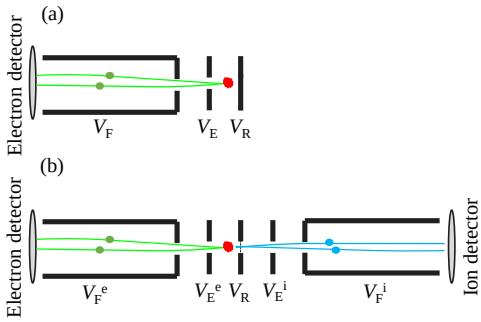

FIG. 1. Sketch of the electrode geometries for a standard VMIS (a), and the double VMIS designed in this work (b). Ionization takes place in between the repeller and electron extractor plate.

tion of the design details such as the electrode design and the mounting that allows floating voltages. Further, we describe the used simulation procedure and present data on the estimated performance in the different operation modes. In Section III we show results from the first measurements with the spectrometer, both at the high-intensity XUV beamline and the Max-lab synchrotron facility in Lund, and compare these with the expected performance. Finally, we conclude in Section IV.

II. APPARATUS

The design of the double VMIS is an extension of the standard VMIS suggested by Eppink and Parker in 1997[16]. The standard VMIS, shown in Fig. 1(a), consists of a repeller plate, an open extractor plate and a field-free flight tube. In the simplest case, where the flight tube is grounded, the ratio between the extractor voltage (V_E) and the repeller voltage (V_R) defines the imaging mode of the VMIS. In the general case, the ratio deciding the imaging mode can be written

$$\eta = \frac{V_E - V_F}{V_R - V_F} \quad (1)$$

where V_F is the voltage applied to the flight tube. By changing η, the curvature of the field in the interaction region is changed, allowing for different imaging modes. Velocity map imaging mode is usually achieved for $\eta \approx 0.75$, with the exact value depending on the specific design geometry. In this mode, electrons (or ions) with the same momentum in the plane parallel to the detection plane will be projected onto the same spot on the detector even if they are generated at different positions in the interaction region. While it is only the projection of the momentum in the plane perpendicular to the detector axis that is imaged, the full three-dimensional momentum distribution can be obtained through inversion procedures, as long as there is an axis of cylindrical symmetry in the ionization process[17,18]. The other mode of operation, often referred to as the spatial imaging mode, is achieved for $\eta \approx 1$. The position on the detector is then most sensitive to where the charged particle is created and therefore an image of the interaction region is achieved. This is a useful mode for alignment purposes, providing a means to ensure precise positioning of the laser focal spot, as well as good overlap between the laser beam(s) and the molecular beam[22].

A. Design

The design of the double VMIS was done with the following goals: first, we wanted to add the capability to detect ions without compromising the resolution on the electron side as compared to a standard VMIS. Second, as molecules have a typical ionization potential of 5-10 eV and, with HHG, the typical photon energies are up to 100 eV, the spectrometer should be able to focus electrons with energies up to ≈ 90 eV, and ions with kinetic energies up to ≈ 10 eV, typical for e.g. Coulomb explosion. Third, the spectrometer had to be compatible with the existing experimental chamber used for high-intensity HHG experiments containing the all-reflective short focal length XUV focussing optics[23].

The single-sided VMIS depicted in Fig. 1(a) has been tested with very good results. To that end, when extending the spectrometer to be able to record ions and electrons simultaneously, the design of the electron side, adapted from reference 24, was retained and the repeller electrode replaced by an electrode with a mesh, as shown in Fig. 1(b). On the ion side, an open extractor electrode and a flight tube, similar to that on the electron side, was added. There are two advantages with this choice of design. First, we are not changing the imaging conditions on the electron side and, second, once the optimum voltages have been found for the electrons the voltages on the ion side can be tuned independently without affecting the electron image quality. The drawback is that the ions are to some extent diffracted on the grid, which has a transmission of $\sim 80\%$, and that they have to pass through a drift region before they pass the repeller and get focussed by the fields on the ion side. This affects the energy resolution that can be achieved in the ion imaging by about a factor of two, as discussed in Section II C, but this is in most cases acceptable.

The maximum electron or ion energy is restricted by the fact that the electrons or ions move away from the detector axis due to their initial velocity perpendicular to it and, the longer the flight tube is, the bigger detector is needed to catch them. Thus, to increase the maximum detectable energy one need to decrease the flight tube length, increase the flight tube and detector diameters or use higher acceleration voltages. In our case,

the maximum detector size and the flight tube diameters were set by the existing chamber to $\sim$ 100 mm, leading to the choice of a standard detector diameter of 75 mm mounted on a CF160 flange. Similarly, the minimum flight tube lengths were set by the flange-to-flange distance of the existing experimental chamber to 690 mm. In principle, shorter flight tube lengths could have been achieved by a design where the detectors are mounted inside the vacuum chamber, but this would have led too a more complicated design, and was thus avoided. With restrictions imposed on the detector size and flight tube length, the ratio between the maximum detectable kinetic energy and the acceleration voltage scales approximately as $(r/L)^2$, where r is the detector radius and L is the flight tube length. Under the chosen conditions, this means that particles with kinetic energies up to $\approx 1\%$ of the acceleration voltage can be detected, meaning that a total voltage difference of almost 9 kV between the front of the electron detector and the front of the ion detector is required to detect electrons and ions with 90 eV and 10 eV kinetic energy, respectively. On top of this, the phosphor screens of the detectors have to be biased with an additional 5 kV above the front potentials, leading to a required total voltage difference of 14 kV over the entire spectrometer assembly. To enable this, while staying within reasonable specifications for the voltage feedthroughs of the detectors, a choice of detectors with 10 kV feedthroughs was made, and the design of the assembly made in such a way that both detectors, electrodes and flight tubes could be supplied with floating voltages of $\pm$10 kV. While the front of the detectors are not electrically connected to the flight tubes, for the following discussion and simulations we assume that the same voltage is applied to the front of the detector and the flight tube.

The resulting design of the double VMIS is shown in Fig. 2 together with the relevant dimensions. The spectrometer is mounted horizontally and the electron and ion sides are separable between the repeller electrode and the ion extractor electrode to facilitate mounting of the spectrometer on the two opposite CF200 flanges of the experimental chamber. The mounting flanges are CF200 to CF160 zero-length reducers, allowing for convenient mounting of the detectors after the spectrometer has been installed. To allow for floating voltages on the flight tubes, they are supported via ceramic spacers by the grounded mount tubes made of stainless steel. While the ion flight tube is made out of stainless steel, the electron flight tube is made out of μ-metal to provide shielding from external magnetic fields. In addition, a μ-metal cylinder, not shown in the figure, is used to cover the electrode package. The flight tubes have a front brim which is supported by four rods via ceramic spacers (white) and bushings (yellow). These brims also hold the electrode packages which can be conveniently reached and exchanged from the top of the chamber without unmounting the flight tube assemblies. The electrodes are mounted with ceramic bushings (yellow) on rods made

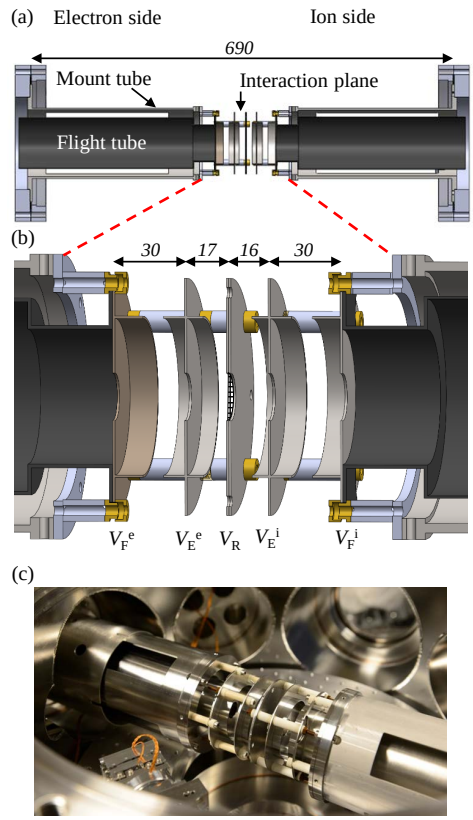

FIG. 2. Drawing of the double VMIS (a) and an expanded view of the electrode package (b). The indicated voltages are applied to the electron side flight tube (V_F^e), the electron side extractor (V_E^e), the repeller (V_R), the ion side extractor (V_E^i) and the ion side flight tube (V_F^i). A photo of the spectrometer mounted in the experimental chamber is shown in panel (c).

out of vespel and separated by ceramic spacers (white). No electrode or grounded parts are closer than 10 mm apart to allow for large voltage differences without risk of arcing.

The final design offers a large versatility by allowing for voltages of $\pm$10 kV to be applied to any of the spectrometer components (electrodes or flight tubes), and the choice of a mesh in the repeller electrode allows for independent tuning of the ion sides without affecting the electron imaging. The physical design makes it easy to mount and dismount the whole or parts of the spectrometer and, while being dimensioned for use in the existing

Operation mode	V_F^e (kV)	V_E^e (kV)	V_R (kV)	V_E^i (kV)	V_F^i (kV)
1(a) Ion TOF	0	2.354	3.000	not used	not used
1(b) Ion VMI	0	2.275	3.000	not used	not used
2(a) Electron VMI + ion TOF	5.000	-5.775	-9.200	-10.000	-10.000
2(b) Electron VMI + ion VMI	5.000	-5.775	-9.200	-8.802	-10.000

TABLE I. Simulated optimum voltages for the different operation modes.

experimental chamber, the assembly can be easily transferred also to chambers with other geometries. As an example, as shown in Section III, with the use of an additional pair of adapter flanges, the spectrometer can be installed in a standard CAMP chamber[25].

B. Operation modes

The spectrometer can be operated in a number of different photoelectron and -ion detection modes, listed below:

1. High resolution ion modes
   (a) Ion TOF
   (b) Ion VMI
2. High resolution electron modes
   (a) Electron VMI, ion TOF
   (b) Electron VMI, ion VMI

In the high resolution ion modes, the voltages are set to accelerate and detect ions on the electron side, either in TOF mode [1(a)] under Wiley-McLaren conditions[26], or in VMI mode [1(b)]. With this setting, the mesh in the repeller electrode does not impose any restriction on the achievable mass or energy resolution, since the ion side of the spectrometer is not used. In the high resolution electron modes, the electron side of the spectrometer is configured for optimum velocity map imaging conditions for electrons, while the ion side voltages are set either for ion TOF [2(a)] or ion VMI [2(b)]. The different modes are explored in Section II C.

C. Simulations

To evaluate the expected performance of the spectrometer, simulations were performed using SIMION[27] for the different operation modes listed above. An interaction region, defined by the overlap between the laser beam and the molecular beam, with a size of $100 \times 100 \times 2000$ μm^3 was used. For the VMI calculations, the electron kinetic energies were chosen in steps of 5 eV from 10 to 90 eV and the ion kinetic energies in steps of 1 eV from 2 to 10 eV. For each operation mode the optimum voltages, defined as the voltages for which the best resolution is obtained for electrons with a kinetic energy of 30 eV and singly charged ions with a kinetic energy of 6 eV and mass $m = 100$, were found. These voltages are summarized in Table I.

To find the optimum voltages for the VMI modes, a simplified simulation procedure was used, in which the trajectories of 27 particles arranged on a $3\times3\times3$ grid covering the interaction region and with their velocity component perpendicular to the detector axis were calculated and the energy or mass resolution calculated from the spread in space on the detector. For the found optimum voltages, a more elaborate procedure based on Monte Carlo sampling was used[28], resulting in more realistic resolution estimates. The method consisted in launching a large number of electrons or ions ($\sim 10^6$) with a random starting position chosen from a Gaussian distribution over the interaction volume and with a random, isotropically distributed initial momentum. The particle impacts on the detector were then sampled to generate a simulated detector image or time-of-flight trace, which was then treated similarly to experimental data in order to extract the resolution. The simulated images were inverted using an iterative algorithm[18] to retrieve the 3D momentum distribution from the 2D image. From the 3D momentum distribution the energy spectrum was calculated and the resulting peaks were fitted with Gaussian functions to calculate the energy resolution. The TOF simulations were done for ions with zero kinetic energy and only the Monte Carlo method was used, calculating the mass resolution from the width of Gaussian functions fitted to the peaks in the mass spectrum.

1. High resolution ion modes

For the high resolution ion modes, ions are detected on the electron side of the spectrometer, and for the simulations the choice was made to ground the front of the detector and the flight tube ($V_{\rm F}^{\rm e} = 0$ kV). The repeller voltage was set to $V_{\rm R} = 3$ kV to allow for detection of ions with kinetic energies up to 10 eV. Figure 3(a) shows the resulting mass resolution in operation mode 1(a) for extractor voltages from 1400 to 3000 V. The optimum extractor voltage, for which a mass resolution of $m/\Delta m = 35000$ was achieved, was found to be $V_{\rm E}^{\rm e} = 2.354$ kV. This corresponds to Wiley-McLaren conditions[26].

Figure 3(b) shows the resulting energy resolution for ion VMI in operation mode 1(b) for three different set-

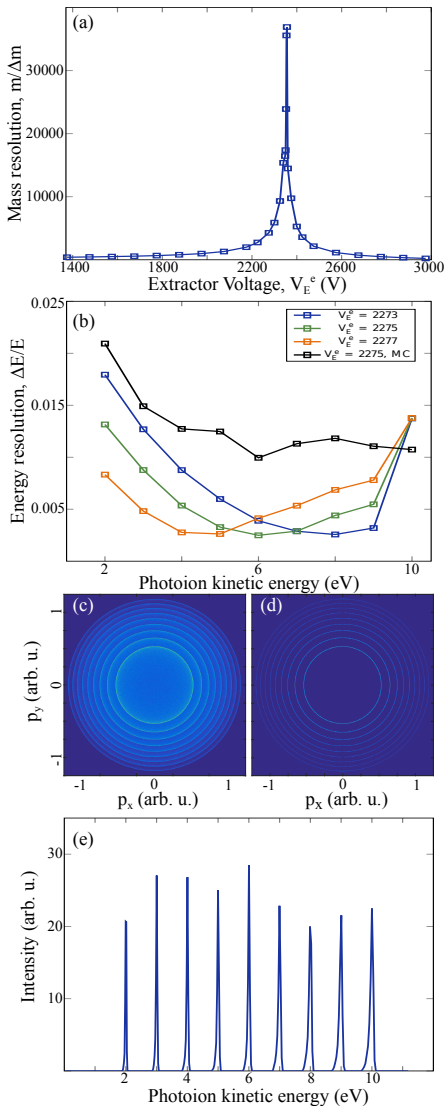

FIG. 3. Simulation results for the high resolution ion modes. Panel (a) shows the resulting mass resolution as a function of extractor voltage, $V_{\rm E}^{\rm e}$. Panel (b) shows the resulting VMI energy resolution for three different extractor voltages (V_E^e) using the 27-particle model (blue, green and orange lines) and the Monte Carlo model for the optimum setting (black line). Panels (c) and (d) show the simulated detector image and the 3D momentum distribution after inversion, for the optimum voltages. Panel (e) shows the kinetic energy spectrum calculated from the 3D momentum distribution.

tings for the extractor voltage, $V_{\rm E}^{\rm e}$, calculated using the 27-particle model (blue, green and orange lines). The optimum extractor voltage, for which the best resolution was achieved for a kinetic energy of 6 eV, was found to be $V_{\rm E}^{\rm e} = 2.275$ kV and for this setting the resulting energy resolution from the Monte Carlo simulation is shown (black line), indicating an energy resolution better than 1.5% for kinetic energies between 3 and 10 eV. In Fig. 3(c) and (d) the corresponding simulated detector image and the 3D momentum distribtion after inversion is shown, respectively. Figure 3(e) shows the kinetic energy spectrum calculated from the 3D momentum distribution.

2. High resolution electron modes

For the high resolution electron modes, electrons and ions are detected on their respective sides of the spectrometer. To maximize the possible total voltage difference over the spectrometer, the voltage on the electron side flight tube was set to $V_{\rm F}^{\rm e} = 5$ kV, so that the phosphor screen could still be operated at its full voltage bias without exceeding the limit of the electrical feedthroughs. The repeller voltage was set to $V_{\rm R} = -9.2$ kV to allow for detection of electrons with kinetic energies up to 90 eV.

Figure 4(a) shows the resulting energy resolution for electron VMI for three different settings for the extractor voltage, $V_{\rm E}^{\rm e}$, calculated using the 27-particle model (blue, green and orange lines). The optimum extractor voltage, for which the best resolution was achieved for a photoelectron energy of 30 eV, was found to be $V_{\rm E}^{\rm e} = -5.775$ kV ($\eta = 0.76$) and for this setting the resulting energy resolution from the Monte Carlo simulation is shown (black line), indicating an energy resolution better than 2% for photoelectron energies between 20 and 90 eV. In Fig. 4(b) and (c) the corresponding simulated detector image and the 3D momentum distribtion after inversion is shown, respectively. Figure 3(d) shows the photoelectron energy spectrum calculated from the 3D momentum distribution.

With the electron side conditions optimized for electron VMI, and the voltage on the ion side flight tube set to $V_{\rm F}^{\rm i} = -10$ kV to detect ions with kinetic energies up to 10 eV, the ion side can be tuned either for TOF [operation mode 2(a)] or VMI [operation mode 2(b)] by varying the ion extractor electrode voltage, $V_{\rm E}^{\rm i}$.

Figure 5(a) shows the resulting mass resolution in operation mode 2(a) for different extractor voltages , $V_{\rm E}^{\rm i}$. It is clear that it is not possible to reach Wiley-McLaren conditions within the voltage limits of the setup, due to the initial drift region between the interaction point and the mesh that the ions have to travel through. In addition, the best mass resolution of $m/\Delta m = 110$, achieved for $V_{\rm E}^{\rm i} = -10$ kV, is a factor of 300 worse than that achieved in operation mode 1(a). Figure 5(b) shows the resulting energy resolution for ion VMI in operation mode 2(b) for three different settings for the extractor voltage, $V_{\rm E}^{\rm i}$, calculated using the 27-particle model (blue, green and

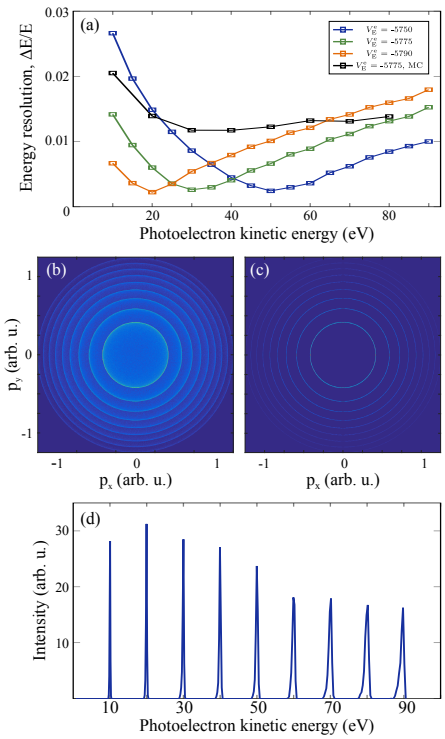

FIG. 4. Simulation results for high resolution electron VMI mode. Panel (a) shows the resulting energy resolution for three different extractor voltages (V_E^e) using the 27-particle model (blue, green and orange lines) and the Monte Carlo model for the optimum setting (black line). Panels (b) and (c) show the simulated detector image and the 3D momentum distribution after inversion, for the optimum voltages. Panel (d) shows the photoelectron energy spectrum calculated from the 3D momentum distribution.

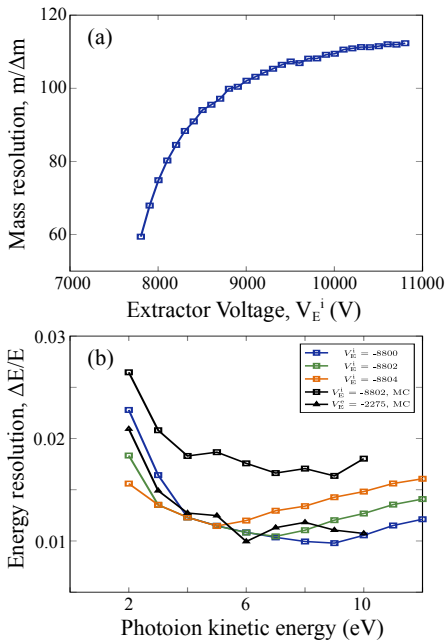

FIG. 5. Simulation results for ion detection when the electron side is optimized for electron VMI [operation modes 2(a) and 2(b)]. Panel (a) shows the resulting mass resolution as a function of extractor voltage, V_E^i. Panel (b) shows the resulting VMI energy resolution for three different extractor voltages using the 27-particle model (blue, green and orange lines) and the Monte Carlo model for the optimum setting (black line with squares). The black line with triangles shows the resolution in operation mode 1(b) obtained by the Monte Carlo method, reproduced from Fig. 3.

orange lines). The optimum extractor voltage, for which the best resolution was achieved for a kinetic energy of 6 eV, was found to be $V_E^i = -8.802$ kV and for this setting the resulting energy resolution from the Monte Carlo simulation is shown (black line with squares), indicating an energy resolution better than 2.5% for kinetic energies between 3 and 10 eV. This is a degradation in resolution of almost a factor of two as compared to the resolution obtained in operation mode 1(b) (shown by the black line with triangles), but it is still an acceptable resolution for ions in most experiments. It is interesting to note that even in operation mode 2(b), for $V_E^i = -8.802$ kV, the mass resolution of the ion TOF is $m/\Delta m = 100$, which is acceptable unless isotope resolution of heavier fragments is required.

III. FIRST EXPERIMENTAL RESULTS

To evaluate the performance of the instrument first measurements have been performed at two different light sources, the high-intensity XUV beamline at the Lund Laser Centre[23] and the I1011 beamline at the Max-lab synchrotron facility. While the double VMIS was designed to be used in the experimental chamber of the high-intensity XUV beamline in Lund, it is also designed to fit in a CAMP chamber[25] to enable using it at e.g. FELs or synchrotron facilities. There are many differences between the sources used, for example the photon energies used, length of the light bunches and the intensity. In both experiments, the target gas was intro-

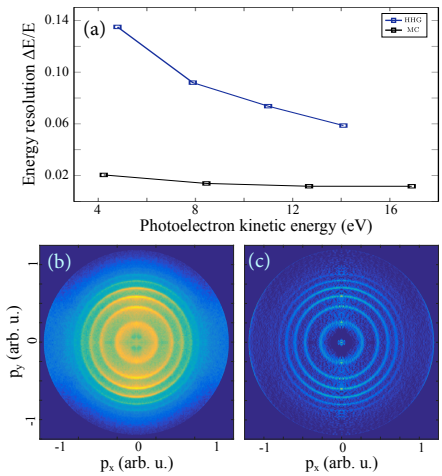

FIG. 6. Experimental results for high resolution electron VMI mode using high-order harmonics to ionize neon. In panel (a) the blue line shows the measured energy resolution for $\eta = 0.76$ and the black line line shows the simulated resolution from Fig. 4. Panels (b) and (c) show the measured detector image and the 3D momentum distribution after inversion.

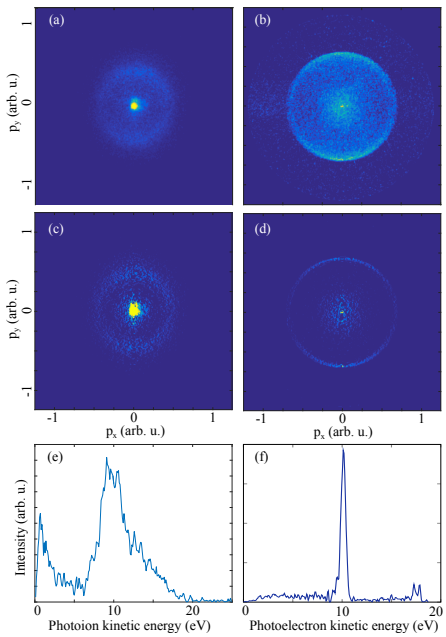

FIG. 7. Experimental results from ionization of N_2 using 420 eV photons at Max-lab beamline I1011. The measured detector images for photions (a) and -electrons (b) are shown together with the corresponding 3D momentum distributions [(c) and (d)] obtained through inversion. Panels (e) and (f) show the photoion and -electron kinetic energy spectra calculated from the 3D momentum distributions.

duced using a pulsed molecular beam from an Even-Lavie solenoid valve able to produce high density pulses with durations as short as 10 μs[29,30]. To be able to apply covariance analysis, synchronized single-shot data needs to be acquired. At the intense XUV beamline the repetition rate is 10 Hz, set by the laser repetition rate, and acquisition of single-shot data is relatively straightforward. For the synchrotron experiments, the repetition rate is far too high to take single shot data. Therefore, the pulsed molecular beam and the camera shutter was used to define the repetition rate, and we set it to 20 Hz, which was the maximum frame rate of the camera. In addition, another difference between the sources that is important for covariance analysis is that a synchrotron is a stable light source compared to laser-driven HHG, and in the latter case the XUV intensity will vary on a shot-to-shot basis. A fluctuating light source will introduce correlations between channels that are physically not correlated. To circumvent this problem, it is likely that methods like partial covariance have to be used[31].

A. HHG experiments

In an attempt to estimate the experimental energy resolution, the electron side of the VMIS was tested at the intense XUV beamline in Lund using high-order harmonics generated in argon. The spectrum of the harmonics, after removal of the generating infrared pulse by means of metallic filters, spanned from 23 to 42 eV, corresponding to harmonics 15 to 27. Neon, with an ionization potential of 21.6 eV, was used as the target gas. Fig. 6 summarizes the result of the measurement, that was done using voltages $V_F^e = 0$ kV and $V_R = -6$ kV in order to cover the relevant energy range. Figure 6(a) shows the measured energy resolution for electron VMI (blue line) for the expected optimum setting of the extractor voltage ($\eta = 0.76$). The black line shows the simulated resolution from Fig. 4. In Fig. 6(b) and (c) the measured detector image and the 3D momentum distribtion after inversion is shown, respectively. From the results, it is clear that the resolution is limited by the bandwidth of the harmonics (~ 0.5 eV) rather than the electron imaging.

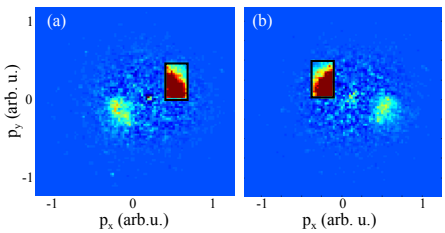

FIG. 8. Ion-ion covariance analysis of the N^+ momentum distributions from ionization of N_2 using 420 eV photons. Both panels show the covariance between the signal in the area marked by the black rectangle and the signal in each pixel of the image.

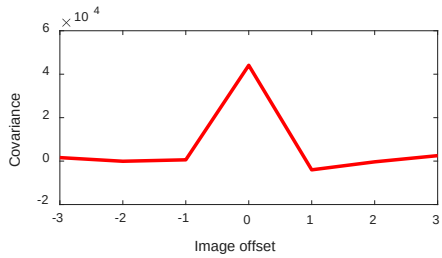

FIG. 9. Covariance between the total ion signal and the total photoelectron signal for different offsets between the two image streams.

B. Experiments at Max-lab

The capability of the DVMIS to simultaneously record photoions and -electrons was tested at the I1011 beamline at Max-lab using a photon energy of 420 eV and N_2 as the target gas. The 1s-ionization threshold of N_2 is 409.9 eV, resulting in an ion in either the $1\sigma_g^{-1}$ or $1\sigma_u^{-1}$ state, but the splitting between the two states is too small to be resolved in the experiment. After removing a 1s electron, the excited molecular ion may relax via Auger processes and the resulting doubly charged molecular ion can undergo Coulomb explosion resulting in N^+ fragments with energies around 10 eV[32]. The electrons from the first ionization step, with an energy of 10.1 eV, and the N^+ fragments can be recorded simultaneously with the DVMIS, making N_2 a good candidate for evaluating the covariance imaging capabilities of the instrument. Figure 7 shows the recorded 2D momentum distributions of ions [panel (a)] and electrons [panel (b)] together with their 3D momentum distributions obtained through inversion of the 2D images [panels (c) and (d)]. In panels (e) and (f) the photoion and -electron kinetic energy spectra calculated from the 3D momentum distributions are shown. From the angular distribution, an asymmetry parameter for the direct photoelectron peak at 10.1 eV of $\beta \approx 0.8$ was extracted, in good agreement with values reported in literature[33]. The Auger electrons are too energetic to be imaged by the VMI. On the ion side, the ring originates from Coulomb explosion and therefore exhibits a broad energy distribution.

In a first attempt to use the instrument to study correlation between the products of the ionization, the covariance within the ion images was studied. Using an acquisition of 20000 shots, the covariance between the signal in a selected region of the ion image and each pixel in the image was calculated, with the results shown in Fig. 8. The black rectangle marks the selected region, chosen from the Coulomb explosion ring, naturally exhibiting a high covariance since it is correlated to itself. In addition, a corresponding area on the opposite side of the Coulomb explosion ring shows a peak in covariance. This is a clear indication that the feature indeed comes from the ejection of two N^+ ions with the same kinetic energy, but with opposite directions. In addition, it shows that the covariance analysis is able to catch such correlations also under multi-event imaging conditions.

Ultimately, the development of the DVMIS instrument aims to make possible the study of correlations between ions and electrons and, to that end, we have started performing covariance analysis of correlation between the photoion and -electron images. Figure 9 shows the covariance calculated between different observables in the ion and electron images, made for a varying frame offset between the two image streams, in order to confirm that any observed correlation is connected to the fact that the images are acquired synchronously for ions and electrons. The red line shows the covariance calculated between the total ion signal and the total photoelectron signal, showing a clear peak for perfect synchronization, confirming that the synchronization between the two acquisitions is working as intended.

IV. CONCLUSION AND OUTLOOK

In conclusion, we have reported on the design and performance of a velocity map imaging (VMI) spectrometer optimized for experiments using high-intensity extreme ultraviolet (XUV) sources such as laser-driven high-order harmonic generation (HHG) sources and free-electron lasers (FELs). The instrument is versatile and allows for combining photoelectron and -ion detection modes, such as ion time-of-flight (TOF), ion VMI and electron VMI, in different ways, depending on the required information and the process under study. The performance for the different detection modes was estimated using simulations, and first experimental results from an intense HHG source and a synchrotron beamline were presented.

While the presented results confirm that the acquired data contains information about the correlation between

the photion and -electron images, efforts are currently being made to extract signatures of the molecular frame photoelectron angular distributions (MFPADs) by studying the covariance between ions from Coulomb explosion along a certain direction, indicating the alignment of the molecules at the time of ionization, and the photoelectron images. So far, this analysis has not revealed any conclusive results, likely because of lack of statistics.

ACKNOWLEDGMENTS

This research was supported by the Swedish Research Council, the Swedish Foundation for Strategic Research and the European COST Action CM1204 XLIC. This project has received funding from the European Union's Horizon 2020 research and innovation programme under the Marie Sklodowska-Curie grant agreement no. 641789 MEDEA.

[1]M. Ferray, A. L'Huillier, X. Li, L. Lompre, G. Mainfray, and C. Manus, J. Phys. B **21**, L31 (1988).

[2]P. Agostini and L. F. DiMauro, Rep. Prog. Phys **67**, 813 (2004).

[3]W. Ackermann, G. Asova, V. Ayvazyan, A. Azima, N. Baboi, J. Bhr, V. Balandin, B. Beutner, A. Brandt, A. Bolzmann, R. Brinkmann, O. I. Brovko, M. Castellano, P. Castro, L. Catani, E. Chiadroni, S. Choroba, A. Cianchi, J. T. Costello, D. Cubaynes, J. Dardis, W. Decking, H. Delsim-Hashemi, A. Delserieys, G. D. Pirro, M. Dohlus, S. Dsterer, A. Eckhardt, H. T. Edwards, B. Faatz, J. Feldhaus, K. Flttmann, J. Frisch, L. Frhlich, T. Garvey, U. Gensch, C. Gerth, M. Grler, N. Golubeva, H.-J. Grabosch, M. Grecki, O. Grimm, K. Hacker, U. Hahn, J. H. Han, K. Honkavaara, T. Hott, M. Hning, Y. Ivanisenko, E. Jaeschke, W. Jalmuzna, T. Jezynski, R. Kammering, V. Katalev, K. Kavanagh, E. T. Kennedy, S. Khodyachykh, K. Klose, V. Kocharyan, M. Krfer, M. Kollewe, W. Koprek, S. Korepanov, D. Kostin, M. Krassilnikov, G. Kube, M. Kuhlmann, C. L. S. Lewis, L. Lilje, T. Limberg, D. Lipka, F. Lhl, H. Luna, M. Luong, M. Martins, M. Meyer, P. Michelato, V. Miltchev, W. D. Mller, L. Monaco, W. F. O. Mller, O. Napieralski, O. Napoly, P. Nicolosi, D. Nlle, T. Nuñez, A. Oppelt, C. Pagani, R. Paparella, N. Pchalek, J. Pedregosa-Gutierrez, B. Petersen, B. Petrosyan, G. Petrosyan, L. Petrosyan, J. Pflger, E. Plnjes, L. Poletto, K. Pozniak, E. Prat, D. Proch, P. Pucyk, P. Radcliffe, H. Redlin, K. Rehlich, M. Richter, M. Roehrs, J. Roensch, R. Romaniuk, M. Ross, J. Rossbach, V. Rybnikov, M. Sachwitz, E. L. Saldin, W. Sandner, H. Schlarb, B. Schmidt, M. Schmitz, P. Schmser, J. R. Schneider, E. A. Schneidmiller, S. Schnepp, S. Schreiber, M. Seidel, D. Sertore, A. V. Shabunov, C. Simon, S. Simrock, E. Sombrowski, A. A. Sorokin, P. Spanknebel, R. Spesyvtsev, L. Staykov, B. Steffen, F. Stephan, F. Stulle, H. Thom, K. Tiedtke, M. Tischer, S. Toleikis, R. Treusch, D. Trines, I. Tsakov, E. Vogel, T. Weiland, H. Weise, M. Wellhfer, M. Wendt, I. Will, A. Winter, K. Wittenburg, W. Wurth, P. Yeates, M. V. Yurkov, I. Zagorodnov, and K. Zapfe, Nature Photonics **1**, 336 (2007).

[4]P. Emma, R. Akre, J. Arthur, R. Bionta, C. Bostedt, J. Bozek, A. Brachmann, P. Bucksbaum, R. Coffee, F.-J. Decker, Y. Ding, D. Dowell, S. Edstrom, A. Fisher, J. Frisch, S. Gilevich, J. Hastings, G. Hays, P. Hering, Z. Huang, R. Iverson, H. Loos, M. Messerschmidt, A. Miahnahri, S. Moeller, H.-D. Nuhn, G. Pile, D. Ratner, J. Rzepiela, D. Schultz, T. Smith, P. Stefan, H. Tompkins, J. Turner, J. Welch, W. White, J. Wu, G. Yocky, and J. Galayda, Nature Photonics **4**, 641 (2010).

[5]T. Ishikawa, H. Aoyagi, T. Asaka, Y. Asano, N. Azumi, T. Bizen, H. Ego, K. Fukami, T. Fukui, Y. Furukawa, S. Goto, H. Hanaki, T. Hara, T. Hasegawa, T. Hatsui, A. Higashiya, T. Hirono, N. Hosoda, M. Ishii, T. Inagaki, Y. Inubushi, T. Itoga, Y. Joti, M. Kago, T. Kameshima, H. Kimura, Y. Kirihara, A. Kiyomichi, T. Kobayashi, C. Kondo, T. Kudo, H. Maesaka, X. M. Maréchal, T. Masuda, S. Matsubara, T. Matsumoto, T. Matsushita, S. Matsui, M. Nagasono, N. Nariyama, H. Ohashi, T. Ohata, T. Ohshima, S. Ono, Y. Otake, C. Saji, T. Sakurai, T. Sato, K. Sawada, T. Seike, K. Shirasawa, T. Sugimoto, S. Suzuki, S. Takahashi, H. Takebe, K. Takeshita, K. Tamasaku, H. Tanaka, R. Tanaka, T. Tanaka, T. Togashi, K. Togawa, A. Tokuhisa, H. Tomizawa, K. Tono, S. Wu, M. Yabashi, M. Yamaga, A. Yamashita, K. Yanagida, C. Zhang, T. Shintake, H. Kitamura, and N. Kumagai, Nature Photonics **6**, 540 (2012).

[6]B. W. J. McNeil and N. R. Thompson, Nature Photonics **4**, 814 (2010).

[7]J. M. Glownia, J. Cryan, J. Andreasson, A. Belkacem, N. Berrah, C. I. Blaga, C. Bostedt, J. Bozek, L. F. DiMauro, L. Fang, J. Frisch, O. Gessner, M. Ghr, J. Hajdu, M. P. Hertlein, M. Hoener, G. Huang, O. Kornilov, J. P. Marangos, A. M. March, B. K. McFarland, H. Merdji, V. S. Petrovic, C. Raman, D. Ray, D. A. Reis, M. Trigo, J. L. White, W. White, R. Wilcox, L. Young, R. N. Coffee, and P. H. Bucksbaum, Optics Express **18**, 17620 (2010).

[8]F. Lépine, M. Y. Ivanov, and M. J. J. Vrakking, Nature Photonics **8**, 195 (2014).

[9]A. Sorokin, M. Wellhöfer, S. Bobashev, K. Tiedtke, and M. Richter, Physical Review A **75**, 051402 (2007).

[10]N. Berrah, J. Bozek, J. Costello, S. Düsterer, L. Fang, J. Feldhaus, H. Fukuzawa, M. Hoener, Y. Jiang, P. Johnsson, E. Kennedy, M. Meyer, R. Moshammer, P. Radcliffe, M. Richter, A. Rouzée, A. Rudenko, A. Sorokin, K. Tiedtke, K. Ueda, J. Ullrich, and M. Vrakking, Journal of Modern Optics **57**, 1015 (2010).

[11]P. H. Bucksbaum, R. Coffee, and N. Berrah, in *Advances In Atomic, Molecular, and Optical Physics* (Elsevier BV, 2011) pp. 239–289.

[12]L. Fang, T. Osipov, B. Murphy, F. Tarantelli, E. Kukk, J. P. Cryan, M. Glownia, P. H. Bucksbaum, R. N. Coffee, M. Chen, C. Buth, and N. Berrah, Physical Review Letters **109** (2012).

[13]R. Neutze, R. Wouts, D. van der Spoel, E. Weckert, and J. Hajdu, Nature **406**, 752 (2000).

[14]M. M. Seibert, T. Ekeberg, F. R. N. C. Maia, M. Svenda, J. Andreasson, O. Jnsson, D. Odić, B. Iwan, A. Rocker, D. Westphal, M. Hantke, D. P. DePonte, A. Barty, J. Schulz, L. Gumprecht, N. Coppola, A. Aquila, M. Liang, T. A. White, A. Martin, C. Caleman, S. Stern, C. Abergel, V. Seltzer, J.-M. Claverie, C. Bostedt, J. D. Bozek, S. Boutet, A. A. Miahnahri, M. Messerschmidt, J. Krzywinski, G. Williams, K. O. Hodgson, M. J. Bogan, C. Y. Hampton, R. G. Sierra, D. Starodub, I. Andersson, S. Bajt, M. Barthelmess, J. C. H. Spence, P. Fromme, U. Weierstall, R. Kirian, M. Hunter, R. B. Doak, S. Marchesini, S. P. Hau-Riege, M. Frank, R. L. Shoeman, L. Lomb, S. W. Epp, R. Hartmann, D. Rolles, A. Rudenko, C. Schmidt, L. Foucar, N. Kimmel, P. Holl, B. Rudek, B. Erk, A. Hmke, C. Reich, D. Pietschner, G. Weidenspointner, L. Strder, G. Hauser, H. Gorke, J. Ullrich, I. Schlichting, S. Herrmann, G. Schaller, F. Schopper, H. Soltau, K.-U. Khnel, R. Andritschke, C.-D. Schrter, F. Krasniqi, M. Bott, S. Schorb, D. Rupp, M. Adolph, T. Gorkhover, H. Hirsemann, G. Potdevin, H. Graafsma, B. Nilsson, H. N. Chapman, and J. Hajdu, Nature **470**, 78 (2011).

[15]J. Ullrich, R. Moshammer, A. Dorn, R. Dörner, L. P. H. Schmidt, and H. Schniidt-Böcking, Reports on Progress in Physics **66**, 1463 (2003).

[16]A. T. J. B. Eppink and D. H. Parker, Rev. Sci. Instr. **68**, 3477 (1997).

[17]L. M. Smith, D. R. Keefer, and S. Sudharsanan, Journal of Quantitative Spectroscopy and Radiative Transfer **39**, 367 (1988).

[18]M. J. J. Vrakking, Rev. Sci. Instr. **72**, 4084 (2001).

[19]L. J. Frasinski, K. Codling, and P. A. Hatherly, Science **246**, 1029 (1989).

[20]L. J. Frasinski, M. Stankiewicz, P. A. Hatherly, G. M. Cross,

K. Codling, A. J. Langley, and W. Shaikh, Physical Review A **46**, R6789 (1992).
[21] J. Zhu and I. W. T. Hill, Journal of the Optical Society of America B **14**, 2212 (1997).
[22] P. Johnsson, A. Rouzée, W. Siu, Y. Huismans, F. Lépine, T. Marchenko, S. Düsterer, F. Tavella, N. Stojanovic, H. Redlin, A. Azima, and M. J. J. Vrakking, Optics Letters **35**, 4163 (2010).
[23] B. Manschwetus, L. Rading, F. Campi, S. Maclot, H. Coudert-Alteirac, J. Lahl, H. Wikmark, P. Rudawski, C. M. Heyl, B. Farkas, T. Mohamed, A. L'Huillier, and P. Johnsson, Phys. Rev. A **93**, 061402 (2016).
[24] F. Rosca-Pruna, *Alignment of Diatomic Molecules Induced by Intense Laser Fields*, Ph.D. thesis, VU University of Amsterdam (2001).
[25] L. Strüder, S. Epp, D. Rolles, R. Hartmann, P. Holl, G. Lutz, H. Soltau, R. Eckart, C. Reich, K. Heinzinger, C. Thamm, A. Rudenko, F. Krasniqi, K.-U. Khnel, C. Bauer, C.-D. Schrter, R. Moshammer, S. Techert, D. Miessner, M. Porro, O. Hlker, N. Meidinger, N. Kimmel, R. Andritschke, F. Schopper, G. Weidenspointner, A. Ziegler, D. Pietschner, S. Herrmann, U. Pietsch, A. Walenta, W. Leitenberger, C. Bostedt, T. Mller, D. Rupp, M. Adolph, H. Graafsma, H. Hirsemann, K. Grtner, R. Richter, L. Foucar, R. L. Shoeman, I. Schlichting, and J. Ullrich, Nuclear Instruments and Methods in Physics Research Section A: Accelerators, Spectrometers, Detectors and Associated Equipment **614**, 483 (2010).
[26] W. C. Wiley and I. H. McLaren, Review of Scientific Instruments **26**, 1150 (1955).
[27] "Simion ion and electron optics simulator," `http://simion.com`.
[28] O. Ghafur, W. Siu, P. Johnsson, M. F. Kling, M. Drescher, and M. J. J. Vrakking, Rev. of Sci. Instr. **80**, 033110 (2009).
[29] U. Even, Advances in Chemistry **2014**, 1 (2014).
[30] U. Even, EPJ Techniques and Instrumentation **2** (2015).
[31] L. Frasinski, A. Giles, P. Hatherly, J. Posthumus, M. Thompson, and K. Codling, Journal of Electron Spectroscopy and Related Phenomena **79**, 367 (1996).
[32] T. Weber, O. Jagutzki, M. Hattass, A. Staudte, A. Nauert, L. Schmidt, M. H. Prior, A. L. Landers, A. Bruning-Demian, H. Bruning, C. L. Cocke, T. Osipov, I. Ali, R. D. Muiño, D. Rolles, F. J. G. de Abajo, C. S. Fadley, M. A. V. Hove, A. Cassimi, H. Schmidt-Böcking, and R. Dörner, Journal of Physics B: Atomic, Molecular and Optical Physics **34**, 3669 (2001).
[33] B. Kempgens, A. Kivimäki, M. Neeb, H. M. Köppe, A. M. Bradshaw, and J. Feldhaus, Journal of Physics B: Atomic, Molecular and Optical Physics **29**, 5389 (1996).